Generation and growth of wind waves over a viscous liquid

Anna Paquier

NNT : 2016SACLS183

THESE DE DOCTORAT
DE
L'UNIVERSITE PARIS-SACLAY
PREPAREE A
L'UNIVERSITE PARIS-SUD

ECOLE DOCTORALE N°579
Sciences Mécaniques et Énergétiques, Matériaux et Géosciences

Spécialité de doctorat : Mécanique des fluides

Par

Mme Anna Paquier

Génération et croissance des vagues à la surface d'un liquide visqueux sous l'effet du vent

Thèse présentée et soutenue à Orsay, le 11 juillet 2016 :

Composition du Jury :

M. Hubert BRANGER	Chercheur CNRS, IRPHE	Examinateur
M. Olivier CADOT	Professeur, ENSTA-ParisTech, IMSIA	Président
M. François CHARRU	Professeur, Université de Toulouse, IMFT	Rapporteur
M. Frédéric MOISY	Professeur, Université Paris-Sud, FAST	Co-directeur de thèse
M. Marc RABAUD	Professeur, Université Paris-Sud, FAST	Directeur de thèse
M. Peter SPELT	Professeur, Université de Lyon, LMFA	Rapporteur

THESIS

submitted for the degree of

DOCTOR OF PHILOSOPHY OF THE UNIVERSITY PARIS-SACLAY

Thesis conducted at the University of Paris-Sud
in the laboratory Fluides Automatique et Systèmes Thermiques

Graduate School ED n°579
Sciences Mécaniques et Energétiques, Matériaux et Géosciences (SMEMaG)
Field: FLUID MECHANICS

Anna PAQUIER

Generation and growth of wind waves over a viscous liquid

Thesis directed by Marc RABAUD and Frédéric MOISY

defended publicly on July, 11th 2016 at Orsay, France

In front of the jury composed by:

Hubert BRANGER	Researcher CNRS (IRPHE)	-	*Examiner*
Olivier CADOT	Professor, ENSTA-ParisTech (IMSIA)	-	*President*
François CHARRU	Professor, University of Toulouse (IMFT)	-	*Reviewer*
Frédéric MOISY	Professor, University of Paris-Sud (FAST)	-	*PhD co-supervisor*
Marc RABAUD	Professor, University of Paris-Sud (FAST)	-	*PhD supervisor*
Peter SPELT	Professor, University of Lyon (LMFA)	-	*Reviewer*

NNT: 2016SACLS183

À mes frères.
To my brothers.

Remerciements

Je tiens tout d'abord à remercier l'ensemble des membres du jury pour l'interêt qu'ils ont porté à mes travaux de thèse. Je remercie Olivier Cadot pour sa présidence du jury (et plus tôt pendant ma thèse pour son expertise sur les fils-chauds et les souffleries), Peter Spelt et François Charru pour avoir accepté d'être rapporteurs de cette thèse ainsi que pour leur lecture attentive et les questions et remarques pertinentes dont ils m'ont fait part, et Hubert Branger pour avoir accepté de faire partie de mon jury de thèse. Je regrette que Christophe Clanet n'ait pu assister à ma soutenance et je le remercie ici pour l'intérêt porté à mon travail et pour le matériel généreusement prêté. Je lui adresse aussi avec retard mes remerciements pour avoir largement renforcé ma passion de la mécanique des fluides durant mes années à l'X par sa vision enthousiasmante de ce domaine.

À Marc et Frédéric, le duo sans faille de mes directeurs de thèse, j'adresse ma plus vive gratitude pour cette belle aventure doctorale, depuis notre rencontre par Skype Seattle-Orsay jusqu'à la soutenance un après-midi de juillet. Durant toute ma thèse, ils ont encadré mes travaux avec beaucoup d'enthousiame et de présence tout en encourageant les initiatives et en me laissant une agréable liberté de façon de faire. Leurs idées pertinentes, leurs conseils éclairés, leur disponibilité et la confiance qu'ils m'ont toujours accordées ont fortement contribuées au bon déroulement et à la réussite de cette thèse et je les en remercie chaleureusement. Merci pour tout ce que vous m'avez appris.

Je remercie les ingénieurs et techniciens de l'atelier, Lionel, Alban et Rafaël, ainsi que Christian maintenant à la retraite ; sans vous, mon montage aurait tourné deux fois moins bien en deux fois plus de temps. Il aura quand même fallu un an d'acharnement pour que tous les morceaux se mettent à fonctionner en même temps... juste à temps pour le début des travaux sur le chantier voisin. Le jour où les tractopelles ont commencé à creuser dans la roche à 50 m de mon montage expérimental, je ne me doutais pas que j'en retirerais une connaissance aussi fine de la douce musique de l'alarme du labo et des horaires des derniers RER.

Pendant toute ma thèse, j'ai aussi eu l'opportunité au travers de ma mission doctorale de prendre part au projet de la Maison d'Initiation et de Sensibilisation aux Sciences. J'y ai travaillé et échangé avec un grand nombre de personnes animées par le même goût pour la vulgarisation scientifique. Merci à elles : en plus d'avoir énormement appris, j'ai partagé de très bons moments, notamment avec les autres doctorants-animateurs. Je tiens également à remercier plus spécialement Philippe pour son encadrement passionné sur l'atelier Science des Bateaux, et Valérie qui n'a cessé de m'impressionner par son indéfectible motivation et son enthousiasme à la tête de la MISS. Je mentirais si je disais que les nombreuses animations d'atelier pendant ma rédaction ne m'ont pas donné quelques sueurs froides concernant l'avancement de mon manuscrit mais j'ai cependant pris beaucoup de plaisir à animer ces ateliers. Finalement, rien de tel que de passer la journée avec des enfants de huit ans survoltés pour vous changer les idées pendant votre rédaction.

Je tiens à remercier l'ensemble des membres du laboratoire FAST pour ces trois années passées dans une super ambiance. Merci à tous ceux avec qui j'ai échangé lors de discussions scientifiques et moins scientifiques au labo, dans les couloirs, à la cafèt' ou au CESFO (y compris ceux qui y mangent après 11h30). Leur bonne humeur et leur bon humour ont rendu ces années de thèse très agréables. Des remerciements tout particuliers aux thésards et postdocs : j'ai partagé avec vous de super moments, au labo et en dehors du labo, autour d'un café, d'une grille de mots fléchés, d'une bière, d'un film, d'un mur d'escalade, d'un jeu de plateau ou d'une bouteille de rhum arrangé ananas-vanille. En particulier, Antoine, que j'ai fait déménager de son bureau trois mois après mon arrivée

pour y installer ma manip ; Johan, qui m'entendait à travers les murs proférer des interjections plus ou moins polies quand le glycérol de ma cuve tentait une évasion ; Sarah, dont la bonne humeur et les gâteaux ont toujours eu mon admiration ; Aurore, qui a toujours bien pris mes blagues à base de cailloux ; et Nathanaël, pour sa capacité à faire sortir les gens de leurs bureaux pour les rassembler sympathiquement ailleurs.

Un grand merci à mes amies et amis, ceux tout proches comme ceux de l'autre côté de la planète, qui m'ont soutenue et encouragée et avec qui j'ai pu décompresser d'une façon ou d'une autre durant cette thèse. Mentions spéciales à Amélie, Pauline, Charles, Anaïs, Françoise, Alexia, Marie, Thibault P, Hoel, Chloé, Antoine L, Jérémy, Thibaut H et Martin. Une pensée aussi pour la joyeuse bande de théâtreux qui ont partagé mes oublis de texte sous l'oeil désapprobateur mais patient de Xavier. Merci à tout ceux qui se sont déplacés pour la soutenance et m'ont aidée pour l'organisation et l'installation du pot de thèse et la récupération en voiture des divers membres de ma famille égarés sur le chemin vers le labo (merci Ludo !). Enfin, je remercie ma famille pour leur soutien, en particulier mes parents qui me le transmettent depuis des milliers de kilomètres de distance, littéralement. Des remerciements également à mes frères avec qui je défais et refais le monde si souvent et avec tant de plaisir. J'espère que vous savez à quel point vous êtes géniaux.

Merci à tous.

About wind waves...

"No really satisfactory explanation of the phenomenon has been offered and not even the physical processes involved can be regarded as known."

O. M. Phillips,
On the generation of waves by turbulent wind,
(1957) J. Fluid Mech., vol. 2 (5), pp. 417–445

"If one talks to a typical physicist about this question, one is likely to encounter surprise that such an obvious problem remains unsolved. [...] We can only say that the subject of the mechanics of the air-sea interface still requires more measurements and more ideas."

R. W. Stewart,
Mechanics of the Air–Sea Interface,
(1967) Phys. Fluids, vol. 10, pp. S47–S55

"Many formidable challenges are still ahead for a better understanding of physics of wind and waves."

T. Hara & C. C. Mei,
Frequency downshift in narrowbanded surface waves under the influence of wind,
(1991) J. Fluid Mech., vol. 230, pp. 429–477

"A definitive explanation of the wave growth mechanism either physical or theoretical remains to be propounded at the present time."

Y. S. Tsai, A. J. Grass & R. R. Simons,
On the spatial linear growth of gravity-capillary water waves sheared by a laminar airflow,
(2005) Phys. Fluids, vol. 17 (9), 095101

"[T]he mechanisms that generate these surface waves are still an open issue"

M.-Y. Lin, C.-H. Moeng, W.-T. Tsai, P. P. Sullivan & S. E. Belcher,
Direct numerical simulation of wind-wave generation processes,
(2008) J. Fluid Mech., vol. 616, pp. 1–30

"Despite a significant progress and numerous publications over the last few decades a comprehensive understanding of the process of waves' excitation by wind still has not been achieved."

D. Liberzon & L. Shemer,
Experimental study of the initial stages of wind waves' spatial evolution,
(2011) J. Fluid Mech., vol. 681, pp. 462–498

List of symbols:

c_φ	phase velocity
f	frequency
g	gravity constant
h	depth of the tank
k	wavenumber
k_c	capillary wavenumber
u	mean velocity profile in the tank
u^*	friction velocity
u_c^*	critical friction velocity
x	distance along the test section (fetch)
y	transverse distance to the center of the channel
z	vertical distance to the interface
z^+	dimensionless distance from the interface
H	height of the wind tunnel
L	length of the tank
Re	Reynolds number in the liquid
Re_τ	half-height channel Reynolds number
U	mean air velocity profile
U^+	dimensionless mean velocity in the air
U_a	mean air velocity at the center of the channel
U_c	critical velocity
U_s	surface velocity
V_c	convection velocity
V_{conv}	experimental convection velocity
W	width of the tank and wind channel
β	spatial growth rate of the squared amplitude of the waves
$\delta_{0.99}$	thickness of the boundary layer in the air
δ_ν	thickness of the viscous sublayer in the air
γ	surface tension
λ	wavelength
λ_c	capillary wavelength
ν	kinematic viscosity of the liquid
ν_a	kinematic viscosity of the air
ρ	density of the liquid
ρ_a	density of the air
τ	interfacial shear stress
ζ	amplitude of the surface deformation
Λ_x	correlation length in the x direction
Λ_y	correlation length in the y direction

Table of contents

Chapter 1

General introduction

The encounter of a perfectly still mirror-like stretch of water outdoors is a relatively rare occurrence. Indeed, it may look like slight wind is enough to create oscillations at the surface of any body of water, be it a lake, the ocean, or a simple puddle. True, these deformations may be tiny tremors, only visible when light reflects adequately on the water. If the wind is only a faint breeze, the water surface retains a general flat smooth appearance, with at the most minute barely distinguishable deformations. However, when the wind grows stronger, the surface becomes rougher and small ripples start to emerge. After a prolonged wind action or propagation from their point of origin, these first waves may evolve greatly, getting longer and longer, shifting from the short wavelengths of a few centimeters of the first ripples to the greater wavelengths of the order of ten to a hundred meters that can be observed at sea. Depending on the wind, hardly visible perturbations may grow into waves so steep they break.

Figure 1.1: Small surface waves generated by wind over a lake. The wind is blowing roughly diagonally from the bottom left to the top right corner. Photography taken at Xuanwu Lake, in Nanjing, China.

Wind waves are a fascinating phenomenon and their generation is a fundamental problem of fluid mechanics that has lead to more than a century of research. Since the surface motions caused by wind and swell play an important role in the mass and heat exchanges between oceans and atmosphere, this question is deeply related to the fields of

oceanography, meteorology and coastal engineering [LeBlond and Mysak, 1981, Janssen, 2004] [Babanin et al., 2012]. Oceans are indeed far from being flat and smooth. The mean wind velocity over the ocean surface is of the order of 7 $m.s^{-1}$, while waves amount to more than a meter of average height [Tokinaga and Xie, 2011]. Many works of research have been motivated by the accurate inclusion of the effects of wind waves into air-sea fluxes [Bretschneider, 1951] [Kudryavtsev et al., 2014] towards applications in meteorological forecasting, marine transportation safety or coastal protection. More recently, the increasing demand for ecologically clean energy sources has encouraged attempts towards the efficient harnessing of the largely available energy of waves and has fueled more research into the field [Falcão, 2010].

The great interest for the understanding of wind waves may only be equaled by the difficulty of grasping the details of their generation and evolution. Indeed, a wide panel of parameters come to play a role and the intrinsic coupling between wave and wind (the airflow acts on the waves and vice versa) leads to complex interactions. Independently from the propagation, amplification and general behavior of the waves once they have been generated, the generation process of waves under the action of wind is somewhat still obscure. Energy is transferred from the air motion to the liquid, creating a drift current and surface waves in a process than has still not been made entirely clear. A great number of scientists have attempted to characterize the different stages of generation and growth of water waves under the action of wind, but despite the numerous works of research, the specifics of wind wave formation remains poorly explained.

One may be surprised that such a simple system is not fully understood. The problem looks straightforward and its apparent simplicity is reinforced by the fact that almost everybody has seen waves created by wind over water. Nevertheless, the more we seem to learn about wind waves, the more we unearth questions. After a century of theoretical analyses, numerical simulations, experiments in laboratory and field observations, there are still major gaps in our understanding of the phenomenon, as quotes from various publications in the past sixty years may attest (see page vii).

The physics of wind wave generation has indeed been under investigation for quite a long time. In 1844, Russel describes the visual aspect of a air-water interface for a wind of increasing strength [Russell, 1844]. He notes the "considerable regularity" of the small waves generated uniformly over smooth water by a wind stronger than two miles per hour (about 1 $m.s^{-1}$). A couple of decades later, Helmholtz and Kelvin lay the first bases for the theoretical analysis of the wind waves problem [von Helmholtz, 1868] [Thomson, 1871], subsequently giving their names to what is now known as one of the most classical instability in fluid mechanics. The next leap in the understanding the wind waves phenomenon then waited until 1957, a pivotal turn for wind wave research. It was indeed a prolific year as no less than two models, developed independently by Phillips and Miles, were proposed that same year [Phillips, 1957] [Miles, 1957]. While these two models both provide extremely interesting theoretical analyses, they are based on different approaches and lead to quite different predictions. Phillips' and Miles' works brought a renewed interest to the problem of wind wave generation and growth, and an abundance of publications came to be, to test, improve, validate or confront these models, as well as explore the problem through new approaches or more advanced techniques.

This chapter is intended as an introduction to the general understanding of wind wave generation and growth. However, the bibliography in this field is so vast [1] that this chapter cannot give an exhaustive review of the state of the art for the entire literature on the subject. Therefore, it only reviews the most relevant publications and provides the necessary background to understand the scientific context in which the work of my PhD has been carried out.

The structure of this chapter loosely follows the historical development. First, the theoretical frame is defined, with emphasis on the Kelvin-Helmholtz instability. The importance of the multiple parameters at play are discussed in the context of the experimental study of the early stages of wind wave generation (section 1.1). Next, Phillips and Miles models are presented (section 1.2). The most relevant experimental and numerical findings from this point onward are then introduced (section 1.3), insisting on the latest advances in direct numerical simulation and instrumentation. Finally, this chapter concludes with the goals and scope of this PhD thesis (section 1.4).

1.1 Theoretical framework

1.1.1 Free surface waves

If the interface between two fluids initially at rest is disturbed, restoring forces work to bring back the system to equilibrium and waves can propagate at this interface. The restoring forces are gravity (through the density contrast between the two fluids) and capillarity (through the interfacial surface tension). Depending on the relative importance of gravity and surface tension, waves are labeled as "capillary waves", "gravity waves" or "capillary-gravity waves". Let us consider two Newtonian, incompressible and inviscid fluids, the lighter fluid on top of the denser one. Neglecting mean flow, the dispersion relation for free linear surface waves is:

$$\omega^2 = \frac{\Delta\rho}{\rho_1 + \rho_2 \tanh(kh)} gk \left[1 + \left(\frac{k}{k_c}\right)^2\right] \tanh(kh), \tag{1.1.1}$$

with $k = 2\pi/\lambda$ the wavenumber associated to the wave, ρ_1 and ρ_2 the densities of the lower and upper fluids respectively, $\Delta\rho = \rho_1 - \rho_2$ the density difference, g the gravitational acceleration, h the depth of the lower fluid (the upper fluid is supposed infinite), $k_c = \sqrt{\Delta\rho g/\gamma}$ the capillary wavenumber and γ the surface tension. Note that in the case of large depth, $\tanh(kh)$ can be approximated by 1, yielding the simplified dispersion relation $\omega^2 = (\Delta\rho/(\rho_1 + \rho_2))(gk + \gamma k^3/\Delta\rho)$. Equation (1.1.1) takes into account both gravity and surface tension (capillary-gravity waves); the corresponding relations for capillary or gravity waves are obtained by imposing $g = 0$ or $\gamma = 0$, respectively. It follows from equation (1.1.1) that the phase velocity c_φ is given by:

$$c_\varphi = \frac{\omega}{k} = \left[\frac{\Delta\rho}{\rho_1 + \rho_2 \tanh(kh)} \left(\frac{g}{k}\right) \left[1 + \left(\frac{k}{k_c}\right)^2\right] \tanh(kh)\right]^{1/2}. \tag{1.1.2}$$

The separation between the two branches of the dispersion relation (i.e. the theoretical separation between the waves primarily controlled by gravity and the waves primarily

1. In 2009, Ardhuin listed more than 2600 publications on ocean waves, with at least 300 of them concerning directly wind waves and/or wind-sea interactions. The entire bibliography can be found under different formats at `http://surfouest.free.fr/WISEBIB/`.

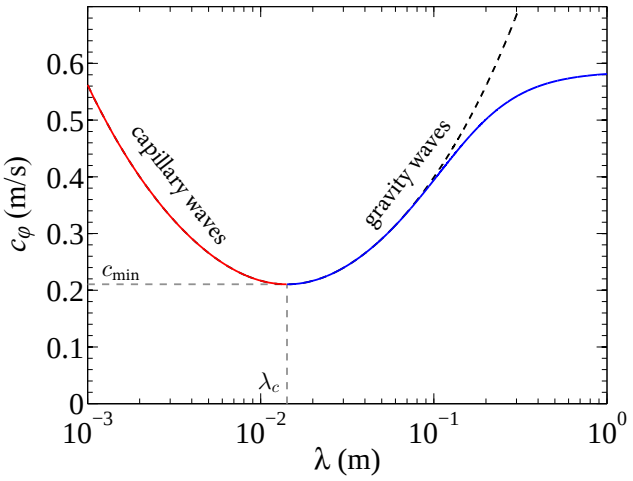

Figure 1.2: Phase velocity of waves as a function of their wavelength, from the dispersion relation for free linear surface waves on an inviscid liquid at rest and of finite depth (with $\gamma = 0.06$ N/m, $\rho_1 = 1.2 \times 10^3$ kg.m^{-3}, $\rho_2 = \rho_{\text{air}} = 1.2$ kg.m^{-3} and $h = 35$ mm). The black dashed line corresponds to the dispersion relation for infinite depth. Note that the dispersion relations for finite and infinite depth depart from one another only at relatively large λ (here for $\lambda > 10$ cm $\simeq 3h$). When the wavelength becomes large compared to the liquid depth, the phase velocity asymptotically reaches its shallow-depth limit $\sqrt{gh}$.

controlled by surface tension) occurs at the capillary wavelength $\lambda_c = 2\pi/k_c$ for the following phase velocity (see figure 1.2):

$$c_{\min} = \left(\frac{4g\gamma}{\Delta\rho}\right)^{1/4} \left(\frac{\Delta\rho \tanh(k_c h)}{\rho_1 + \rho_2 \tanh(k_c h)}\right)^{1/2}. \tag{1.1.3}$$

In practice, waves of wavelength close to λ_c are controlled by both surface tension and gravity (hence the term capillary-gravity waves).

The dispersion relation (1.1.1) applies for *free* surface waves: waves are not amplified or damped. The situation of wind waves is quite different: wind (and a number of other parameters like viscosity or current) can affect the waves' propagation. In this case, the dispersion relation (1.1.1) is not necessarily respected.

Moreover, in the case of wind waves, the upper fluid is a gas while the lower one is a liquid. The strong density contrast often leads to neglecting the density of the upper fluid for the wave propagation, yielding the following relations ($\rho_1 = \rho$ and $\rho_2 = 0$):

$$\omega^2 = \left(gk + \frac{\gamma}{\rho}k^3\right)\tanh(kh), \tag{1.1.4}$$

$$c_\varphi = \frac{\omega}{k} = \sqrt{\left(\frac{g}{k} + \frac{\gamma k}{\rho}\right)\tanh(kh)}, \tag{1.1.5}$$

with the capillary wavelength becoming $\lambda_c = 2\pi\sqrt{\gamma/\rho g}$. Note that whether (1.1.2) or (1.1.5) is used makes a difference of order 0.1% in the results presented in figure 1.2. As shown in this figure, depth correction on the phase velocity is negligible (< 1 %) for all wavelengths at $\lambda < 10$ cm (for $h = 35$ mm).

1.1.2 The Kelvin-Helmholtz instability

Let us start with the simplest model possible for the wind wave problem: two fluids, the lighter on top, each one occupying an half-infinite space, with the flow in each fluid being laminar, parallel to the interface at rest, constant and uniformly equal to U_i in the laboratory reference frame. The velocity and density jumps are thus entirely located at the interface (no boundary layer). As before, the phase on the bottom is denoted by the index 1 while the upper one is referred by the index 2. The system is represented in figure 1.3 in the reference frame of the lower fluid, in which the upper fluid has a velocity $U_2 = \Delta U$ and the lower fluid is at rest ($U_1 = 0$).

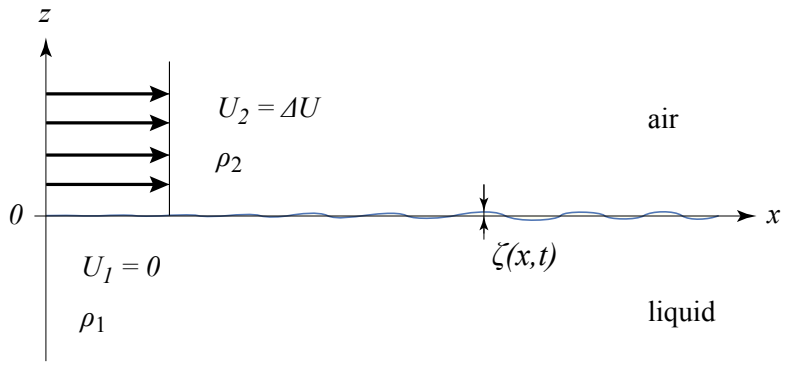

Figure 1.3: Sketch of the simplified velocity profile in the reference frame of the lower fluid used for the Kelvin-Helmholtz analysis.

The first works on this system may be attributed to Helmholtz [von Helmholtz, 1868] and Lord Kelvin [Thomson, 1871]. In particular, the stability analysis of Kelvin leads to a velocity criterion for the generation of waves at the interface between the two fluids. If the relative motion between the two fluids exceeds a critical value, a small upwards perturbation of the interface will create an upward force due to the local pressure decrease above the interface greater than the downward stabilizing forces associated with gravity and surface tension: the perturbation grows (the same destabilizing effect occurs for a negative deformation). The system becomes unstable and waves can grow from perturbations if the difference of velocity ΔU is greater than a certain value U_{KH}:

$$U_{\mathrm{KH}} = \left[4 g \gamma \Delta\rho \left(\frac{\rho_1 + \rho_2}{\rho_1 \rho_2} \right)^2 \right]^{1/4} = c_{\min,\infty} \frac{\rho_1 + \rho_2}{\sqrt{\rho_1 \rho_2}}, \tag{1.1.6}$$

with $c_{\min,\infty} = (4g\gamma/\Delta\rho)^{1/4} (\Delta\rho/(\rho_1+\rho_2))^{1/2}$ the minimal phase velocity in infinite depth.

Below this velocity, no disturbance of any wavenumber grows. As the wind increases and U_{KH} is finally reached, waves of a single critical wavenumber, the first wavenumber to become unstable, start to grow. As it turns out, this wavenumber at onset is the capillary wavenumber k_c. For a velocity difference ΔU further past U_{KH}, a wider range of wavenumbers (containing k_c) becomes unstable.

For wind over water, the Kelvin-Helmholtz instability yields a theoretical onset of about 6.6 m.s^{-1} at which point wind waves of wavelength approximately $\lambda_c = 17$ mm are generated. However, in-fields observations as well as laboratory experiments are in strong disagreement with these theoretical results. Indeed, ripples can be observed at the surface

of the sea for winds as small as 1 m.s^{-1}. In the controlled environment of a laboratory, the observed threshold velocities are greater, at usually about 3 m.s^{-1}, but still way below the theoretical value of 6.6 m.s^{-1} (see table 5.3 on page 104).

Kelvin was well aware of this discrepancy. He postulated that the difference between his theoretical prediction and the observed onset on a air-water interface comes from the viscosity of the water that is not included in his computations [Thomson, 1871]. Generally speaking, the few theoretical analyses on the influence of the viscosity on the Kelvin-Helmholtz instability lead to only a small effect of viscosity on the critical velocity. For example, Lindsay investigates through a stability analysis the influence of the viscosity of the lower denser fluid on the onset of the Kelvin-Helmholtz instability, still with the assumption that the mean velocity profiles are discontinuous [Lindsay, 1984]. Surprisingly, it is found that whatever its value, the viscosity reduces the classical destabilizing velocity U_{KH} by a factor based on the *density* of the two fluids: $U_{\mathrm{c,\ visc}} = (\rho_1/(\rho_1 + \rho_2))^{1/2} U_{\mathrm{KH}}$ (which in the case of a gas over a liquid leads to a very small correction). Taking the viscosity of both fluids into account leads to similar results. The viscosity ratio in a gas-liquid system can have a significant influence on the critical velocity only if the gas is strongly confined compared to the liquid, if the height of gas is less than 20% of the sum of the liquid depth and wind channel height, which is very possible in pipe flows but uncommon in experimental studies of wind waves [2] [Funada and Joseph, 2001] [Kim et al., 2011]. These results are in contradiction with the experimental observations of the critical velocity of wind waves in a typical configuration. Indeed, a more viscous liquid yields a higher threshold velocity (again, see table 5.3 on page 104).

1.1.3 Wind waves' parameters

Since the Kelvin-Helmholtz description appears too simple to fully grasp the complexity of the wind waves problem, more parameters need to be taken into account. Generally speaking, wind waves should depend on the exact velocity profiles in the air and liquid and therefore may depend on the viscosity of the liquid, the drift currents induced in the liquid, the boundary layer turbulence, and the distance over which the wind blows, but also on the time variation of the wind strength and direction, the time since the wind started, the heat and mass exchanges at the interface, and so on. One would argue that surely some of these parameters can still be neglected. This PhD thesis is based on an experimental approach of the study of the early stages of wind wave generation and growth in a laboratory. Consequently, in order to narrow down the relevant parameters, this section is dedicated to an overview of the importance of the wind waves' parameters in the context of laboratory experiments.

Mean wind velocity profile

Since turbulence is not necessary for the generation of surface waves, some authors have studied waves induced by laminar airflows [Blennerhassett, 1980] [Gondret and Rabaud, 1997] [Gondret et al., 1999] [Tsai et al., 2005b]. However, more often than not, experimentalists do focus on turbulent airflows, since it is the natural state of wind. In order to improve over the crude simplification of a constant uniform wind velocity at all elevations above the interface, it is interesting to take a look at the mean velocity profile of a typical turbulent flow.

2. The Kelvin-Helmholtz instability is also important in engineering applications involving liquid and gas transport in pipes [Hewitt, 2013].

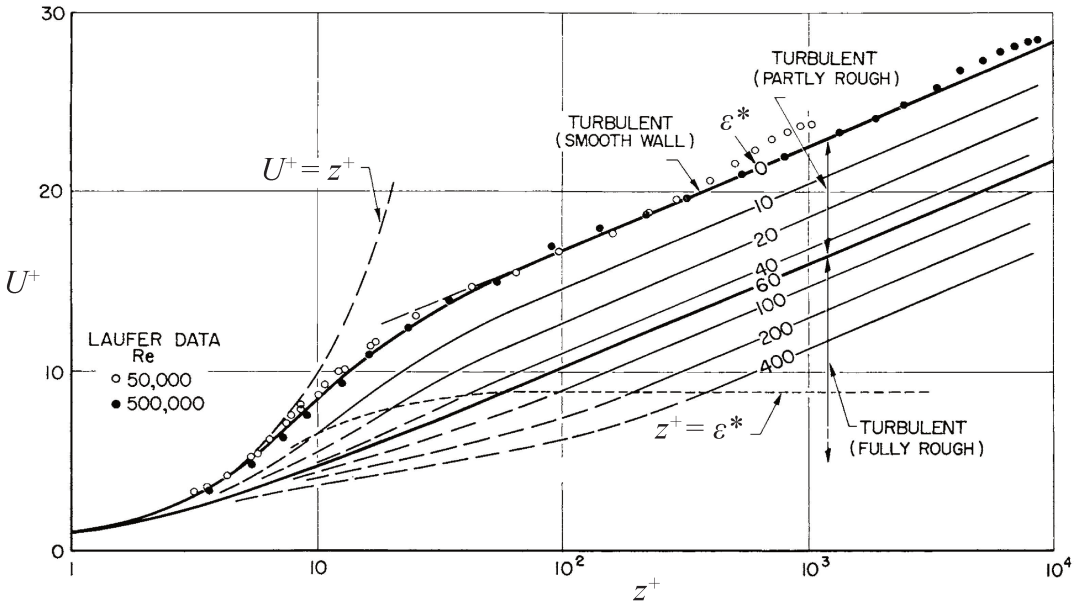

Figure 1.4: Mean velocity profiles for turbulent flows over smooth and rough walls. U^+ and z^+ are the mean velocity and the altitude over the boundary adimensionalized by the friction velocity u^* and the thickness of the viscous sublayer δ_ν, respectively (see section 2.2.a). $\epsilon^* = \epsilon/\delta_\nu$ is the non-dimensional size of the roughness. Adapted from [Van Driest, 1956].

Supposing the wind has a constant uniform mean velocity *far from the interface*, the mean air velocity at the interface is much lower than this far-field value. Indeed, at the interface, the mean velocities of the air and liquid flows are the same: they are equal to the surface drift. The surface drift is fairly small compared to the wind velocity (see below), therefore there is a layer, the boundary layer, above the interface in which the mean velocity increases from the surface drift to a much higher wind velocity far above the liquid.

The mean velocity profile of a boundary layer turbulent airflow is quite classical. From the interface, the mean air velocity grows linearly with elevation in the viscous sublayer, then grows logarithmically in the inertial sublayer until reaching a constant wind velocity, for altitudes greater than the boundary layer thickness (more details about the mean velocity profile in a turbulent flow and the turbulent boundary layer theory will be given in section 2.2.a on page 35).

The existence of a region of logarithmic velocity profile has been widely stated experimentally [Francis, 1954] [Plate et al., 1969] [Hsu et al., 1981] [Hsu and Hsu, 1983] [Liberzon and Shemer, 2011] [Longo, 2012] [Zavadsky and Shemer, 2012] [Buckley and Veron, 2016] and numerically [Lombardi et al., 1996] [Tsai et al., 2005a] [Lin et al., 2008] for a turbulent wind above a liquid interface, provided that the amplitude of the surface deformation is not too large [Plate et al., 1969]. Indeed, laboratory measurements of the mean velocity profile above an air-water interface that is only slightly perturbed (using Particle Image Velocimetry (PIV), Pitot tubes, hot-wire anemometry, etc.) yield profiles that follow a logarithmic-type law in the boundary layer, similarly to the boundary layer over a solid wall. Waves of higher amplitude may increase the roughness of the surface leading to a slight modification of the logarithmic law [Van Driest, 1956] [Raupach et al.,

1991] [Schlichting, 2000] [Longo, 2012]: the mean velocity is smaller in the logarithmic region (see figure 1.4).

Note that, if the wind is not stationary (either in strength or direction), the response of the interface is more complicated. For example, an increasing wind can result in a transition from laminar to turbulent flow and waves can strongly interact with the Langmuir circulations initiating this transition [Veron and Melville, 2001]. At sea, wind is commonly intermittent and gusty, but in the context of laboratory experiments, the gustiness of the wind and the heat and mass exchanges are neglected (though they would not be in oceanographic context). The wind forcing thus is taken to be sustained in time.

Liquid depth

As wind waves experiments are usually designed such that the infinite depth approximation can be assumed, depth is usually not a remarkably important parameter. Most analyses take the liquid depth to be infinite or equal to a constant value great enough to yield only small corrections. The study of liquid films acted upon by wind is not expected to lead to similar results. It is beyond the scope of our study and will not be reviewed here [3].

Drift current

If the thickness of the liquid layer is supposed large enough not to have a significant effect of the waves, the current in the liquid can however be more important. Indeed, the wind does not only transfer momentum at the interface to create waves but also to the bulk of the liquid to create a current drift, which may be laminar or turbulent.

The surface drift, the current velocity at the interface, is particularly important as it gives the wind forcing its boundary condition. The ratio of the drift velocity to the mean wind speed is usually of a few percents, typically around 2-3% of the wind velocity in the case on an air-water interface [Plate et al., 1969] [Gottifredi and Jameson, 1970] [Wu, 1975] [Veron and Melville, 2001] [Caulliez et al., 2008] [Liberzon and Shemer, 2011] [Pomeau and Le Berre, 2011]. In the case of fluids of higher viscosity than water, the drift is significantly smaller [Keulegan, 1951]. The base flow in the liquid may also affect the waves' propagation, so it is important to know the current in the liquid to apply possible corrections.

The laminar-turbulent transition and the turbulence below the surface in general have been investigated experimentally, often with the role of heat and mass exchanges or mixing at the air-sea interface in mind [Caulliez et al., 2007] [Siddiqui and Loewen, 2007] [Schnieders, 2015]. Teixeira & Belcher have developed an analytical model to study separately the influence of the turbulence in the air and in the water on the growth of surface waves [Teixeira and Belcher, 2006]. They found that the pressure fluctuations in water leads to steeper waves compared to a turbulent flow in the air producing pressure fluctuation of similar magnitude. Their results suggest that the turbulence in water may play a more important role than previously thought. This is consistent with the experimental results of [Caulliez et al., 1998] that supports that the laminar-turbulent transition in the water induces an explosive wave growth. However, it can be argued that, starting from a liquid at rest, the turbulence in the liquid come from momentum transfer from the wind, so there will be stages in which the turbulence in the air is predominant. While

3. Another parameter related to the liquid depth is the confinement of the liquid and gas flows. While it can be an important parameter in an instability mechanism [Matas, 2015], the confinement in our case is negligible and its influence is not reviewed here.

the turbulence in the liquid may be important, waves can also be generated before the laminar-turbulent transition in the liquid. The influence of this laminar-turbulent transition will not be further reviewed and in the context of laboratory experiments, the current will be assumed unequivocally either laminar or turbulent.

Surface contamination

Surface properties are of a great importance in the wind waves system. For example, the inception of waves by wind is strongly inhibited and delayed if the surface is contaminated, whether from the addition of surfactants [Keulegan, 1951] [Gottifredi and Jameson, 1970] [Kiefhaber, 2014] or by natural aging of the liquid [Tang and Wu, 1992] [Savtchenko et al., 1997]. Indeed, surfactants reduce the surface roughness, leading to a smooth water surface at wind velocities where ripples would cover a clean surface. Such suppression of wind waves over water is most effective below 6 $\mathrm{m.s^{-1}}$, as at higher wind velocity the film of pollutant may be disrupted and the interface reacts to wind like a clean surface [Tang and Wu, 1992]. However, if this disruption does not occur, the inhibition remains: Keulegan reports that over water contaminated with soap or detergent, even the maximal wind velocity of his facility (12 $\mathrm{m.s^{-1}}$) is unable to produce ripples or even simply the tremors easily seen on clean water at low wind velocity. The generation of waves is therefore highly influenced by the state of the interface. This makes perfect sense as in the situation of capillary-gravity waves, the surface tension works as a competing restoring force against gravity. Surface tension should not be neglected in the study of the early stage of wind wave generation since it is mainly populated by capillary-gravity waves. However, *gradients* of surface tension are neglected: the interface is supposed clean and therefore of constant surface tension.

Viscosity

As mentioned in paragraph 1.1.2, the viscosity of the liquid has a significant effect on the velocity onset of the waves, as experiments show that the critical wind velocity is higher for more viscous liquids [Keulegan, 1951] [Francis, 1956]. Recently, it has been postulated that the viscosity of the methane-ethane-nitrogen lakes on Titan may explain the fact that no waves can be seen on Titan's lakes despite winds stronger than the theoretical estimates of wave onset [Ghafoor et al., 2000] [Lorenz et al., 2010] [Hayes et al., 2013].

The viscosity of the liquid can also directly affect the wave propagation. Lamb suggests the following correction [Lamb, 1995]:

$$c_\varphi = \sqrt{\left(\frac{g}{k} + \frac{\gamma k}{\rho}\right)\tanh(kh) - \nu^2 k^2}. \tag{1.1.7}$$

The complete dispersion relation of linear capillary-gravity wave on a viscous liquid of finite depth is presented in [LeBlond and Mainardi, 1987] (equation (21) in their paper) and numerical results for this fairly complicated relation are given for four liquids of viscosity ranging from 0.01 to 18.5 $\times 10^{-4}$ $\mathrm{m^2.s^{-1}}$. The parameter θ is defined as the ratio squared of the diffusion scale $D = \sqrt{\nu/\omega}$ over the inverse of the wavenumber : $\theta = \nu k^2/\omega$, ω being the radian frequency of undamped free waves (i.e. verifying the inviscid dispersion relation (1.1.4)). In the case of infinite depth, the only cut-off is for short wavelengths for $\theta_0 \simeq 1.31$ (the corresponding wavelength is noted λ_0). Periodic motions of wavelength smaller than λ_0 are over-damped, blocking their propagation (see figure 1.5). If the liquid height is finite, the short wave cut-off remains at $\theta_0 \simeq 1.31$ but a long wave cut-off also

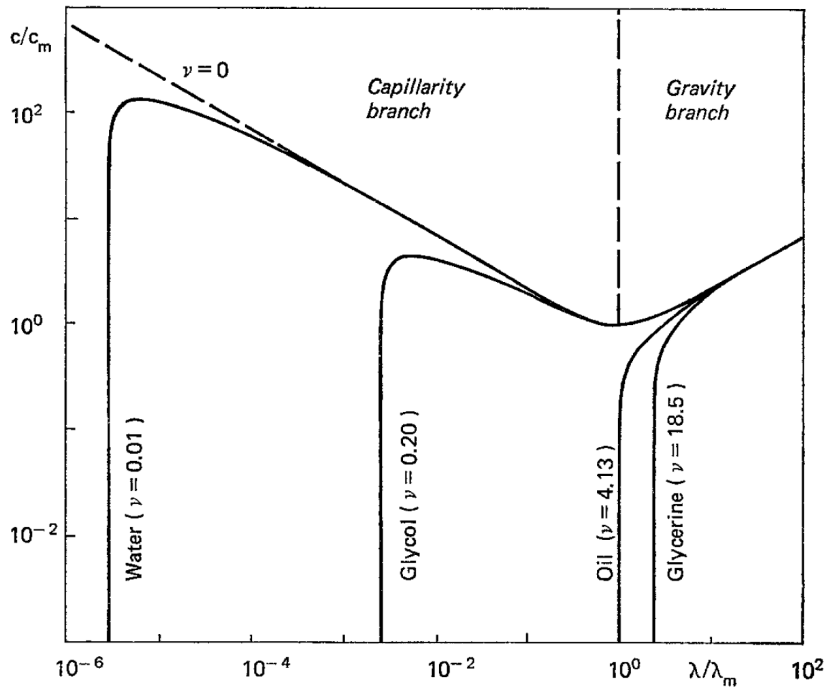

Figure 1.5: Figure 2 in [LeBlond and Mainardi, 1987]. Phase velocity (scaled with $c_m = (4\gamma g/\rho)^{1/4}$) as a function of the wavelength (scaled with $\lambda_m = 2\pi\sqrt{\gamma/\rho g}$) for four viscous liquids of infinite depth (water, glycol, oil, glycerine). The viscosities are in $\times 10^{-4}$ m^2.s^{-1}.

occurs (not shown in Fig. 1.5 as it presents results in infinite depth). It arises for liquid depth small enough that the influence of the bottom friction reaches the interface: long waves such that $D = \sqrt{\nu/\omega} > h$ cannot propagate.

Figure 1.5 also conveys the range where the liquid can be considered as quasi-inviscid, that is to say, when the waves are weakly damped but with a frequency unaffected by viscosity. The range of validity of the quasi-inviscid regime correspond to the portion of the graph over which the dispersion curve almost coincide with the inviscid dispersion curve, i.e. $\lambda > 10\lambda_0$. The quasi-inviscid approximation leads to a correction of ω into $\omega - 2i\nu k^2$.

All these results show that viscosity can have a major influence on the wind wave generation. As a consequence, the viscosity of the liquid will not be neglected in our system (its influence will even be closely studied).

Wind waves in the laboratory

Based on the importance of each of the parameters discussed above, let us refine the system that will be considered for wind wave generation. This more complete system departs from the simplified system of the Kelvin-Helmholtz instability (Fig. 1.3) and is presented in figure 1.6. Both fluids are supposed incompressible of constant uniform density and viscosity, separated by an interface over which the surface tension is uniform. The depth of the liquid is constant and large enough that corrections due to finite-depth effects are small. The wind is a turbulent airflow whose mean velocity is parallel to the interface at rest and the current in the liquid is taken into account.

While wind waves have been studied in different configurations than this one, the rest

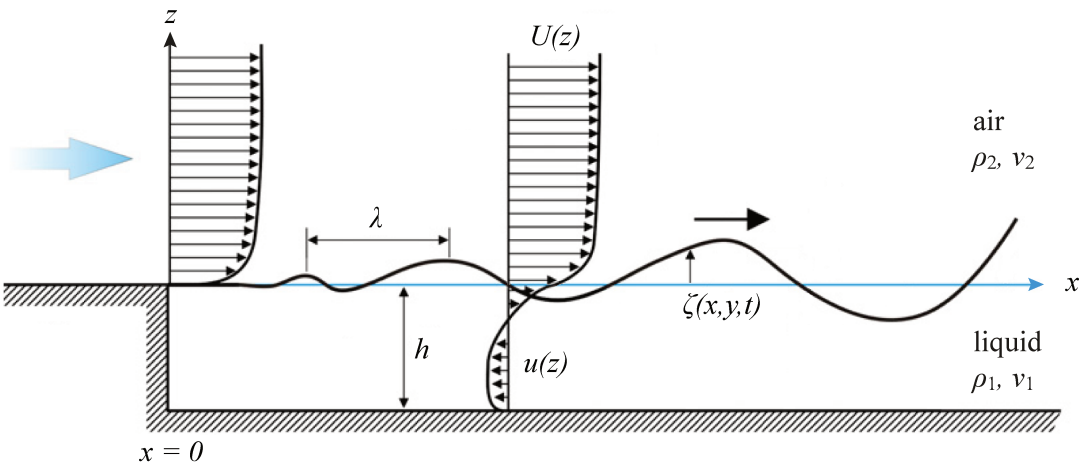

Figure 1.6: Sketch of the system. Adapted from [Longo, 2012].

of this chapter mainly focuses on publications that concern similar systems. In accordance with the literature, we use the term *fetch* to refer to the distance over which the wind blows, which in wind waves experiments is usually the distance from the beginning of the liquid surface.

1.2 Mechanisms for wind wave generation and growth

Beyond the Kelvin-Helmholtz instability, the first to venture into suggesting a mechanism for wind wave generation was Jeffreys [Jeffreys, 1925]. Jeffreys proposes a 'sheltering' model in which each wave crest is partially sheltered by the previous crest from the full effect of the wind, based on a sheltering coefficient. This supposes the separation of the airflow above each crest and leads to a greater pressure on the slopes facing the wind than on those away from it, resulting in the wave development. However, measurements revealed a sheltering coefficient an order of magnitude smaller than predicted, and Jeffreys' mechanism was proven beyond doubt not efficient enough to account for the generation of the first wind waves [Phillips, 1957].

The next models were presented three decades later. Published simultaneously in 1957, the groundbreaking works of Phillips and Miles on wind wave generation were entirely independent from one another and consider the wind wave generation from two very different approaches, complementary rather than competitive.

1.2.1 Phillips resonant model: wave generation by turbulent fluctuations

In 1957, Phillips proposes in an easily readable article a theory for the generation of wind waves [Phillips, 1957]. Contrary to the Kelvin-Helmholtz approach, Phillips does not view wind waves as a stability problem but as a resonance one, between the pressure fluctuations in the airflow and the modes of the free surface.

Wind wave generation through the pressure fluctuations in the turbulent airflow was first proposed by Eckart [Eckart, 1953]. While Eckart studies the effect of a known en-

semble of gusts of prescribed extent in space and time, Phillips generalizes this approach with a random distribution of normal pressure into a resonant model for the generation of wind waves over water. In his model, the water, assumed to be inviscid [4], is initially at rest and becomes deformed by the pressure fluctuations, but without any countereffect on the air profile due to these deformations of the interface. Based on this assumption of decoupling between waves and wind, Phillips expresses the spectrum of the surface waves as a function of the spectrum of the pressure fluctuations in the turbulent wind. He shows that if the convection velocity V_c of the pressure fluctuation of length Λ is equal to the phase velocity c_φ of the wave of this specific wavelength Λ, resonance occurs and the wave is amplified.

On this basis, it can be considered that the waves develop in two stages. At times shorter than the time of development of the pressure fluctuations, the "initial stage of development", only short waves are generated, prominently capillary waves propagating in the direction $\cos^{-1}(c_\varphi/V_c)$ relatively to the wind direction. The "principal stage of development", where most of the wave growth occurs, happens at later times, when the waves created in the first stage enter in resonance. The theory predicts a linear growth in time of the mean square of the amplitude of the wave (i.e. a linear growth of the wave energy):

$$\overline{\zeta^2} \simeq \frac{\overline{p^2}t}{2\sqrt{2}\rho^2 V_c g}. \tag{1.2.1}$$

This growth of the wave amplitude as the square root of time continues until the waves' amplitude becomes so high that nonlinear effects are not negligible anymore. According to Phillips, this occurs when the mean square slope of the waves reaches a certain limit value. He postulates that past that point, an equilibrium is attained (the waves do not grow anymore).

This is a very different approach from the Kelvin-Helmholtz model, in which the wind must reach a certain threshold before perturbations can be amplified. In Phillips' model, the minimum wind velocity capable of setting off the resonance is the minimal phase velocity $c_{\min} = (4g\gamma/\rho)^{1/4}$ (approximately 0.23 m.s^{-1} for water waves). However, surface deformations will occur for a turbulent wind of any velocity since any turbulent flow necessarily includes some level of fluctuations.

Phillips' model can be criticized on the basis of its complete disregard of the correlations between air and liquid motions. This coupling, as well as other parameters like the liquid viscosity entirely neglected in his theory, may have an important role in wave generation. Consequently, Phillips acknowledges that his resonance effect of the pressure fluctuations cannot be claimed as the sole mechanism capable of generating waves. Other instabilities may occur and a critical wind velocity may be defined at their arrival.

1.2.2 Miles shear flow model: wave generation by shear flow

Only a few months after the publication of [Phillips, 1957], Miles suggests an entirely different approach to the problem and proposes a shear flow mechanism for the wind wave generation [Miles, 1957]. Contrary to Phillips, Miles studies this problem from a stability point of view.

As for the Kelvin-Helmholtz instability, the air is assumed to be inviscid and incompressible. The disturbances in velocity and pressure due to interfacial waves are assumed

4. Phillips states that the viscosity of the water is "probably unimportant" for all but the shortest waves over moderate intervals of time.

to be 2D and small enough to be able to use linearized equations of motion. The turbulent fluctuations are neglected, except for the development of the mean velocity profile. In this sense, Miles model is said to be *quasi-laminar* as the turbulence of the airflow is taken into account only through the base flow of the turbulent airflow. The liquid is supposed inviscid as well, incompressible and irrotational, and its mean motion is neglected. Using Rayleigh's equation (i.e. the inviscid Orr-Sommerfeld equation), Miles analyses the energy transfer from an airflow of mean velocity profile $U(z)$ (in absence of waves) to a wave of phase velocity c. He demonstrates that this energy transfer rate is proportional to the profile curvature $-U''(z_c)$ at the critical altitude z_c above the interface where the mean air velocity is equal to the phase speed of the wave: $U(z_c) = c$. Depending on the sign of the curvature $U''(z_c)$, the energy transfer rate will be either negative or positive, and the waves are either damped (stable profile) or amplified (unstable profile). In case of amplification, the wave energy grows exponentially.

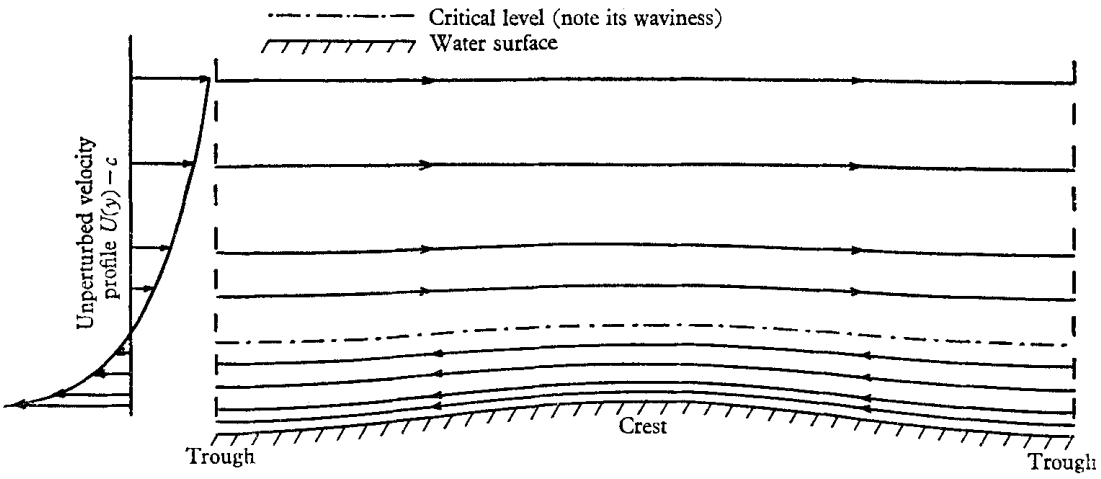

Figure 1.7: Sheared airflow relative to a travelling sinusoidal wave of velocity c. The front and back of the crest (terms used in the text) correspond here respectively to the right and left sides on the figure. From [Lighthill, 1962].

Lighthill gives a physical interpretation of Miles model in [Lighthill, 1962]. Let us consider a sheared airflow over the crest of a sinusoidal wave propagating at a velocity c. The wind decreases the pressure over the wave crests and increases it in the troughs. The streamlines follow the shape of the interface and the critical height is therefore wavy. Since the mean air velocity at the critical height z_c is equal to the wave phase velocity, in the reference frame of the wave, the air flows in the direction of the wave propagation above this critical elevation and in the opposite direction below z_c, close to the interface (see Fig. 1.7). A perturbation just above the critical height slowly overtakes the crest, moves down below the critical layer because of the higher pressure above the trough, and returns towards the crest. An upward air motion occurs at the critical height behind the crest. Since the vorticity of the turbulent undisturbed airflow decreases with altitude, the downflow ahead of the crest produces a local vorticity deflect and the upflow behind the crest a local vorticity excess. As a consequence, the mean vortex force $-\rho\overline{\omega v}$ (with ω the vorticity and v the vertical velocity) is negative and reduces the mean momentum at the critical height, by energy transfer to the wave. The energy transfer rate varies as the

square of the wave amplitude (since it governs the pressure distribution), which means that the energy transfer rate varies as the wave energy itself. Consequently, the wave energy grows exponentially.

Despite the considerable positive interest taken in Miles model [Janssen, 2004], it also aroused some controversy [Komen et al., 1996]. The quasi-laminar approach was said to oversimplify the problem and ignore nonlinearities. In particular, this leads to a significant issue concerning the location of the critical layer at which the mean wind velocity equals the wave phase velocity. For short waves, the altitude at which the mean velocity equals the phase velocity lies in the viscous sublayer, where the mean air velocity linearly increases with the altitude. Therefore, the curvature of the profile there is zero, which leads to a zero energy transfer rate according to [Miles, 1957], and Miles' mechanism cannot play a role in the generation of waves. Miles' mechanism as defined in [Miles, 1957] is relevant only provided that the critical layer is located outside the viscous sublayer, that is to say for waves of sufficiently high wavelength and for a wind velocity that is not too large.

To deal with this issue, Miles extends his model in [Miles, 1959a] by taking into account (to some extent) the viscosity. Following the approach of [Benjamin, 1959], he includes the dominant viscous term in the Orr-Sommerfeld equation and uses a more accurate numerical model to obtain results for the air-water case, leading to a wave generation mechanism also applicable to shorter waves. Miles continues to improve his model in later papers [Miles, 1962] [Miles, 1967] [Miles, 1993] [5]. The core of his model remains the same as in [Miles, 1957], with the shared result of an exponential growth of the wave energy. Note that when later papers compare their results to "Miles' model", this is not necessarily in reference to [Miles, 1957].

Miles applies his model to deep-water waves generated by wind, with the mean air velocity profile taken to be logarithmic so as to mimic the profile in the boundary layer in turbulent flows [Miles, 1957] [Miles, 1959a] [Conte and Miles, 1959] [6]. The minimum wind velocity for the initiation of gravity waves is calculated to be about 1 $m.s^{-1}$ in qualitative agreement with the onset of ripples over a calm sea, but much smaller than the onset velocity of about 3 $m.s^{-1}$ observed in controlled laboratory experiments. Miles notes that the energy transfer due to turbulent fluctuations as described by [Phillips, 1957] renders the question of the critical wind velocity of secondary significance, as Phillips' mechanism is bound to have produced surface waves beforehand. He applies the same method to revisit the Kelvin-Helmholtz instability in [Miles, 1959b] and generalizes the problem for a parallel shear flow with a light inviscid fluid over a denser viscous fluid. Applying his results to a air-water interface, he concludes that including viscous forces in the liquid have no effect on the critical velocity and that Kelvin-Helmholtz instability is unlikely to appear at the typically observed wind speeds. He also finds that his modified Kelvin-Helmholtz model may adequately explain the onset of waves for a parallel shear flow over a fairly viscous liquid like oil.

5. He incorporates the energy transfer through viscous stresses [Miles, 1962], the energy transfer through turbulent Reynolds stresses [Miles, 1967] and the wave-induced perturbations of the Reynolds stresses [Miles, 1993]. Note that in [Miles, 1962], Miles prefers the term *viscous Reynolds stress* over *viscous stress*, stating that "[i]t must be emphasized that, in first approximation, the energy transfer at the interface is through the out-of-phase component of the pressure and that energy transfer through the shear stress enters only in the next approximation. It was, among other things, to emphasize this distinction that the term *viscous Reynolds stress*, rather than *viscous stress*, was selected and has been retained."

6. [Conte and Miles, 1959] provides the details of the computation and results.

1.2.3 Limitations and complementarity of Phillips' and Miles' models

It is interesting to note that Phillips' and Miles' models are less competitive than they are complementary. Neither of the two models fully encompasses the complexity of a turbulent airflow. Phillips' model takes into account the fluctuations independently of the base flow while Miles' model is based on the stability of the mean velocity profile alone, neglecting any effect of the fluctuations except for the development of the turbulent base flow. Phillips' model is three dimensional, while Miles' model is purely 2D. Miles' model works on a positive feedback of the interface response; Phillips' model injects energy into surface waves at all frequencies independently of the amount already there, be it zero (flat interface). Phillips' model is uncoupled as the excitation (the turbulent fluctuations) is assumed to remain independent of the response of the interface. In contrast, coupling between the airflow and the interface is central in Miles' model, as it is based on stability analysis, where the excitation is proportional to the response when the flow becomes unstable. Based on their description, it also appears that Phillips' mechanism is more suitable for the growth of short waves while Miles' mechanism would better govern the longer wind waves, calling into question the response to their competition at intermediate wavelengths.

Due to their complementarity, Phillips and Miles theories are sometimes combined into the Miles-Phillips' model [Hidy and Plate, 1966] [Stewart, 1967] [Plate et al., 1969]. In this approach, the first deformations of the interface are generated by the pressure fluctuations of the turbulent airflow as proposed by [Phillips, 1957], leading to a linear growth in time of the wave energy, until Miles' mechanism [Miles, 1957] takes over and the wave energy starts to grow exponentially. Therefore, Phillips' mechanism would be responsible for the first surface perturbations, populating the interface with capillary-gravity waves of small amplitude. These small deformations create a surface roughness that "trips" Miles' mechanism into action, shifting the preceding linear wave growth to an exponential growth. This growth then continues until an equilibrium (saturation) is reached. Note that this implies that neither model is expected to give a full picture of the interface response for all times.

Also note that both Phillips' and Miles' models provide predictions for the *temporal* growth rate of the wave energy. In experiments, the available instrumentation and set-up configuration usually leads to the measurement of either the temporal or the spatial growth rate. The spatial growth rate β and temporal growth rate β_t are related at onset through the group velocity $c_g = \partial\omega/\partial k$ [Gaster, 1962] [7]:

$$\beta_t = c_g \beta, \tag{1.2.2}$$

but experimentally, the surface drift also has to be included, especially if the current is non-uniform in the direction of the wave propagation [Longuet-Higgins and Stewart, 1961]. Moreover, the Gaster relation is valid only in the limit of weak departures from the threshold (small rates of amplification).

7. In our notations, waves are amplified in time or space for positive β_t and β respectively. [Gaster, 1962] uses another notation where temporal amplification corresponds to $\beta_t > 0$ while spatial amplification occurs for $\beta < 0$, which leads to a negative sign in his equation (12).

1.3 Experimental and numerical results

1.3.1 Comparison with the models

Since the publications of Phillips' and Miles' models, many attempts have been made to test these predictions or to improve these models. Experiments concerning the effect of wind over waves can be separated into two categories: purely wind-generated waves [Plate et al., 1969] [Mitsuyasu and Rikiishi, 1978] [Kawai, 1979] [Kahma and Donelan, 1988] [Veron and Melville, 2001] [Liberzon and Shemer, 2011] [Grare et al., 2013], and wind-ruffled mechanically-generated waves, in which waves are not generated by wind but by a forcing at a certain frequency [Bole and Hsu, 1969] [Gottifredi and Jameson, 1970] [Wilson et al., 1973] [Mitsuyasu and Honda, 1982].

Mechanically-generated waves amplified by wind

Mechanically-generated waves have the advantage of the accurate knowledge of the aspect the wave has in absence of wind. The amplification by wind at a particular frequency can be evaluated without any filtering by the direct measurement of the wave amplitude. Using a wave generator in a wind wave tank at low wind velocity (at 1.1 and 1.8 $m.s^{-1}$), Wilson et al. observe growth rates two to five times larger that Miles predictions [Wilson et al., 1973]. At higher wind velocity (5 to 12.5 $m.s^{-1}$) in a comparable configuration, Mitsuyasu & Honda measure growth rates twice as great as Miles theory [Mitsuyasu and Honda, 1982]. However, in a similar experiment, Gottifredi & Jameson find growth rates much closer to Miles theory [Gottifredi and Jameson, 1970]. Generating waves with a paddle and measuring their amplification by wind over water or dilute glycerol solutions, they witness that liquids of higher viscosity show lower growth rates. Contrary to [Wilson et al., 1973], they find their experimental results to be in accordance with Miles theory, at least up to a certain wind velocity. In the case of water, the agreement runs up to 3 $m.s^{-1}$. With a glycerol-water mixture of kinematic viscosity eleven times greater that the one of water, it continues up to 5 $m.s^{-1}$. Above these values, experiments and theory show no common trends. The results of [Gottifredi and Jameson, 1970] and [Wilson et al., 1973] are however subject to caution. Indeed, Tsai [Tsai, 2002] comments that the wind profiles parameters in [Gottifredi and Jameson, 1970] is likely to contain large errors due to the growth of the turbulent boundary layer and the absence of correction of the shear effect on their Pitot-tube measurements close to the interface, while the meniscus on the wave wire gauge used in [Wilson et al., 1973] reduces the accuracy on the wave amplitude (it ranges from 0.02 to 0.3 mm). In any case, it is difficult to conclude on the validity of Miles' model based on these experiments of mechanically-generated waves amplified by wind.

Wind waves experiments

Numerous publications deal with the experimental measurement of wind wave growth in laboratory. To do so, most experiments are conducted under similar conditions: a wind blower injects a turbulent wind over a tank filled with water [8]. The tank is usually quite long (5 to 40 meter long) and deep enough that finite-depth effects are weak. If the tank is short enough for reflected waves to be an issue, the end of the tank may be equipped with a wave absorber or a sloped beach to damp or break the incoming waves.

8. To my knowledge, no experimental work has presented growth rates of wind-induced waves over a liquid other than water.

The air generally flows above a portion of smooth floor before suddenly transition to the liquid boundary. Different methods can be used to determine the wave growth rate. For example, the temporal growth rate can be measured easily by a wave elevation probe. With more than one of these probes arranged along the tank, the spatial growth rate can be assessed. Growth rates can be measured by other means than the spatial change of wave energy from surface elevation records. Indeed, wave growth rates can also be derived from microwave backscatter [Larson and Wright, 1975] [Ebuchi et al., 1987] [Savtchenko et al., 1997], static air pressure measurements [Donelan et al., 2006] or tangential stress measurements [Grare et al., 2013]. For more details on these methods and a review and comparison of a selection of data sets from the literature, see [Peirson and Garcia, 2008]. Note that determining the growth rate associated with a particular frequency is however not as easy as in wave experiments with a mechanical forcing. In the case of waves purely generated by wind blowing over the liquid surface, the forcing by the wind can excite all frequencies. Just above the wave onset, the ripples generated by wind are usually close to being monochromatic. However, further away from the wave generation threshold, the surface waves may be composed of various components and a wider spectrum of frequencies may be produced. In this case, spectral decomposition is required to obtain the growth rate for a particular frequency.

Many publications report a temporal exponential growth rate [Larson and Wright, 1975] [Plant and Wright, 1977] [Mitsuyasu and Rikiishi, 1978] [Kawai, 1979] or a spatial exponential growth rate [Hidy and Plate, 1966] [Sutherland, 1968] [Plate et al., 1969] [Mitsuyasu and Rikiishi, 1978] [Liberzon and Shemer, 2011]. While this is a point in favor for Miles' model, the associated growth rate is not necessarily close to the one predicted. For a wind velocity of about 11 m.s^{-1}, Plate et al. find an exponentional growth rate with fetch with an error of more than 60% relatively to Miles' model [Plate et al., 1969]. For wind speeds between 4 and 16 m.s^{-1}, Plant & Wright also find a temporal exponential growth of short gravity waves at higher rates than predicted [Plant and Wright, 1977]. On the contrary, in [Hidy and Plate, 1966], Hidy & Plate observe spatial exponential growth in the range of the predictions of Miles' model, for wind velocities between 10.8 and 14.5 m.s^{-1}. They comment that their measurements are too inaccurate at small fetch and time to be able to detect the linear growth predicted by Phillips. Sutherland reports regions of spatial linear growth at his lowest velocity (6.7 m.s^{-1}) and exponential growth at higher velocities (9.4 to 15.2 m.s^{-1}) [Sutherland, 1968]. The exponential growth rates are in agreement with the theory for wave frequency below 3.5 Hz and an order of magnitude smaller for higher frequencies. The scatter in the regions of linear growth is too important for a quantitative comparison with Phillips' model.

Using microwave backscatter responding to waves of wavelengths of 0.7-7 cm, Larson & Wright also note exponentional wave growth with time for wind velocities ranging from 1.4 to 15 m.s^{-1} [Larson and Wright, 1975]. They do not compare their results with theoretical predictions but with data from others wind waves experiments. They find little overlap between their experimental results and those of the publications they are compared with. They explain the discrepancies by the fact that the way the data is reduced (through the wavenumber) does not take the drift into account. The only datasets leading to an acceptable agreement with their results are the ones from [Gottifredi and Jameson, 1970] and [Wilson et al., 1973] for which the wind drift was small. In [Plant, 1982], Plant introduces the data presentation of wind wave growth rates through the non-dimensional ratio β_t/f as a function of u^*/c_φ, where f is the wave frequency and u^* the air friction velocity. He summarizes the data collected at sea and in laboratories available at that time, reconciling some discrepancies and proposing the empirical relation

$\beta_t/f = 2\pi(0.04 \pm 0.02)(u^*/c_\varphi)^2 \cos\theta$ over a large range of frequencies, with θ the angle between the wind and wave directions. Plant's representation has often been used since then for data comparison, even though the comparison sometimes leads to disagreements with his empirical relation [Mitsuyasu and Honda, 1982] [Lin et al., 2008]. Measuring spatial growth rates based on the momentum transfer and based on direct determination of the wave amplitude increase with fetch, Liberzon & Shemer find that the spatial growth rates based on the momentum transfer are greater than those obtained through the direct measurement of the spatial growth of the wave amplitude [Liberzon and Shemer, 2011]. The latter are in better agreement with Miles' model than the former in terms of value, but both their evolutions with u^*/c_φ are completely different from the theory.

To summarize, the comparison between the models of wind wave generation and laboratory experiments lead to mixed results. A qualitative agreement can be shown with Phillips and Miles theories but not a quantitative one [Stewart, 1967] [Massel, 1996] [Liberzon, 2010]. Phillips' model concerns waves of such weak amplitude that definitive conclusions cannot be drawn, and the experimental exponential growth rates are usually at least an order of magnitude higher than the predicted values by Miles' model [Massel, 1996]. In addition to that, the format of the data comparison itself is not trivial [Plant, 1982] and different measurements techniques can lead to significant differences in growth rates [Morland and Saffman, 1993] [Liberzon and Shemer, 2011]. It should also be noted that many of the wind wave experiments are conducted at high wind velocity, well above the threshold of wave generation, even in ranges where airflow separation can occur above wave crests [Wilson et al., 1973].

1.3.2 Beyond Phillips' and Miles' models

Phillips' and Miles' models of 1957 are not the only mechanisms for wind wave generation that have been proposed. Mention may be made for example of [Deardorff, 1967], [Kahma and Donelan, 1988] and [Belcher and Hunt, 1993], among others. The range of validity of each of these mechanisms is still discussed.

Generally speaking, the full stability analysis of the system amounts to an Orr-Sommerfeld problem on each fluid, coupled through conditions at the perturbed interface. The literature is abundantly populated with stability analyses of parallel two-phase flows and tentative improvements of already existing models ([Taylor, 1940] [Yih, 1967] [Valenzuela, 1976] [Blennerhassett, 1980] [Hooper and Boyd, 1983] [Katsis and Akylas, 1985] [van Gastel et al., 1985] [Hooper and Grimshaw, 1985] [Charru and Hinch, 2000] [Teixeira and Belcher, 2006] [Montalvo et al., 2013] [Otto et al., 2013] [Young and Wolfe, 2014], to name a few). This profusion can be explained by the large number of parameters that can be taken into account in the analysis, as well as different ways to take them into account. The complexity comes from the fact that the stability analysis can take into account some parameters while neglecting others, like the surface tension, the density difference, the viscosity, the current in the lower fluid, etc, which leads to different equations. Once the stability equation has been derived, the stability of a given profile can be studied, usually with the help of the computational capacity of a computer. Moreover, the numerical applications of these equations require specification of the profiles of the parameters in the two fluids. The density is generally chosen to be constant in each fluid, and the same goes for the viscosities (when they are not neglected). But for the mean velocity profiles, the issue is not straightforward. While the influence of changes in current profile is weak, a slight change in the shape of the wind profile can yield very different results [van Gastel et al., 1985].

Indeed, Boomkamp & Miesen argue that due to the great number of parameters, the

studies found in the literature only apply to a relatively small portion of the parameter space and it is not always clear which instability is actually examined [Boomkamp and Miesen, 1996]. Aiming for a clarification of the literature, they devise a classification of the two-phase flows based on the five different ways of energy transfer from the primary to the disturbed flow, in the context of the Orr-Sommerfeld analysis in both fluids coupled at the interface. Grouping together the instabilities driven by the same energy terms, they list five classes of instability: (i) Rayleigh-Taylor instability, originating from density stratification; (ii) Miles instability, originating from velocity profile curvature; (iii) instability induced by tangential disturbances, originating from density and viscosity stratification [9]; (iv) shear mode instability, originating from shear effects; (v) internal mode, originating from a combination of viscosity stratification and shear effects. They also indicate which papers study the same instability and fall into which class of instability.

Boomkamp & Miesen particularly discuss the viscosity-induced type of instability, first theorized by Yih [Yih, 1967]. Indeed, considering the stability of a plane Couette-Poiseuille of two superposed fluids of different viscosities, Yih shows that the viscosity stratification alone can cause instability. His work has paved the way to numerous investigations of the stability of the interface between two shearing fluids of different viscosities [Hooper and Boyd, 1983] [Hooper and Grimshaw, 1985] [Barthelet et al., 1995] [Charru and Hinch, 2000] and Boomkamp & Miesen insist on the importance of viscosity stratification in liquid-liquid flows but also in gas-liquid flows.

Two other observations of [Boomkamp and Miesen, 1996] are of particular relevance to our experimental study of wind waves. First, they note that the classical Kelvin-Helmholtz instability is lacking from their classification. Applying their scheme to the Kelvin-Helmholtz instability, they find that the assumption of inviscid fluids makes some of the energy terms vanish and only the Reynolds stresses remain. Stating that none of their computations for various air-liquid combinations provided any evidence of the Kelvin-Helmholtz instability (as they lead to a viscosity-induced instability), they conclude that including viscous effects into the stability problem, even to a small extent, excludes the possibility of the inviscid Kelvin-Helmholtz instability. Second, they also apply their classification scheme to the Miles instability for a system as defined in [Miles, 1962] [10] and find that the energy transfer through Reynolds stresses are too small to explain the generation of capillary-gravity waves. They conclude that capillary-gravity wind waves are not generated by the mechanism proposed by Miles but originates from a viscosity-induced energy transfer at the liquid-air interface.

This existence of multiple mechanisms capable of generating wind waves makes it harder to define the threshold of wave generation. Should it be defined on the first visible surface deformations? On the arrival of the first ripples? On the transition between two particular mechanisms? On the growth of the waves? This asks the question of the recognition without failure of all the instabilities at play during an experiment and the accuracy of the intruments used to detect this threshold. The possible existence of multiple stages of wave development also fosters the ambiguity [Caulliez, 1987].

Generally speaking, in a lot of works (including [Phillips, 1957] and [Miles, 1957]), the emphasis is put on the theoretical, numerical or experimental determination of the wave growth rate. Many studies focus on the waves' behavior far above the threshold and on the generation and amplification of long wavelengths and the conditions related to the onset

9. The instabilities induced by tangential disturbances are separated into three sub-categories: viscosity-induced instability, gravity-induced instability and viscosity-gravity-induced instability.

10. In which the energy transfer to capillary-gravity waves through viscous Reynolds stresses is included.

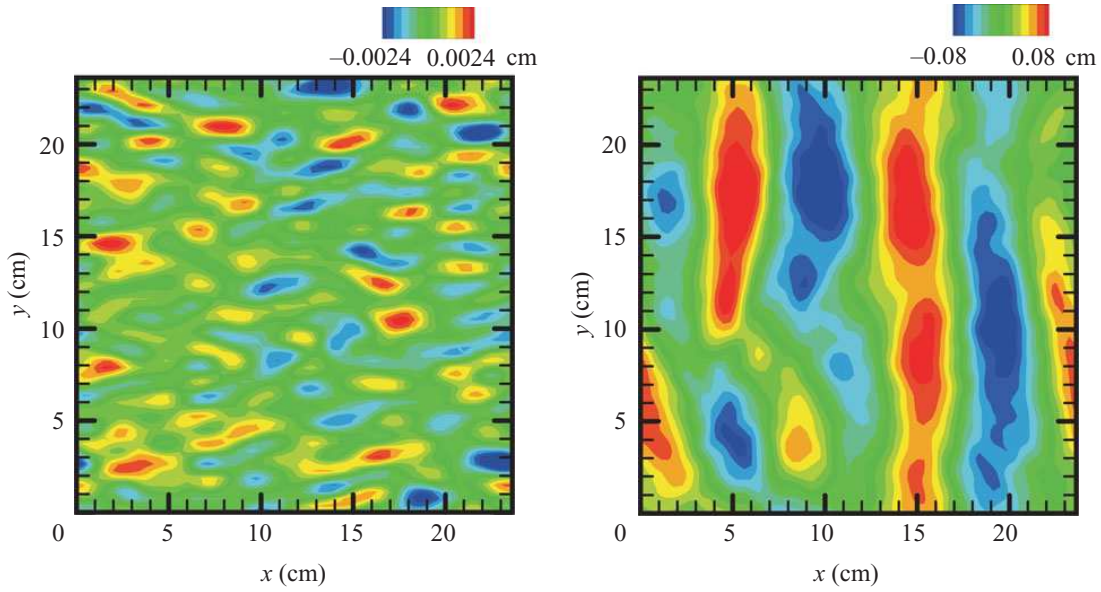

Figure 1.8: Snapshots of the instantaneous water surface elevation under the threshold, at time $t = 2.6$ s (left) and above the threshold, at $t = 66$ s (right). The wind is blowing in the direction of positive x. Adapted from [Lin et al., 2008].

of wave generation of wave growth are often only mentioned. The threshold is generally defined in experiments either as the minimal wind velocity at which waves can be observed, or as the minimal wind velocity at which waves start to grow. This begs the question of the accurate detection of the threshold. A detection based on wave amplitude or growth necessarily carries an embedded bias due to the limitation of the instrumentation. The debatable definition of the threshold wind velocity and the issues related to this question may partially explain the discrepancies between the different wave generation thresholds found in the literature for water waves (see table 5.3 on page 104).

1.3.3 Recent advances

Direct numerical simulation

Direct numerical simulation (DNS) of wind waves is not an easy task. To obtain results representing accurately the physical system, a lot of parameters have to be taken into account. The main difficulty lays in the coupling between the two fluids, whose integration into simulations had not been made possible until recently [Lombardi et al., 1996] [Fulgosi et al., 2003] [Tsai et al., 2005a] [Lin et al., 2008] [Yang and Shen, 2011] [Liao and Kaihatu, 2012] [Ó Náraigh et al., 2014]. Before this improvement, direct numerical simulations were restricted to the turbulent airflow, above flat, rough or wavy undeformable walls [De Angelis et al., 1997] [Cherukat et al., 1998] [Sullivan et al., 2000] [Jimenez et al., 2004] [Deck et al., 2014]. These DNS provide crucial information on the characteristics of the turbulent wind and bring some insight on the airflow above the waves. However, they do not, of course, offer any more details on the waves themselves.

As more advanced computational resources became progressively available, it became possible to include the coupling between air and liquid motions into the DNS of wind waves. In [Tsai et al., 2005a], Tsai et al. simulate numerically the turbulent shear flow

beneath a stress-driven flat free surface. The formation of surface waves is inhibited: the surface motion is allowed horizontally but not vertically. Thus, the focus is put on the two-way interaction between the stress-imposed surface and the turbulent flow. The numerical simulations are carried out for three wind speeds (3, 4 and 5 $m.s^{-1}$). It is found that there are streamwise velocity streaks at the interface, whose spacing decreases with wind velocity. In [Lin et al., 2008], Lin et al. take the numerical simulation a step further. They perform a complete 3D numerical simulation of the turbulent airflow and the flow in the water, including the coupling between the two and the initiation of surface waves. The fully developed turbulent airflow is obtained by starting the simulation over an undeformable flat free surface, then at time $t = 0$ the boundary becomes suddenly deformable, mimicking a liquid surface acted upon by a fully developed turbulent wind. The DNS is executed in a periodic box: they can therefore only observe the temporal evolution of the surface deformations over a field of 24×24 cm, not their spatial evolution. The simulation is stopped before nonlinear effects become significant. They report two regimes of generation of wind wave generation: a first regime of light tremors where the temporal growth is linear, and a second regime of transverse waves of exponential growth (see Fig. 1.8). At short times, below the wave onset, surface deformations are not organized in transverse waves yet and the streamwise velocity presents high-speed streaks similar to those reported in [Tsai et al., 2005a]. At later times, the interface becomes populated with transverse waves. As the surface goes from streak to wave patterns, wave energy goes through a linear stage followed by an exponential stage. This evolution is supported by the combined model of Phillips-Miles. Comparing their results in the linear growth stage to Phillips' model [Phillips, 1957], Lin et al. obtain a simulated growth rate that is about 1.5 times greater than the theoretical prediction [Lin et al., 2008]. In the exponential stage, the simulated wave growth is found consistent with the mechanism of Belcher & Hunt [Belcher and Hunt, 1993] and larger by a factor of two relatively to the empirical relation given in [Plant, 1982]. Their numerical simulations also allow to access the pressure and stress fields at the interface, which are very difficult to measure in experiments. Comparing the pressure fields in air and water and the field of surface elevation, they conclude that the energy transfer mechanisms originate from turbulence-induced pressure fluctuations in the early linear growth regime and from in-phase relationship between wave-induced pressure fluctuations and wave slope in the later exponential growth regime.

Liao & Kaihatu improve the work of [Lin et al., 2008] by imposing the nonlinear boundary conditions for normal stress at the interface while Lin et al. used linearized forms [Liao and Kaihatu, 2012]. They obtain results similar to those of [Lin et al., 2008] but with relatively faster growth in the linear stage and slower growth in the exponential stage, compared to the case with linearized normal stress boundary conditions.

Note that the surface perturbation obtained by numerical simulation below the wave onset are extremely small: less than 25 μm. Experimentalists often report slight interface motions below the threshold velocity [Keulegan, 1951] [Kunishi, 1963] [Hidy and Plate, 1966] [Plate et al., 1969] [Gottifredi and Jameson, 1970] [Wu, 1978] [Kahma and Donelan, 1988] [Ricci, 1992] [Caulliez et al., 1998] [Lorenz et al., 2005]. Usually by watching the variations in reflected light on the interface, they observe over the entire surface very small oscillations of the liquid that appear not to be growing. For example, [Ricci, 1992] describes small waves of very weak amplitude (0.01-0.02 mm) and states that the first ripples amplified by wind slowly emerge from the "noise" of these surface oscillations of random frequency. These surface deformations are of such small amplitude that their measurements in experiments is a challenge, heightened by the major effect of outside vibrations at this scale [Kahma and Donelan, 1988]. As far as I have been able to discover,

these small surface deformations at low wind velocity below wave onset have not been the focus of any experimental study. Consequently, a fair part of my work has been dedicated to their analysis.

Instrumentation

The accurate measurement of the deformation amplitude of the liquid surface is of primary importance in the study of surface waves. It allows access to the evolution in time and space of the surface deformations, the wave parameters, its temporal spectrum, its steepness, its growth rate, etc. Nowadays, the measurement of the topography of a free surface can be achieved through a wide variety of instruments employed in laboratory or in open sea.

The simplest method consists in using a local probe, like a capacitance or resistive wave gauge. Generally speaking, local probes are the easiest instrument to implement on a set-up. In the case of surface waves, they make it easy to do long temporal measurements and study the statistics of the waves. Conventional capacitance and resistive wave probes are so convenient that they have been used for decades [Kunishi, 1963] [Sutherland, 1968] [Wu, 1975] [Kawai, 1979] [Caulliez, 1987] [Hasselmann and Bösenberg, 1991] [Ricci, 1992] [Veron and Melville, 2001] [Caulliez et al., 2007] [Longo, 2012] [Grare et al., 2013]. They can accurately measure the height of the liquid (with a typical precision of 0.1 to 1 mm) but because they go through the interface they have an embedded limitation in resolution of the order of a tenth of the height of the meniscus around the probe. This can be problematic if the deformation that is being studied is smaller than this limit, which is bound to be the case at an early stage of wave generation. To circumvent this problem, non intrusive probes measuring the wave height or slope have also been developed and used, for instance laser slope gauge [Kahma and Donelan, 1988] [Tang and Wu, 1992] [Savtchenko et al., 1997], ultrasound distance meter [Longo et al., 2012] [Longo, 2012] or profile detection using a laser sheet crossing the interface [Siddiqui and Loewen, 2007] [Caulliez, 2013] [André and Bardet, 2014] [Buckley and Veron, 2016]. These methods have different measuring ranges and precisions but usually allow access to smaller wave amplitudes than capacitance or resistive wave gauges. In particular, the smallest amplitude of surface deformation measured unintrusively by a local probe seems to have been achieved by Kahma & Donelan [Kahma and Donelan, 1988]. Using a sensitive slope gauge based on the reflection of a laser beam on the interface, they are able to measure surface deformations of amplitude as small as 10 μm.

Intrusive or not, local gauges are inherently restricted in the information they can provide: spatial information can only be recovered by using multiple probes or by repeating runs with the probe moved to a different location. As a consequence, optical methods have been explored quite early on in order to have access to full two dimensional measurements of the topography of a free surface. Indeed, global optical methods are usually more difficult to implement and imply some degree of calibration and computations, but they give access to the spatio-temporal dynamics of the interface over a relatively large field of view. The principles at the core of quite a few of these optical techniques have be known for a relatively long time, but recent technological advances have drastically simplified their implementation and improved their accuracy and resolution. A recent review of the optical methods for the measurements of the deformations of a free surface can be found in chapter 2 of [Gomit, 2013] [11].

For example, stereo-imaging of a free surface, a method using the image correlation

11. In French.

between two cameras, has largely improved thanks to faster image processing and the availability of better cameras. [Leckler et al., 2015] describes a stereo video system using two synchronized cameras installed at sea. Each point recorded by a camera is associated to another point in the recordings of the other camera. The processing of the video data provides a surface elevation map $\zeta(x, y, t)$ over a large area: a field of approximately 15×20 m with a resolution of 5 cm in each direction.

In a laboratory, another technique consists in injecting white dye into the liquid and projecting a pattern on the interface. Thanks to the dye, the instantaneous liquid surface appears as a white diffusive surface and its topography can be reconstructed by comparing the projected pattern to the deformed pattern on the interface. In [Tsubaki and Fujita, 2005], the projection of an irregular greyscale pattern allows to measure waves as small as 1 mm with a 16% accuracy (~ 0.15 mm), over a 18×14 cm field, with a spacing of 0.6 cm in each direction. Similarly, Cobelli et al. have devised an optical method of topography measurements based on the projection of fringes (fringe projection profilometry) [Cobelli et al., 2009]. A fringe pattern of known characteristics is projected by videoprojector on the interface while a camera records the deformed fringes resulting from the surface deformation (dye is added to the water to enhance its diffusivity). The surface can be reconstructed from the comparison between the reference (undeformed) fringes to the recorded (deformed) ones. This method is able to measure surface perturbations in the range $0.2 - 100$ mm with a 0.2 mm vertical resolution, over a field of view of 45×30 cm with a 0.1 mm spatial resolution. The vertical resolution depends on the size on the projected pixel, which means that it can be improved by a better projector resolution or a reduced size of sampled windows. Other measurement methods of free surface deformation based on fringe projection profilometry have been developed (for example [Cochard and Ancey, 2008]) but the technique of [Cobelli et al., 2009] seems to have the best vertical resolution. Note that the choice of the coloring dye added to the liquid is important since most paint pigments contain surfactants that will strongly affect the surface waves. For fringe projection profilometry to be efficiently used, the coloring additive mixed with the liquid has to be carefully chosen so that it does not significantly change the surface tension [Przadka et al., 2012].

Refraction of a specific light source through the liquid-air interface can also be used to measure the surface elevation. Indeed, if the light source is coded in intensity or color, its refraction through the interface allows for the measurement of the local slope by combining the refraction laws and the light coding pattern. An integration of this surface gradient then provides the topography over the whole field of visualization. For instance, in [Zhang and Cox, 1994], the local slopes of wind waves of a few centimeters of amplitude are measured using collimated color-encoded light. The area of visualization is of 20×14 cm, with a spatial resolution of 0.6 mm and a vertical resolution depending on the color-coding of the slopes. Likewise, in [Veron and Melville, 2001], the local slope of the surface is measured by Color Imaging Slope Gauge (CISG), based on the refraction of a color-coded light screen through the interface. The screen is such that each point on it has a unique color, which allows to measure the slope by the color difference resulting from the refraction. Their field of view is of 27×37 cm with a spatial resolution of 0.6 and 1.1 mm in the x and y directions, respectively. Using the refraction of a rapid sequence of four intensity gradients in different directions combined into one slope image, Kiefhaber et al. [Kiefhaber et al., 2014] are able to capture the 2D distribution of surface slope over 20×16 cm field with an excellent spatial resolution of 0.22 mm (see figure 1.9).

Like [Zhang and Cox, 1994] but unlike [Veron and Melville, 2001], they use a lens so that their light source is collimated into parallel rays. This is an important limitation

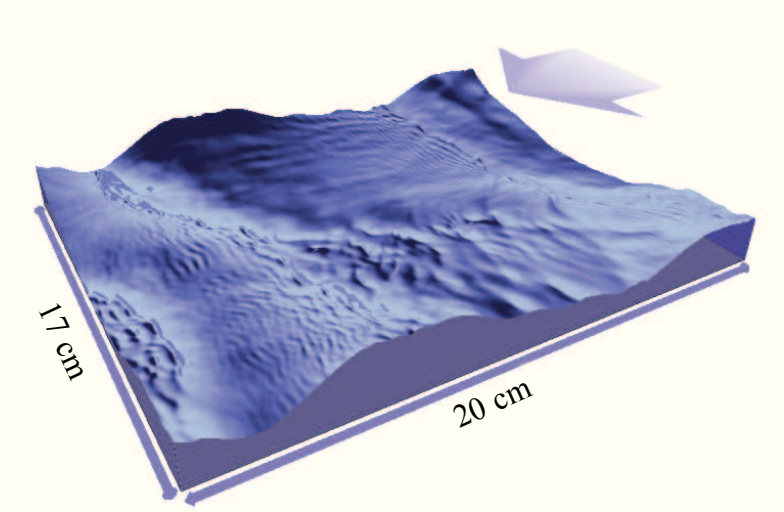

Figure 1.9: 3D rendering of the wave field at 6.4 m.s^{-1}. The arrow indicates the wind direction. Adapted from [Kiefhaber et al., 2014] .

of their technique: the field of view can be only as large as the lens that is used. This restriction incites use of an optical method based on the refraction, not of collimated light, but of scattered light from a grating or a random set of dots. In this case, each point of the light source is not coded to correspond to a particular height or slope, but a pattern deformed by refraction is compared to its original image [Kurata et al., 1990]. This leads to a simpler set-up and calibration than in the case of collimated light. This approach has first been applied to stratified fluids, where the index of refraction changes with density resulting in a different refraction and the measurement of the density field [Dalziel et al., 2000] [Meier, 2002]. Building on these works, Moisy et al. have modified this technique for the measurement of the deformation of a free surface [Moisy et al., 2009]. Their method, the Free Surface Synthetic Schlieren method (FS-SS), is based on the apparent displacement of a refracted random dot pattern through an interface. Correlating a recorded image to a reference image taken when the liquid is at rest allows for the reconstruction of fluid height. Strong curvatures leading to caustics limit this method, but under certain conditions, the vertical resolution of FS-SS can be more than a 100 times smaller than the one in [Cobelli et al., 2009]. This method, successfully used for the study of small-amplitude surface waves in the context of the parametric instability due to an harmonic forcing [Moisy et al., 2012], is adapted to the experimental set-up for this PhD and is described in more details in chapter 2.

All measurement techniques have a combination of assets and drawbacks based on their range of application, accuracy, size of field of view, spatial resolution, easiness of implementation and use, sensitivity, etc. In the study of the first stages of wind wave generation, the limiting parameter would be the range and accuracy of the instrumentation. The measurement method must be able to measure surface deformations of very small amplitude (less than a tenth of a millimeter) with a great accuracy. These criteria are both verified by the FS-SS method of visualization, as it is an optical method of measurement of the instantaneous topography of a fluid interface with an excellent vertical resolution, with a field of view only limited by the sizes of the pattern and camera field of view.

1.4 Goals and scope of this PhD

Exploring experimentally the early stages of wind wave generation requires an instrumentation allowing for a precise measurement of submillimetric amplitude of surface deformation. As seen in the previous section, the FS-SS method seems to be an appropriate tool for this study. The first goal of this PhD is to study experimentally, taking advantage of the great vertical resolution of the FS-SS technique, the evolution of the shape of an interface under the action of a turbulent airflow. Departing from the large literature on water waves, the experiments are carried out with a liquid much more viscous than water. This represents a double advantage. First, the drift current in the tank is simpler and weaker than in the typical situation of a turbulent current in water. Second, the high viscosity of the liquid implies that the perturbations of the interface that are not amplified are rapidly damped. At low wind speed, the surface deformations are therefore expected to be the direct local response to the wind. The liquid viscosity being a central parameter in our system, the second objective of this PhD is then to study the influence of the viscosity, both below and above the onset of wave generation.

The structure of this manuscript is as follows. The theoretical framework and relevant literature have been introduced in the present chapter. Chapter 2 describes in details the set-up and method of visualization on which stand the results presented in chapters 3, 4 and 5. In the same chapter are presented the results of the base flow characterization in the air and liquid flows. In chapter 3, the early stages of wave generation are explored experimentally over a liquid thirty times more viscous than water. Two regimes of wave generation are reported and described in detail. The nonlinear behavior observed beyond the critical wind velocity are presented in chapter 4. In chapter 5, experiments are conducted with different liquids in order to study the influence of the liquid viscosity on the system. A particular interest is taken in the effect of viscosity on the wave generation threshold and on the earliest stage of interface deformation before wave onset. It is shown that the earliest stage of generation of surface deformation can be explained by a model based on the influence of pressure fluctuations on the viscous interface. Finally, the thesis concludes in chapter 6 with a general conclusion and the possible outlooks to this work. For the reader's convenience, each chapter is quickly summarized in a boxed text at the end before the subsequent chapter.

1.5 Conclusion

The generation of waves under the action of wind over a liquid interface is a long-standing problem incepted by the universal observations of natural wind waves over water. Despite the considerable body of literature on the subject, there still exist significant gaps in our understanding of the mechanisms associated with wind wave generation.

The first attempt to explain wind wave formation consisted in the inviscid Kelvin-Helmholtz instability, but it leads to predictions that are in strong disagreement with the observations at an air-water interface. The pioneering works of Phillips and Miles later brought major theoretical contributions. Phillips proposed a model based on the direct effect of the pressure fluctuations of the turbulent wind over the interface. Disregarding the coupling between wind and wave motion, he obtained a linear temporal growth of the wave amplitude squared. Using a completely difference approach, Miles introduces a mechanism based on the stability analysis of the shear flow. Neglecting viscosity, surface tension, drift current and turbulent fluctuations, he showed that this stability depends on the sign of the curvature of the mean velocity profile at the critical height at which

the wind speed equals the wave phase velocity. If this curvature is negative, the flow is unstable, resulting in an exponential growth in time of the amplitude of the wave.

The numerous attempts to confirm experimentally or improve the theoretical models of wind wave generation yield no definitive conclusion at the present time. However, direct numerical simulations are nowadays capable to address the coupling between the air and liquid motions and their influence on the generation of surface deformations. These simulations fuel the approach of the combined Phillips-Miles' model and have shown the existence of streamwise streaks at the interface below the wave generation threshold. While small tremors at the liquid surface before the onset of wave generation are often reported during experiments, no study focuses on their analysis due to the challenge of measuring such weak deformations.

Recent improvements in optical methods have made it possible to study the early stage of wind wave generation. During my PhD, I have implemented such an optical technique of excellent vertical resolution, the Free Surface Synthetic Schlieren method of visualization, for the study of the generation and growth of wind waves over a viscous liquid. The choice of a liquid more viscous than water is motivated by the simplification of the system's response due to a rapid damping of the unamplified perturbation and by the particular importance that viscosity seems to have in the behavior of wind waves.

Summary:

- Wind waves are a complex and fascinating phenomenon that involves numerous parameters. Despite a large literature on the subject, a great number of questions remain concerning the physical mechanisms of wind wave generation.
- The two central models of wind wave generation originate from Phillips [Phillips, 1957] and Miles [Miles, 1957]. Phillips' model deals with the direct effect on the interface of the pressure fluctuations in the turbulent wind and leads to a linear growth in time of the wave amplitude squared. Miles' model is based on a shear-flow instability and leads to an exponential growth in time of the wave amplitude.
- Direct numerical simulations have benefited from recent improvements and are now able to take into account the complex coupling between wind and wave motions. They report surface deformations of very small amplitude below the threshold velocity of wave generation but can only access their temporal evolution, not their spatial evolution.
- This PhD thesis presents an experimental work conducted using the Free Surface Synthetic Schlieren method of visualization, an optical method of excellent vertical resolution, in order to study the wind wave generation and growth over a viscous liquid.

Chapter 2

Experimental set-up and flow characterization

The experiments described and discussed in the present thesis have been carried out in a new set-up built at the laboratory FAST. In this chapter are presented first the experimental set-up and the method of visualization, then the characterization of the base flows in the air and liquid.

2.1 Experimental set-up

2.1.1 Design and general view

In order to investigate the generation and growth of wind waves, a set-up combining a wind tunnel and a wave tank was designed, built and tested at the laboratory FAST. The objective was to adapt the Free Surface Synthetic Schlieren (FS-SS) method of visualization onto a wind wave tank so as to study the initial stages of wave generation under the action of wind. As a matter of fact, the FS-SS method has several advantages compared to the techniques previously used to study this phenomenon (see chapter 1). First, it allows to visualize the surface deformation induced by wind with an unequaled vertical accuracy. The micrometric resolution we are able to achieve makes it possible to study the first surface perturbations at small wind speeds, which, to our knowledge, has not been done globally with such precision. Indeed, unlike local probes, this visualization method also enables access to the entire topography of the liquid surface. The field of view covers almost the entire width of the tank and about 40 cm in the downstream direction. Thanks to our good spatial and temporal resolutions, the FS-SS method thus gives access to the spatio-temporal dynamics of the interface deformation.

The set-up features a tank and a wind blower creating the airflow above the liquid. The wind blower was provided by the Laboratory of Hydrodynamics of the École Polytechnique. The tank and wind tunnel were designed so that the dimensions of the internal rectangular section of the wind channel match precisely the internal dimensions of the wind blower at its exit. Figures 2.1 and 2.2 provide a sketch and a picture of the final set-up. The turbulent airflow is injected by a wind blower into the wind channel at the bottom of which is fitted a tank containing the liquid. The method of visualization, requiring a camera and a dot pattern, will be described in section 2.1.3.

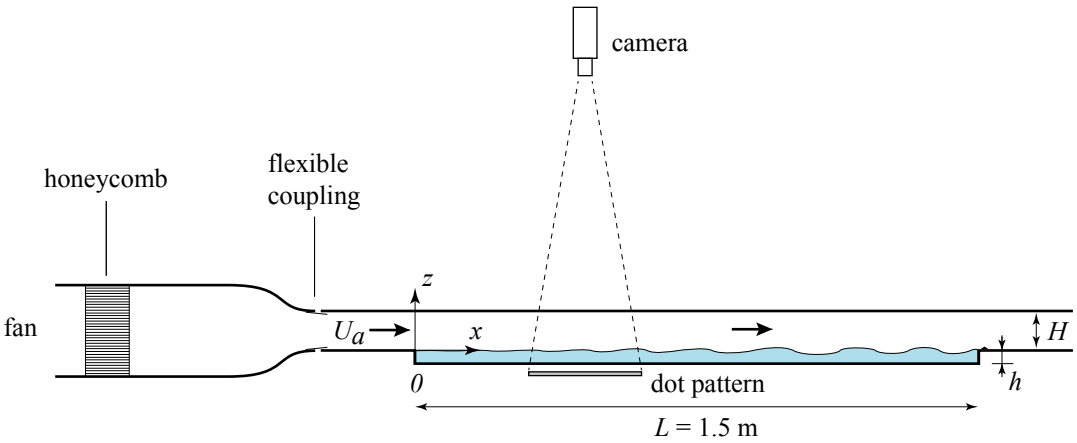

Figure 2.1: Sketch of the experimental set-up.

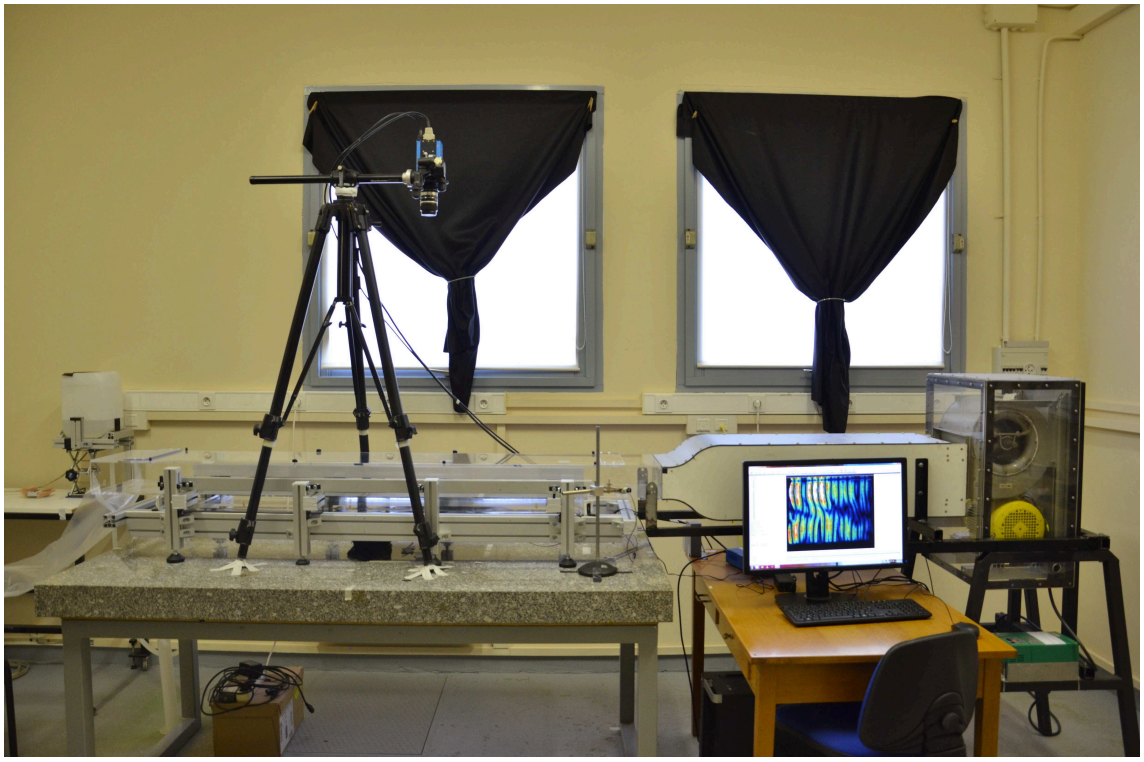

Figure 2.2: Photography of the experimental set-up.

2.1.2 Liquid tank and wind tunnel

Tank and wind channel body

The experimental set-up is composed of a fully transparent Plexiglas rectangular tank of length $L = 1.5$ m and width $W = 296$ mm fitted to the bottom of a horizontal channel of rectangular cross-section. While the total depth of the tank is 50 mm, 15-mm thick Plexiglas plates were added at the bottom of the tank in order to decrease the volume of liquid to be used. Thus, the depth of the tank was reduced to $h = 35$ mm. The channel width is identical to that of the tank, its height is $H = 105$ mm, with two horizontal floors of length 26 cm before and after the tank.

The tank and wind channel were manufactured by the company Abaqueplast from 8-mm thick laser-cut Plexiglas plates. Careful attention was paid to the locations of the junctions of the panels. These locations were specified to the contractor in order to make sure that the entrance and exit horizontal floors were kept smooth. A draining hole was drilled at the end of the tank in a corner. A T-connection allows to separate the flow from this opening into a draining duct and a pipe leading to a container placed on a laboratory jack used for the filling of the tank and rough adjustment of the level of the liquid. Apart from the draining orifice, the tank and wind tunnel body is symmetrical. The tank is propped up on Norcan beams on its side walls only, so that the support beams do not restrict the visualization through the bottom of the tank. Slender Norcan beams are also fixed along the set-up to prevent the side walls from bending (Plexiglas plates tends to bend after a prolonged contact with a water-based liquid). The upper part of the wind channel can be removed to access the inside of the set-up if needed. When the insertion of a probe is necessary inside the wind channel, a second Plexiglas plate with holes is used while the original ceiling is kept untouched for optical measurements.

We define the coordinate axes (x, y, z) in the streamwise, spanwise and upwards vertical direction, respectively. The origin (0,0,0) is located at the free surface at mid-distance between the lateral walls of the wind channel. Thus, $z = 0$ is defined at the level of the liquid at rest and the liquid fills the negative z space until the depth $-h$. As mentioned in the previous chapter, in accordance with the literature, the term *fetch* refers to the distance over which the wind blows; in our case, the fetch is the distance x from the beginning of the tank.

Wind blower

The airflow is generated by a centrifugal fan with forward-curved impellers that produces little to no swirl in the outgoing flow. The fan is connected by a belt to a three-phase 3 kW motor and the motor is controlled via a variator with an input frequency range of 0-50 Hz with a 0.1 Hz accuracy. The relationship between the wind speed and the variator frequency is linear. The air is injected from the fan through a honeycomb and a convergent (ratio 2.4 in the vertical direction) into the wind channel. The wind velocity U_a, measured at the center of the outlet of the wind tunnel with a hot-wire anemometer, can be adjusted in the range $1 - 10$ m.s^{-1}. The wind profile will be described in details in section 2.2.1.

The wind channel and the wind blower are not in contact. To minimize the air leaks and the transmission of vibrations induced by the fan, they are are separated by a gap of a few millimeters and are only connected via a flexible coupling. To further isolate the tank from outside vibrations, the wave tank is placed on a 2 m $\times$ 1 m, 10 cm thick, granite plate weighting about 500 kg, itself on top of a thick metal frame. The entire experimental

set-up is on a concrete floor that isolates it well from the vibrations created by a person's motion in the room. Nevertheless, the experiments being very sensitive to vibrations, they had to be carried out during evenings because of sources of strong vibrations during the day, due to the traffic outside and a nearby construction site. Residual vibrations induce surface deformations of less than 1 μm.

Liquid mixture

During the experiments later described and discussed, the tank is filled with a mixture of water and either glycerol or glucor. The properties of the various liquid mixtures that were used are specified in the first sections of chapters 3 and 5. Regardless of the mixture used, the fluid is always assumed to be Newtonian and incompressible. The liquid is thoroughly mixed outside the tank by an overhead stirrer then mixed again in the tank under the wind action until no density gradient is visible anymore. A small dam of height 8 mm is placed at the end of the tank in order to avoid overflow.

In a turbulent flow, the shear stress at the liquid surface and at the lateral and upper walls is balanced by a small longitudinal pressure gradient $\Delta p/L$ in the air along the channel. This pressure gradient introduces a complication in the set-up: the liquid surface becomes slightly tilted, with the inlet liquid height below the outlet height (this is analogous to the "wind tide" effect observed on lakes [Keulegan, 1951]). Assuming equal stress τ on the liquid surface and on the solid walls, this pressure gradient reads $\Delta p/L \simeq 2\tau(1/W + 1/H)$. For a wind velocity $U_a = 4$ m.s^{-1}, the pressure drop along the tank is $\Delta p \simeq 2$ Pa, which results in a hydrostatic height difference between the two ends of the tank of $\Delta p/\rho g \simeq 0.2$ mm, in good agreement with our measurement. We observed that the resulting backward facing step at $x = 0$ significantly increases the turbulent fluctuations and enhances the wave amplitude at small fetch by typically a factor of 2. It is therefore critical to maintain the liquid level at $x = 0$ by carefully tilting the channel. Thus, the surface of the liquid is leveled to precisely coincide with the bottom of the wind tunnel. We achieve a leveling of the liquid at $x = 0$ better than 20 μm by using the tangential reflection of a laser sheet intersecting the upstream plate and the liquid surface.

2.1.3 Surface deformation measurement: Free Surface Synthetic Schlieren method

The FS-SS method of visualization

We measure the surface deformation of the liquid using the Free Surface Synthetic Schlieren (FS-SS) method developed by Moisy, Rabaud and Salsac [Moisy et al., 2009]. This optical method is based on the analysis of the refracted image of a pattern visualized through the interface. A random dot pattern is placed under the tank and a camera is placed above it, on the other side of the liquid-air interface. A reference image of the undeformed pattern is taken when the liquid is flat, at rest in absence of wind. When the wind blows, the interface deforms under its action and the refracted image of the dot pattern is acquired through the liquid-air interface. The apparent displacement field $\delta\mathbf{r}$ between the reference image and the distorted image in presence of waves is computed using an image correlation algorithm. In the linear approximation of small slopes, the displacement field induced by the refraction is proportional to the gradient of the surface height.

The relation between the surface height gradient and the displacement field can be written as (see Eq. (13) in [Moisy et al., 2009]):

$$\nabla\zeta = -\frac{\delta\mathbf{r}}{h^*} \text{ with } \frac{1}{h^*} = \frac{1}{\alpha h_p} - \frac{1}{H}. \tag{2.1.1}$$

$\alpha = 1 - n_{\text{air}}/n_{\text{liquid}}$ is a coefficient based on the refractive indices n_{air} and n_{liquid} of the air and of the liquid, respectively. H is the pattern-camera distance and h_p is the equivalent height of liquid, computed from on the thicknesses h_{i} and refractive indices n_{i} of the different layers of matter between the pattern and the interface. In our case (see Fig. 2.3), the interface is separated from the pattern by liquid (in the tank), Plexiglas (the bottom of the tank) and air (from the bottom of the tank to the pattern). Thus, the equivalent height is (see Eq. (14) in [Moisy et al., 2009]):

$$h_p = h + \frac{n_{\text{liquid}}}{n_{\text{plexiglas}}} h_{\text{plexiglas}} + \frac{n_{\text{liquid}}}{n_{\text{air}}} h_{\text{air}}. \tag{2.1.2}$$

Using equation (2.1.1), the integration of the displacement field thus allows to reconstruct the surface topography and gives the height field $\zeta(x, y, t)$ (see examples in figures 2.4 on the following page and 3.1 on page 60).

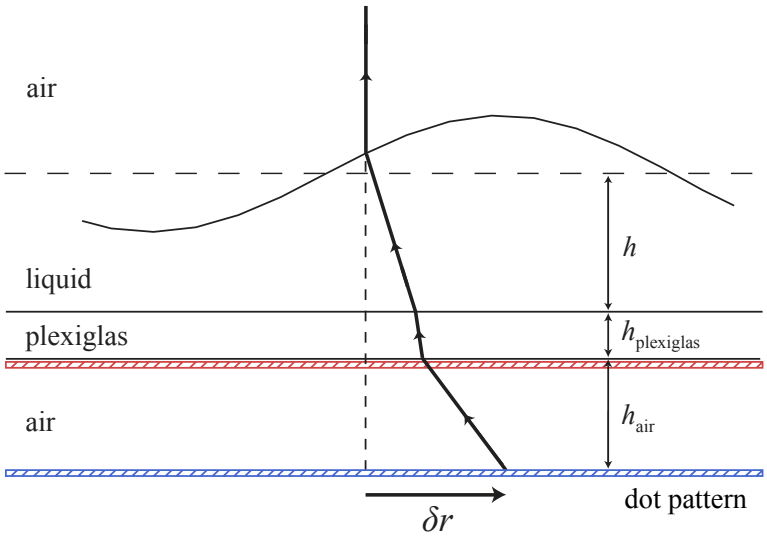

Figure 2.3: Sketch of the optical path through the liquid, Plexiglas and air. The dot pattern colored in blue correspond to the pattern placed the furthest away from the interface, on the granite table; the pattern in red correspond to the position of the pattern closest to the interface, directly under the tank.

Implementation

The acquisitions are done with a PCO 1200hs fast camera mounted with a 35 mm Nikon lens. The camera is centered on the field of view and adjusted to a right angle with the dot pattern. The PCO camera is controlled using the software Camware 3.14 under Windows 7. Each image is recorded separately in *.tiff* format at the full frame resolution of 1280×1024 pixels. The images are transferred from the internal memory of the camera

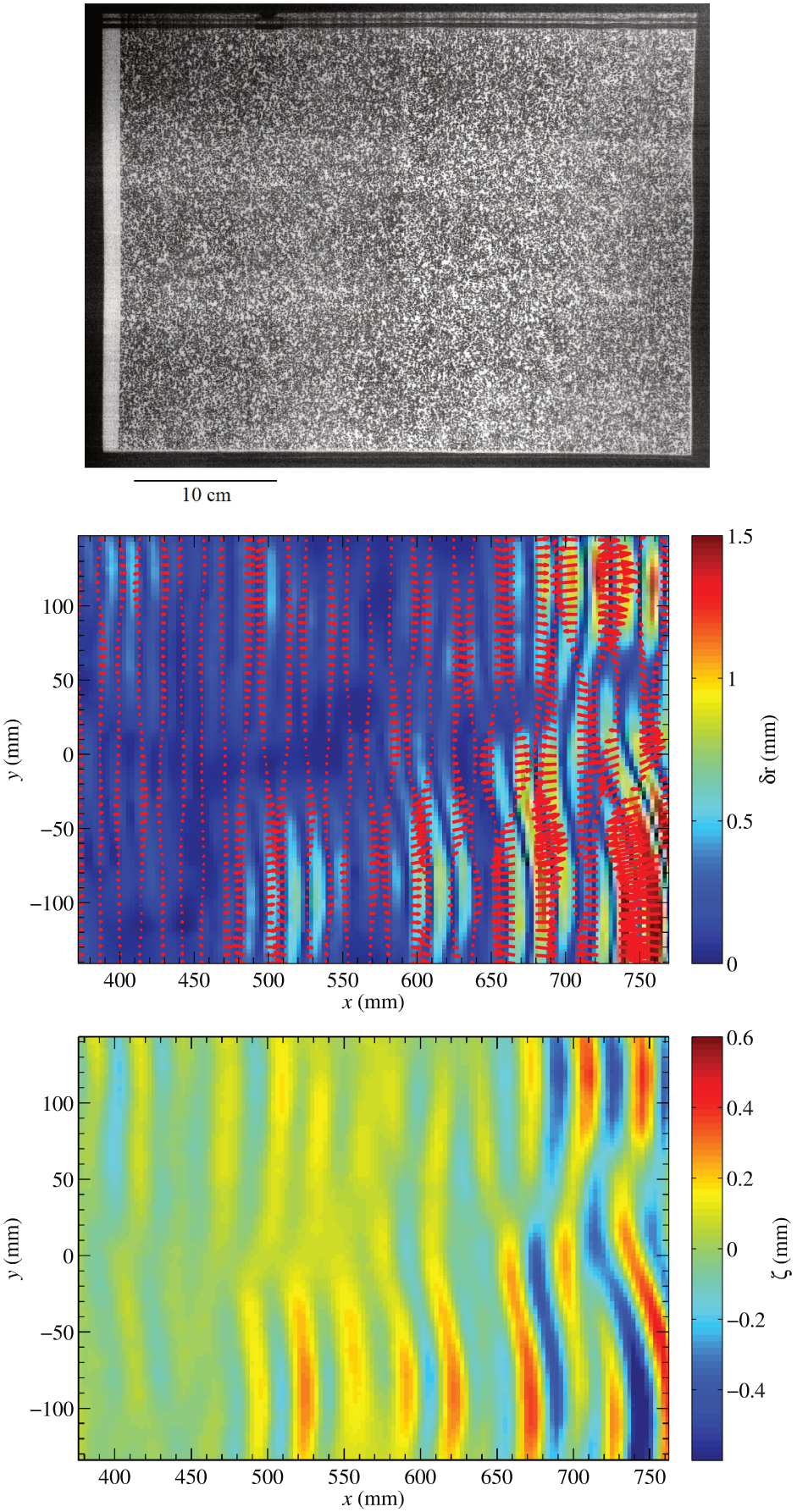

Figure 2.4: (Top to bottom) Dot pattern, displacement field and height field obtained by FS-SS. The wind is blowing from left to right at 6.9 m.s^{-1}.

to the computer through a Firewire IEEE 1394a connection. This camera memory buffer is of 4 Go, which represents a little over 2000 images. At first, the camera was mounted on a tripod 1 m above the set-up as in figures 2.1 and 2.2. The experiments described in chapter 3 were done in this configuration. Later on, to minimize the distortions due to parallax, a mirror was installed at a 45° angle above the set-up, the camera was moved 3 m away from the set-up, and the 35 mm lens was changed for a 105 mm one. The experiments described in chapters 4 and 5 were done in this configuration. It was later found that the distortions due to parallax were much smaller than the distortion implied by waves entering or leaving the field of visualization (it induces an artificial change in the mean displacement field, see appendix A). The accuracy is thus actually very similar in both configurations.

The dot pattern has to be random in order to maximize the information content and avoid fortuitous image matching. Indeed, if the pattern were periodic (a grid for example), the displacement would be known only modulo the pattern periodicity, leading to an incorrect apparent displacement. The random dot pattern is created [1] in such a way that the dots diameter is between 2 and 5 pixels in the acquired images, and that the smallest interrogation windows later used in the image correlation algorithm (16×16 pixels) contains 5 to 10 dots. In practice, we use an A3 sheet randomly covered by 50 000 dots of diameter 2 mm. The pattern is printed on a transparent plastic sheet and positioned over a LED light sheet that provides an uniform light source, allowing to avoid stroboscopic effects. This light sheet is a FlexLedLight CFEA3 electroluminescent foil of dimensions 30×40 cm. In order to maximize contrast and avoid fluctuations in light intensity, the lens aperture is set to its maximum and the lighting of the room is turned off.

The displacement fields are computed by the software Davis (version 8.1) by image correlation. To obtain the surface height $\zeta(x, y, t)$ from equation (2.1.1), an inversion of the gradient $\nabla\zeta$ is required. Numerically, ζ is taken as the best solution in the least-square sense, that is to say the solution minimizing the residual $\parallel \nabla\zeta - (-\delta\mathbf{r}/h^*) \parallel^2$ where $\delta\mathbf{r}$ is the measured apparent displacement field. This is achieved using the Matlab function *surfheight*. Appendix A provides the details of the different steps during an FS-SS experiment and the computations that follow.

Resolution and limitations

The distance h_p between the random dot pattern and the liquid surface sets the sensitivity of the measurement. The further away the pattern is below the tank, the smaller are the slopes that can be measured, since the same apparent displacement will correspond to a smaller slope. However, a curved surface acts as a convergent lens of focal length decreasing as the curvature increases. Thus, crossing of light rays can appear for large equivalent height or below waves of large curvature, creating caustics and preventing the measurement of the apparent displacement field, and the FS-SS method is no longer applicable in this situation (see Fig. 2.5). The greater the distance from the pattern to the surface, the smaller the highest slope can be (caustics arise at a lower surface steepness). Therefore, the pattern-interface distance is actually chosen according to the typical steepness of surface deformation. Because they are quite sinusoidal, it is found experimentally that in our case of wind waves, this steepness criterion is quite equivalent to a limitation of amplitude. We choose to put the pattern the furthest away, on the granite table, at a

1. Using the Matlab function *makebospattern* of the PIVmat toolbox, see `http://www.fast.u-psud.fr/pivmat/`.

distance of 29 cm for waves of weak amplitude (of order of $1 - 10$ μm), and the closest away, just below the tank, at 6 cm for waves of large amplitude (up to 1 mm). The two positions of the pattern are presented in figure 2.3 on page 31. With this distance of 6 cm, numerous caustics prevent the FF-SS method from being used for wave amplitudes larger than a few millimeters.

The observation and reconstruction of the liquid surface can be carried out over the entire width of the tank, but about 1 cm is excluded near each walls because of the deformation induced by the meniscus close to the vertical walls. This leads to a rectangular field of view elongated in the x direction of dimensions 390×280 mm. The resolution in x and y is 3 mm, and the vertical resolution is of order of 1% of the wave amplitude (but it is important to keep in mind that the residual vibrations can induce surface deformation of amplitude up to 1 μm).

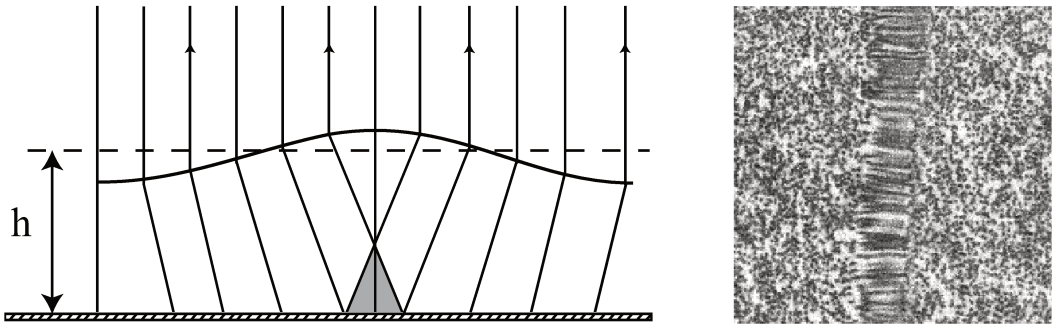

Figure 2.5: (Left) Large curvature or large pattern-interface distance induce ray crossings (adapted from [Moisy et al., 2009]). (Right) Visual result of caustics on the recorded image. The stretched dots lead to incorrect FS-SS reconstruction.

2.2 Characterization of the base flows

In order to better understand the conditions under which the liquid-air interface is deformed and wind waves are created, the base flows in the wind tunnel and tank were characterized, respectively by hot-wire anemometry and Particle Image Velocimetry (PIV). For both flow characterizations, the liquid is a glycerol-water mixture of 80% glycerol and 20% water (in weight) maintained at temperature 25 °C, of density $\rho = 1.20 \times 10^3$ kg.m^{-3} and kinematic viscosity $\nu = 30 \times 10^{-6}$ m^2.s^{-1}. For this liquid, the threshold of wave generation is $U_c = 6.3$ m.s^{-1} (see chapter 3).

2.2.1 Airflow

This section focuses on the characterization by hot-wire anemometry of the flow in the upper part of the set-up, in the air above the interface ($0 < z < H$, see figure 2.6). While it also addresses the velocity fluctuations in the airflow, this characterization of the airflow is centered on the mean flow profile. U is the mean velocity in the x direction and u' is the fluctuating part of the wind velocity in the x direction. The mean airflow is supposed to be essentially unidirectional and to barely change in the y direction. The mean velocity at the center of the wind channel is denoted by U_a (velocity outside the boundary layers). The air is considered incompressible and its density is taken as the tabulated air density

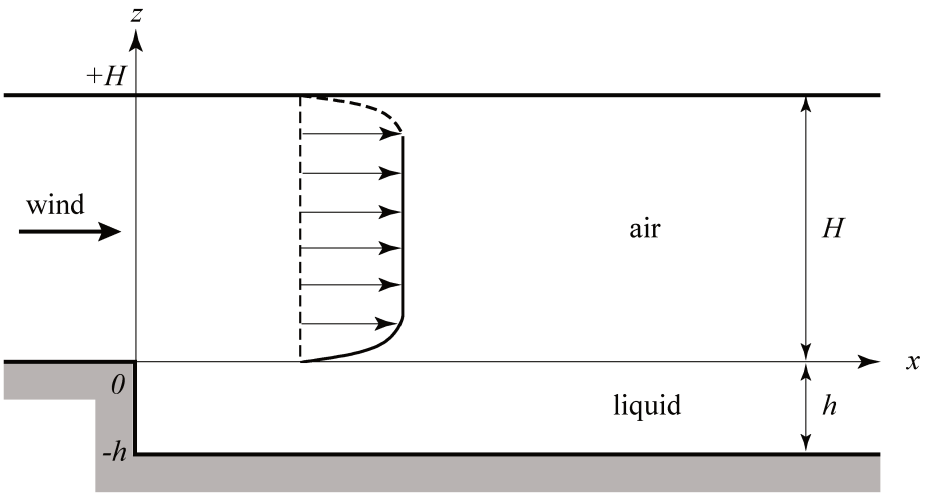

Figure 2.6: Sketch of the airflow.

at 25 °C and 1 atm: $\rho_a = 1.2$ kg.m^{-3}. The kinematic viscosity of the air is also supposed to be equal to its tabulated value for the same parameters of temperature and pressure: $\nu_a = 1.5 \times 10^{-5}$ m^2.s^{-1}.

In accordance with the notation in the literature, the friction velocity u^* is defined from the interfacial shear stress τ through the relation:

$$u^* = \sqrt{\frac{\tau}{\rho_a}}. \tag{2.2.1}$$

The friction velocity is taken as the characteristic velocity scale in the airflow boundary layers. From the friction velocity is built the viscous length scale:

$$\delta_\nu = \frac{\nu_a}{u^*}. \tag{2.2.2}$$

The superscript + indicates a quantity normalized using these scales: $U^+ = U/u^*$ is the dimensionless mean velocity and $z^+ = z/\delta_\nu$ the dimensionless distance from the wall or interface. The Reynolds number is defined based on the half-height of the wind channel:

$$Re_\tau = \frac{u^* H}{2\nu_a} = \frac{H}{2\delta_\nu}. \tag{2.2.3}$$

a) Turbulent boundary layer theory: Mean velocity profile in a turbulent flow over a wall

In this section, we recall the classical results from the turbulent boundary layer theory that details the mean velocity profile in a turbulent flow over a solid boundary. This description will later be used to characterize our data.

Let us consider a turbulent flow over a flat fixed wall. The mean velocity is zero at the wall and U_a far from the wall. At the vicinity of the wall stands a boundary layer where the mean velocity rapidly increases from 0 to U_a. The theory of the turbulent boundary layer states that the turbulent airflow over a wall can be separated into three main regions:

the viscous sublayer, the inertial sublayer, and the outer layer. The mean velocity profile can be approximated by a different law in each of these layers [Schlichting, 2000] [Guyon et al., 2012]. Note that the boundary layer thickens in the downstream direction if the flow is not fully developed, so the different variables are slightly dependent on the fetch x, even when this dependence is omitted to lighten the notations.

Close to the wall, the viscous sublayer extends up to about $10\delta_\nu$ (i.e., up to $z^+ \simeq 10$). In this first layer, the dimensionless velocity increases linearly with the dimensionless altitude from the wall:

$$U^+ = z^+. \tag{2.2.4}$$

In the inertial sublayer, spreading from the outer layer towards the viscous layer, the classic logarithmic law expressed in its non dimensional form writes:

$$U^+(x,z) = \frac{U(x,z)}{u^*(x)} = \frac{1}{\kappa}\ln\left(\frac{z}{\delta_\nu(x)}\right) + C^+, \tag{2.2.5}$$

where $\kappa = 0.4$ is the von Kármán constant and C^+ is constant. In the case of a smooth wall, C^+ is approximatively 5 [Schlichting, 2000] [Guyon et al., 2012]. The intersection between the two theoretical profiles of the viscous sublayer and the inertial sublayer occurs at $z^+ = 11$ (for $\kappa = 0.4$ and $C^+ = 5$).

Past this logarithmic growth, the profile connects to a constant velocity profile:

$$U^+ = \frac{U_a}{u^*}. \tag{2.2.6}$$

In the literature, the mean profile of the airflow over the liquid is always considered as logarithmic in the inertial sublayer, which is confirmed experimentally [Francis, 1954] [Plate et al., 1969] [Hsu et al., 1981] [Hsu and Hsu, 1983] [Liberzon and Shemer, 2011] [Longo, 2012] [Zavadsky and Shemer, 2012] [Buckley and Veron, 2016]. At the center of the channel, the literature gives u^*/U_a to be around 3% ($U^+ \simeq 30$) [Liberzon and Shemer, 2011], while our measurements show u^*/U_a to be roughly 5% ($U^+ \simeq 20$) in our set-up (see § 2.2.3). This difference may be explained by the fact that this ratio slightly depends on Re_τ. Figure 2.7, that presents the three connected profiles (viscous sublayer (Eq. (2.2.4)), inertial sublayer (Eq. (2.2.5)), and center of the channel (Eq. 2.2.6)), uses this value of 5% for the center of the channel [2].

This description of the mean profile given by the turbulent boundary layer theory still holds for a fully developed turbulent channel flow, in the theoretical case of a wind tunnel of infinite length, or for channel flow numerical simulations as they use periodical boundaries in the downstream direction. Thus, figure 2.7 also features the simulated mean velocity profile obtained at $Re_\tau = 1000$ for a fully developed 3D turbulent channel flow [Perlman et al., 2007] [Li et al., 2008] [Graham et al., 2013] [3]. This profile derived by direct numerical simulation (DNS) gives a better idea of the smooth transition from the viscous to the inertial sublayer.

2. Depending on this value U_a/u^*, the connection between the logarithmic and constant profiles occurs at a different altitude $z_a^+ = \exp(\kappa(U_a/u^* - C^+))$. For $U_a/u^* = 30$, z_a^+ is about 2 200, while for $U_a/u^* = 20$, the junction happens closer to the interface, at z_a^+ approximately equal to 400.

3. These three references correspond to the same database, the John Hopkins Turbulence database, available at `http://turbulence.pha.jhu.edu`.

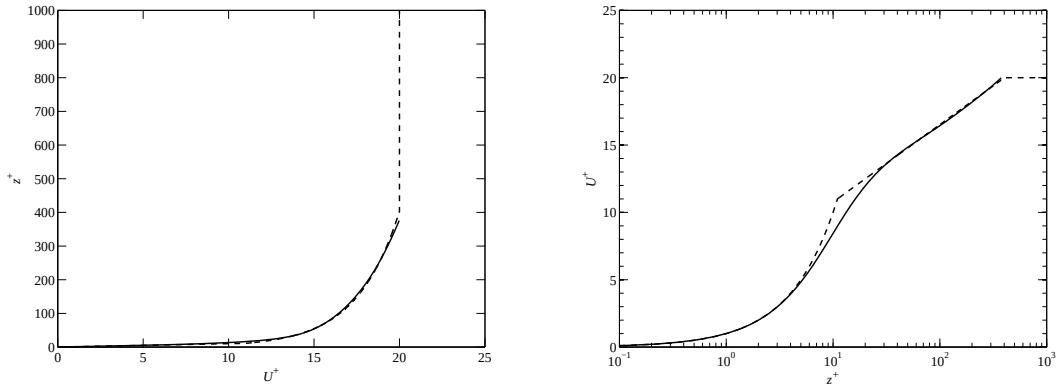

Figure 2.7: Theoretical law of the wall (dashed line) compared to direct numerical simulations (continuous line) from the John Hopkins Turbulence Database (see footnote 3 on the previous page) in linear and semilogarithmic coordinates. Note that the axes are inverted between the two plots. The simulated profile is truncated when U^+ reaches 20.

b) Hot-wire measurements

Equipment

All the equipment used for the hot-wire measurements is of brand Dantec Dynamics. The probe is a 55P01 hot-wire used with a 55H21 support and a 4-meter-long A1863 cable. The hot-wire is of 5 μm in diameter with an active length of 1.25 mm (for a total length of 3 mm). The probe is mounted on a sliding arm allowing vertical displacement with a 0.1 mm accuracy. Because of the surface deformation with the wind action, the hot-wire probe was not positioned closer to the interface than 0.5 mm. The part of the support introduced into the channel is of 4 mm in diameter. The hot-wire probe is inserted in the set-up by a set of holes of 7 mm of radius drilled into a Plexiglas plate closing the top part of the channel. In order to minimize leakage, a rubber cover closes the interstice around the probe and the openings that are not being used are taped shut.

The hot-wire probe is connected to a MiniCTA 54T30 (4-20 Ω) box, itself connected to a NI PCI-6023E acquisition board. The signal is acquired through the MiniCTA software. Before acquisition, the probe is calibrated using this software in order to convert the measured voltage into the velocity of the airflow. Once the acquisition and conversion are completed, the signal is transferred to Matlab for the analysis.

Acquisitions

The airflow reaches its stationary mean velocity profile in less than three seconds after the wind blower is turned on, and comes back down to zero in about ten seconds after stopping the wind blower. Therefore, the set-up is not adapted to the study of the transitory states of the wind action and is only used once the stationary state is reached. The characteristic viscous time of installation is of order $h^2/\nu \simeq 40$ s (for $\nu = 30 \times 10^{-6}$ m^2.s^{-1}). The flow is considered stationary if the wind has been blowing for longer than this characteristic time. All acquisitions (by hot-wire anemometry, PIV or FS-SS) are performed once this stationary state is reached, after a safety margin of two

to three minutes after the wind blower has been switched on.

Each data point by hot-wire anemometry corresponds to an acquisition of 20000 points at the acquisition frequency of 1 kHz, hence a total time of acquisition of 20 seconds. In order to study the evolution of the wind profile with wind speed and fetch, two series of acquisitions are performed at different wind speeds and fetches. In the first series, the probe is positioned at the center of the wind channel at fetch $x = 500$ mm and the mean wind velocity at the center of the channel is set in turns at 1.0, 1.9, 3.9, 5.8 and 6.6 m.s^{-1}. The velocity is acquired at different altitudes above the interface. A second series of acquisitions is realized at a fixed wind speed and the velocity profiles are recorded at different fetches. The wind velocity is chosen below the threshold of wave generation at $U_a = 3.9$ m.s^{-1} and the measurements are taken at fetch -100, 20, 500 and 1000 mm (a negative fetch stands for a location upstream of the liquid, above the flat Plexiglas floor).

Post-processing

Due to the small amplitude of the signal, sources of electromagnetic perturbations can interfere with the acquisition. In particular, the motor of the wind blower is a source of noise that can not be avoided without stopping the airflow. Despite the installation of aluminum foils around the acquisition equipment to decrease the reception of this electromagnetic noise, the level of remaining noise made it necessary to process the signals. The data points that are affected by the noise are rejected using the Matlab function *smooth* with the option 'rlowess' applied with its default parameters [4]. This processing does not affect the value of the mean velocity U.

c) Results and interpretations

Vertical profiles of mean velocity

The mean wind velocity profiles at the center of the channel are presented in figures 2.8 and 2.9. Figure 2.8 shows the profiles at fetch $x = 500$ mm for different wind velocities while figure 2.9 displays the profiles taken at $U_a = 3.9$ m.s^{-1} at different fetches along the tank. The mean velocity profiles are compatible with a logarithmic region and they keep appreciably similar shapes at the different fetches and wind speeds, remaining close to the theoretical profiles presented in part 2.2.a.

Using equation (2.2.5), logarithmic fits can be used to obtain the experimental friction velocities. We find u^* to slightly decrease with fetch: for $U_a = 3.9$ m.s^{-1}, u^* decreases from 0.22 m.s^{-1} at $x \simeq 0$ down to 0.17 m.s^{-1} at $x = 1$ m. Accordingly, $\delta_\nu(x)$ slightly increases with fetch, from 0.07 to 0.09 mm. The procedure is repeated for different wind velocities at a fixed fetch, $x_0 = 500$ mm. Measurements are restricted to $U_a < 6.6$ m.s^{-1}, when the surface deformations remain weak (less than 10 μm, see chapter 3), because the hot-wire could not be positioned too close to the liquid. We find that in this range u^* is almost proportional to U_a, $u^*(x_0) \simeq 0.05 U_a$ (see figure 2.23 on page 54). The corresponding half-height channel Reynolds number at this fetch, $Re_\tau = Hu^*/2\nu_a$, varies in the range $200 - 1200$, and the thickness of the viscous sublayer δ_ν decreases from 0.3 to 0.05 mm when U_a increases from 1 to 6.6 m.s^{-1}.

4. The option 'rlowess' corresponds to a robust local regression using weighted linear least squares and a first degree polynomial model. For more information on the function *smooth* and its different options, see `http://fr.mathworks.com/help/curvefit/smooth.html` and `http://fr.mathworks.com/help/curvefit/smoothing-data.html`.

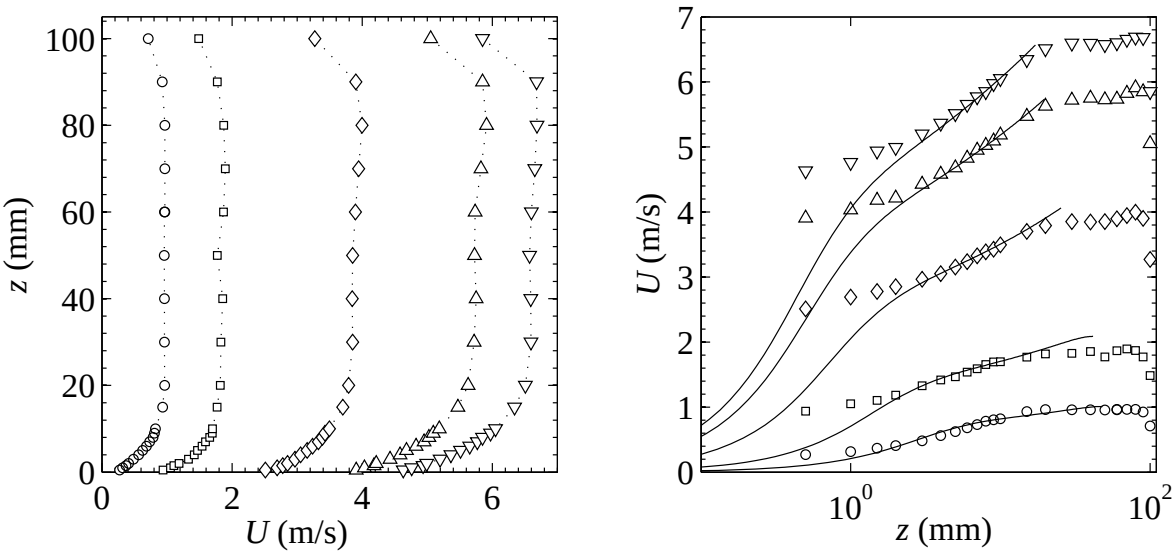

Figure 2.8: Mean wind velocity profiles at $x = 500$ mm at the center of the wind channel at wind speeds 1.0 m.s^{-1}(○), 1.9 m.s^{-1}(□), 3.9 m.s^{-1}(◊), 5.8 m.s^{-1}(△) and 6.6 m.s^{-1}(▽). (Left) In linear coordinates. (Right) Compared in semilogarithmic coordinates with direct numerical simulations (continuous lines). Note that the axes are inverted between the two plots. The simulated profiles correspond from bottom to top to the increasing Re_{sim} in table 2.1.

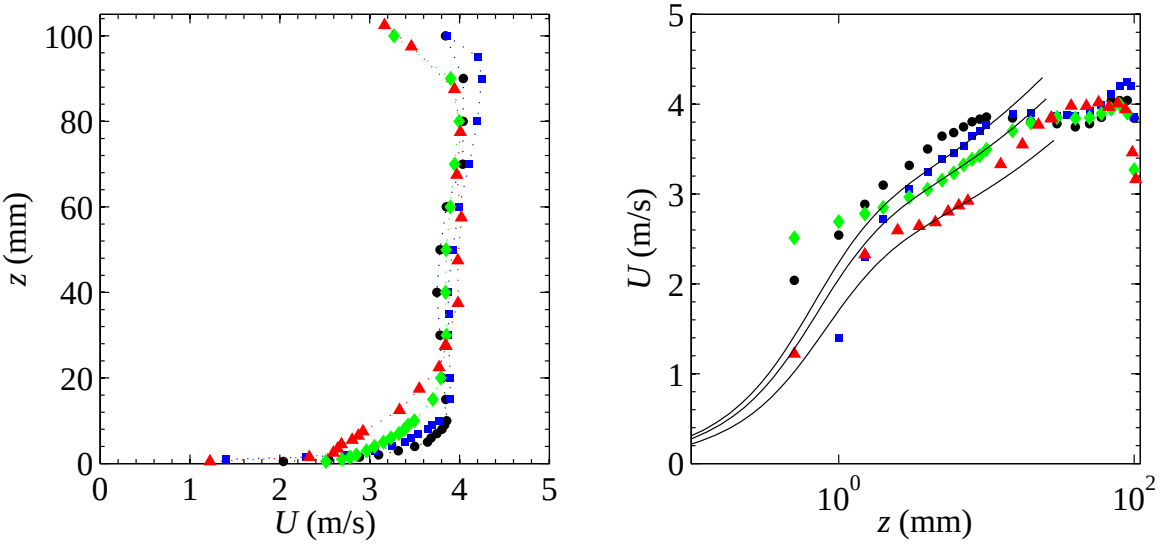

Figure 2.9: Mean wind velocity profiles at $U_a = 3.9$ m.s^{-1}at the center of the wind channel at fetch -100 mm (●), 20 mm (■), 500 mm (♦) and 1000 mm (▲). (Left) In linear coordinates. (Right) Compared in semilogarithmic coordinates with direct numerical simulations (continuous lines). Note that the axes are inverted between the two plots. The simulated profiles correspond from top to bottom to the increasing fetch x in table 2.2.

U_a (m.s^{-1})	u^*_{exp} (m.s^{-1})	$\delta_\nu = \nu_a/u^*_{\text{exp}}$ ($\pm$0.005 mm)	$Re = \frac{U_a H}{2\nu_a}$	$Re_\tau = \frac{u^*_{\text{exp}} H}{2\nu_a}$	Re_{sim}
1.0	0.06	0.268	3.4×10^3	200	180
1.9	0.11	0.140	6.5×10^3	380	300
3.9	0.20	0.074	1.4×10^4	710	650
5.8	0.29	0.052	2.0×10^4	1000	1000
6.6	0.33	0.046	2.3×10^4	1200	1000

Table 2.1: Parameters used for the comparison between numerical simulation and experimental data at $x = 500$ mm.

x (mm)	u^*_{exp} (m.s^{-1})	$\delta_\nu = \nu_a/u^*_{\text{exp}}$ ($\pm$0.005 mm)	$Re = \frac{U_a H}{2\nu_a}$	$Re_\tau = \frac{u^*_{\text{exp}} H}{2\nu_a}$	Re_{sim}
20	0.22	0.068	1.4×10^3	710	650
500	0.20	0.074	1.4×10^3	710	650
1000	0.17	0.088	1.4×10^3	710	650

Table 2.2: Parameters used for the comparison between numerical simulation and experimental data for $U_a = 3.9$ m.s^{-1}.

The mean velocity profiles are compared to numerical simulation data obtained at the University of Tokyo ([Iwamoto, 2002], [Iwamoto et al., 2002]) [5] and Johns Hopkins University ([Li et al., 2008], [Perlman et al., 2007], [Graham et al., 2013]) [6]. These openly accessible datasets provide data from direct numerical simulations of 3D turbulent channel flow developed over smooth fixed walls for different Reynolds numbers. Among this data, we choose those whose Reynolds numbers Re_τ are closest of the experimental Re_τ. To compare the simulated velocity profiles to the experimental profiles, we modify the dimensionless profiles $U^+_{\text{sim}} = f(z^+_{\text{sim}})$ using the results of the local logarithmic fit, the experimental friction velocities u^*_{exp}, into $U_{\text{sim}}(z_{\text{sim}}) = U^+_{\text{sim}} u^*_{exp}$ with $z_{\text{sim}} = z^+_{\text{sim}} \nu_a / u^*_{exp}$. Dimensional fluctuations profiles are obtained by a similar transformation (see figures 2.11 and 2.12).

There are obvious differences between simulations and experimental results close to the interface. Two phenomena can explain this divergence. First, while the probe can be moved vertically with a 0.1 mm accuracy, the distance from the probe to the interface can only be known with a 0.5 mm precision. While this does not visibly affect the profiles in the logarithmic region, the possible differences are very visible in logarithmic coordinates at small z. Secondly, when the hot-wire probe is that close to the interface, its mere presence may be enough to modify the airflow.

Nevertheless, the experimental data and the data obtained by DNS are in agreement in the logarithmic region. Therefore, we can consider that the classical description of the turbulent boundary layer theory applies to the present flow in our system despite the obvious differences in its underlying hypotheses. Hence, while the liquid-air interface in our set-up differs through many aspects from a stationary solid boundary, as long as the surface deformation remains small, the airflow over it is essentially the same as it

5. See the DNS Database of Turbulence and Heat Transfer of the University of Tokyo, available at `http://www.thtlab.jp/DNS/dns_database.html`.

6. See the John Hopkins Turbulence database, available at `http://turbulence.pha.jhu.edu`.

would be above a smooth fixed wall (this was previously noticed by [Plate et al., 1969]). This is further confirmed by the smallness of the interface roughness. Indeed, if the behaviour of the boundary itself changes (from a solid smooth wall to a deformable liquid-air interface), the roughness does not change much along the tank. The amplitude of the surface perturbations remains small and does not increase the roughness much until the wind velocity is large enough to create transversal waves. It will later be shown that below the wave generation threshold, the surface deformation does not exceed a dozen microns (see chapter 3). Using the values of δ_ν obtained by hot-wire measurement and the root mean square of the amplitude of the surface deformation (see Fig. 3.2 on page 61) as the size of the roughness ϵ, the non dimensional roughness $\epsilon^* = \epsilon/\delta_\nu$ only reaches 0.2 under the wave threshold. A boundary with a roughness this small can easily be considered as smooth [Van Driest, 1956] (see figure 1.4 on page 7). Therefore, we can consider the airflow to be close to a canonical turbulent flow over a no-slip flat wall, at least for a wind velocity up to 6 m.s^{-1}. This does not hold for larger wind velocity, for which the roughness induced by the waves decreases the value of C^+ in equation (2.2.5), affecting the mean velocity profile [Longo, 2012] [Zavadsky and Shemer, 2012].

Development of the boundary layer with fetch

If the experimental mean velocity profiles present the correct shape, it is however clear that these profiles evolve with fetch (see Fig. 2.9). This evolution with fetch can be attributed to the fact that the flow is not fully developed yet. While an estimate of the extent of the turbulence would be provided by the fit of *both* the friction velocity u^* and the coefficient C^+, the lack of data points close enough to the interface to be in the viscous boundary layer makes this kind of fit impossible.

A better way to estimate the extent of the turbulence in the airflow is through the thickness of the boundary layer. The turbulence in our wind channel being not fully developed, the boundary layer, the layer from the interface to the central constant portion of the airflow, must grow along the tank. The boundary layer thickness $\delta_{0.99}$ is defined as the distance from the surface at which the mean velocity is $0.99U_a$. It is deduced from the velocity profiles $U(z)$ in the air measured using hot-wire anemometry at different fetches along the liquid-air interface. These profiles are shown in figure 2.10 for a wind velocity $U_a = 3.9$ m.s^{-1} at fetch $x = 20$, 500 and 1000 mm. They show the development of the boundary layer along the channel: the boundary layer thickness $\delta_{0.99}$ increases nearly linearly, from 13 mm at $x = 2$ cm to 32 mm at $x = 1.0$ m (slope of order of 2%). The fact that $\delta_{0.99}(x)$ approaches the channel half-height $H/2 \simeq 52$ mm at the end of the channel indicates that the flow becomes fully developed there.

In order to accelerate the transition to a fully turbulent airflow in our wind tunnel, the flexible coupling between the wind blower and the wind channel was slightly modified. This coupling was previously made from thin flexible plastic covering the gap between the blower and the rest of the set-up, fixed inside the wind blower but free to move at the entrance of the wind tunnel. It was replaced with strips of coarse sandpaper of the same dimensions and positioned in the same way. The idea was to locally increase the roughness of the wall to start up the growth of the boundary layer sooner. However, this attempt was not successful and no significant change was observed.

Velocity fluctuations and turbulence rate

The root mean square u' of the wind velocity fluctuations is computed at the same

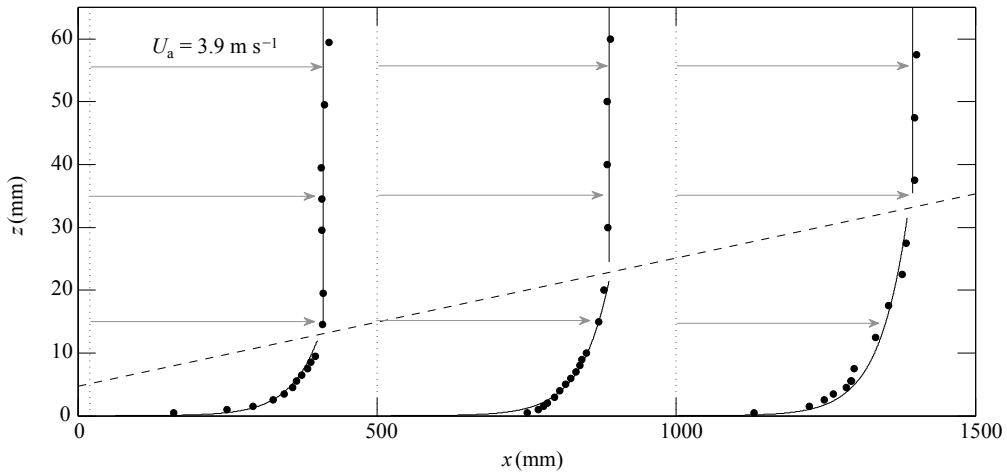

Figure 2.10: Mean velocity profiles $U(z)$ in the air for $U_a = 3.9$ m.s^{-1} at the centerline $y = 0$ and at fetch $x = 20$, 500 and 1000 mm. The dotted line shows the streamwise development of the 99% boundary-layer thickness, $\delta_{0.99}(x) \simeq 12.6$ mm + $0.02x$. The curves for $z < \delta_{0.99}(x)$ show the fit with the logarithmic law (Eq. (2.2.5)).

location and wind speeds as the mean velocities: at the center of the channel at $x = 500$ mm for different wind velocities (Fig. 2.11) and at the center of the channel for a fixed wind speed $U_a = 3.9$ m.s^{-1} at different fetches (Fig. 2.12).

Similarly to the fluctuations profiles derived from DNS, the fluctuations are minimal and constant at the center of the channel and maximal close to the walls. The turbulence rate of the wind blower, the ratio of the turbulent fluctuations over the mean value of the wind velocity outside the upper and lower boundary layers, is calculated to determine the "cleanliness" of the wind blower. Experimentally, the turbulence rate is computed as the ratio of the fluctuation level in the central 4 cm of the airflow over the wind velocity averaged over the same part of the flow. Measurements show that the turbulence rate is between 1.5% and 2.5% with a mean value of 2.1%, which is consistent with the turbulence rate of a few percents generally found in wind tunnels.

Contrary to the mean velocity profiles, the fluctuation profiles are relatively far from the results obtained by numerical simulations. In particular, the experimental results are always smaller than the simulations. This may mainly come from the fact that the flow is not fully developed, but note that the post-processing may also contribute to slightly weaken the root mean square of the velocity fluctuations.

Transverse profiles of mean velocity

Transverse profiles measured by a simpler commercial hot-wire anemometer (of brand Testo, model 425) are presented in figure 2.13. The velocity is averaged over 20 seconds of measurement acquired at 2 Hz. The anemometer calibration was verified beforehand using a professionally calibrated anemometer of the same brand and type. For small and high wind velocities alike, there is no major disparity of velocity between the left and right sides of the wind blower (see profiles for $U_a = 2.9$ m.s^{-1} and for $U_a = 10.0$ m.s^{-1} at $x = -10$ cm). The boundary layers over side walls evolve in the x direction (see profiles at $x = -10$ cm and $x = 175$ cm for $U_a = 2.9$ m.s^{-1}), a priori in a likewise manner that the

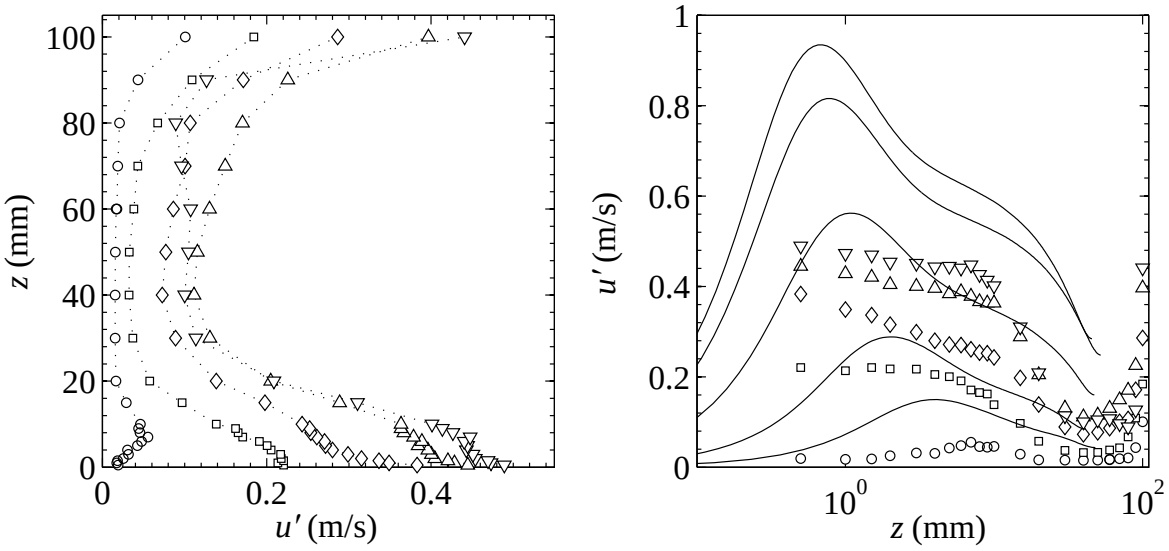

Figure 2.11: Root mean square of the velocity fluctuations at $x = 500$ mm at the center of the wind channel at wind speeds 1.0 m.s^{-1}(○), 1.9 m.s^{-1}(□), 3.9 m.s^{-1}(◇), 5.8 m.s^{-1}(△) and 6.6 m.s^{-1}(▽). (Left) In linear coordinates. (Right) Compared in semilogarithmic coordinates with numerical simulations (continuous lines). Note that the axes are inverted between the two plots. The simulated profiles correspond from bottom to top to the increasing Re_{sim} in table 2.1 on page 40.

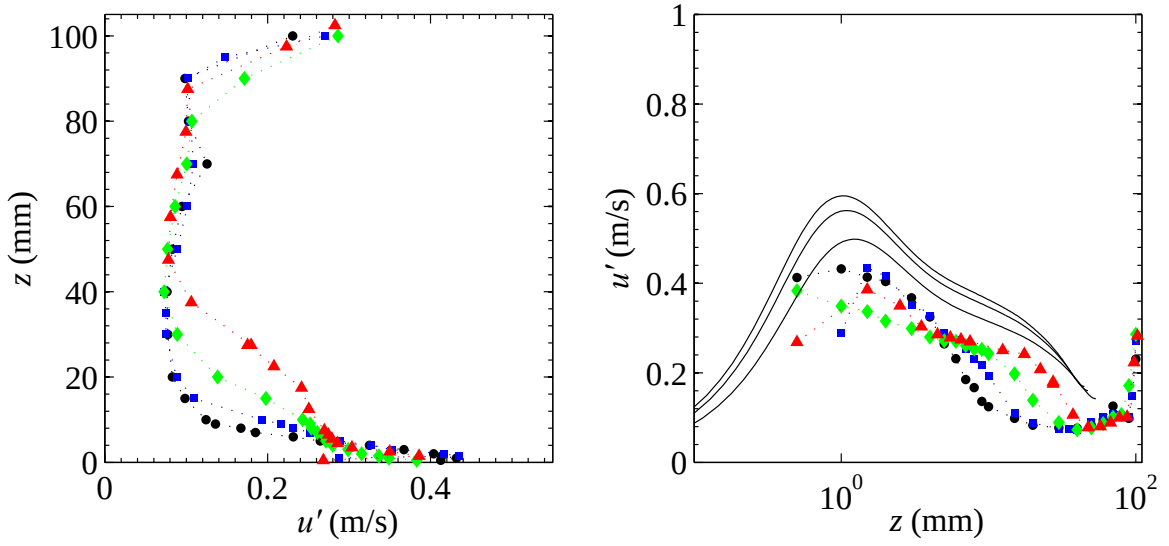

Figure 2.12: Root mean square of the velocity fluctuations at $U_a = 3.9$ m.s^{-1}at the center of the wind channel at fetch -100 mm (●), 20 mm (■), 500 mm (◆) and 1000 mm (▲). (Left) In linear coordinates. (Right) Compared in semilogarithmic coordinates with numerical simulations (continuous lines). Note that the axes are inverted between the two plots. The simulated profiles correspond from bottom to top to the increasing fetch x in table 2.2 on page 40.

boundary layer above the interface, but their development is expected not to be crucial to the system response. Moreover, a slight convergence of the turbulent airflow is expected to occur close to the free surface from the walls towards the corners (secondary flow of Prandtl's second kind [Schlichting, 2000], see Fig. 2.14). This is unavoidable for a turbulent channel flow in a rectangular geometry. The secondary velocities usually correspond to a few percents of the bulk velocity. This secondary flow may be the origin of the central dislocation observed in presence of transverse waves (see chapter 3, in particular figure 3.1 on page 60).

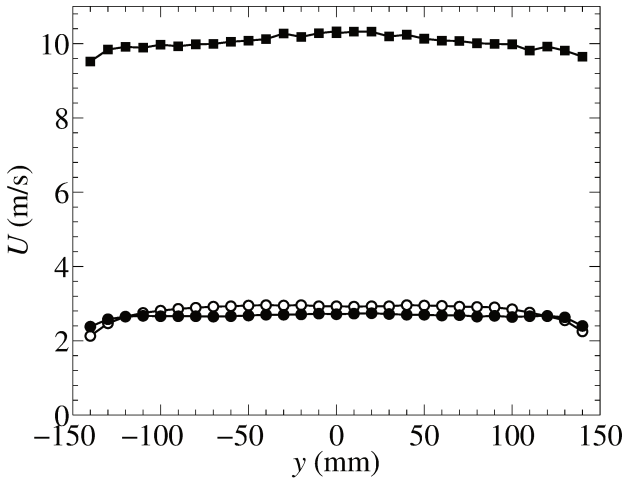

Figure 2.13: Transverse profiles of the mean velocity measured over the flat floor at $x = -10$ cm at half the total height of the channel for $U_a = 2.9$ m.s^{-1}(•) and $U_a = 10.0$ m.s^{-1}(■), and at the exit of the set-up at $x = 175$ cm for $U_a = 2.9$ m.s^{-1}(○).

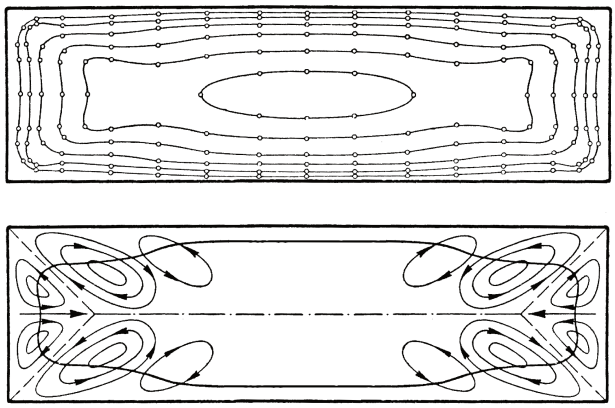

Figure 2.14: (Top) Curves of constant velocity in a rectangular duct. (Bottom) Sketch of the secondary flow of Prandtl's second kind expected in a rectangular duct. Figures adapted from [Schlichting, 2000].

Temporal analysis

In order to check that no frequency is predominantly present in the airflow, a temporal spectral analysis is performed on the signal acquired by the hot-wire probe. Figure 2.15 displays the power spectrum of the hot-wire signal recorded at $x = 500$ mm at the center of the channel for the wind speed $U_a = 3.9$ m.s^{-1} (spectra have similar shapes independently of the wind speed and location of the probe). No peak is observed at low frequency (up to 20 Hz). This suggests that the wind blower vibrations are not transmitted to the tank and that the liquid will "naturally" choose the waves' frequency. Thus, the low frequency peaks detected in the later chapters during spatio-temporal analyses of the surface height correspond to the natural response of the interface to the turbulent airflow, and not to a forcing at a particular frequency originating from the wind blower.

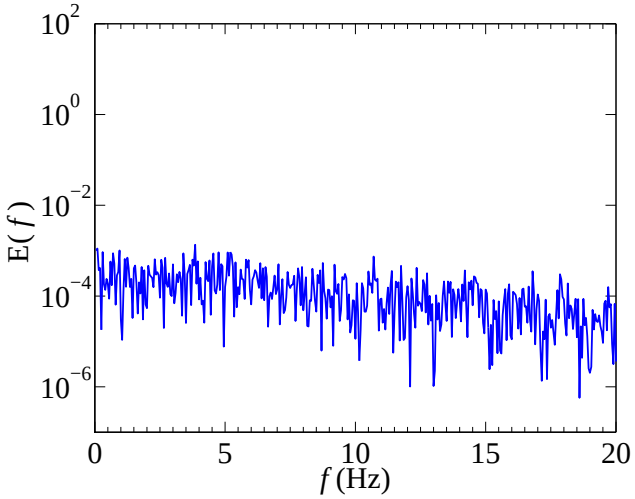

Figure 2.15: Power spectrum of the velocity signal at the center of the channel at $x = 500$ mm and for a wind velocity of $U_a = 3.9$ m.s^{-1}.

2.2.2 Flow in the liquid

It is visually obvious that a drift current appears at the surface under the wind action, which implies that the liquid cannot be considered at rest anymore. Since this flow can possibly have an influence on the surface waves, it is important to have an accurate knowledge of the motion of the liquid in the tank. To do so, Particle Image Velocimetry (PIV) measurements are performed in various conditions and results are compared to the laminar theory.

This section focuses on the characterization by PIV of the flow in the lower part of the set-up, below the interface ($-h < z < 0$, see Fig. 2.16). The characterization of the flow in the tank is performed in the same fluid as for the hot-wire measurements.

a) Laminar theoretical profile

The viscous fluid is considered incompressible of density ρ. For the performed experiments, the Reynolds number in the liquid $Re = U_s h/\nu$ remains under the relatively small value of 80. Therefore, we can consider that the flow in the liquid stays laminar. The flow is supposed stationary, unidirectional in the x direction and invariant by translation

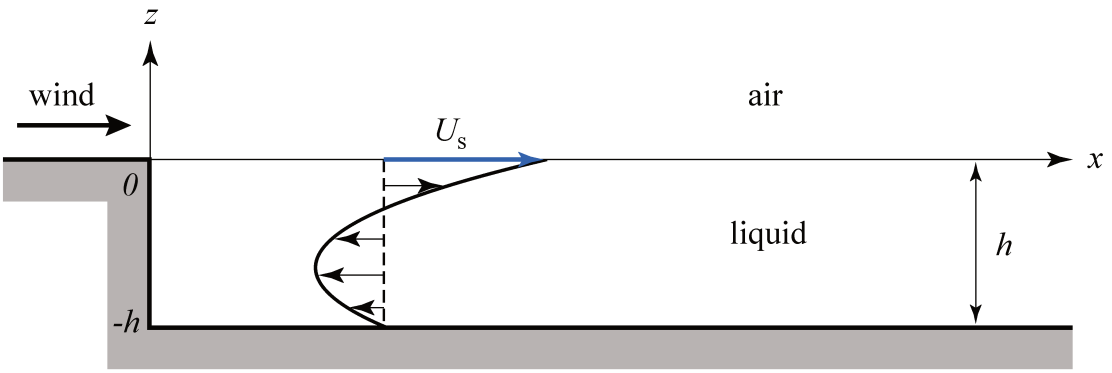

Figure 2.16: Sketch of the flow in the tank.

in x and y. The pressure p counteracts the hydrodynamic effects in the z direction: the pressure variation is supposed linear in the x direction. These hypotheses lead to the simplification of the Stokes equation projected in the x direction into $\frac{d^2u}{dz^2} = \text{constant}$.

Combined with the boundary conditions that the velocity is zero at the bottom of the tank and equal to the surface drift at the interface and that the flow rate through a vertical cut is zero (since the tank is closed), we obtain the following parabolic law, unique solution of the stationary Stokes problem:

$$u(x,z) = U_s(x)\left(1+\frac{z}{h}\right)\left(1+3\frac{z}{h}\right), \tag{2.2.7}$$

for $-h \leq z \leq 0$, where $U_s(x) = u(x, z=0)$ is the surface velocity. This profile is sketched in figure 2.16: the shear stress induced by the wind at the interface drives a drift flow in the liquid, compensated by a backflow at the bottom of the tank. Note the zero velocity at $z = -h/3$.

b) Direct observations and surface contaminants

The water-glycerol mixture is extremely sensitive to surface contamination, which may induce strong surface tension gradients and alter both the mean flow in the liquid and the generation of waves [Keulegan, 1951] [Gottifredi and Jameson, 1970] [Kahma and Donelan, 1988] [Tang and Wu, 1992]. Indeed, independently of the initial cleanness of the liquid mixture, contaminants settle at the liquid-air interface in only a few minutes. Direct observations of the displacement of particles at the liquid surface are enough to see that there exists two distinct flow zones in the tank depending on the surface contamination. When the wind starts to blow, the film of pollutants is entrained downstream and a clear line of separation can be observed. The stronger the wind, the further away the contaminants are blown downstream, until they are blocked at the end of the tank. Upwards the contaminated region, in the upstream part of the tank, a first zone of quasi uniform streamwise flow can be observed. There, the liquid is brought about at the surface under the action of the wind with a counterflow at the bottom of the tank. In the polluted part, the flow is more complex and shows longitudinal recirculation cells organized in the wind direction.

This issue of surface contaminant is recurrent in experimental works focusing on wind waves [Wilson et al., 1973] [Larson and Wright, 1975] [Kawai, 1979] [Kahma and Donelan, 1988] [Liberzon and Shemer, 2011] and it might even explain some discrepancies in the

values of wind speed threshold obtained by different authors [Kahma and Donelan, 1988]. To overcome this problem, we let the wind blow for a few minutes, and we remove the contaminated part of the surface liquid by collecting it at the end of the tank. The procedure is repeated frequently, and in normal operating conditions less than 30 cm of polluted surface remain at the end of the tank. The rest of the liquid bath acts as a self-cleaning interface where the first three quarters of the tank are kept clean by the supply of fresh clean fluid from the counterflow in the bulk. The polluted section of the tank is excluded from all PIV, hot-wire anemometry and FS-SS acquisitions.

c) PIV measurements

The PIV measurements are done in the vertical plane at the center of the tank using a pulsed laser of brand Continuum Minilite PIV. A cylindrical lens at the exit of the laser allows to spread the beam into a laser sheet. The acquisition is performed using a LaVision Image Pro X camera operated by the software Davis (version 7.2). The laser pulses and the camera frames are synchronized at an acquisition frequency of 10 Hz over a total time of recording of 2 seconds. The PIV field of visualization covers the entire depth of the liquid and spreads over 10 cm in the streamwise direction. The PIV computation is performed by the software Davis. The velocity profiles thus obtained are averaged temporally over all the measurements taken and spatially in the x direction. The measurements are done at fetch $x = 200$, 415, 720 and 870 mm.

d) Results and interpretations

Base flow profiles

The mean velocity profiles measured at the centerline of the tank using PIV in vertical planes (x, z) are presented in figures 2.17 and 2.18 (mean velocity profiles outside the centerline will be presented and discussed later in this section, see figure 2.22 on page 53). As expected from direct observation, except at small fetch (on a distance of the order of the liquid height) and over the last 30 cm of the tank (where surface contamination cannot be avoided), the velocity profiles are found nearly homogeneous in x. However, slight differences can be observed depending on the wind velocity.

For wind speeds under 7 m.s^{-1}, the flow is laminar, parabolic and bidimensional. The velocity profiles are well described by the parabolic law, solution of the stationary Stokes problem (Eq. (2.2.7)). The flow is stationary and uniform: the instantaneous and temporally averaged velocity fields are almost equivalent. Alike the parabolic law, the velocity is zero at the bottom of the tank and at $z \simeq -h/3$.

Disturbances start to arise for higher wind velocities. While waves appear for U_a greater than $U_c = 6.3$ m.s^{-1}, the flow is not significantly affected by the waves until the wind velocity exceeds 7 m.s^{-1}. Small streamwise fluctuations of mean velocity occur in the lower two thirds of the tank. Close to the interface, circular orbits superimpose on the base flow (see Fig. 2.19). The averaging being done only over 2 seconds, we cannot consider that enough waves went through the PIV field of view to guarantee a proper time average close to the interface. Therefore, the mean velocity profiles displayed in the region $-h/3 \leq z \leq 0$ in figure 2.18 are not correctly averaged and no conclusion can be inferred from them. In particular, the possible change of flow rate in presence and absence of waves cannot be assessed based on these PIV data.

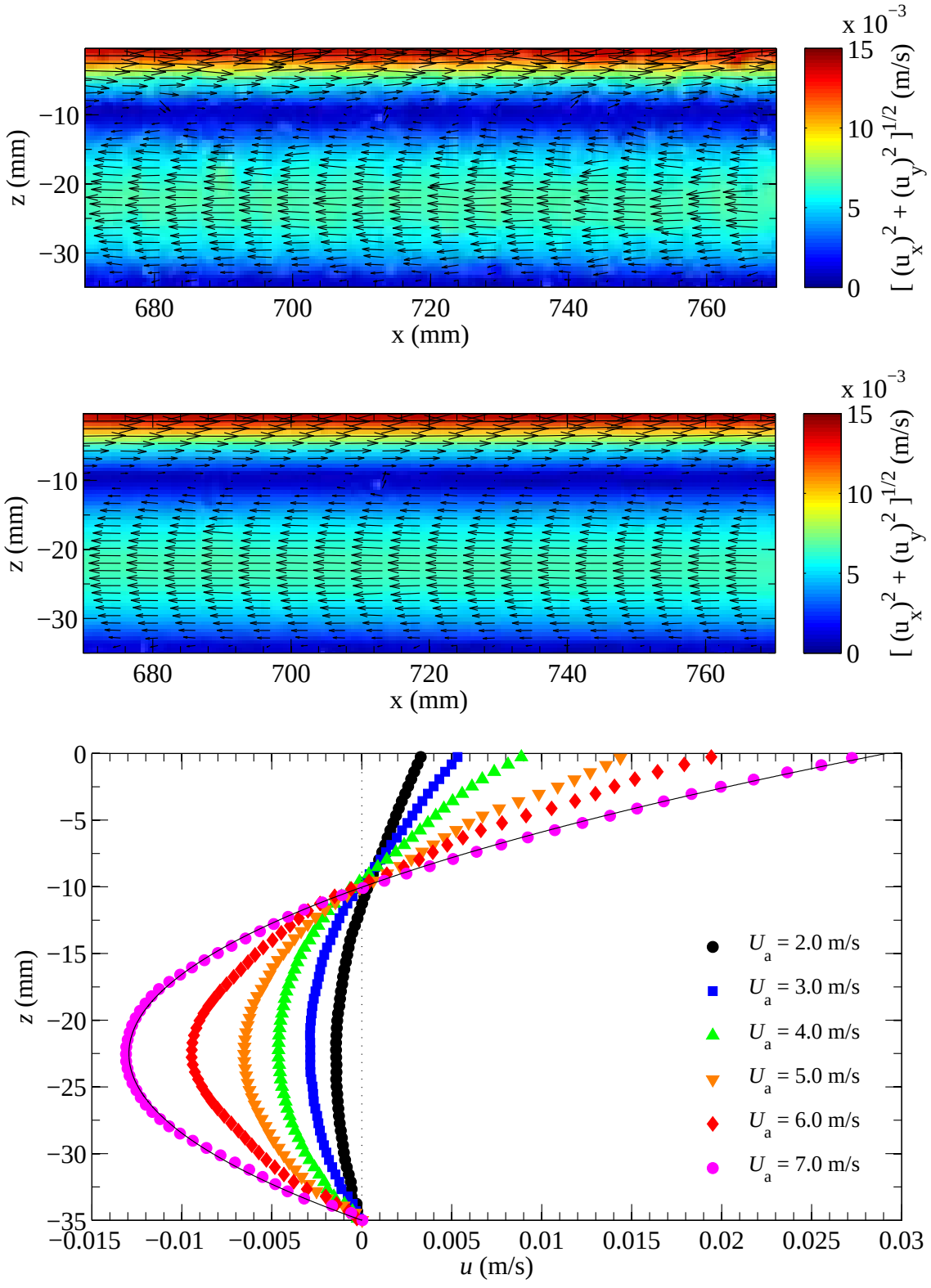

Figure 2.17: PIV measurements in the liquid at fetch $x = 72$ cm at the center of the tank. The wind is blowing left to right. (a) Instantaneous velocity field at $U_a = 5.0$ m.s^{-1}. (b) Temporally averaged velocity field at $U_a = 5.0$ m.s^{-1}. (c) Mean velocity profiles for various wind velocities U_a under 7 m.s^{-1}. The profiles are averaged in time and in the streamwise direction over $\Delta x = 100$ mm. The continuous line shows the quadratic profile (2.2.7) for $U_a = 7.0$ m.s^{-1}, with U_s fitted at 0.029 m.s^{-1}.

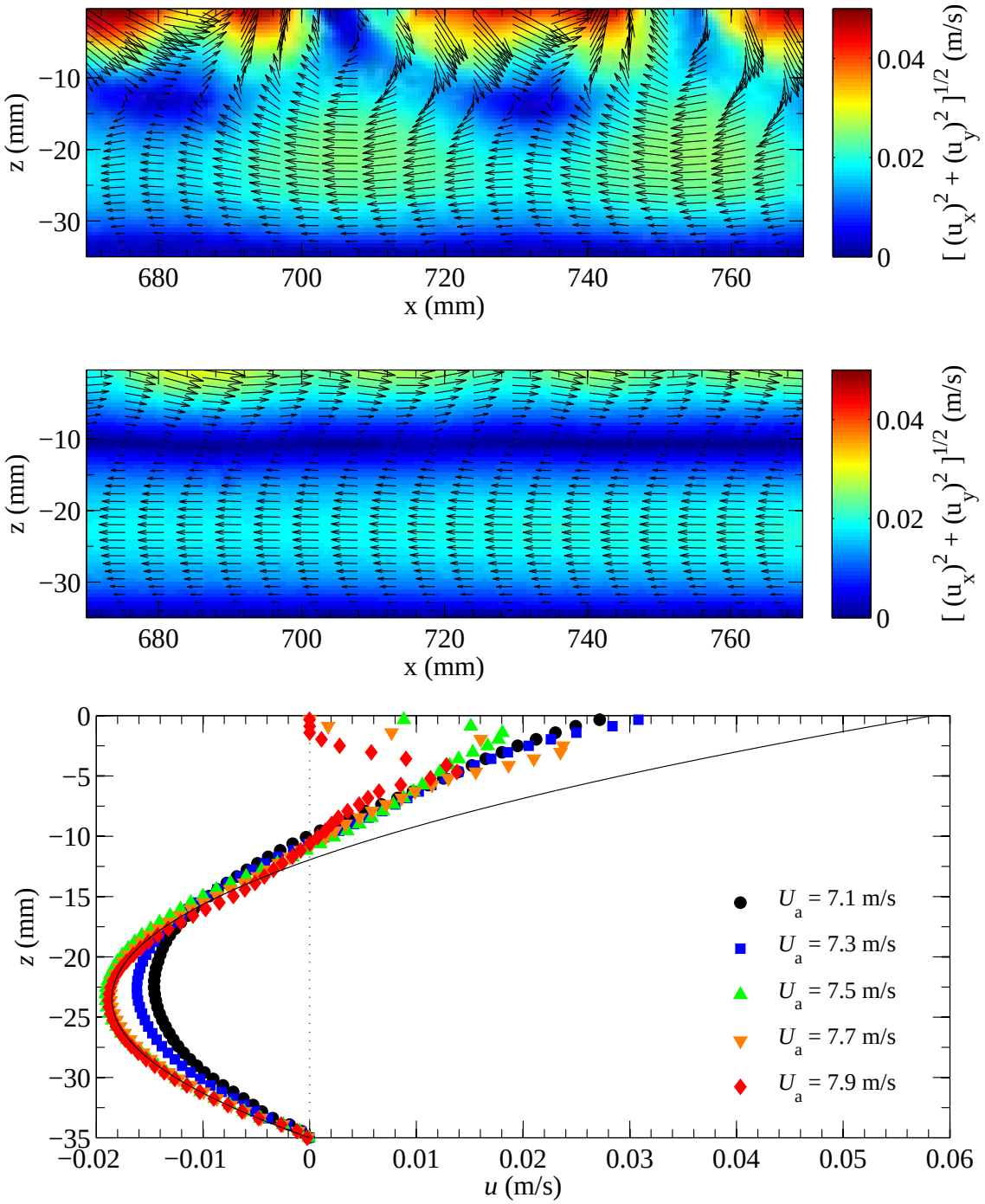

Figure 2.18: PIV measurements in the liquid at fetch $x = 72$ cm at the center of the tank. The wind is blowing left to right. (a) Instantaneous velocity field at $U_a = 7.5$ m.s^{-1}. (b) Temporally averaged velocity field at $U_a = 7.5$ m.s^{-1}. (c) Mean velocity profiles for various wind velocities U_a over 7 m.s^{-1}. The profiles are averaged in time and in the streamwise direction over $\Delta x = 100$ mm. The continuous line shows the quadratic profile (2.2.7) fitted on the lower two third of the profile for $U_a = 7.9$ m.s^{-1}.

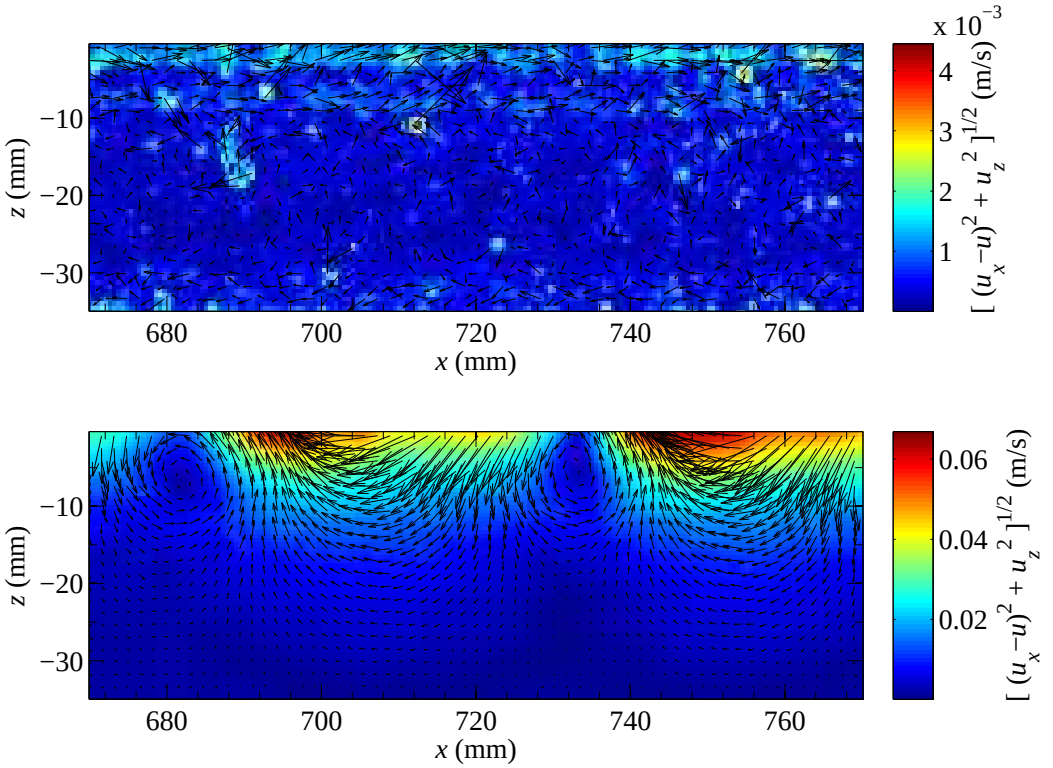

Figure 2.19: Velocity fields after subtraction of the base flow from the instantaneous velocity fields in figures 2.17(a) and 2.18(a) obtained by PIV in the liquid at fetch $x = 72$ cm at the center of the tank at $U_a = 5.0$ m.s^{-1} (top) and $U_a = 7.5$ m.s^{-1} (bottom).

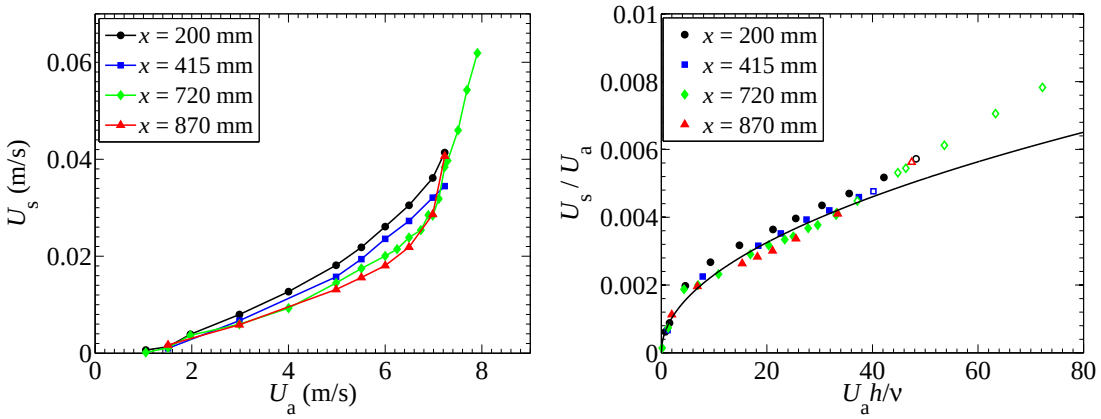

Figure 2.20: At fetches $x = 200$, 415, 720, 870 mm. (Left) Evolution of the surface drift U_s with the wind speed U_a. (Right) Growth of the ratio U_s/U_a with $Re = U_a h/\nu$. Open symbols correspond to wind velocities above 7 m.s^{-1}. The continuous line corresponds to Keulegan's law (Eq. (2.2.8)) with $K = 7.3 \times 10^{-4}$.

Surface velocity and evolution with fetch

The surface velocity $U_s(x)$ is computed from the parabolic fit of the mean velocity profile (Eq. (2.2.7)). In the case of wind speeds above 7 m.s^{-1}, the parabolas are fitted only in the lowest two thirds of the profile ($-h \leq z \leq -h/3$), this part being mostly unaffected by the waves. Note that in figure 2.18 on page 49, the parabolic fit is extended to the interface despite the obvious change in the velocity field close to the surface in presence of waves.

Unsurprisingly, the surface drift increases with wind speed (see Fig. 2.20 (left)) while remaining small relatively to the wind velocity. For $U_a = 4$ m.s^{-1} the surface velocity is of order of 1 cm.s^{-1}, which leads to a Reynolds number $Re = U_s h/\nu \simeq 10$. This drift velocity is in agreement with measurements at small Reynolds number [Keulegan, 1951], but is much smaller than the 2-3% of wind velocity typically found in classical air-water experiments [Plate et al., 1969] [Gottifredi and Jameson, 1970] [Veron and Melville, 2001] [Tsai et al., 2005b] [Caulliez et al., 2008] [Liberzon and Shemer, 2011] [Pomeau and Le Berre, 2011]. Even at the highest wind speeds and fetches, the drift velocities always remain small compared to the wind velocity; the surface drift never reaches 1% of the wind speed. This is consistent with the findings of [Keulegan, 1951] that if the Reynolds number in the liquid is smaller than about 100 (which is always the case in our system), the surface velocity is noticeably affected by the viscosity of the liquid. Based on a dimensional analysis, Keulegan proposes the experimental law

$$\frac{U_s}{U_a} = KRe^{1/2} = K\left(\frac{U_s h}{\nu}\right)^{1/2} \tag{2.2.8}$$

which leads to a quadratic evolution of the surface drift with wind speed:

$$U_s = K^2 \frac{h}{\nu} U_a^2. \tag{2.2.9}$$

Experimentally, we find K to be between 6.7×10^{-4} (at $x = 20$ cm) and 7.9×10^{-4} (at $x = 87$ cm), with a mean value of 7.3×10^{-4}. This is in good agreement with the value of about 7.6×10^{-4} found by Keulegan.

The surface velocity U_s decreases slightly along the tank for wind velocity under 7 m.s^{-1}(see Fig. 2.21). This is consistent with the development of the boundary layer and the resulting decreasing friction velocity (see § 2.2.3).

By blocking waves' formation with surfactants, Keulegan also find that there is no effect of the presence of wind on the surface drift. This is only partially consistent with our results, since the surface drift is in good agreement with Keulegan's law past the threshold $U_c = 6.3$ m.s^{-1}, but departs from it for $U_a > 7$ m.s^{-1} (open symbols in figure 2.20). More than by the presence of waves, the surface drift is affected by the amplitude of those waves. Indeed, bigger waves have a higher "windload" than the smaller waves and will be entrained by the wind, increasing the drift velocity.

In addition to the surface velocity coming from the shear stress effect on the interface, a small drift implied by wave propagation, the Stokes drift, may reinforce the current in the tank. The Stokes drift at the interface, where it is maximal, can be written for a potential flow as $U_{St} = 4\pi^2 a^2/\lambda T$, with a the wave amplitude, λ the wavelength and T the wave period [Longuet-Higgins, 1953]. The wave amplitude does increase with fetch above the wave threshold (see chapters 3 and 4), so the Stokes drift is expected to grow with fetch. However, even considering the extreme values of each of this parameters, the maximal Stokes drift is only of order 0.008 m.s^{-1} (with $a = 1$ mm, $\lambda =$35 mm and $T = 0.15$ s) and the Stokes drift is therefore negligible.

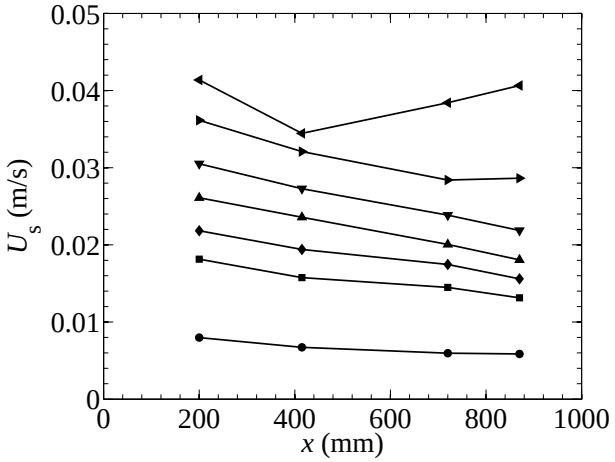

Figure 2.21: Evolution of surface drift U_s with fetch at various wind speeds: 3.0, 5.0, 5.5, 6.0, 6.5, 7.0 and 7.2 m.s^{-1} (from bottom to top plot).

The small surface velocity here is expected to have negligible effect on the dispersion relation of free waves (Eq. (1.1.1)): Lilly (see appendix of Hidy and Plate [Hidy and Plate, 1966]) shows that the correction to the phase velocity for this parabolic profile is $U_s(1 - 2/kh)$, which is 10% of the phase velocity for the most unstable wavelength ($\lambda \simeq 30 - 40$ mm). This will be explained in more details in chapter 4.

Transverse evolution of the base flow profile

The base flow profiles are measured at $x = 720$ mm for wind speeds $U_a = 3.0$, 5.0 and 7.0 m.s^{-1} at different y from the centerline. The results are presented in figure 2.22 on the next page. The mean profiles appear to be quite invariant in the transverse direction for the considered wind velocities. However, the slight difference in the profile at $y = -50$ mm for $U_a = 7.0$ m.s^{-1} tends to indicate that the profiles outside the centerline may be more affected by the waves' presence. Indeed, we will see in chapter 3 that the maximum amplitude of transverse waves is not located on the centerline $y = 0$.

2.2.3 Friction velocity and interfacial shear stress

Now that the mean velocities profiles have been measured on both sides on the interface, we will relate these results obtained in the liquid and in the air through the friction velocity. The profiles are related through the condition of no jump in shear stress at the liquid-air interface:

$$\tau_{\text{air}} = \tau_{\text{liq}} = \tau \qquad \text{with} \qquad \begin{cases} \tau_{\text{air}} = \rho_a u^{*2} \\ \tau_{\text{liq}} = \eta \left(\dfrac{du}{dz} \right)_{z=0} \end{cases}$$

Using the parabolic law (2.2.7), interfacial shear stress from the liquid becomes $\tau_{\text{liq}} = 4\eta U_s/h$. Measuring U_s thus provides another way to determine u^*: using the continuity of the stress at the interface, one has $\tau = \rho_a u^{*2} = 4\eta U_s/h$, yielding:

$$u^* = \sqrt{\frac{4\eta U_s}{\rho_a h}}. \tag{2.2.10}$$

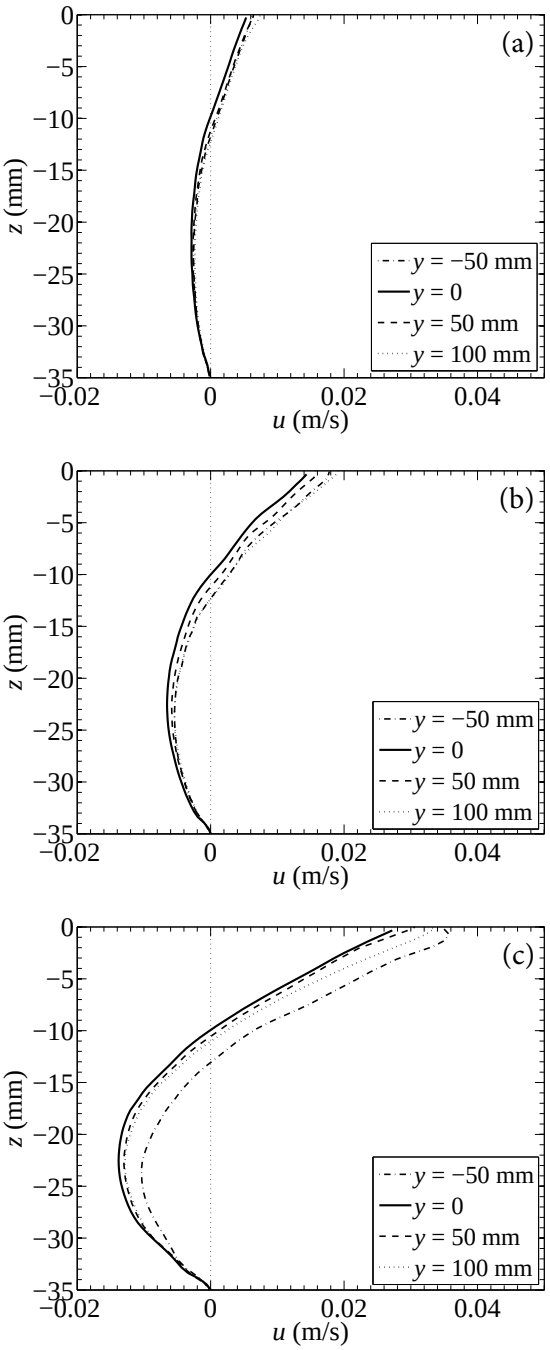

Figure 2.22: Mean velocity profiles obtained by PIV measurement in the liquid at fetch $x = 72$ cm at various y. The wind is blowing from left to right at wind velocity (a) $U_a = 3.0$ m.s^{-1}; (b) $U_a = 5.0$ m.s^{-1}; (c) $U_a = 7.0$ m.s^{-1}.

The friction velocity deduced from the PIV measurements is plotted in figure 2.23 and gives a linear growth of u^* with U_a: $u^* \simeq 0.05U_a$. This result is consistent with the quadratic evolution of the surface drift with U_a observed for wind velocities below 7 m.s^{-1} (see Fig. 2.20). Indeed, combining equations (2.2.9) and (2.2.10), we obtain:

$$K = \frac{1}{2}\left(\frac{u^*}{U_a}\right)\sqrt{\frac{\rho_a}{\rho_l}} \simeq 7.9 \times 10^{-4}$$

which is close to the average experimental coefficient $K = 7.3 \times 10^{-4}$ found in section 2.2.2.

Let us compare this friction velocity to the one that can be extracted from the mean velocity profile in the air. As mentioned before (see Eq. (2.2.5)), the evolution of the friction velocity $u^*(x)$ along the channel can be obtained by fitting the velocity profiles for $z < \delta_{0.99}(x)$ with the classical logarithmic law [Plate et al., 1969] [Schlichting, 2000] [Zavadsky and Shemer, 2012]. Measurements at fetch $x_0 = 500$ mm show u^* to be almost proportional to U_a, $u^*(x_0) \simeq 0.05U_a$ (see Fig. 2.23).

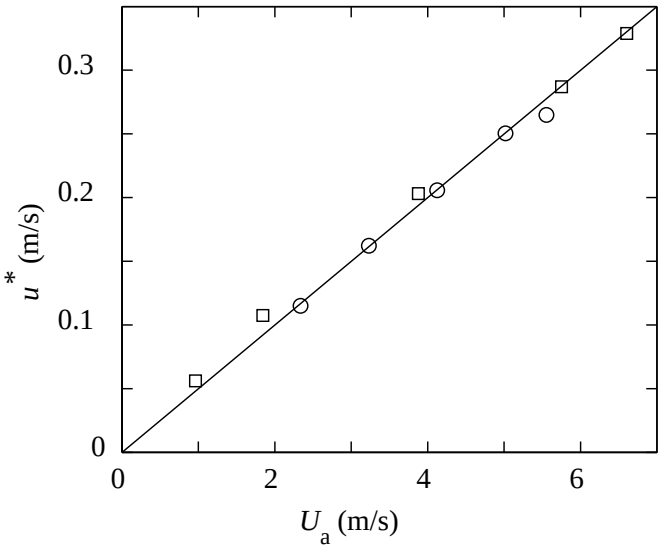

Figure 2.23: Friction velocity u^*, deduced from the mean profile in the airflow at $x_0 = 500$ mm (□) and deduced from the shear stress at the liquid surface (Eq. (2.2.10)) (○), as a function of the wind velocity U_a. The continuous line corresponds to $u^* = 0.05U_a$.

As a consequence, both the friction velocity u^* measured by PIV in the liquid and the one measured in air with the hot-wire at $x_0 = 500$ mm are in excellent agreement with the result that the friction velocity grows linearly with the wind velocity. Despite the slight evolution of the surface drift with fetch (and thus the slight evolution of the corresponding friction velocity u^*), for simplicity, the ratio of u^*/U_a is taken in chapters 3 and 5 as constant and equal to 0.05 for all fetches. By comparison, the ratio of u^*/U_a is generally found of the order of 3% in air-water experiments [Plate and Hidy, 1967] [Wu, 1975] [Mitsuyasu and Rikiishi, 1978] [Liberzon and Shemer, 2011] with weak dependence on the wind velocity [Mitsuyasu and Rikiishi, 1978].

Note that the continuity of the interfacial shear stress implies that we can consider that τ is imposed by the wind and thus is the same independently of the liquid. Similarly, given a fixed wind velocity, the friction velocity is supposed to be the same for the different liquid mixtures used (see chapters 3 and 5). The only limitation of this consideration would be if the drift velocity becomes large enough to have an influence back onto the airflow. The surface drift remaining smaller than 1% of the wind velocity, this effect is negligible and the hypothesis of the invariance of the friction velocity with the liquid is expected to hold for all mixtures (except in the case of water for which the flow may not longer be laminar and the drift may be greater).

2.3 Conclusion

In this chapter, we have presented the experimental set-up and the FS-SS method of visualization that I later used to study the generation and growth of wind waves. The FS-SS technique is particularly well adapted to study this problem since it is non intrusive, global and allows to measure the first surface deformation under the action of small wind speeds. The flows in the wind channel and in the tank have also been characterized, by hot-wire and PIV measurements, respectively. While flow characterization was performed for a liquid 30 times more viscous than water, the conclusions that are inferred can be extrapolated to the more viscous liquids used later.

The turbulent airflow, while not fully developed, was found to be similar to the turbulent airflow above a smooth fixed wall for wind velocity under the threshold of wave generation. In agreement with the literature, the mean air velocity profile presents a logarithmic region in the inertial sublayer and can be described by locally applying the turbulent boundary theory. The friction velocity can be evaluated by a fit in this logarithmic region. The ratio u^*/U_a is found to be 5%, above the 3% generally found in the literature in air-water experiments. As the airflow is not fully developed until the end of the channel, the boundary layer slowly grows linearly with fetch at a 2% rate. Boundary layers also develop in the vicinity of the side walls but the transverse mean velocity is observed to be constant and symmetrical outside these boundary layers. A temporal analysis confirmed that the wind waves' frequency is chosen freely, and not by a forcing from the wind blower.

The flow in the liquid can easily be affected by the presence of surface contaminants. A maximum of the pollutants are removed and no acquisition is performed in the last 30 cm of the tank where contamination cannot be avoided. All the results described and discussed in this manuscript concern the non contaminated rest of the tank (on the first meter). Thanks to the high viscosity of the liquid, the flow remains laminar for all wind speeds. Up to 7 $\mathrm{m.s^{-1}}$ of wind velocity, the flow in the liquid is almost uniform and bidimensional. The base flow is well described by the parabolic law solution of the stationary Stokes problem. The surface velocity can be obtained from this parabolic fit. For wind speeds above 7 $\mathrm{m.s^{-1}}$, the presence of waves starts to affect the base flow. This effect occurs mainly in the upper third of the liquid depth but the surface drift can still be evaluated by a parabolic fit on the other two thirds. While it increases with wind speed and decreases slightly with fetch, the surface velocity remains small compared to the wind velocity in all cases.

The friction velocities deduced from the profiles in the air and in the liquid were compared and shown to be compatible. The friction velocity decreases slightly with fetch, consistently with the decrease of drift velocity. This evolution is slow enough to consider that the friction velocity is uniform and simply evolves linearly with the wind speed

through the empirical law $u^* = 0.05U_a$, for wind velocity up to the wave threshold.

Note that the flow characterization shows that the conditions in which our experiments are carried out are quite different from those of natural wind waves. Indeed, atmospheric boundary layers are not bounded in the same way that laboratory channel boundary layers are. The flow in the liquid is also different. In water, it is generally turbulent with different type of currents under the surface and can also depend on the wind duration. All of this can affect the behavior of waves and results found in our set-up are not expected to be in good agreement with data gathered at sea or on lakes.

Summary:

- Wind waves initiation and growth are studied by using a global optical method of visualization of the deformation of the interface, with an excellent vertical resolution.
- The turbulent airflow can be described by applying locally the turbulent boundary layer theory. Under the wave threshold, the mean velocity profile can be considered the same as if the airflow was over a smooth fixed wall.
- Until the waves start to significantly affect the mean profiles at wind velocities higher than the wave threshold, the flow in the liquid is laminar, almost uniform and bidimensional, and follows the parabolic law solution of the stationary Stokes problem. In all situations, the surface velocity remains small.
- Measurements in the air and liquid are consistent with each other and under the wave threshold, they lead to a friction velocity linearly increasing with the wind velocity.
- Flow characterizations were performed by measurements in a liquid 30 times more viscous than water but the conclusions that are inferred can be extrapolated to the more viscous liquids used later.

Chapter 3

Wind waves initiation: two regimes of surface deformation

Using the set-up and visualization method detailed in the previous chapter, experiments are conducted so as to investigate the early stages of wave generation by a turbulent wind over a viscous liquid. Exploring the response of the surface to winds of different strengths, the spatio-temporal structure of the surface deformation is analyzed and two regimes of deformation of the liquid-air interface are identified. The experimental results presented in this chapter have been published in [Paquier et al., 2015].

3.1 Experiments

Liquid mixture

The viscous liquid used in these experiments is a mixture of glycerol and water. The choice of an aqueous glycerol solution was motivated by the advantageous characteristics of glycerol. Indeed, glycerol is transparent, nontoxic and stable under most conditions [1], which allows for long term use and storage [Soap and Detergent Association, 1990].

The viscosity of a glycerol-water solution is dependent on the concentration and temperature of the mixture (see figure 5.1 on page 92), so we use here an evenly mixed solution of 80% glycerol and 20% water and the room temperature is regulated to 25°C. The density and temperature of the liquid are measured in situ using a densimeter Anton Paar DMA 35. A resistance thermometer Pt100 is used to track the temperature in the room. The viscosity of the mixture is measured by a Contraves low shear rheometer after the experiments. At 25°C, the density of the mixture is found to be $\rho = 1.20 \times 10^3$ kg.m^{-3} and its kinematic viscosity is $\nu = \eta/\rho = 30 \times 10^{-6}$ m^2.s^{-1}, in agreement with the tabulated value of viscosity found for a glycerol-water mixture of such composition and temperature. The surface tension of the mixture, measured with a Wilhelmy plate tensiometer, is $\gamma = 60 \pm 5$ mN.m^{-1}.

From these measurements, we can compute that the capillary wavelength is $\lambda_c = 2\pi\sqrt{\gamma/(\rho - \rho_a)g} \simeq 14.2$ mm and the minimum phase velocity $c_{\min} = 21.5$ cm.s^{-1} (see Eq. (1.1.3)). The depth correction factor, $\tanh(kh)$, in the dispersion relation (Eq. (1.1.1)) is larger than 0.98 for wavelength smaller than 90 mm, so finite depth effects are quite negligible in the present experiments. For this interface, the velocity threshold for the Kelvin-Helmholtz instability is predicted to be $U_{\mathrm{KH}} \simeq 6.7$ m.s^{-1} (Eq. (1.1.6)).

1. Except in very high concentrations, in which case its hygroscopicity can be a problem, see chapter 5.

As discussed in chapter 1 (see § 1.1.3 on page 9), the viscosity of the liquid implies the existence of two wavelength cut-offs and the wavelengths between these two limits are the only ones that can propagate [LeBlond and Mainardi, 1987]. In the case of our mixture of viscosity $\nu = 30 \times 10^{-6}$ m^2.s^{-1}, the wavelength cut-offs are calculated to occur for wavelengths shorter than 0.06 mm or greater than 150 m. These values being considerably far from all the wavelengths considered here, this means that we can safely assume that these cut-offs do not affect the wave propagation in our experiments.

Generally speaking, despite the large viscosity of the liquid used in our experiments, the liquid can be considered as quasi-inviscid, i.e. the surface waves are damped but their dispersion relation is unaffected by the viscosity of the liquid. Indeed, the phase velocity with the viscous correction (Eq. (1.1.7)) matches the inviscid prediction with a difference of less than 0.2% for all wavelength greater than λ_c [Lamb, 1995] [Padrino and Joseph, 2007]. However, the damping of the waves' amplitude cannot be neglected. It is even an advantage in the way the set-up has been designed: since the large viscosity of the liquid induces a strong attenuation of the surface deformations, the distance over which an unamplified perturbation can propagate is rather limited. Generally speaking, wave damping comes from the friction with the bottom and sides of the tank as well as the dissipation in the bulk [Lamb, 1995] [Lighthill, 1978]. For the wave tank geometry and the typical wavelengths considered here, friction with the bottom and side walls is negligible, and the attenuation length for free waves is governed by the dissipation in the bulk, $L_v = c_g/(2\nu k^2)$, with c_g the group velocity. Accordingly, in the range of wavelengths observed experimentally, a free disturbance at these wavelengths cannot propagate over a distance much larger than a few wavelengths. For example, for $\lambda \simeq 35$ mm the attenuation length is $L_v \simeq 80$ mm. In water, the corresponding attenuation length would be 25 times greater. Such great attenuation length leads to issues of reflecting waves and this is usually why wind waves experiments with water are carried out in long tanks. Although the tank we use is of limited size, thanks to the high viscosity of the liquid, reflections on the walls or at the end of the tank are not observed in our experiments.

Mean velocity profiles

The wind-induced shear stress drives a current drift close to the interface compensated by a backflow at the bottom of the tank (see section 2.2.2). Except at small fetch ($x \lesssim h$) and at the end of the tank where surface contamination cannot be avoided ($x \gtrsim 120$ cm), the velocity profiles in the liquid are well described by a parabolic law. Thanks to the high viscosity of the liquid, the flow induced by the wind in the liquid remains laminar, with a relatively weak surface drift (of the order of a few centimeters per second). This surface drift is expected to have only a small effect on the dispersion relation. Indeed, Lilly shows that the correction to the phase velocity of free waves for a parabolic mean velocity profile in the tank is $U_s(1 - 2/kh)$ (see appendix of [Hidy and Plate, 1966]). The first term (U_s) corresponds to a simple transport, attenuated more and more strongly for higher wavelength λ by the second term ($-2U_s/kh$) due to the backflow in the tank. For the most unstable wavelength $\lambda \simeq 35$ mm, this correction amounts to about 10% of the phase velocity.

As detailed in section 2.2.1, the airflow generated by the wind blower is similar to a canonical turbulent airflow above a smooth fixed wall for wind velocities under the wave generation threshold. It presents a mean velocity profile with a logarithmic region in the inertial sublayer and can be locally described by the turbulent boundary layer theory. The friction velocity u^* is very similar independently of whether it is deduced from the velocity

profile in the liquid or in the air: it is approximately 5% of U_a the mean air velocity of the center of the channel.

FS-SS measurements

The surface deformation of the liquid is measured using the Free Surface Synthetic Schlieren (FS-SS) method described in section 2.1.3. The acquisitions are performed over 390×280 mm windows centered at three different fetches, so that the fields of visualization roughly correspond to the first three quarters of the tank with a small overlap: $x \in [10, 400]$ mm; $x \in [370, 760]$ mm; $x \in [700, 1090]$ mm (no measurement are carried over the last quarter because of surface pollutants, see section 2.2.b). Examples of surface reconstruction are provided in figure 3.1 (over the second quarter, centered on $x = 570$ mm). Two types of recordings are performed: acquisitions of 2 s at 200 Hz for time-resolved wave reconstruction, and acquisitions of 100 s at 10 Hz to ensure a good convergence of the wave statistics.

3.2 Evolution of the surface characteristics with wind velocity

3.2.1 Evolution of the deformation amplitude with wind velocity

The change of the surface appearance for winds of increasing velocity is easily visible by the direct analysis of the surface fields reconstructed by FS-SS. Figure 3.1 presents four snapshots of the surface deformation at increasing wind velocity, $U_a = 3.2$, 5.9, 7.0 and 7.8 m.s^{-1}, taken at intermediate fetch $x \in [370, 760]$ mm. At small wind velocity, the surface is populated with rapidly moving disorganized perturbations of weak amplitude, of order 10 μm, elongated in the streamwise direction (Fig. 3.1(a)). Note that such slight interface motions are often reported below the threshold velocity during wind waves experiments [Keulegan, 1951] [Kunishi, 1963] [Hidy and Plate, 1966] [Plate et al., 1969] [Gottifredi and Jameson, 1970] [Wu, 1978] [Kahma and Donelan, 1988] [Ricci, 1992] [Caulliez et al., 1998] [Lorenz et al., 2005]. However, there is no consensus on their designation and the terms used to refer to them are quite diverse ("tiny undulations", "small oscillations", "shimmering of the surface", "surface disturbances", "initial wavelets", "tremors", etc). In the rest of this manuscript, these streamwise surface deformations of weak amplitude at low wind velocity are designated by the term "wrinkles".

When the wind velocity is increased, noisy spanwise crests, normal to the wind direction, gradually emerge in addition to the streamwise deformations (Fig. 3.1(b)). As the velocity is further increased ($U_a \simeq 6 - 7$ m.s^{-1}), the amplitude of these spanwise crests rapidly grows with U_a and the streamwise deformations, of weaker amplitude in comparison, become less and less visible. Finally, the surface does not display a combination of streamwise and spanwise surface deformations anymore but is dominated by transverse waves. At wind velocity $U_a = 7.0$ m.s^{-1}, the surface field is covered by a regular wave pattern of typical amplitude 0.2 mm, with a well defined wavelength in the streamwise direction (Fig. 3.1(c)). Note that the wave crests are not strictly normal to the wind direction as there are dislocations near the center line $y = 0$. Since the wind mean velocity profile bears no significant disparity between the left and right halves of the channel (see Fig. 2.13 on page 44), these dislocations may rather be due to a slight convergence of the turbulent airflow close to the free surface towards the walls, unavoidable for a turbulent channel flow in a rectangular geometry (secondary flow of Prandtl's second kind [Schlicht-

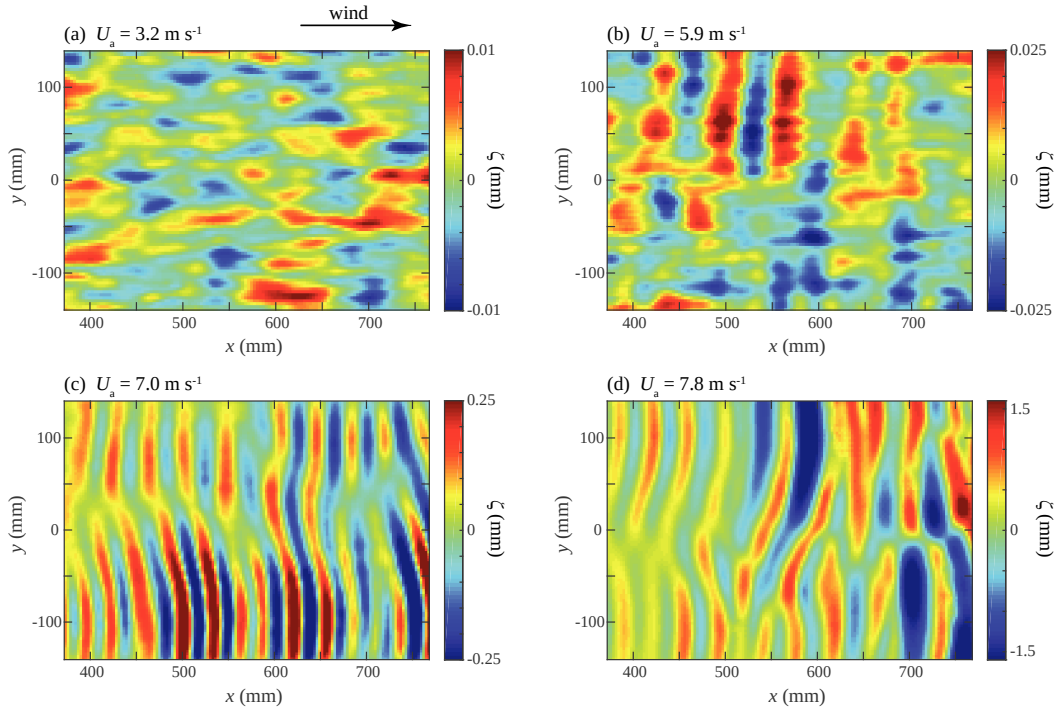

Figure 3.1: Instantaneous surface height $\zeta(x, y)$ measured by FS-SS centered at intermediate fetch $x = 570$ mm, at increasing wind velocities. (a) $U_a = 3.2$ m.s^{-1}, showing disorganized wrinkles of small-amplitude elongated in the streamwise direction ($\zeta_{\text{rms}} = 0.0032$ mm). (b) $U_a = 5.9$ m.s^{-1}, showing a combination of streamwise wrinkles and spanwise waves ($\zeta_{\text{rms}} = 0.009$ mm). (c) $U_a = 7.0$ m.s^{-1}, showing well-defined spanwise waves of mean wavelength $\lambda = 35$ mm ($\zeta_{\text{rms}} = 0.12$ mm). (d) $U_a = 7.8$ m.s^{-1}, showing large-amplitude waves of mean wavelength $\lambda = 44$ mm with increasing disorder ($\zeta_{\text{rms}} = 0.6$ mm). The wind is blowing from left to right. Note the change of scale in the color map between all four fields of surface deformation.

ing, 2000], see figure 2.14 on page 44). For wind velocities even greater, the wave amplitude continues to grow and the disorder of the wave pattern increases, with more dislocations appearing, not necessarily on the center line (Fig. 3.1(d)). Simultaneously, the typical wavelength becomes larger.

These patterns below and above wave onset are quite similar to those obtained by direct numerical simulations of temporally growing waves with periodic boundary conditions [Lin et al., 2008] [Liao and Kaihatu, 2012] (see figure 1.8 on page 20). It should be noted that dislocations in the wave patterns can also be seen in their results despite the absence of secondary flows (the periodic boundary at the "walls" imply that there are no corner causing the secondary flows). This suggests that an inherent destabilization of the wave crests is possible.

To study the evolution from the disorganized streamwise wrinkles to the transverse waves, the root mean square of the deformation amplitude averaged in time and space

$$\zeta_{\text{rms}} = \langle \zeta^2(x, y, t) \rangle^{1/2} \tag{3.2.1}$$

is plotted as a function of the wind velocity. Here, the brackets are both a temporal average and a spatial average over the entire field of view. Figure 3.2 shows the evolution

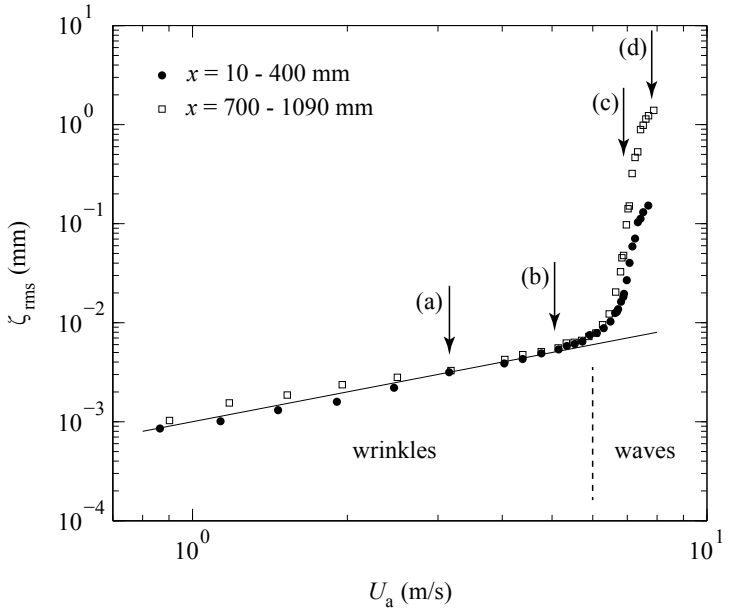

Figure 3.2: Root mean square of the surface height $\zeta_{\rm rms}$ as a function of wind velocity U_a. The data is averaged over the measurement window of dimensions 390×280 mm centered at two values of the fetch $x = 205$ mm (•) and $x = 895$ mm (□). The letters and vertical arrows show the velocities corresponding to the four snapshots in figure 3.1. The continuous line corresponds to the linear fit $\zeta_{\rm rms} = \alpha U_a$, with $\alpha = 10^{-6}$ s.

of this quantity $\zeta_{\rm rms}$ with respect to the wind velocity, on the first and third quarter of the tank ($x \in [10, 400]$ and $x \in [700, 1090]$). Two regimes are clearly visible. At low wind velocity, the interface is dominated by longitudinal wrinkles and the surface deformation amplitude slowly increases with U_a. However, past a velocity threshold of order 6 m.s^{-1}, the increase of $\zeta_{\rm rms}$ becomes much sharper: while $\zeta_{\rm rms}$ rises by a factor of 10 between 1 and 6 m.s^{-1}, it grows by a factor of 100 for U_a increasing from 6 to 8 m.s^{-1}. A similar transition in the wave amplitude is observed in air-water experiments [Kahma and Donelan, 1988] [Caulliez et al., 1998]. This fast growth with wind velocity slows down at higher U_a: at the largest velocity ($U_a \simeq 8$ m.s^{-1}), the sharp increase of the wave amplitude seems to start to saturate. In any case, this wind velocity represents an upper limit for the FS-SS measurements. Because of the caustics induced by strong wave curvatures, surface visualization by FS-SS is impaired at larger wind velocities [2].

Comparing the wave height at the two different values of fetch in figure 3.2, it is found that in the wrinkles regime ($U_a < 6$ m.s^{-1}), the amplitude of the surface deformation is almost independent of the fetch. The wave height in this regime is simply following an approximately linear law with respect to the wind velocity: $\zeta_{\rm rms} \simeq \alpha U_a$, with $\alpha = 10^{-6}$ s. The independence of the surface deformation with fetch suggests that the interface response to the wind is not a function of the surface deformations created upstream but is only function of the wind at the current fetch. The perturbations generated at shorter fetch do not propagate over a distance great enough to significantly affect the evolution of the wave height with fetch. This suggests that the wrinkles can be viewed as imprints

2. At least for this liquid and particular viscosity. A different liquid may respond to the same wind velocity with a smaller wave amplitude still measurable by the FS-SS method.

on the free surface of the pressure fluctuations in the turbulent airflow.

Expressing the correlation between the fluctuations in surface height and the fluctuations in pressure in order to quantitatively validate this approach is however not a simple exercise. Let us try the simplest representation. A crude estimate can be given by neglecting all capillary and viscous effect and assuming the instantaneous hydrostatic response of the liquid interface. This leads to a deformation amplitude linearly increasing with pressure fluctuations:

$$\zeta_{\rm rms} \simeq \frac{p_{\rm rms}}{\rho g}. \tag{3.2.2}$$

While accessing the pressure fluctuations at an interface is particularly difficult experimentally, such information is now available by direct numerical simulations, at least on a smooth undeformable boundary. Since the airflow above the liquid-air interface can be approximated by a flat fixed wall for wind velocity below the wave onset (see chapter 2), the results of these DNS are used here to complete our calculations. The pressure fluctuations at the wall in a fully developed turbulent channel is well described by the empirical law [Hu et al., 2006] [Jimenez and Hoyas, 2008]:

$$p_{\rm rms} = f(Re_\tau)\rho_a u^{*2}, \tag{3.2.3}$$

with:

$$f(Re_\tau) = (2.60\ln(Re_\tau) - 11.25)^{1/2}. \tag{3.2.4}$$

In the range $U_a \simeq 1 - 6$ m.s^{-1}, the corresponding Reynolds number is $Re_\tau \simeq 160 - 1000$. Neglecting the logarithmic variation over this range and taking $u^* \simeq 0.05U_a$, this empirical law yields $p_{\rm rms} \simeq 0.006\rho_a U_a^2$, and thus:

$$\zeta_{\rm rms} \simeq \frac{0.006\rho_a U_a^2}{\rho g} \simeq 0.3 - 20\ \mu\text{m}. \tag{3.2.5}$$

The order of magnitude is consistent with Fig. 3.2 but the predicted scaling ($\zeta_{\rm rms} \propto U_a^2$) is not compatible with the data. A more complete (but more complex) approach would require accounting for the viscous response time of the surface to a local change in pressure, with the added difficulties that the pressure fluctuations are not permanent but transient and are moving at a certain speed above the interface (more details will be given in chapter 5).

3.2.2 Spatial growth rate

The data comparison at the two different fetches in figure 3.2 leads to the clear conclusion that beyond a certain wind velocity, the amplitude of the surface deformation ceases to be approximately independent of fetch and starts to evolve with fetch. Indeed, contrarily to the wrinkles, the amplitude of the transverse waves strongly increases with x. In order to study more closely the spatial evolution of the surface height, the root mean square amplitude $\zeta_{\rm rms}(x)$ is computed locally at a certain fetch, that is to say using an average over y and time only. The amplitude of the surface deformation is plotted in semilogarithmic coordinates for different wind velocities in figure 3.3 (the wind velocity increases from the bottom to top plot). In agreement with the data presented in figure 3.2, the amplitude of the surface deformation in the wrinkles regime does not change much with fetch, while it does in the wave regime. At small fetch ($x < 400$ mm), the spatial growth is approximately exponential, which is expected for a convective supercritical instability in an open flow [Huerre and Rossi, 1998] and has been reported in many air-water

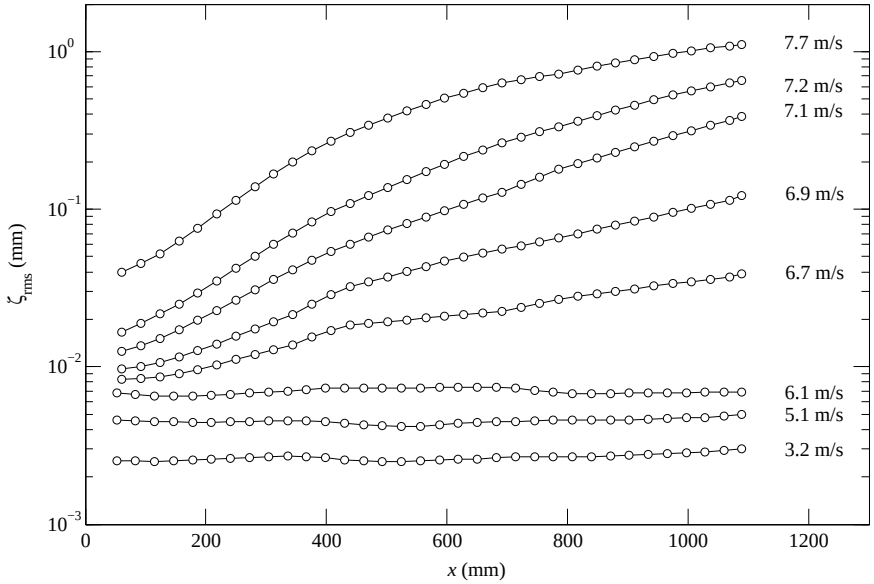

Figure 3.3: Wave amplitude ζ_{rms} (averaged over time and the spanwise coordinate y) as a function of the fetch x for various wind speeds U_a from 3.2 to 7.7 m.s^{-1}. In the wrinkle regime ($U_a < 6.3$ m.s^{-1}) $\zeta_{\mathrm{rms}}(x)$ is almost constant, whereas it increases with fetch in the wave regime ($U_a > 6.3$ m.s^{-1}).

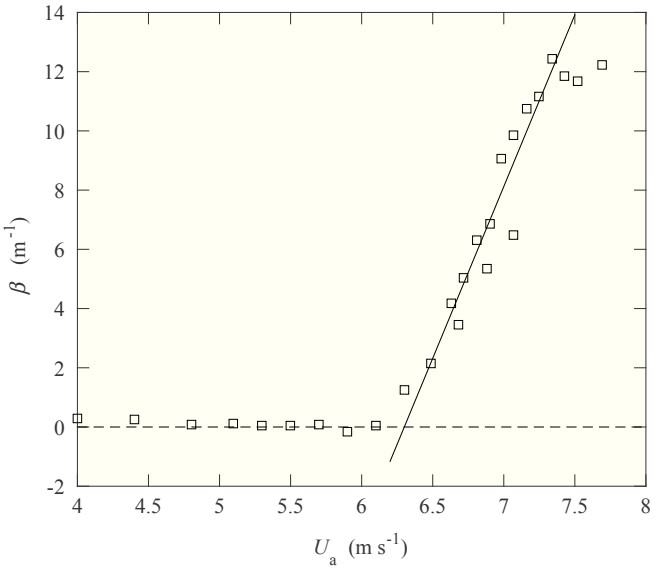

Figure 3.4: Spatial growth rate β, measured at small fetch ($x < 400$ mm), as a function of wind velocity. The continuous line shows the linear fit (3.2.7).

experiments [Hidy and Plate, 1966] [Sutherland, 1968] [Plate et al., 1969] [Mitsuyasu and Rikiishi, 1978] [Liberzon and Shemer, 2011]. At larger fetches however, the wave amplitude grows less rapidly, which suggests that nonlinear effects come to be important, resulting in this weaker wave growth (see chapter 4).

The spatial growth rate β is estimated in the initial exponential growth region ($x <$ 400 mm) by fitting the squared amplitude as:

$$\zeta_{\text{rms}}^2(x) \propto \exp(\beta x). \tag{3.2.6}$$

Figure 3.4 presents this growth rate β as a function of the wind velocity U_a: β is almost zero before a certain wind velocity and becomes positive past this value. This allows to accurately define the onset U_c of the wave growth. For $U_a < U_c$, there is next to no spatial growth ($\beta \simeq 0$), and for $U_a > U_c$, the spatial growth rate increases linearly, as it can be fitted by:

$$\beta \simeq b(U_a - U_c) \tag{3.2.7}$$

with $U_c \simeq 6.3 \pm 0.1$ m.s^{-1} and $b \simeq 11.6 \pm 0.8$ s m^{-2}. Interestingly, in the small range of fetch over which β is computed, the waves are nearly monochromatic, with $\lambda \simeq 35$ mm (see section 3.2.3). This indicates that although computed from the total wave amplitude, the growth rate measured here corresponds roughly to the growth rate of the most unstable wavelength (see also section 4.1.4 on page 80).

One may note that the velocity threshold $U_c \simeq 6.3$ m.s^{-1} turns out to be close to the onset prediction of the Kelvin-Helmholtz instability (Eq. (1.1.6)). This agreement is however coincidental as the wave threshold depends on viscosity. Since the critical velocity increases with viscosity (see chapter 5), it makes sense that a certain viscosity will lead to the same result as the inviscid Kelvin-Helmholtz prediction. It should also be noted that the critical wind velocity as it is defined implies that U_c corresponds to the minimal wind velocity at which waves start to *grow*, and not to the inception velocity, the minimal wind velocity at which waves start to *appear*. Indeed, as shown in figure 3.1b, transverse waves may be locally generated below U_c (this point will be further discussed on page 67).

To compare with other experiments and theoretical results, it is interesting to express equation (3.2.7) in terms of a temporal growth rate instead of a spatial one. In the frame moving with the group velocity, this temporal growth rate writes $\beta_t = c_g\beta$ [Gaster, 1962]. Using the group velocity $c_g \simeq 0.16$ m.s^{-1} corresponding to the most unstable wavelength $\lambda \simeq 35$ mm, and writing U_a in terms of the friction velocity $u^* \simeq 0.05U_a$, we obtain:

$$\beta_t \simeq (36 \pm 8)(u^* - 0.31) \tag{3.2.8}$$

(in s^{-1}). These values are smaller by a factor of order of 2 to 5 than the ones given by theoretical predictions [Miles, 1959a] or reported in air-water experiments [Larson and Wright, 1975] [Mitsuyasu and Honda, 1982] [Plant, 1982]. This is not a surprising result as one would intuitively expect the wave growth to be weakened by the high viscosity of the liquid.

An interesting question is whether the wrinkles are perturbations on which the transverse waves are initiated. To address this, let us compare the wrinkles' amplitude and the initial wave amplitude. From figure 3.3, the initial wave amplitude ζ_{rms} can be extrapolated at $x = 0$ for $U_a > 6.3$ m.s^{-1}. This initial amplitude $\zeta_{\text{rms}}(x = 0)$ grows with U_a much more rapidly than the amplitude of the wrinkles. Indeed, for U_a increasing from 6.3 to 7.7 m.s^{-1}, $\zeta_{\text{rms}}(x = 0)$ increases from 8 to 30 μm, which corresponds to a much quicker growth that the linear one $\zeta_{\text{rms}} = \alpha U_a$ with $\alpha = 10^{-6}$ s observed for the wrinkles. As a consequence, it appears that the wrinkles are not necessary for the growth of the waves

and cannot be considered as the seed noise for the exponential growth of the waves at larger velocity. The seed noise may instead result from the surface disturbance at $x = 0$, where the boundary condition suddenly changes from no-slip to free-slip. In agreement with this idea, the root mean square of amplitude of surface deformation can be described as the sum of the wrinkle amplitude (linearly increasing with U_a) and the wave amplitude (exponentially increasing with U_a):

$$\zeta_{\text{rms}} \simeq \alpha U_a + \zeta_n(U_a) \exp\left[b\,(U_a - U_c)\,x\right], \tag{3.2.9}$$

with $\zeta_n(U_a)$ the amplitude of the noise at $x = 0$. The fact that the wave amplitude is quite sensitive to the liquid level at $x = 0$ (see page 30) agrees with this description.

3.2.3 Spatial structures

In order to characterize the spatial structure of the surface deformations, both in the wrinkles and wave regimes, a two-point correlation function is used:

$$C(\mathbf{r}) = \frac{\langle \zeta(\mathbf{x}, t)\zeta(\mathbf{x} + \mathbf{r}, t)\rangle}{\langle \zeta(x, y, t)^2\rangle}, \tag{3.2.10}$$

where $\langle\,\cdot\,\rangle$ is both a spatial and temporal average. Figure 3.5 presents the correlation [3] in the streamwise direction ($\mathbf{r} = r_x\mathbf{e}_x$) for the same four wind velocities as for the snapshots in figure 3.1. Oscillations in the correlation indicate a periodic structure in the streamwise direction. In contrast, the monotonic decay of $C(r_x)$ as it can be observed at low wind velocity is a signature of the spatial disorder in the wrinkles regime. The presence of slight oscillations below the critical velocity (at $U_a = 5.9$ m.s^{-1}) confirms that there are transverse waves under the threshold $U_c \simeq 6.3$ m.s^{-1} (see also Fig. 3.1b). This suggests that the transition between the wrinkles and wave regimes is not abrupt but continuous. Both wrinkles and transverse waves coexist with different relative amplitude over a significant range of velocity around U_c. This was already intuited by the slow transition in figure 3.2 and strengthens the importance of the spatial growth in the criterion for the determination of the critical velocity.

To further characterize the smooth transition between the wrinkles and wave regime, the correlation lengths Λ_i in the direction $\mathbf{e}_i$ ($i = x, y$), defined as 6 times the first value of r_i satisfying $C(r_i) = 1/2$, are computed. The correlation lengths could a priori be defined based on any other value of $C(r_i)$ than $1/2$ (as long as $C(r_i)$ reaches this value for all wind velocities). The definition with $1/2$ and the factor 6 is chosen so that the correlation length may take on a physical meaning. Indeed, for a monochromatic wave propagating in the direction $\mathbf{e}_i$, the correlation length Λ_i defined in this way and the wavelength coincide. Of course, no wavelength can be defined in the wrinkles regime because of the inherent disorder of these surface deformations. Nevertheless, below the threshold, the correlation lengths Λ_x and Λ_y give estimates of the characteristic size of wrinkles, in the streamwise and spanwise directions respectively.

Figure 3.6 presents the correlation lengths Λ_x and Λ_y relative to the wind velocity [4]. At very low wind (~ 1 m.s^{-1}), both lengths are approximately of the same order, $\Lambda_x \simeq \Lambda_y \simeq 250$ mm. Slightly larger wind velocity leads to a quick decline of Λ_y to about

3. All correlations are computed using the Matlab function *corrf* from the toolbox PIVMat.

4. The correlation lengths presented in figure 3.6 are averaged over $x \in [700, 1090]$. The plots at other fetches are similar, with the only difference that the increase past the threshold of Λ_x is less pronounced at smaller fetch. As the evolution of the wavelength will be discussed in the next chapter, these differences are not detailed here. The same remark applies to figure 3.10.

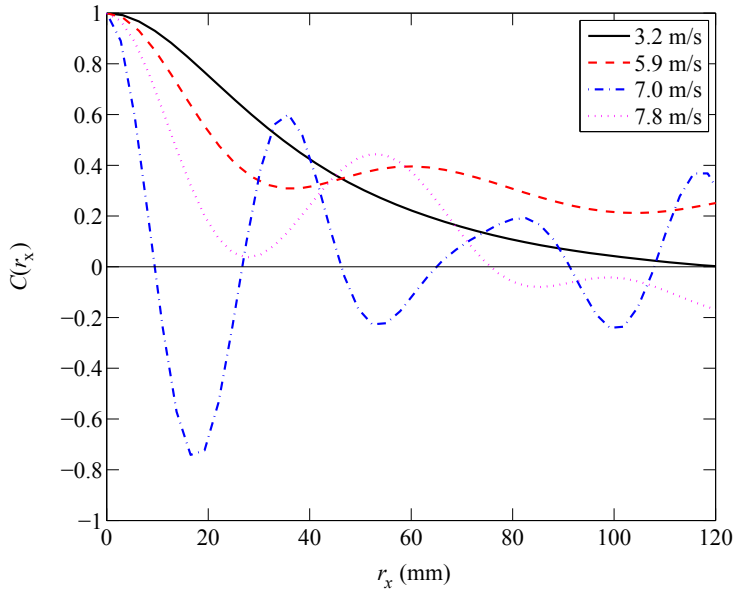

Figure 3.5: Spatial correlation function in the streamwise direction, $C(r_x)$, at four wind velocities for $x \in [370, 760]$ mm.

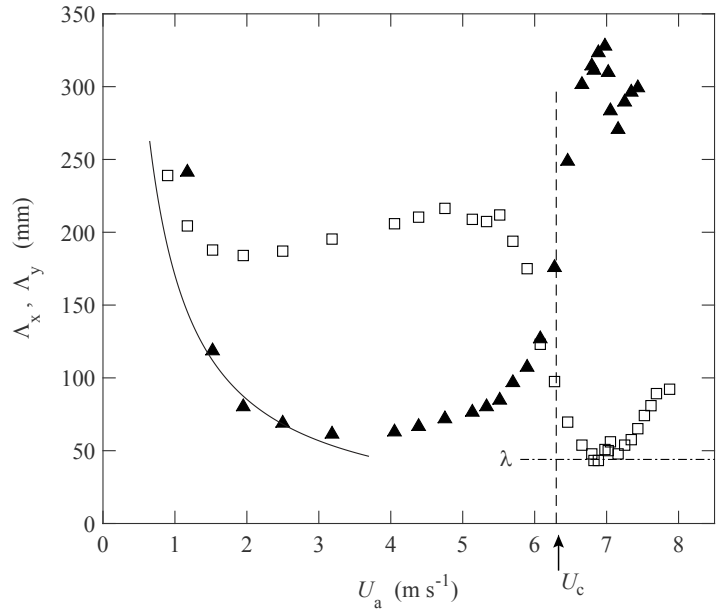

Figure 3.6: Streamwise and spanwise correlation lengths Λ_x (□) and Λ_y (▲), averaged over $x \in [700, 1090]$ mm, as a function of the wind velocity U_a. The continuous line is a fit $\Lambda_y \simeq 550\delta_\nu$, with $\delta_\nu = \nu_a/u^*$ the thickness of the viscous sublayer. The vertical dashed line at $U_a = 6.3$ m.s^{-1} indicates the onset of the wave growth. The horizontal dashed line corresponds to the local wavelength $\lambda = 44$ mm.

70 mm, while Λ_x remains of the same order of magnitude. Between 2 and 5 m.s^{-1}, both correlation lengths do not evolve much and the surface deformations are mostly in the streamwise direction ($\Lambda_x/\Lambda_y \simeq 3$). Between 5 and 7 m.s^{-1}, Λ_x decreases while Λ_y increases, and past 7 m.s^{-1}, the surface deformations are now essentially in the spanwise direction ($\Lambda_x/\Lambda_y \simeq 0.15$). Note that a pure monochromatic wave propagating in the x direction would lead to a constant correlation in the y direction ($C(r_y) = 1$) and therefore the associated correlation length would be infinite ($\Lambda_y = \infty$). The fact that the correlation length Λ_y saturates in our case past the velocity threshold indicates that the transverse waves do not span over the entire width of the tank. Instead, dislocations are visible near the center line $y = 0$ (see Fig. 3.1(c,d)) and the saturation of Λ_y is the result of these dislocations.

As mentioned above, the decrease of Λ_x and the increase of Λ_y start at a wind velocity of approximately 5 m.s^{-1}. This indicates that transverse waves are present simultaneously with the wrinkles well before the critical velocity $U_c \simeq 6.3$ m.s^{-1} where waves start to be amplified. The coexistence of wrinkles and transverse wave below U_c, coupled with the other experimental results presented above, allows to propose the following view for the evolution of the surface deformation with wind velocity. At low wind velocity, below the wave onset, wrinkles locally excite waves. However, these waves are not amplified but are damped exponentially ($\beta < 0$). If this excitation was not randomly distributed on the interface but at a well-defined fixed location (like in the case of a mechanical forcing), this decay would be measurable. In our case, the interface response is the sum of a large number of spatially decaying transverse waves, locally excited by the randomly distributed wrinkles, themselves generated by the turbulent fluctuations in the airflow above the surface. Since the wrinkles' amplitude is essentially independent of the fetch, the result of the combination of the wrinkles and the decaying transverse waves locally excited by them is independent of the fetch as well. This leads to an apparent zero growth rate that can be seen below the threshold in figure 3.4. To put it another way, the negative growth rate expected below the threshold is hidden by the spatial average induced by the random distribution of the decaying waves.

Working under the assumption that the elongated wrinkles visible at low velocity are the traces of the pressure fluctuations in the turbulent boundary layer located above the interface, one would expect to find correlations between their characteristic spanwise and streamwise dimensions. A full validation through experiments of this would require to compare the spatial structure of the pressure fluctuations and of the interface deformations directly in the set-up. Unfortunately, accurate measurements of pressure fluctuations very close to an interface are experimentally extremely difficult to achieve. As a result, we use again data obtained by direct numerical simulation. The data here refered to is from [Jimenez and Hoyas, 2008] [5] and was obtained at Re_τ up to 2000 [[6]]. Starting from the center of the airflow (large z), the intensity of the pressure fluctuations increases logarithmically with a decreasing altitude down to $z \simeq 30\delta_\nu$. It then remains essentially constant in the viscous sublayer down to the interface (see Fig. 3.7(left)). In the region close to the interface where the pressure fluctuations are close to being maximal ($0 < z < 30\delta_\nu$), the most energetic pressure structures have approximately the same characteristic dimensions in both the streamwise and spanwise direction: $\ell_x \simeq \ell_y \simeq 160\delta_\nu$ (see Fig. 3.7(right)). Since the thickness of the viscous sublayer $\delta_\nu = \nu_a/u^*$ decreases with increasing wind velocity, these characteristic dimensions ℓ_x and ℓ_y also decrease as U_a increases. Comparing these features with the correlation lengths Λ_x and Λ_y, it is found that they are compatible, at

5. The dataset is available at `http://torroja.dmt.upm.es/ftp/channels/`.
6. The results presented here vary little with the Reynolds number.

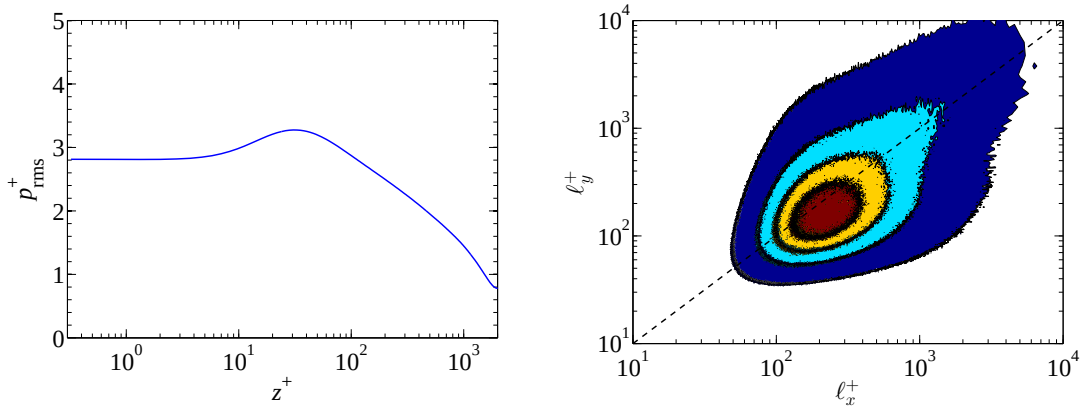

Figure 3.7: (Left) Pressure fluctuation profile as a function of the adimensionalized altitude above the wall $z^+ = z/\delta_\nu$; (right) Normalized energy at lengths ℓ_x and ℓ_y at the elevation $z^+ = z/\delta_\nu = 30$. Colored regions from the outside in (from dark blue to red) present the energy between 0.1 and 0.3, 0.3 and 0.5, 0.5 and 0.7 and larger than 0.7. The central red region thus corresponds to the most energetic structures. The continuous line represents the relation $\ell_x = \ell_y$. Both graphs present the data obtained at $Re_\tau = 2000$ refered to in [Jimenez and Hoyas, 2008].

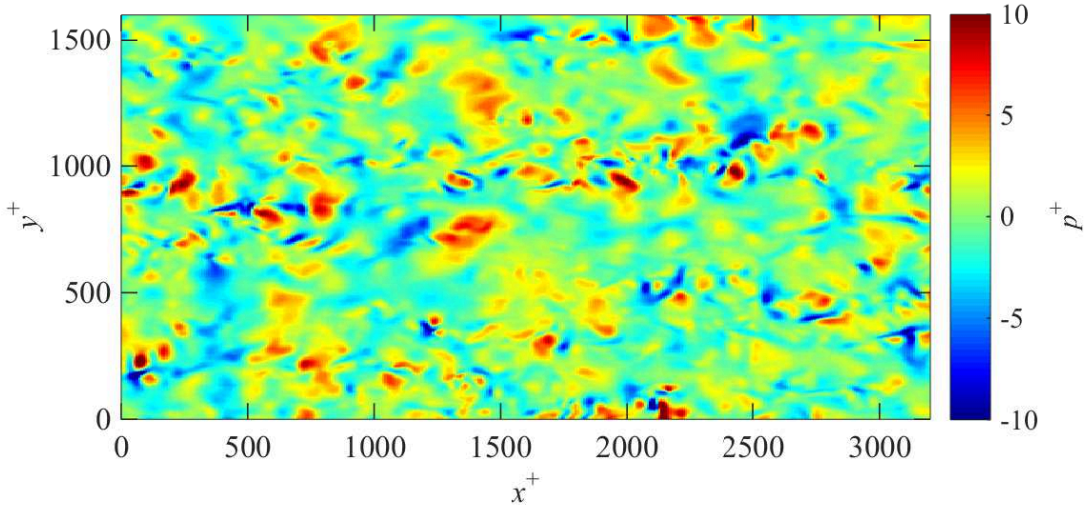

Figure 3.8: Pressure field at the interface. DNS data obtained at $Re_\tau = 550$ refered to in [Jimenez and Hoyas, 2008].

least at low wind speeds (see Fig. 3.6). Indeed, at very low wind velocity, the wrinkles are nearly isotropic (see Fig. 3.8): $\Lambda_x \simeq \Lambda_y \simeq 250$ mm. However, for wind speeds slightly higher, the evolution of Λ_x and Λ_y departs from one another. The spanwise correlation length decreases as $\Lambda_y \simeq 550\delta_\nu$, following the evolution of the width ℓ_y of the pressure fluctuations up to 3 m.s^{-1}. In contrast, the streamwise correlation length Λ_x does not display the same decrease and stays relatively large. This may result from the viscous time response of the interface to a moving pressure perturbation (since pressure fluctuations are advected with the wind in the streamwise direction while leaving traces on the liquid

surface).

3.2.4 Spatio-temporal dynamics

To further confirm the central importance of the pressure fluctuations in the surface deformation in the wrinkles regime, let us now compare their spatio-temporal dynamics.

Figure 3.9(left) presents the spatio-temporal diagrams at the same four wind velocities as in figure 3.1, constructed by plotting the surface deformation $\zeta(x, y, t)$ in the plane (x, t) along the center line $y = 0$. The oblique lines in these diagrams indicate the characteristic velocity of the patterns of surface deformation. The closer these lines are to the horizontal, the larger the characteristic velocity is. Figure 3.9(right) displays the two-point two-time correlation in the streamwise direction at the same increasing velocities. This spatio-temporal correlation is defined as:

$$\mathcal{C}(r_x, \tau) = \frac{\langle \zeta(\mathbf{x} + r_x \mathbf{e}_x, t + \tau)\zeta(\mathbf{x}, t)\rangle}{\langle \zeta(\mathbf{x}, t)^2\rangle}, \tag{3.2.11}$$

where $\langle \cdot \rangle$ represents a spatial and temporal average. For statistically stationary and homogeneous deformations, the spatio-temporal correlation is such that $\mathcal{C}(-r_x, -\tau) = \mathcal{C}(r_x, \tau)$ and consequently, only the positive domain (here, in time) needs to be shown.

At small wind speed ($U_a = 3.2$ m.s^{-1}), the surface displays rapidly propagating disorganized structures, with a life time of order of their transit time (Fig. 3.9(a)). The broad correlation in figure 3.9(b) is the signature of the distribution of their characteristic velocity being broad.

At $U_a = 5.9$ m.s^{-1}, wrinkles and waves coexist: slow wave packets with well-defined velocity appear embedded in rapid disorganized fluctuations (Fig. 3.9(c)). These wave packets further confirm the picture presented above for the wrinkles-wave transition: wrinkles locally excite evanescent transverse waves that rapidly fade away. Furthermore, the corresponding spatio-temporal correlation (Fig. 3.9(d)) allows inferring the wavelength and phase velocity of these decaying waves.

At $U_a = 7.0$ m.s^{-1}, the interface becomes dominated by spatially growing transverse waves: the spatio-temporal diagram is populated with well defined oblique lines (Fig. 3.9(e)) and the spatial growth is indicated by the gradual change of color along these lines. In the spatio-temporal correlation, the waves translate into a marked spatial and temporal periodicity (Fig. 3.9(f)). However, wave packets delimited by boundaries propagating at the group velocity are still visible, which indicates that the transverse waves are not strictly monochromatic. For this wind velocity ($U_a = 7.0$ m.s^{-1}) and fetch ($\overline{x} = 570$ mm), the local wavelength is $\lambda = 37$ mm, for which the predicted phase and group velocities are $c = 0.26$ m.s^{-1} and $c_g = 0.16$ m.s^{-1}, in accordance with the slopes observed in figure 3.9(f) (black and white dashed lines correspond respectively to the phase and group velocity).

Finally, at even larger wind velocity ($U_a = 7.9$ m.s^{-1}), the phase velocity and wavelength both somewhat increase. Accordingly, the spatial and temporal periodicity weakens in the corresponding spatio-temporal correlation (Fig. 3.9(h)).

For monochromatic waves propagating in the x direction with a wavenumber k and a radian frequency ω, the two-point two-time correlation yields $\mathcal{C}(r_x, t) = \cos(kr_x - \omega t)$. This means that the correlation is equal to 1 along characteristic lines parallel to $r_x/t = c$, with $c = \omega/k$ the phase velocity. For non-monochromatic waves propagating in the same direction, the correlation $\mathcal{C}(r_x, t)$ is weaker but is still the largest along a line r_x/t given

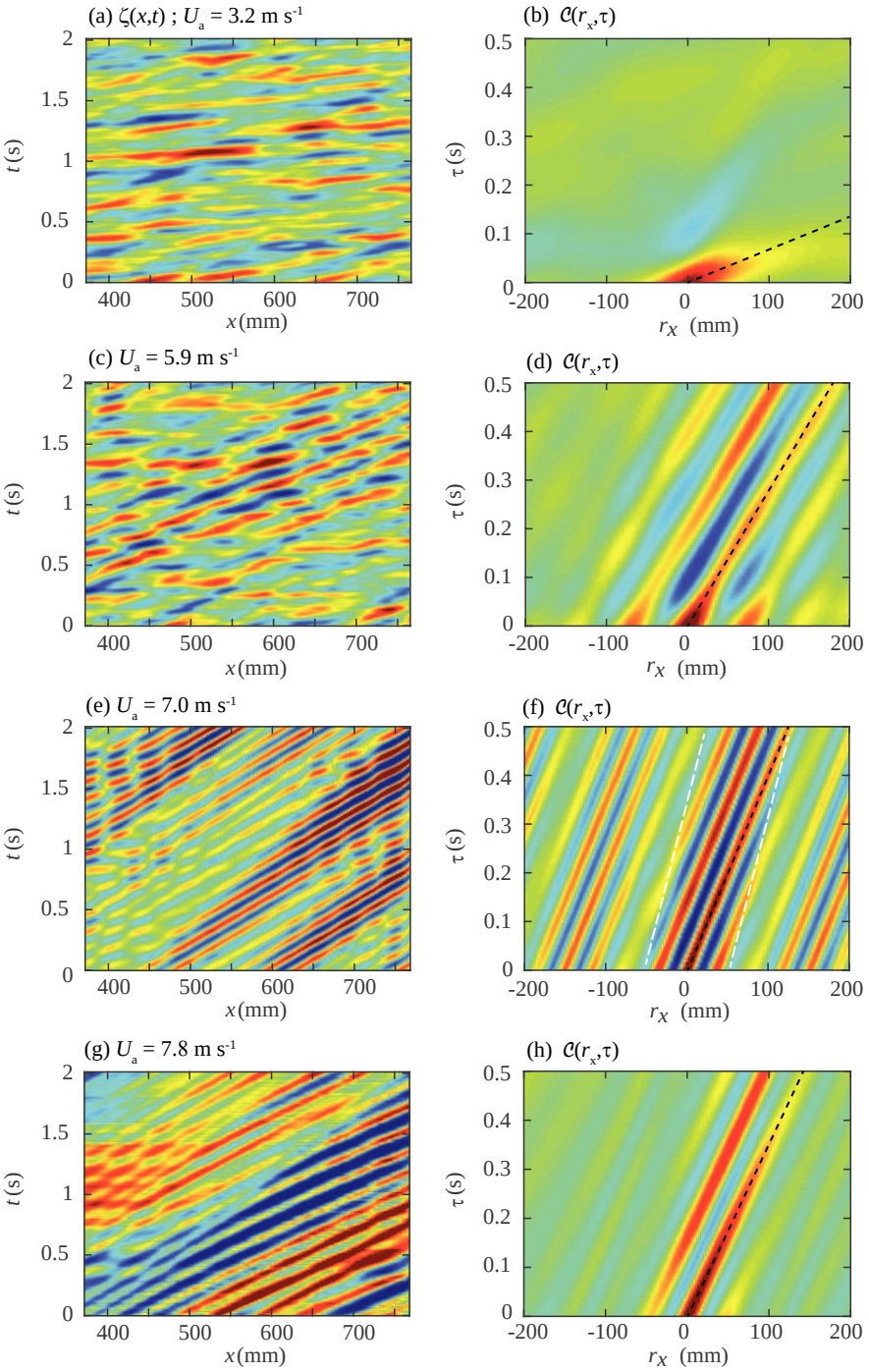

Figure 3.9: (a,c,e,g) Spatio-temporal diagrams $\zeta(x,t)$ taken along the line $y = 0$. Same velocities and scales as in figure 3.1. (b,d,f,h) Corresponding longitudinal spatio-temporal correlation $\mathcal{C}(r_x, \tau)$ (Eq. (3.2.11)). Colormap is $[-1, 1]$ from blue to red. The black dashed line shows the convection velocity V_{conv} (Eq. (3.2.12)). In (f), the two white dashed lines show the group velocity $c_g = 0.16$ m.s^{-1} corresponding to the observed wavelength $\lambda = 37$ mm, which delimit the wave packets.

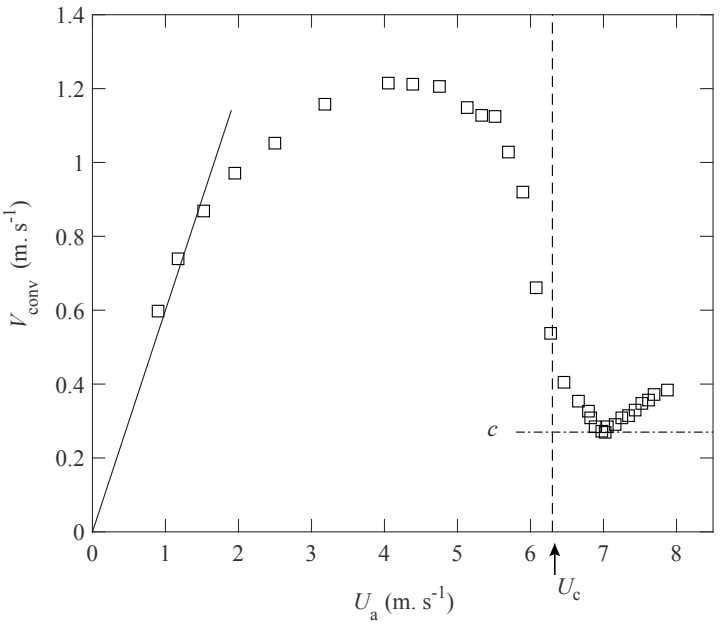

Figure 3.10: Convection velocity $V_{\text{conv}} = \Lambda_x/\text{T}$, averaged over $x \in [700, 1090]$ mm, as a function of the wind velocity U_a. The continuous line shows $V_{\text{corr}} = 0.6U_a$. The vertical dashed line indicates the onset of wave growth at $U_c = 6.3$ m.s^{-1}, where the growth rate β transitions from zero to positive values. The horizontal dashed line shows the local phase velocity $c = 0.27$ m.s^{-1} corresponding to the local wavelength $\lambda = 44$ mm.

by the characteristic velocity of the pattern. As a consequence, the characteristic velocity, referred to as the convection velocity, can be defined as:

$$V_{\text{conv}} = \frac{\Lambda_x}{\text{T}}, \tag{3.2.12}$$

with Λ_x and T the first value such that $\mathcal{C}(\Lambda_x/6, 0) = 1/2$ and $\mathcal{C}(0, \text{T}/6) = 1/2$, respectively. Similarly to the correlation length, the convection velocity could be defined with different factors. Here, Λ_x and T are defined such that they corresponds to the wavelength and period for monochromatic waves, in which case the convection velocity V_{conv} is simply the phase velocity.

The convection velocity is represented by a black dashed line in the spatio-temporal correlation in figure 3.9 and is plotted as a function of the wind speed U_a in figure 3.10. It is found that at very small velocity, V_{conv} increases approximately linearly as $V_{\text{conv}} \simeq 0.6U_a$, until $U_a \sim 2$ m.s^{-1}. This evolution is remarkably similar to the one of the convection velocity of the pressure fluctuations in turbulent boundary layers [Choi and Moin, 1990]. Let us recover the convection velocity from the characteristics of the turbulent airflow close to the interface. In a turbulent boundary layer, the maximum of pressure fluctuation is located at about $z_m/\delta_\nu \simeq 20 - 50$ (see Fig. 3.7(left)). Following the logarithmic law in the inertial sublayer (Eq. 2.2.5), the mean velocity at this altitude is $u(z_m) \simeq (13 \pm 1)u^*$. Using the approximation $u^* \simeq 0.05U_a$, we obtain $u(z_m) \simeq (0.65 \pm 0.05)U_a$. This result suggests that the response of the interface to the moving pressure fluctuation is essentially instantaneous and local up to $U_a \simeq 2$ m.s^{-1}.

The convection velocity departs from the linear growth $0.6U_a$ at wind velocity larger than 2 m.s^{-1} and saturates at $V_{\text{conv}} \simeq 1.2$ m.s^{-1}. This saturation is possibly the conse-

quence of the high viscosity of the liquid: the viscous damping prevents the surface from having an instantaneous response to the turbulent fluctuations because of the too rapid propagation of the pressure disturbances. As the wind speed is further increased, the convection velocity decreases down to $c \simeq 0.27$ m.s^{-1}, matching the expected phase velocity of free waves of the observed wavelength. Note that this decrease does not correspond to the wrinkles slowing down. It is rather due to an average over the rapid wrinkles propagating at velocities of about 1.2 m.s^{-1} and the slow transverse waves at velocity of about 0.27 m.s^{-1}. As the wind velocity increases, the interface is less and less dominated by the wrinkles and progressively features predominantly the transverse waves, leading to a decreasing average velocity. Finally, from $U_a \sim 7$ m.s^{-1}, the convection velocity increases again, in accordance with the wavelength increase in figure 3.6. It should be noted that these increases of wavelength and convection velocity do not necessarily occur at shorter fetches. This implies that at high wind velocity, the wave characteristics may change with fetch. This phenomenon is similar to the wavenumber and frequency downshift observed at sea [Dias and Kharif, 1999] and suggests that nonlinear effect are not negligible anymore. These evolutions of the wave characteristics with fetch will be described and discussed in the next chapter.

3.3 Conclusion

This chapter presents the results of an experimental investigation of the surface deformation of a viscous interface by a turbulent airflow for a given viscosity. The data obtained by FS-SS shows the existence of two regimes of deformation of the liquid-air interface.

In the first regime, at low wind velocity, rapidly propagating disorganized perturbations elongated in the streamwise direction are observed. These wrinkles have a small amplitude (< 10 μm) that increases approximately linearly with the wind velocity but is almost independent of fetch. At larger wind velocity, above a certain threshold, the surface is dominated by well-defined transverse waves propagating downstream. The crests of these gravity-capillary waves are nearly perpendicular to the wind direction but with some dislocations close to the center line. Contrary to the wrinkles, these waves are of a larger amplitude (from a dozen microns to a few millimeters) and grow with the downwind distance from the beginning of the tank. At small fetch, this evolution agrees with an exponential growth but the growth slows down at larger fetch. Using the exponential growth rate measured at small fetch, a critical velocity can be accurately defined as the velocity where the growth rate becomes positive.

The experimental data suggest that the wrinkles are traces on the interface of the pressure fluctuations in the turbulent boundary layer above the surface. This is confirmed at low wind velocity by the comparison of the spatial structures and spatio-temporal dynamics of the surface deformation and those of the pressure fluctuations advected by the turbulent airflow. However, quantitative validation is achieved only at very low wind speed. At higher velocity, the interface response changes, probably due to the viscous response time of the surface to too rapidly traveling pressure perturbations. The FS-SS acquisitions also indicate that at the transition between the two regimes, both wrinkles and waves are present. The following picture has been proposed: below the critical velocity, waves are locally excited by the wrinkles but are spatially damped. The presence of these evanescent waves results in the smooth transition relatively to wind speed of the characteristic amplitude, lengths and velocity associated with the surface deformation. Interestingly, the seed noise for the growth of the waves above onset seems not to be governed by the wrinkles. It appears instead to depend on the perturbations at the inlet

boundary condition at zero fetch.

Note that the use of a highly viscous liquid in these experiments implies that certain results may be specific to this system and irrelevant in the context of an air-water interface. For example, the fact that the wrinkles at low wind velocity are compatible with the instantaneous and local response of the interface to the pressure fluctuations in the boundary layer may not hold at lower liquid viscosity. Indeed, in the case of a liquid of lower viscosity, one would expect the surface deformation at a given location to also depend on the perturbations emitted elsewhere on the surface at previous times. The influence of the liquid viscosity on the wrinkles regime and wave onset is later explored in chapter 5.

Summary:

- FS-SS measurements of the response of a viscous interface to a turbulent wind shows the existence of two regimes of surface deformation that we call the wrinkles regime and the wave regime.
- At low wind velocity, the surface is perturbed by small-amplitude elongated streamwise wrinkles that do not grow with fetch. The wrinkles can be interpreted as the imprints on the viscous interface of the pressure fluctuations in the turbulent boundary layer above the surface.
- At higher wind velocity, beyond a critical velocity, well-defined transverse waves propagate downstream. Their amplitude grows exponentially with fetch over a certain distance, before nonlinearities are not negligible anymore and this spatial growth slows down at higher fetch.
- The separation between the wrinkles and wave regimes can be accurately defined by the velocity at which the spatial growth rate becomes positive. However, there is a significant range of velocity where wrinkles and waves cohabit. Experimental results suggest that transverse waves are locally excited by the wrinkles that are amplified and grow only past the critical velocity.

Chapter 4

Nonlinearities in the early growth of wind waves

In the previous chapter, we have shown the existence of two regimes of surface deformation by wind over a liquid thirty times more viscous than water. Depending on the wind velocity, the response of the air-liquid interface is different: at low wind speeds, the surface is populated with disorganized wrinkles of small amplitude that do not grow spatially; at high wind velocity, above a well defined velocity threshold, spatially growing quasi-2D gravity-capillary waves propagate at the interface. In this chapter, we focus on the nonlinear spatio-temporal behavior of these waves slightly above the onset.

4.1 Experimental observations

Experiments are realized in the same set-up and conditions as described in chapters 2 and 3. The liquid is a mixture of glycerol and water of density $\rho = 1.20 \times 10^3$ kg.m^{-3} and of kinematic viscosity $\nu = 30 \times 10^{-6}$ m^2.s^{-1}. The temperature of the liquid is maintained at 25.0 ± 0.5 °C. The threshold of wave generation for this mixture, as defined and measured in chapter 3, is $U_c = 6.3 \pm 0.1$ m.s^{-1}. The surface deformation $\zeta(x, y, t)$ of the interface is measured using the FS-SS method of visualization over series of 2000 images acquired at 40 Hz.

4.1.1 Direct observation of the effects of nonlinearities

As discussed in the previous chapter, one major difference between the wrinkles regime below onset and the wave regime above it is the evolution of the amplitude of surface deformation with fetch. While the wrinkles amplitude is approximately independent of the fetch, the transverse waves generated past the critical velocity U_c grow with the distance from the beginning of the tank (see figure 3.3 on page 63). At small fetch, the spatial wave growth is compatible with an exponential one but it slows down at larger fetch. As the wind velocity increases, the exponential growth is steeper but the region over which the growth is exponential becomes smaller and smaller. The wave growth is clearly visible in figure 4.1 which shows the FS-SS reconstruction of the interface for two wind velocities in the wave regime, at 6.6 m.s^{-1} and 7.8 m.s^{-1}. In addition to that, figure 4.1 also shows the evolution along the tank of the wave pattern. At 6.6 m.s^{-1}, slightly above the onset, the waves remain globally aligned with each other and the wavelength varies very little with fetch. However, further away from the wave generation threshold, at 7.8 m.s^{-1}, the

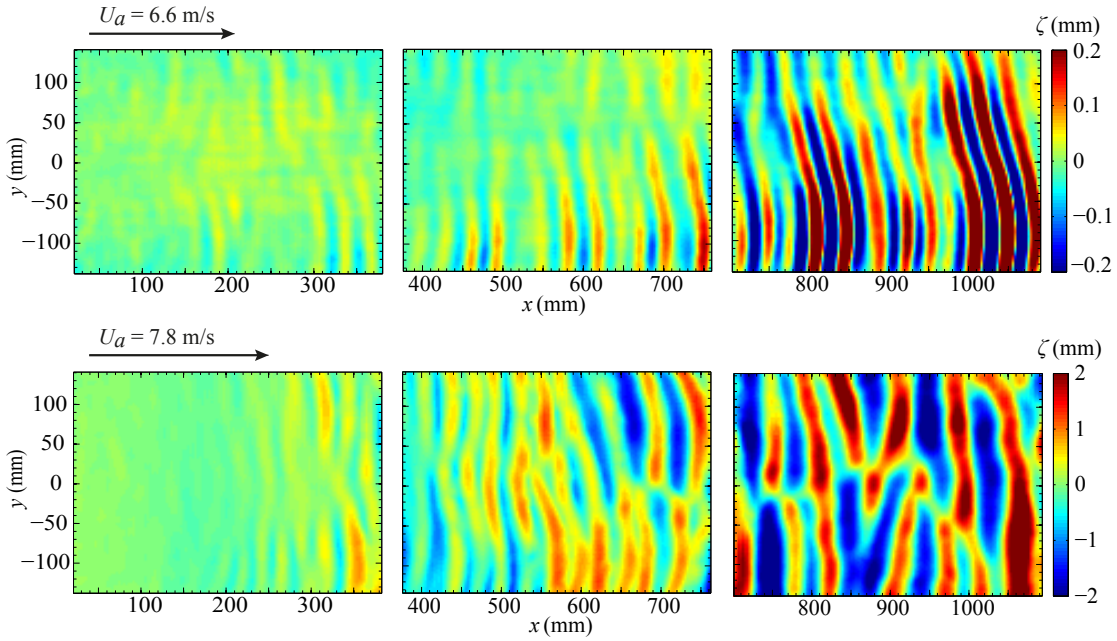

Figure 4.1: Surface height $\zeta(x, y, t)$ for two wind velocities $U_a = 6.6$ m.s^{-1} (top) and $U_a = 7.8$ m.s^{-1} (bottom). Wind is blowing from left to right. The acquisition over each portion of fetch is taken during a different experimental run. Note that the color map is the same on a row but varies between the two rows (the same color represents a deformation amplitude ten times greater on the second row compared to the first row).

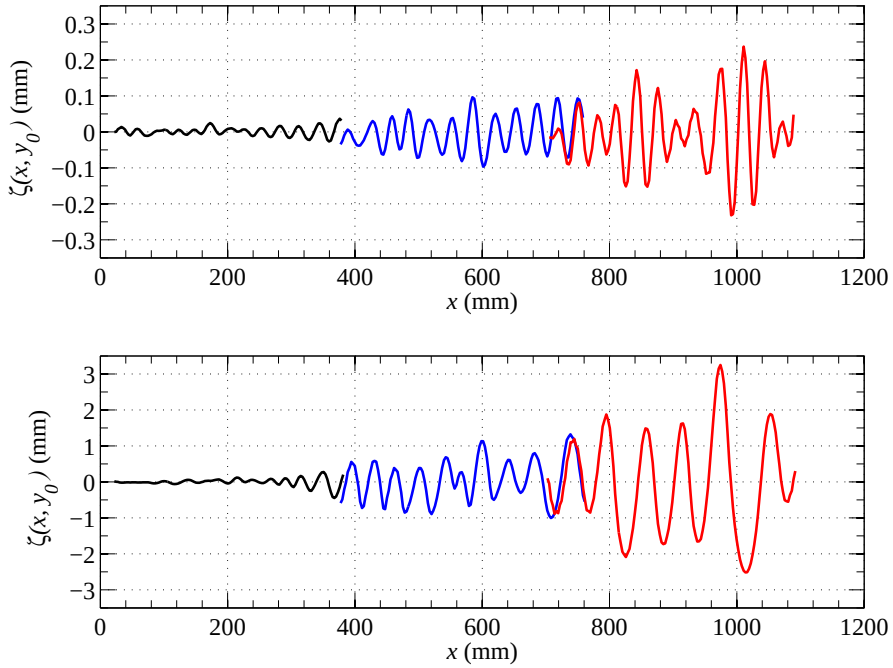

Figure 4.2: Cuts of the surface fields along the line $y_0 = -50$ mm for two wind velocities $U_a = 6.6$ m.s^{-1} (top) and $U_a = 7.8$ m.s^{-1} (bottom). Note the change in scale by a factor of 10 between the vertical axes of the two plots. The acquisition over each portion of fetch is taken during a different experimental run, represented by the three different colors.

wavelength distinctly increases with the downstream coordinate x and more dislocations are visible.

These evolutions with fetch imply that nonlinearities can significantly affect the wind waves behavior in our system for a fetch or wind velocity great enough. Nevertheless, it should be noted that the shape of the waves (as observed by a cut along a line of constant y, see figure 4.2) is not visibly affected by these nonlinearities. Unlike waves about to break [Tulin, 1996] [Siddiqui and Loewen, 2007] [Babanin, 2011], the front-back symmetry of the waves in our set-up is conserved, whatever the fetch or wind velocity [1]. Clearly, no wave breaking or droplet atomization occur during our experiments.

4.1.2 Spatial evolution of the wavelength

In chapter 3, the characteristic length in the x direction of the surface fields (which is equal to the wavelength in the wave regime) was determined using a correlation function (see section 3.2.3 on page 65). While this method allows to evaluate the characteristic length at all wind velocities, it has the embedded limitation to require a field of computation of a great enough spatial extent, i.e. much larger than the characteristic length. As a result, it provides an *average* over this field and is not suitable for a detailed analysis of the spatial evolution of the characteristic length associated to the interface deformation. This is a problem in the wave regime where the wavelength clearly increases with fetch. Past the threshold, in the wave regime, we can use another method, a local one, to compute the wavelength of the transverse waves in presence.

Let us consider a signal $u(x,t) = u_0 e^{i\phi(x,t)}$ with a phase $\phi(x,t) = kx + f(t)$. The local wavenumber can be defined from the gradient of the phase of this signal [Pedlosky, 2003]:

$$\frac{\partial u}{\partial x} = i\left(\frac{\partial \phi}{\partial x}\right) u = iku \quad \Rightarrow \quad \left|\frac{\partial u}{\partial x}\right|^2 = k^2|u|^2.$$

In our case, the signal is the surface deformation $\zeta(x,y,t)$ and we can thus deduce the local wavelength from:

$$k(x) = \sqrt{\frac{\left\langle \left(\frac{\partial \zeta}{\partial x}\right)^2 \right\rangle_{y,t}}{\langle \zeta^2 \rangle_{y,t}}} \tag{4.1.1}$$

where the brackets correspond to a temporal and transverse averaging.

The local wavelength $\lambda_p(x) = 2\pi/k_p(x)$ is computed using equation (4.1.1) and is plotted in figure 4.3 (the index p stands for "predominant"). Generally speaking, it can be inferred from figure 4.3 that the local wavelength starts at the same value of about 40 mm at small fetch then quickly increases with fetch further downstream. This is particularly visible at the highest velocities where the wavelength at the end of the tank is doubled relatively to its value at short fetch. Nevertheless, this increase does not necessarily start from the very beginning of the tank: the higher the wind velocity, the sooner the local wavelength departs from its value at short fetch.

The only wind velocity for which this description does not apply is $U_a = 6.6$ m.s^{-1}, slightly above the wave generation threshold. At this wind velocity, the local wavelength is almost independent of fetch. The wavelength being approximately constant with fetch close to onset is consistent with linear waves propagating over a liquid with constant or low surface drift. Indeed, a surface drift independent of fetch does not change the wavelength, as the wave is advected as a whole, whereas in presence of surface drift evolving with fetch,

1. At least up to 7.8 m.s^{-1}, the highest wind velocity at which experiments were performed.

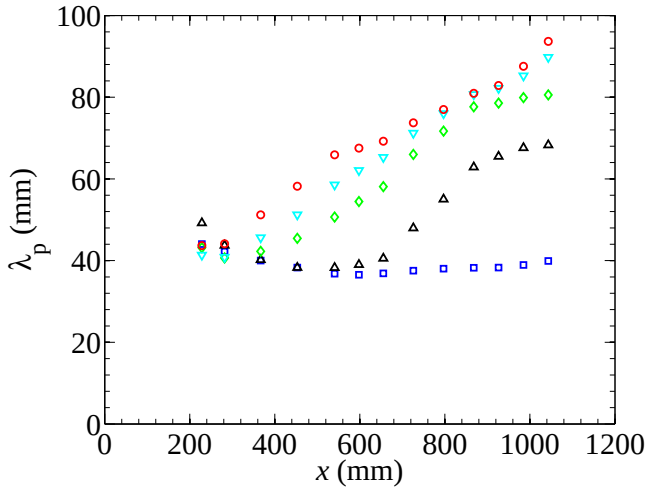

Figure 4.3: Measured predominant wavelength $\lambda_p(x)$ as a function of fetch x for the wind velocities $U_a = 6.6$ (□), 6.9 (△), 7.2 (◇), 7.5(▽) and 7.8 m.s^{-1}(○). In theory, the local wavelength can be measured with the same spatial resolution in the x direction as the FS-SS method. In practice, the wavelength is averaged over 10 data points (2.5 cm in the streamwise direction).

the wavelength can be streched or compressed [Lighthill, 1978]. However, if at all fetches the surface drift remains weak compared to the characteristic phase velocity, the change of wavelength will be small. The influence of surface drift on the wave characteristics will be developed in further detail in section 4.2.1.

Note that if equation (4.1.1) allows to locally measure the wavelength, the very fact that this method is local makes it more sensitive to small defects. To minimize this problem, the surface fields are slightly smoothed before the computation of the wavelength by a 2D convolution with a Gaussian kernel of half-peak width 1.5 mm. As it is obvious that the smoothing can negatively impact the wavelength measurements if applied too strongly, it has been verified that the results of the computation were approximately the same for a range around the parameters chosen for the smoothing, validating these parameters.

4.1.3 Spatial evolution of the dominant frequency

The temporal spectrum $E(f)$ of the waves is also measured at a particular fetch x by using the FS-SS data averaged in the transverse direction y and restricted over the narrow range $[x - \Delta x/2, x + \Delta x/2]$ with $\Delta x = 6$ cm. The temporal spectra obtained at two different wind velocities above the wave generation threshold are presented in figure 4.4. It is found that the wave spectra display a broad peak centered around a certain frequency. This peak frequency f_p can be retrieved by fitting the spectrum with a Gaussian function over the frequency interval [3, 9] Hz (continuous lines in Fig. 4.4):

$$E(f,x) = E_0(x) \exp\left[-\frac{(f - f_p(x))^2}{2\sigma^2(x)}\right] \tag{4.1.2}$$

Figure 4.5 presents the evolution of this dominant frequency with fetch. While f_p is approximately constant with respect to fetch close to wave onset, it is a decreasing function of the fetch for greater wind velocities. As the same time, the energy density associated

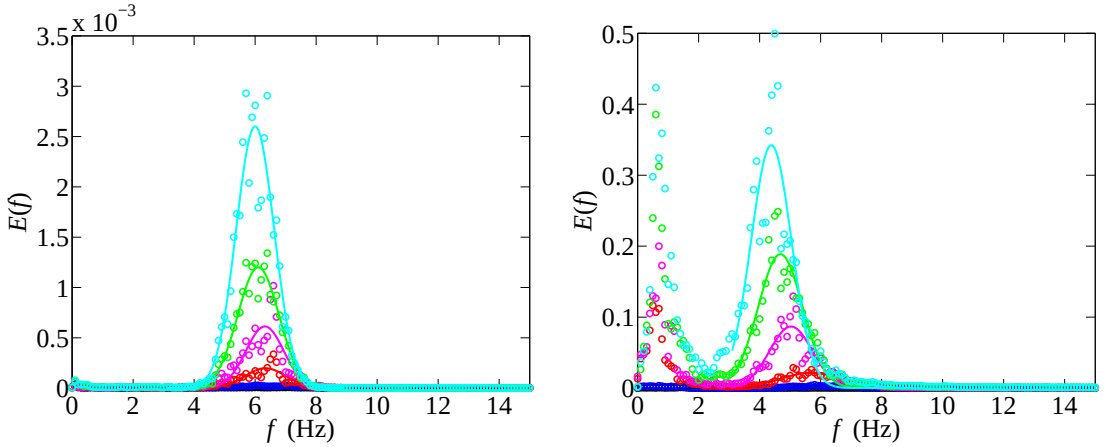

Figure 4.4: Power spectra of the surface elevation at fetch $x = 28$, 48, 65, 81 and 98 cm (from bottom to top), at wind velocity $U_a = 6.6$ m.s^{-1} (left) and $U_a = 7.8$ m.s^{-1} (right). Note that the vertical scale is different between the two graphs. The continuous lines are Gaussian fits applied to the data.

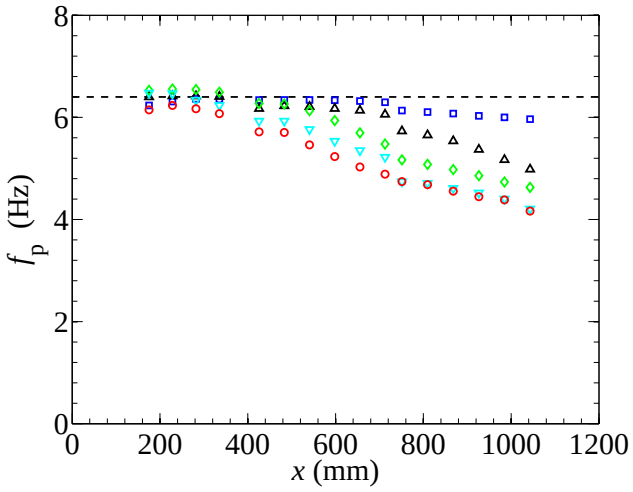

Figure 4.5: Measured dominant frequency $f_p(x)$ as a function of fetch x for the wind velocities $U_a = 6.6$ (□), 6.9 (△), 7.2 (◊), 7.5(▽) and 7.8 m.s^{-1}(○).

with this dominant frequency grows with fetch. This phenomenon of decreasing dominant frequency with fetch is often observed experimentally and is classically called "frequency downshift" [Dias and Kharif, 1999] (more details in the next section). Note however that at short fetch and for all wind velocities, the predominant frequency remains approximately at the same value of 6.4 ± 0.2 Hz.

The evolution with fetch of the dominant frequency is much slower than the relative change in local wavelength. At the highest wind velocity ($U_a = 7.8$ m.s^{-1}), where the nonlinear effects are expected to be the greatest, the dominant frequency decreases from 6.2 to 4.2 Hz in a meter of fetch, which represents a decline of about 30 % from its initial value. Over the same distance at the same wind velocity, the wavelength more than doubles, rising from 44 to 95 mm.

It can be noted that some of the temporal spectra present unusual amounts of energy at very low frequency $f < 2$ Hz (see Fig. 4.4 (right)). The reason for this phenomenon is yet unknown.

4.1.4 Measurement of the growth rate of each frequency

The spatial growth rate of the amplitude of the surface deformation $\beta_f(f)$ associated with each frequency f can be measured directly from the temporal spectra obtained at various fetches (as in Fig. 4.4). To do so, the amplitude of each frequency in the spectrum $E(f)$ is measured at different x and is fitted by an exponential law:

$$E(f) = E_{x=0}(f) \exp\left[\beta_f(f) x\right] \tag{4.1.3}$$

Figure 4.6 gives examples of the spatial evolution of various modes between 3.4 and 9.4 Hz at $U_a = 7.2$ m.s^{-1}. These modes grow exponentially at the beginning of the tank. The fastest growing mode at small fetch is for $f = 6.4$ Hz. All modes corresponding to a larger frequency (see Fig 4.6 (right)) have a lower amplitude at all fetch. However, some modes at slightly smaller frequency than f_c become more energetic at larger fetch ($x > 600$ mm, see Fig 4.6 (left)). Indeed, the amplitude of a mode that grows at the beginning of the tank may saturate or even decay past a certain fetch. As a consequence, the exponential fit is valid only in a certain range of x. In practice, the amplitude of each mode is fitted in the same range $x = 150 - 350$ mm, the largest interval of x over which an exponential fit is possible for all modes and all wind velocities for which the measurement is done. This is consistent with the fact that the exponential growth of the global *wave* amplitude is restricted to small fetch ($x < 400$ mm, see figure 3.3 on page 63).

The evolution of the measured β_f with frequency is shown in figure 4.7 for five wind velocities above the wave onset, and for f ranging from 1.5 to 14 Hz. For all wind velocities, β_f can be fitted by a parabolic function between 4 and 9 Hz (continuous lines in Fig. 4.7). This parabolic form of the modal growth rate is consistent with the expected general characteristics of a threshold instability, i.e. governed by a control parameter (in our case the wind velocity U_a) [Charru, 2011]. However, outside the 4-9 Hz interval, the evolution of β_f is less easily interpreted and not fully understood. Indeed, at lower frequencies, the measured modal growth rate derives from the unexpectedly large amount of energy in the temporal spectra, while at higher frequencies, it comes from the appearance of the first harmonics of the predominant frequency f_p.

Between 4 and 9 Hz, the mode f_c at which the growth rate is maximal (the most unstable mode) is almost the same for all wind velocity: $f_c \simeq 6.4$ Hz (see Fig. 4.8 (left)). Extending the parabolic fit outside the interval over which it is performed allows to estimate the range of unstable modes at each wind velocity. This range Δf of unstable modes

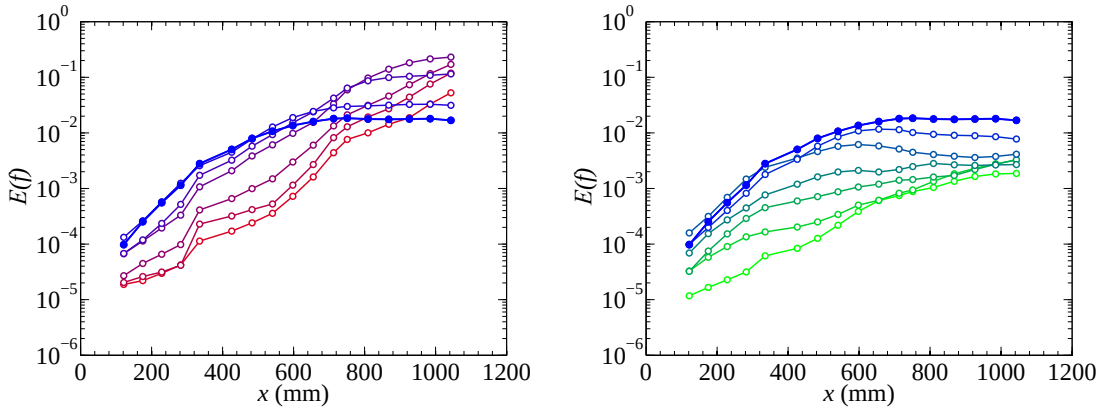

Figure 4.6: Spatial evolution of the amplitude of various modes at wind velocity $U_a = 7.2$ m.s^{-1}. The frequencies associated with these plots vary from one to the next with a step of 0.5 Hz: (left) from 3.4 to 6.4 Hz, the colors of the lines and symbols shifting continuously from red to blue, (right) from 6.4 to 9.4 Hz, with a color shift from blue to green. On both plots, the filled symbols (●) correspond to $f = 6.4$ Hz. For a better readability, the data presented in this figure is smoothed over a running average over three points. However, the exponential fits performed for the computation of the modal growth rate $\beta_f(f)$ are realized over the unsmoothed data (over $x \in [150, 350]$ mm).

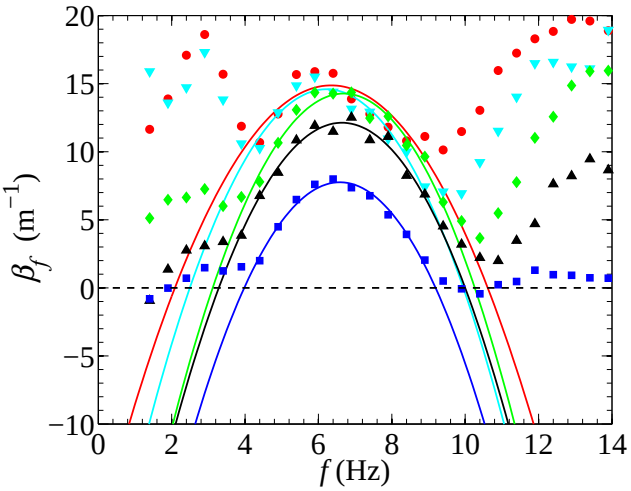

Figure 4.7: Plots of the growth rate $\beta_f(f)$ for the wind velocities $U_a = 6.6$ (■), 6.9 (▲), 7.2 (♦), 7.5 (▼) and 7.8 m.s^{-1} (●), measured from the temporal spectra obtained experimentally. The continuous lines correspond to parabolic fits performed for f between 4 and 9 Hz.

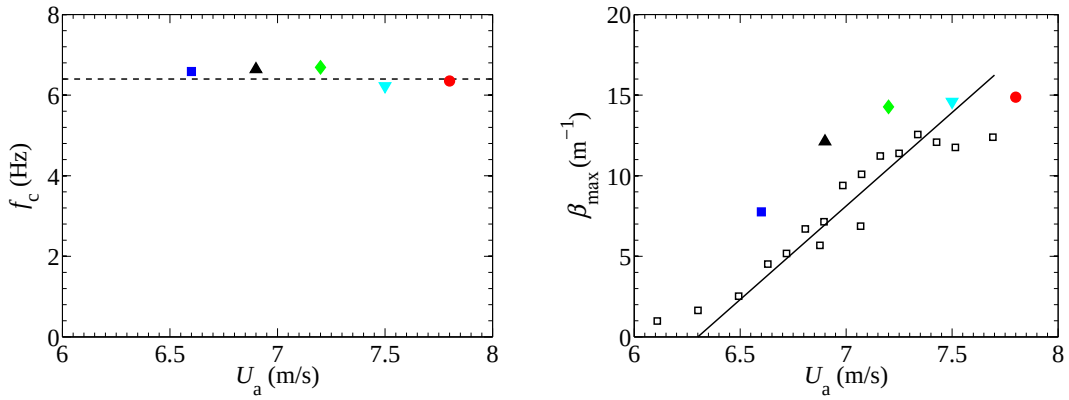

Figure 4.8: (Left) Frequency f_c corresponding to the maximal growth rate as a function of wind velocity. The dashed line indicates $f_c = 6.4$ Hz. (Right) Evolution of the maximal growth rate $\beta_{\max}$ with wind velocity. The black squares (□) correspond to the spatial growth rate of the global wave amplitude obtained by FS-SS measurements (see section 3.2.2 on page 62) and the continuous line is the associated linear fit $\beta = b(U_a - U_c)$ (Eq. (3.2.7)). For both plots, the filled symbols correspond to the same velocities as in Fig 4.7.

appears quite large, even at the smallest wind velocity, at only 5% above the threshold velocity (for $U_a = 6.6$ m.s^{-1}, we have $\Delta f/f_c \simeq 80$ %). As the wind velocity increases, the maximal growth rate increases. At the same time, the range of unstable modes seems to widen, although the evolution of β_f outside the interval of the parabolic fit makes it difficult to reach a definite conclusion.

Figure 4.8 (right) presents the growth rate associated to the frequency f_c as a function of the wind velocity, that is to say the maximal growth rate $\beta_{\max}$ for a given U_a. Comparing it to the growth rates obtained in chapter 3 by the direct measurement of the spatial growth of the global wave amplitude, we can see the $\beta_{\max}$ is always larger than this measured spatial growth rate, whenever the comparison is possible. This is not surprising as $\beta_{\max}$ represents the maximal growth rate associated of a *single* mode (by definition the most unstable mode) while the spatial growth rate measured in chapter 3 is related to the "effective" growth of the overall wave, associated to all the excited modes.

4.1.5 Spatial evolution of the phase velocity

In order to analyze the spatio-temporal dynamics of the waves above the threshold, another wave characteristic, the phase velocity, can be explored. We compute the "local" phase velocity as the product of the measured dominant wavelength and frequency:

$$c(x) = \lambda_p(x) f_p(x). \tag{4.1.4}$$

This velocity is in fact more of a *pseudo* phase velocity, as a phase velocity is only rigorously defined for a monochromatic wave. However, it gives an estimate of the local propagation velocity of the waves at a certain fetch. The local phase velocity obtained from equation (4.1.4) is presented in figure 4.9. The evolution of $c(x)$ is less straightforward that those of the local dominant wavelength and frequency. Nevertheless, a few trends can be observed.

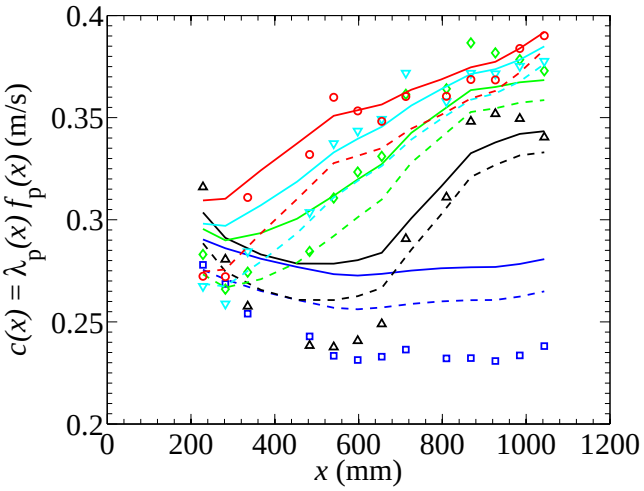

Figure 4.9: Local phase velocity $c(x)$ as a function of fetch for the wind velocities $U_a = 6.6$ (□), 6.9 (△), 7.2 (◇), 7.5(▽) and 7.8 m.s^{-1}(○) (Eq. 4.1.4). The lines present the corresponding phase velocity computed from the dispersion relation for free waves of wavelength $\lambda_p(x)$ without (dashed lines) and with (continuous lines) the correction due to the drift current (Eq. 4.2.5).

At small fetch, the local phase velocity is roughly the same for all wind velocities. At the two wind velocities closest to the velocity threshold ($U_a = 6.6$ and 6.9 m.s^{-1}), the local phase velocity decreases with fetch then becomes approximately constant (for $U_a = 6.6$ m.s^{-1}) or start to grow (for $U_a = 6.9$ m.s^{-1}). At higher wind velocities, c simply increases with fetch without the initial decline. Note that precisely at small fetch and slightly above the velocity threshold, the presence of wrinkles can affect the measurement of the wavelength. In particular, it is slightly visible on the plot of the wavelength as a function of fetch (Fig. 4.3) at the lowest wind velocity $U_a = 6.6$ m.s^{-1}. At this wind velocity, the wavelength is almost independent of fetch but with a slight initial decline at short fetch. As the predominant frequency is highest at small fetch, this decrease is amplified and more visible when the local phase velocity is plotted (Fig. 4.9).

At higher wind velocity, the quick increase of $\lambda_p(x)$ and the moderate decline of $f_p(x)$ in the downstream direction result in an increasing local phase velocity $c(x)$. For example, at wind velocity 7.8 m.s^{-1}, the local phase velocity increases by more than 40%.

The phase velocity $c_0(x)$ computed from the inviscid linear dispersion relation for free waves (Eq. 1.1.5) of wavelength $\lambda_p(x)$ is also plotted in dashed lines in figure 4.9 (the effect of the drift current will be discussed in the next section). Generally speaking, c_0 is smaller than c, except at the first wind velocity above wave onset $U_a = 6.6$ m.s^{-1}, where it is significantly higher. One would have expected the propagation velocity of wind waves to be greater than the phase velocity of free waves, due to the wind "pushing" the waves. However, that the opposite occurs slightly above onset is quite surprising and at the present time unexplained.

4.1.6 Spatial evolution of the local slope of the wave

As both the wave amplitude and the dominant wavelength increase with fetch, the wave slope, which combines the two, is an interesting quantity to look at to further characterize

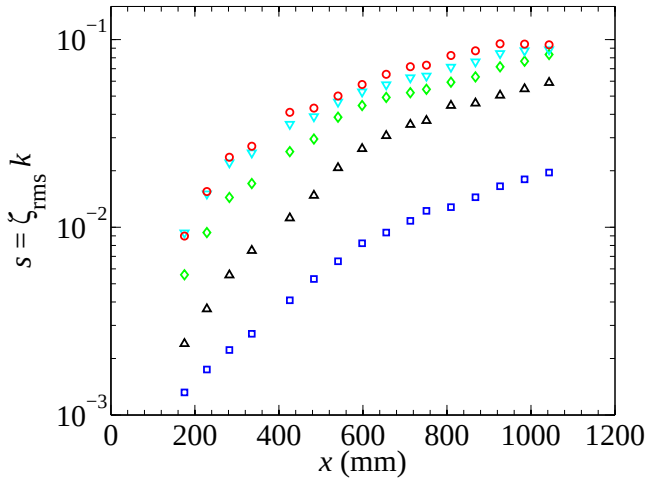

Figure 4.10: Evolution of the estimated typical local slope $s(x) = \zeta_{\rm rms}(x)k_p(x)$ with fetch for the wind velocities $U_a = 6.6$ (□), 6.9 (△), 7.2 (◇), 7.5(▽) and 7.8 m.s^{-1}(○).

the waves evolution. In order to obtain the local wave slope, a rigorous approach would require to filter the wave height ζ at the wavenumber k to get the wave amplitude ζ_k associated to this particular mode and define the slope as $s_k(x) = \zeta_k(x)k(x)$. However, if we suppose that the wave amplitude is governed by the predominant wavelength $\lambda_p(x) = 2\pi/k_p(x)$, we can estimate the typical local slope from the measurements of the local wave amplitude $\zeta_{rms}(x)$ and the local wavenumber $k_p(x)$ as:

$$s(x) = \zeta_{rms}(x)k_p(x) = 2\pi\frac{\zeta_{rms}(x)}{\lambda_p(x)}. \tag{4.1.5}$$

The evolution of this local slope with fetch is displayed in figure 4.10. The typical wave slope increases with fetch at all wind velocities. The higher the wind velocity, the slower the increase at large fetch, leading eventually to a saturation at $s_{\max} \simeq 0.10$.

This saturation in slope, as well as the evolution with fetch of the other waves' characteristics presented in this section, can be related to similar results from the literature. In the next section, these evolutions with fetch will thus be discussed in the context of various arguments from the wind waves literature.

4.2 Evolution of wave characteristics: discussions

The experimental results presented in the previous section show nonlinear effects impacting the wave characteristics: the dominant frequency undergoes a downshift with fetch while the wavelength and phase velocity increase. Such evolutions are often reported in the literature. Indeed, frequency downshift is very commonly observed at large fetch at sea or during wind waves experiments over water [Hidy and Plate, 1966] [Plate and Hidy, 1967] [Plate et al., 1969] [Plant and Wright, 1977] [Mitsuyasu and Rikiishi, 1978] [Bliven et al., 1986] [Caulliez and Collard, 1999] [Veron and Melville, 2001] [Waseda et al., 2001] [Caulliez et al., 2008] [Liberzon and Shemer, 2011] [Longo, 2012] [Zavadsky et al., 2013]. The wavelength is also often observed to be increasing with fetch [Keulegan, 1951] [Hidy and Plate, 1966] [Caulliez and Collard, 1999], and so does the phase velocity [Hidy and Plate, 1966] [Liberzon and Shemer, 2011] [Longo, 2012] [Zavadsky et al.,

2013]. Increase followed by saturation of the wave amplitude or wave steepness are frequently stated too [Lake and Yuen, 1978] [Caulliez and Collard, 1999] [Caulliez et al., 2008] [Longo, 2012]. It is however important to note that these nonlinearities are usually recorded in longer tanks or outdoors, over significantly larger fetches. In our case, likely because of the higher viscosity of the liquid, these evolutions of the waves characteristics already occur unmistakably at somewhat small fetch ($x < 1$ m) and small velocity ($(U_a - U_c)/U_c < 5\%$).

If these symptoms of the nonlinearities, in particular the frequency and wavenumber downshift, are well-documented, the underlying origins of these phenomena have not been clearly explicited yet. Numerous attempts have been made to clarify the sources of these evolutions and different arguments can be found in the literature [Dias and Kharif, 1999]. In this section, we review possible explanations and discuss them in the context of our experiments. First, the corrections to apply to the free waves dispersion relation in the case of wind waves are explored; second, different approaches to the frequency downshift are reviewed.

4.2.1 Modification of the dispersion relation

The free waves dispersion relation applies, by definition, to waves propagating without forcing. As wind waves do precisely include a forcing, this dispersion relation may not hold. If the actual dispersion relation verified by wind waves comprises a spatial evolution, this can partly explain the downstream evolution of the wave characteristics. In the following section, different possible modifications of the inviscid free linear waves dispersion relation are discussed.

- **Effect of the viscosity of the liquid:**

  As discussed in chapter 1, the viscosity of the liquid can modify the dispersion relation (see § 1.1.3 on page 9)). Lamb's correction can be written as [Lamb, 1995] [Padrino and Joseph, 2007]:

  $$c_{\text{visc}} = \sqrt{c_0^2 - \nu^2 k^2}, \tag{4.2.1}$$

  where c_0 denotes the phase velocity associated to free linear waves over an inviscid liquid. Note that this equation is the same as Eq. (1.1.7) on page 9 written in a slightly different form. In the case of our liquid, this correction reaches only 0.2 % at the most (see § 3.1 on page 57): the effects of the liquid viscosity are therefore negligible. In any case, this correction would not have explained the spatial evolution of the wavelength and frequency.

- **Nonlinear dispersion relation:**

  Another possible explanation for the evolution of the phase velocity is the modification of the free waves dispersion relation due to nonlinear effects. Based on the equations given by [Babanin, 2011] and [Newman, 1977] (which give the same results at first order), we have:

  $$c_{\text{NL}} = c_0(1 + a^2k^2), \tag{4.2.2}$$

  where a is the wave amplitude. In our case the typical slope s saturates at 0.10, so the correction factor $a^2k^2 \simeq s^2$ only reaches 1 %, considerably below the 40 % increase that can be observed for $c(x)$ over a meter of fetch at $U_a = 7.8$ m.s^{-1}. As a consequence, the nonlinear effects on the dispersion relation cannot explain the evolution with fetch of the phase velocity.

- **Effect of surface velocity:**

  Because of the wind action at the interface, a drift current develops in the liquid. The effect of the surface current can be an argument to explain the evolution of wind wave with fetch [Liberzon and Shemer, 2011]. An homogeneous current with fetch and depth, U_s, simply transports the wave at a modified phase velocity:

  $$c = c_0 + U_s. \tag{4.2.3}$$

  This equation remains valid for a depth-independent current slowly varying with fetch, but with U_s simply replaced by $U_s(x)$:

  $$c_s = c_0 + U_s(x), \tag{4.2.4}$$

  provided that $\frac{dU_s}{dx} \ll kU_s$. In that case however, the wave is not advected as a whole anymore and its characteristics can change with fetch. Indeed, a non-homogeneous surface drift can stretch or compress the wave, and therefore increase or decrease its wavelength. In the local frame of the liquid at rest, the wave frequency is conserved but not the wavelength because of the stretching of the wave at the interface [Lighthill, 1978]. This approach is particularly pertinent in the case of water, as drift currents can there be important, vary significantly in space but may be considered depth-independent on a certain liquid layer because of the turbulent character of the current. However, in our case of a highly viscous liquid, the surface drift is laminar and changes much more rapidly with depth than with fetch. Correcting the phase velocity by the surface velocity alone (either by equation (4.2.3) or (4.2.4)) leads to an over-evaluation of about 10 to 20% above the observed local phase velocity $c(x)$.

- **Effect of a current inhomogeneous with depth:**

  Even if the surface drift does not change much with fetch, the current in the liquid can still affect the wave propagation. Indeed, if the current is not constant with the depth of the liquid, its vorticity leads to a modification of the dispersion relation [Hidy and Plate, 1966] [Karageorgis, 2012] [Ellingsen and Brevik, 2014]. In our case, the mean velocity profile in the tank is parabolic with maximum drift at the surface (see section 2.2.2). The dispersion relation for such a velocity profile can be written as (see appendix of [Hidy and Plate, 1966] written by Lilly):

  $$c_s = c_0 + U_s \left(1 - \frac{2}{kh}\right), \tag{4.2.5}$$

  assuming that the surface drift U_s is small compared to c_0, which is the case in our experiments. The first term (U_s) corresponds to the simple transport of the wave as a whole (see previous paragraph) while the second term ($-2U_s/kh$) attenuates this transport if the wavelength considered "sees" the bottom of the tank. For a wavelength that is small relatively to the liquid depth, this term becomes negligible. Even though the high viscosity in our case results in the surface drift to remain relatively small (see Fig. 2.20), the corresponding correction to the phase velocity is not quite negligible: 2 to 13 % of c_0, depending on wind velocity and fetch. The phase velocity obtained with this correction from the measured wavelength is plotted in continuous lines in figure 4.9. Although the agreement is not quantitative, including this correction seems to better reconcile the observed local phase velocity and the phase velocity obtained through the dispersion relation, except for the lowest wind velocity.

Based on these considerations, it seems that the evolution of the phase velocity can be qualitatively explained by Lilly's correction of the linear inviscid dispersion relation of free waves due to the vorticity in the tank, and that the other corrections are negligible. However, note that all these modifications of the dispersion relation, first are intended for monochromatic waves; and second, impose that the wave frequency is conserved with fetch. In our case, as in the case of the more classical experiments in water, waves cannot be considered as monochromatic, especially when nonlinear effects arise, and the wave dominant frequency clearly decreases with fetch. The possible origins for this frequency downshift are addressed in the following section.

4.2.2 Frequency downshift with fetch: potential approaches

Many works of research have been devoted to the study of the downshift of wave frequency. The difficulty of the study of the spatial evolution of waves as they propagate start with the issue that even an initially monochromatic wave can be affected by significant changes during its propagation, due to energy transfers, even in absence of wind. Indeed, Benjamin and Feir have shown the existence of what is now called the Benjamin-Feir instability or sideband instability: monochromatic waves of small amplitude subjected to low-frequency perturbations evolve with fetch such that new peaks emerge on each side of the original spectral peak [Benjamin and Feir, 1967] [Dias and Kharif, 1999] [Charru, 2011]. These new frequencies in the wave spectra, located symmetrically on each sideband of the original peak frequency (hence the name sideband instability), induce a time-evolution of the wave train and a cyclic frequency downshift with fetch occurs. Such frequency downshift with fetch originating from this instability have been observed experimentally by [Lake et al., 1977] and [Melville, 1982] using mechanically-generated waves.

One important feature of this instability is that the system's response to the Benjamin-Feir instability, and in particular the frequency downshift, is strongly affected by the presence of wind. Indeed, the wind induces an asymmetric response of the upper and lower sidebands: the lower sideband (lower frequencies) grows at a faster rate than the upper sideband (higher frequencies) resulting in the downward shift of the spectral peak. Deriving a fourth-order evolution equation including wind forcing and dissipation, Hara & Mei show that the nonlinear development of the Benjamin-Feir instability, originally modulational in absence of wind, gives rise to a persistent frequency downshift in presence of wind [Hara and Mei, 1991] [Hara and Mei, 1994].

Since then, it has been speculated that the Benjamin-Feir instability is responsible for the frequency downshift for wind waves over water. This approach is however not fully endorsed [Dias and Kharif, 1999]. Indeed, the Benjamin-Feir instability corresponds to interactions that are predominantly two dimensional, which may not be a valid assumption, especially when the nonlinearities supposedly explained by the sidebands evolution become significant. Secondly, a more problematic issue is that the Benjamin-Feir instability is fundamentally based on the evolution of a *narrow* band of frequencies, which is far from being the case in wind waves systems where wind definitely excites a *broad* band of modes (see Fig. 4.7).

The nonlinear evolution of a quasi-monochromatic wave packet is generally described by one of a handful of equations. The most commonly used are the Ginzburg-Landau equation and the nonlinear Schrödinger equation [Tulin, 1996] [Huang et al., 1999] [Charru, 2011]. These equations are of the third order and the later is sometimes extended to the fourth order into Dysthe's equation [Dysthe, 1979], itself recently extended for weakly viscous liquid in [Carter and Govan, 2016]. Because the exact form of these equations depends on the exact system considered, especially through its invariances by translation

or reflection, they are not explicitly transcribed here. Their common characteristic is the existence of this third order term, necessary to express the saturation of the wave.

Indeed, in situ observations and laboratory experiments show that over large fetches, the slope of wind water waves saturates at a certain value between 0.1 and 0.2 [Lake and Yuen, 1978] [Caulliez and Collard, 1999]. This idea of the saturation of the wave steepness is underlying in some other arguments for the frequency downshift. The general view is the following. As the waves gradually gain energy from the wind and grow, they approach the limiting steepness, shift to lower frequency (or higher wavelength) which allows for the gain of more energy [Lake and Yuen, 1978]. This approach is consistent in the context of our experiments with the fact that the typical wave slope saturates while other waves characteristics like wavelength and frequency still evolve (see Fig. 4.3, 4.5 and 4.10).

Note that viscous dissipation may play a significant role in the slope limitation. Indeed, it has been proposed that the frequency downshift with fetch can be based on the balance between the energy received from the wind and the dissipation due to the liquid motion [Hidy and Plate, 1966]. The smaller waves grow more rapidly but the associated dissipation is also more pronounced. As a consequence, the lower frequencies continue to gain energy from the wind before reaching equilibrium, resulting in the observed frequency downshift. Due to the high viscosity of the liquid used in the experiments, it is not unlikely that dissipation is an important parameter in the nonlinear evolution of the waves characteristics.

4.3 Conclusion

In this chapter, experimental results focused on the wave regime are presented in order to study the spatial evolution of the waves characteristics. The experiments are conducted with the same viscous liquid and in the same conditions as in chapter 3, except for the length and acquisition rate of the recordings that where adjusted for better spatial and temporal analyses.

The dominant wavelength is computed using a local method and is observed to increase with fetch for wind velocity sufficiently greater than the wave generation threshold. The dominant frequency is measured as the peak frequency in the temporal spectrum computed over a short fetch interval. This locally predominant frequency decreases with fetch. The temporal analysis also allows to evaluate the growth of the energy in each frequency mode. It is found that the range of amplified modes is quite large, and that the fastest growing mode at short fetch is overrun at larger fetch by lower frequencies. The nonlinearities can also be noted through the increase with fetch of the phase velocity, although its debatable definition for non-monochromatic waves makes interpretations more difficult. The typical wave steepness increases with fetch as well, and eventually saturates in the case of the highest wind velocities.

This gradual shift with fetch from shorter waves of higher frequencies to longer waves of lower frequencies is commonly reported for wind waves over water, both in laboratory experiments and at sea. However, it should be noted that in our experiments, the frequency downshift is observed for much smaller wave amplitudes and much shorter fetches than in the literature. Despite this difference, different arguments from the literature are considered. The different possible modifications to the inviscid linear dispersion relation for free waves are discussed. Most corrections can be neglected, except the one due to the current in the liquid. Provided that the drift current is taken into account, it is found that the locally dominant wavelength and frequency qualitatively verify the corrected dispersion relation. Concerning the frequency downshift, different approaches from the literature

are reviewed but the question remains open.

Summary:

- Wind waves over a highly viscous liquid shows that nonlinearities can significantly affect the waves behavior even for waves of small amplitude propagating over short fetch, similarly to what can be observed for waves of larger amplitude over larger fetch.
- For wind velocity sufficiently greater than the wave generation threshold, the local wavelength increases with fetch while the dominant frequency decreases with fetch. The pseudo phase velocity obtained by the product of these predominant wavelength and frequency also increases spatially, as well as the typical wave steepness which eventually even saturates. The range of excited modes is found to be relatively large.
- The locally dominant wavelength and frequency seem to qualitatively verify the dispersion relation corrected to take into account the drift current.

Chapter 5

Wind waves over a viscous liquid: influence of the viscosity

In this chapter, we study the influence of the viscosity of the liquid on the initial stages of generation and growth of wind waves. The aim is to extend the results obtained at $\nu = 30 \times 10^{-6}$ m^2.s^{-1} in chapters 3 and 4 to different viscosities. The emphasis is put on the change of surface deformation amplitude and of the threshold wind velocity with respect to viscosity. We observe a new phenomenon at high viscosity and high wind velocity that is not present at $\nu = 30 \times 10^{-6}$ m^2.s^{-1}. This specific phenomenon occurs under the form of solitary waves of large amplitude. These waves are described in the last section of this chapter.

5.1 Experiments

5.1.1 Liquid mixtures

In chapters 3 and 4, the viscosity of the glycerol-water mixture that is used is of 30×10^{-6} m^2.s^{-1}. In this chapter, the viscosity of the liquid over which wind is blown changes from 0.9 to 562×10^{-6} m^2.s^{-1} in order to investigate the influence of viscosity on wind wave generation. While the initial intention was to only use differently concentrated glycerol-water mixtures, practical obstacles related to the chemical properties of highly concentrated aqueous glycerol mixtures lead to the use of an alternative product to reach very high viscosities.

Hygroscopic nature of glycerol

The viscosity of a glycerol-water solution is highly dependent on the concentration and temperature of the mixture, especially for a high concentration of glycerol (see Fig. 5.1). The more concentrated the mixture is, the greater the kinematic viscosity is, in an exponential way. A 99% glycerol-1% water mixture at 25°C is almost five times more viscous than a 90% glycerol-10% water solution at the same temperature (all percentages of concentration mentioned in this chapter are in weight). The evolution is reverse with temperature: the greater the temperature, the smaller the kinematic viscosity. For example, heating a 90% glycerol-10% water mixture from 20 to 30°C divides its viscosity by 2.

Therefore, starting with a pure glycerol solution and gradually diluting it with water seems like a practical and efficient way to repeat experiments in our set-up while reaching a wide range of viscosities. The problem with this strategy is the hygroscopic nature of

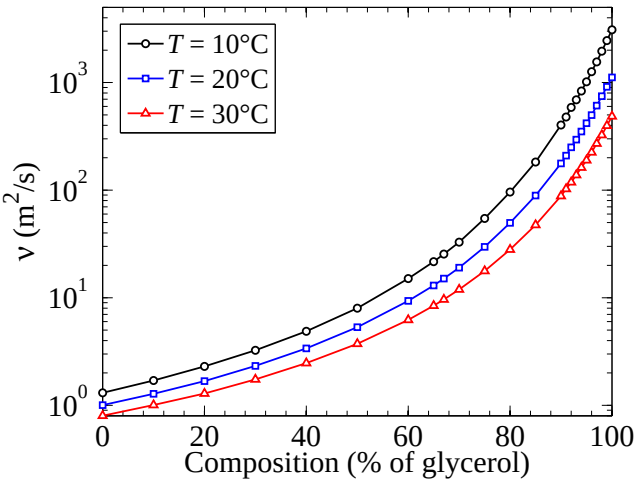

Figure 5.1: Kinematic viscosity of an aqueous mixture of glycerol as a function of the composition in weight, at temperature $T = 10$, 20 and 30 °C, plotted from data of [Segur and Oberstar, 1951].

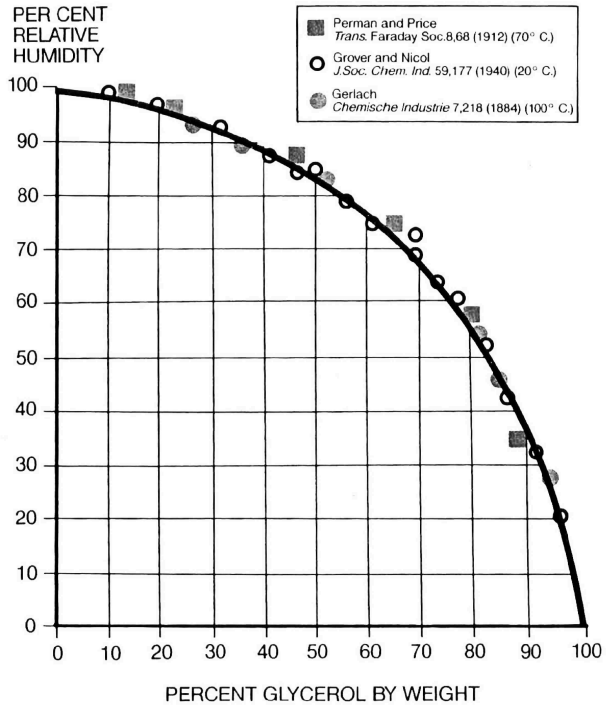

Figure 5.2: Relative humidity at equilibrium as a function of the concentration of glycerol when the exchange of water vapor between air and the solution is in balance (Fig. 1 in [Soap and Detergent Association, 1990]).

glycerol. An aqueous glycerol solution in an open container will absorb or reject water from the atmosphere until an equilibrium concentration of glycerol is reached [Soap and Detergent Association, 1990]. While this is considered an advantage in most of the applications of glycerol, it is a major inconvenience in our case. Since our set-up offers a large surface of exchange through the liquid-air interface, a highly concentrated solution of glycerol and water absorbs the moisture in the air via a slightly exothermic process and the density of the mixture changes significantly over the course of the few hours required for a series of FS-SS acquisitions. This out-of-equilibrium process leads to a significant change in viscosity and refractive index as well, making the FS-SS technique impossible to use and experimental results unexploitable.

The equilibrium concentration depends on the relative humidity of the environment (see Fig. 5.2). At the time of the experiments, the air ventilation kept the humidity level in the room between 45 and 50%. At this level of humidity, the equilibrium concentration is about 85%, a little over the 80% we used in chapters 3 and 4. Experimentally, we observed that the closer the composition is to the stable composition the slower this evolution is. We also noted that a solution above the stability concentration evolves much more quickly towards stability than solutions below stability. While a low concentration solution is stable enough to be used for months for FS-SS acquisitions (as long as the set-up is closed back when not in use, to avoid surface pollution), a highly concentrated solution comes to its equilibrium composition in only a few days. As a result, any glycerol-water mixture with a concentration higher than approximately 85% cannot be used for series of FS-SS acquisitions. To bypass this problem and access higher viscosities, we switched to mixtures of glucor and water instead of glycerol and water.

Glucor

Glucor 60/80HM (referred here simply as glucor) is a glucose syrup used in the food industry. Glucor is transparent with a faint yellow tint that does not interfere with FS-SS acquisitions. In pure or almost pure form, it is more than 10000 times more viscous than water. As for glycerol, aqueous solutions of glucor increases in viscosity with increased concentration or decreased temperature.

Highly concentrated mixtures of glucor and water are much more stable in time than highly concentrated mixtures of glycerol and water. Using glucor thus allowed to have access to liquids of higher viscosity that could be used during FS-SS experiments. A minor downside of this shift from glycerol to glucor is that glucor is a lesser known product than glycerol and unlike glycerol, most of its physical and chemical properties are not tabulated.

Mixtures' properties

A variety of differently concentrated mixtures of glycerol and water or glucor and water are used during the experiments. The composition, temperature T, density ρ, kinematic viscosity ν, surface tension γ and refractive index n of the different mixtures are listed in table 5.1 from least to most viscous. Density and temperature are measured as described in chapter 3 [1]. The kinematic viscosity and refractive index of the glycerol-water mixtures are the tabulated values at these obtained values of ρ and T. The kinematic viscosity of glucor-water mixture is measured by a rheometer Anton Paar Physica MCR 501 and the refractive index is obtained by refraction through the width of the set-up of a laser

1. Except for the glucor-based mixtures, for which a densimeter Anton Paar DMA 5000 is used instead of the densimeter Anton Paar DMA 35 used in chapter 3, due to the high viscosity of these liquids incompatible with the model DMA 35. The accuracy is the same for both models (0.001×10^3 kg.m^{-3}).

ray at different incidence angles. The surface tension is measured by a tensiometer Krüss DSA30S. Note that the temperature can be measured with a 0.1°C accuracy but the control on the temperature over the duration of an experiment is such that the difference between the maximal and minimal measured temperatures is higher than this value, but still remains below 1°C. As a more concentrated aqueous mixture of glycerol or glucor changes viscosity more quickly with temperature compared to a less concentrated mixture, this leads to a higher deviation from the mean viscosity in the various mixtures (labelled 1−10).

	Concentration in water	T (°C)	ρ ($\times 10^3$ kg/m^3)	ν ($\times 10^{-6}$ m^2/s)	γ (N/m^2)	n	Measurements
1	0% (pure water)	**24**	**0.997**	0.91 ±0.02	-	1.33	Laser
2	0% (pure water)	**20**	**0.998**	1.00 ±0.02	**0.072**	1.33	Laser + FS-SS
3	45% glycerol	**25**	**1.12**	3.9 ±0.1	**0.069**	1.39	Laser + FS-SS
4	67% glycerol	**25**	**1.17**	12 ±1	**0.067**	1.42	Laser + FS-SS
5	80% glycerol	**28**	**1.20**	23 ±1	-	1.44	FS-SS
6	80% glycerol	**25**	**1.20**	**30 ± 1**	**0.065**	1.44	FS-SS
7	85% glycerol	**22**	**1.22**	85 ±5	0.063	1.45	Laser + FS-SS
8	88% glycerol	**21**	**1.23**	122 ±10	-	1.46	Laser
9	80% glucor	**25**	**1.34**	**195 ± 10**	**0.079**	**1.45**	Laser + FS-SS
10	85% glucor	**25**	**1.36**	**562 ± 15**	**0.079**	**1.45**	Laser + FS-SS

Table 5.1: Mixtures' parameters. In bold are the parameters that were measured (the other values are obtained from the tables). The line in grey corresponds to the mixture used in chapters 3 and 4.

The density of the liquid does not change much (it only increases by a factor 1.4) while its kinematic viscosity changes over a wide range (it increases by a factor 600). The results presented in chapters 3 and 4 correspond to experiments done with mixture 6 ($\nu = 30 \times 10^{-6}$ m^2.s^{-1}, see line in gray in table 5.1). As explained in section 2.2.3, we can consider the mean air velocity profile to be unaffected by the change in viscosity of the liquid for wind velocities below the threshold. The observations and hypothesis made in chapter 2 about the airflow are supposed to hold true for all the mixtures and we did not perform any additional hot-wire measurements. Similarly, this is also assumed for the flow in the liquid except for the case of pure water (the other mixtures are viscous enough for the flow in the liquid to stay laminar).

Due to the liquid viscosity, there exist two cut-offs at short and long wavelengths and only the wavelengths in between these two cut-offs can propagate [LeBlond and Mainardi, 1987] (see also § 1.1.3 on page 9). In our case, the cut-off at long wavelength does not have the slightest influence for any of our viscous mixtures, as the wavelength corresponding to this cut-off spans from 8 m (for mixture 10) to 5 km (for mixture 1), considerably greater than any wavelength at play in our 1.5 meter long tank! The cut-off at short wavelength also has a very limited influence for almost all of the mixtures. Indeed, the short wavelength cut-off occurs for wavelengths shorter than a limit ranging from 0.04 μm (mixture 1) to 2 mm (mixture 9). However, for mixture 10, the most viscous one, wavelengths shorter than about 12 mm cannot propagate, and wavelengths only a little longer than this limit will see their propagation affected by the liquid viscosity. This point will be further discussed in section 5.4.

5.1.2 Measurements

FS-SS acquisitions

The experimental set-up is the same as described in chapter 2. As in chapter 3, FS-SS acquisitions are realized at various wind velocities and repeated for the different liquid mixtures presented in table 5.1. The experiments and computations are the same as described in chapter 2 and appendix A. Particularly, the threshold can be deduced from FS-SS acquisitions in the same way as in chapter 3. As the index of refraction of all mixtures is fairly similar, the vertical accuracy of the FS-SS method remains approximately the same (1% of the wave amplitude).

However, contrary to chapters 3 and 4, the acquisitions are performed here only at small fetch $x = 10 - 390$ mm. Indeed, the focus is on the influence of the viscosity on the wrinkles' regime and the critical velocity. The whole analysis over the entire tank length is not repeated for the different viscosities.

Slope measurements

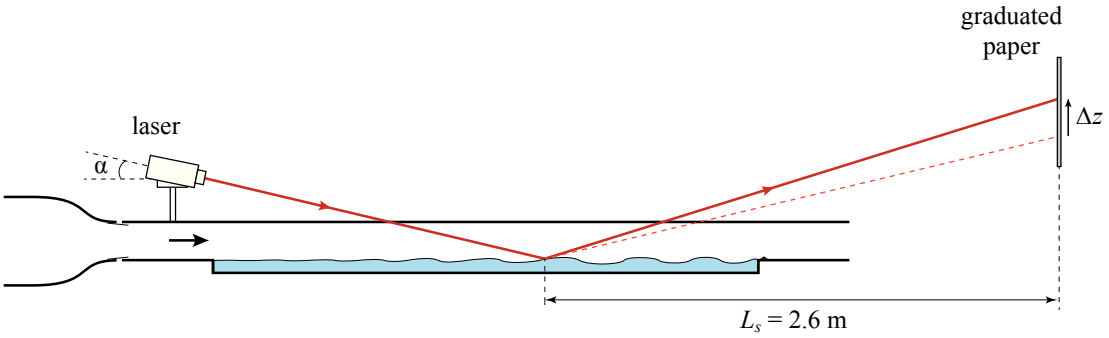

Figure 5.3: Sketch of the set-up equipped with the laser.

While FS-SS acquisitions are rendered impossible for highly concentrated glycerol mixtures by the evolution in time of their viscosities, measurements that only requires a short period of time are still possible. In particular, detecting the wave threshold can be done in a much shorter time than an entire FS-SS campaign. While an estimate by direct observation is always possible (but dependent on the observer's assessment of the threshold), observing the displacement of the laser point reflected on the interface allows for a better precision. The last column of table 5.1 details whether FS-SS acquisition were performed on the mixture or if only the reflection method with the laser was used.

The laser is installed along the direction of the tank (see Fig. 5.3). The incident laser beam is at an angle $\alpha = 17°$ above the interface. The laser dot is reflected on the surface of the liquid in the tank onto a sheet of graph paper taped on the opposing wall of the room at a distance $L_s = 2.6$ m. The laser is aligned with the tank in order to measure the slope in x. The slope $S = \partial\zeta/\partial x$ is related to the vertical displacement Δz of the laser dot on the screen by:

$$S = \tan\left[\frac{1}{2}\arctan\left(\frac{\Delta z}{L_s} + \tan\alpha\right) - \alpha\right]. \tag{5.1.1}$$

Note that the vertical displacement induced by a local change $\zeta(x, y, t)$ is of the order of $\pm\zeta_{rms}$, which is negligible compared the Δz due to the change of slope. Below the

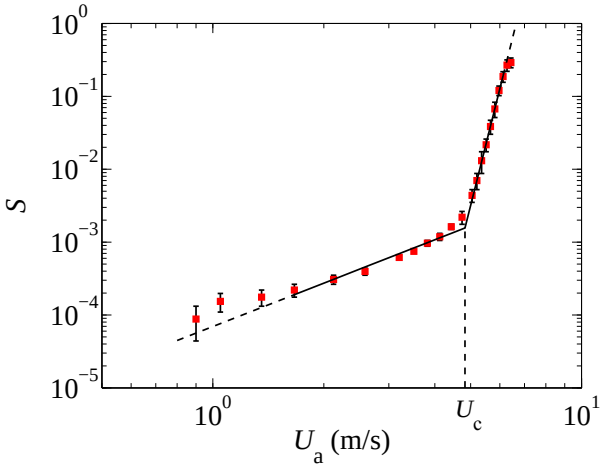

Figure 5.4: Local slope S at $x = 80$ cm based on the vertical deviation Δz of the laser ray due to its reflection on the interface. These results correspond to mixture 4, i.e. for $\nu = 12 \times 10^{-6}$ m^2.s^{-1}.

threshold, the surface gets significantly deformed by the wind in both x and y directions and the laser dot moves inside a small approximately elliptical region. Above the threshold however, since the waves are mostly perpendicular to the wind direction, the surface gradient varies much more in the x direction than in the y direction and the laser dot displacement materializes almost as a line. Figure 5.4 presents typical results for the evolution of S with wind velocity. These results are compatible with the slope that can be derived from the FS-SS acquisitions. The rapid change of slope gives a good evaluation of the threshold velocity. Thus, in a much smaller time scale than a FS-SS series of acquisition, the threshold can be evaluated, but of course without any spatial or temporal information.

5.2 Experimental results

5.2.1 Amplitude of the surface deformation

For the main part, direct observations of the surface height fields yield similar results to those in chapter 3. First, long elongated wrinkles of small amplitudes appear, then transverse waves arise past a certain wind velocity. Figure 5.5 presents snapshots of the surface deformation for different viscosities. Height fields in the left column (Fig. 5.5 (a-e)) are taken for different viscosities below the wave generation threshold, at a wind velocity of about 3.2 m.s^{-1}. The right column (Fig. 5.5 (f-j)) presents surface fields for different viscosities above the threshold velocity. Note that because of the limited number of data points above the threshold U_c, the absolute difference $U_a - U_c$ as well as the relative difference $(U_a - U_c)/U_c$ from the threshold to the chosen wind velocities is not the same for all viscosities. It comes out of the study of the surface height fields that the snapshots of figure 3.1 on page 60 are still somewhat representative of the behavior of the liquid-air interface in these regimes, even though the corresponding velocities change with viscosity. Nevertheless, at very high viscosity, a distinct phenomenon occurs when wind velocity becomes high enough. This phenomenon will be presented in section 5.4.

As in chapter 3, the evolution of the surface deformation amplitude with wind velocity

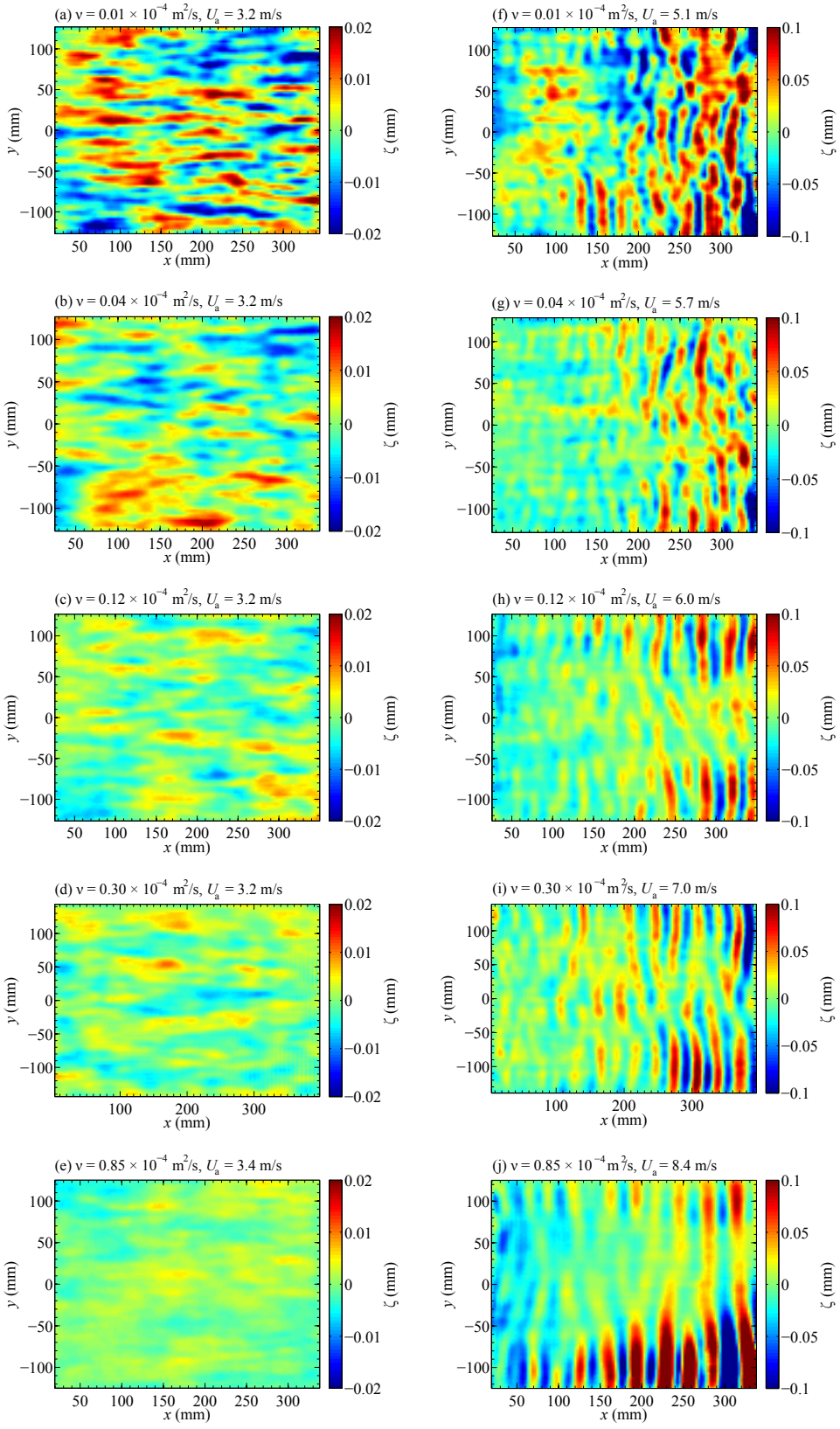

Figure 5.5: Instantaneous surface height $\zeta(x, y)$ measured by FS-SS centered at fetch $x = 190$ mm, for the increasing viscosities $\nu = 0.01$, 0.04, 0.12, 0.30 and 0.85 $\times 10^{-4}$ m^2.s^{-1} (for each pair of fields on a line, from top to bottom); (a-e) below the threshold, at a wind velocity chosen to be about 3.2 m.s^{-1}; (f-j) above the threshold velocity. Note that the color map is the same within each column but varies from one column to the other.

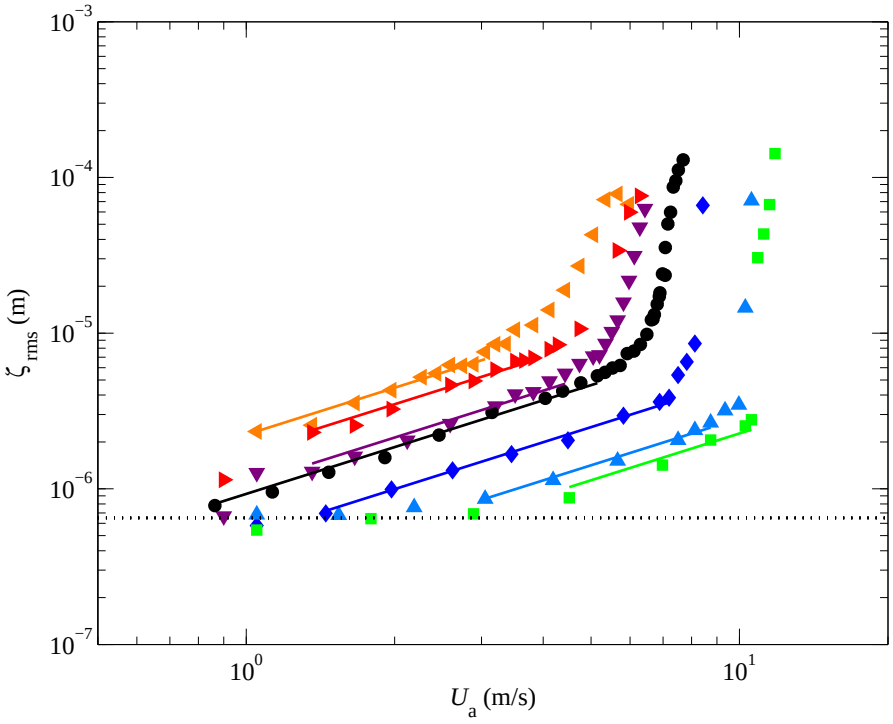

Figure 5.6: R.m.s. of the surface height ζ_{rms} (averaged in time and space over x = 150-300 mm) as a function of the wind velocity U_a. From top to bottom, these results correspond to the viscosities ν = 1.0, 3.9, 12, 30, 85, 195 and 562 $\times 10^{-6}$ m^2.s^{-1}. The continuous lines correspond to linear fits. The horizontal dotted line gives the lower limit $\zeta_{rms} = 0.65$ μm.

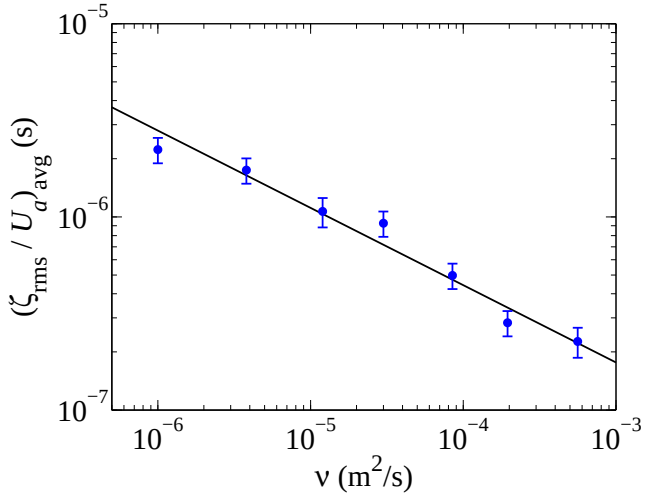

Figure 5.7: Coefficient of the linear fits in the wrinkles' regime in figure 5.6 as a function of the kinematic viscosity. The line shows the fit $(\zeta_{rms}/U_a)_{avg} = K\nu^{-0.4}$ with $K = 1.1 \times 10^{-8}$ SI.

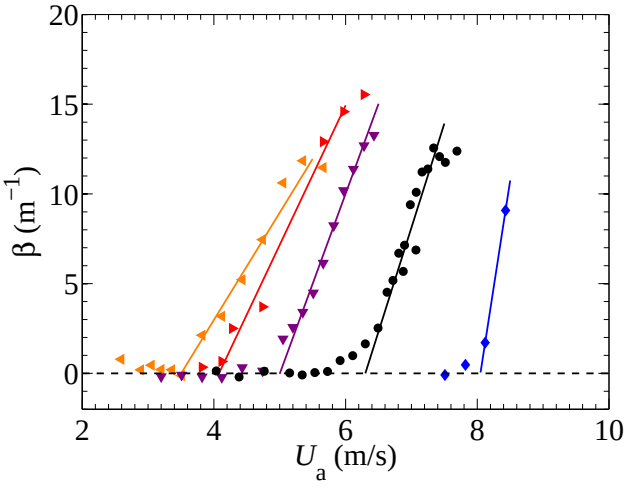

Figure 5.8: Spatial growth rate measured at small fetch ($x \in [150, 300]$ mm) as a function of wind velocity for different viscosities. From left to right, these results correspond to the viscosities $\nu = 1.0$, 3.9, 12, 30 and 85 $\times 10^{-6}$ m^2.s^{-1}. The continuous lines are the linear fits used to obtain the critical wind velocity (equation (3.2.7)).

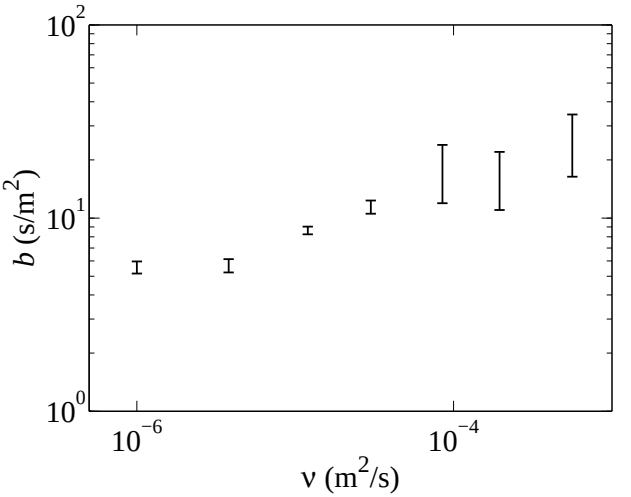

Figure 5.9: Coefficient b of the exponential fit $\zeta_{rms} \propto \zeta_0 \exp[b\overline{x}(U_a - U_c)]$ in the waves' regime (with $\overline{x} = 225$ mm, see also equation (3.2.9)) as a function of the kinematic viscosity.

is presented through the root mean square of the surface height:

$$\zeta_{\text{rms}} = \langle \zeta^2(x, y, t) \rangle^{1/2} \tag{3.2.1}$$

The brackets represent both a temporal average and a spatial average over $x = 150 - 300$ mm. ζ_{rms} is plotted as a function of the wind velocity U_a in figure 5.6 for the mixtures 2, 3, 4, 6, 7, 9 and 10. This plot suggests that ζ_{rms} is the sum of the true height rms and a background noise $\zeta_{noise} \simeq 0.65$ μm, which probably originates from slight residual vibrations due to the camera. Henceforth, reliable measurements of the height rms are obtained for wind velocities satisfying $\zeta_{rms} > \zeta_{noise}$. Not surprisingly, this only affects the plots corresponding to the highest viscosities ($\nu = 85$, 195 and 562 $\times 10^{-6}$ m^2.s^{-1}). Indeed, for viscosities $\nu \leq 30 \times 10^{-6}$ m^2.s^{-1}, the smallest wind velocities at which FS-SS acquisitions are performed are already large enough for the surface perturbations to be bigger than 0.65 μm. Past this lower limit, the evolution of ζ_{rms} with wind velocity is similar for all viscosities to those at $\nu = 30 \times 10^{-6}$ m^2.s^{-1} presented in chapter 3. Up to the wave threshold U_c, the amplitude of the surface deformation grows approximately linearly with U_a: ζ_{rms} can be fitted by the power law U_a^m with $m \in [0.95, 1.20]$. In figure 5.6, this exponent is approximated to $m \simeq 1$ (i.e. we approximate the growth of ζ_{rms} by a linear evolution): the fits in the wrinkles regime in figure 5.6 are linear (as in figure 3.2 on page 61). Then, past the wrinkles regime, from U_c, transverse waves start to appear and the growth of the amplitude is much quicker. As expected intuitively, at a given wind velocity, wind over a more viscous liquid leads to a weaker surface deformation. The transition from the wrinkles' regime to the transversal waves occurs at higher wind velocity and is also more and more abrupt as the viscosity increases, from a slow continuous transition for water to a genuine abrupt break at the highest viscosity (see figures 5.6 and 5.8). The coefficient b of the exponential fit $\zeta_{rms} \propto \zeta_0 \exp[b\overline{x}(U_a - U_c)]$ in the waves' regime (with $\overline{x} = 225$ mm, see equation (3.2.9)), which can be used to characterize this abruptness, increases by a factor of 5 between the least and most viscous mixtures (see Fig. 5.9). The smooth transition to the arrival of transversal waves in the case of water may explain some of the discrepancies in the thresholds found in water in the literature, as discussed in the next section. In order to compare the growth rates obtained in water to the prediction from Miles model $\beta_t/f \simeq 0.16(u^*/c_\varphi)^2$ [Miles, 1959a] [Mitsuyasu and Rikiishi, 1978], we use the wave frequency $f_w \simeq 12$ Hz observed experimentally just above wave onset in water. It is found that our experimental growth rates are 1.5 to 5 times larger than the predicted growth rates.

As mentioned above, figure 5.6 suggests that the approximate linear law $\zeta_{rms} \propto U_a$ found for $\nu = 30 \times 10^{-6}$ m^2.s^{-1} in chapter 3 holds also for other values of ν. In order to check the dependence with respect to ν, we plot in figure 5.7 the coefficient of these linear fits as a function of the viscosity (for wind velocities chosen in the range such that $\zeta_{rms} \propto U_a$). A power law fit gives $\zeta_{rms}/U_a \simeq K\nu^n$ with $n \simeq -0.4 \pm 0.1$ and $K \simeq 1.1 \times 10^{-8}$ SI.

5.2.2 Threshold velocity

Evolution of the wave threshold with viscosity

As explained above, the threshold velocity U_c is deduced either from the FS-SS acquisitions or from the measurements of the laser-dot deviation. The laser method, while leading to a better accuracy than an estimation based on visual observations, is however less precise than the threshold determination based on FS-SS recordings. With FS-SS,

the threshold velocity is defined as the wind velocity at which the spatial growth rate β becomes positive (in practice, $\beta(U_a)$ is fitted linearly above the threshold and the extrapolation of this linear fit to $\beta = 0$ gives the threshold velocity U_c, see figure 5.8). At the two highest viscosities, the presence of solitary waves makes it impossible to estimate the growth rates accurately enough for the threshold velocity to be determined through this method. Instead, the threshold is determined by fitting lines in the wrinkles and wave regimes as in figure 5.6; their intersection gives the threshold velocity. The transition from the wrinkles to the waves regime is so abrupt for these viscosities that there is little doubt on the value of the threshold velocity. With this method, the threshold velocity can be evaluated with an accuracy of 0.1 to 0.2 m.s^{-1} depending on the number and proximity of data points in the vicinity of the threshold. With the laser, the threshold can be measured with only a 0.3 m.s^{-1} accuracy. The threshold velocities measured for each mixture using either the FS-SS acquisitions or the laser, as well as their accuracy, are specified in table 5.2. Experiments in which the threshold is measured from both methods show similar results in both cases. Thresholds based on FS-SS being a little more accurate, they are used instead of the thresholds based on the laser measurements whenever results from both methods are available.

Mixture	Kinematic viscosity ν ($\times 10^{-6}$ m^2/s)	Threshold velocity by laser (m/s)	Threshold velocity by FS-SS (m/s)
1	0.91 ±0.02	2.8 ±0.3	-
2	1.00 ±0.02	3.2 ±0.3	3.4 ±0.2
3	3.9 ±0.1	3.8 ±0.3	4.1 ±0.2
4	12 ±1	4.7 ±0.2	5.0 ±0.1
5	23 ±1	-	5.9 ±0.1
6	30 ±1	-	6.3 ±0.1
7	85 ±5	8.0 ±0.2	8.0 ±0.2
8	122 ±10	8.6 ±0.2	-
9	195 ±10	10.0 ±0.3	10.1 ±0.2
10	562 ±10	10.8 ±0.3	10.7 ±0.2

Table 5.2: Threshold velocities obtained experimentally using mixtures of different viscosities.

The velocity threshold is plotted as a function of the kinematic viscosity in figure 5.10. As one could expect, the threshold velocity increases with viscosity: the more viscous the liquid is, the more difficult it is to amplify perturbations and set off wave generation. The line on figure 5.10 shows the fit $U_c = a\nu^n$. The exponent of this power fit is $n = 0.22 \pm 0.03$. Note that this exponent is compatible both with values of 1/4 and 1/5. The data point at highest viscosity is excluded from this power fit. Indeed, it seems that at very high viscosity ($\nu \gtrsim 300 \times 10^{-6}$ m^2 s^{-1}), the evolution of the threshold velocity changes for a slower growth with viscosity (this is further discussed in section 5.4). This observation is in agreement with the experimental results of [Francis, 1956] (see next paragraph).

Comparison with thresholds from the literature

Figure 5.10 also allows to compare the critical velocities obtained in the present experiments to other thresholds obtained in the literature. Table 5.3 provides some of the wind velocity thresholds found in the literature. As mentioned in chapter 1, most of the

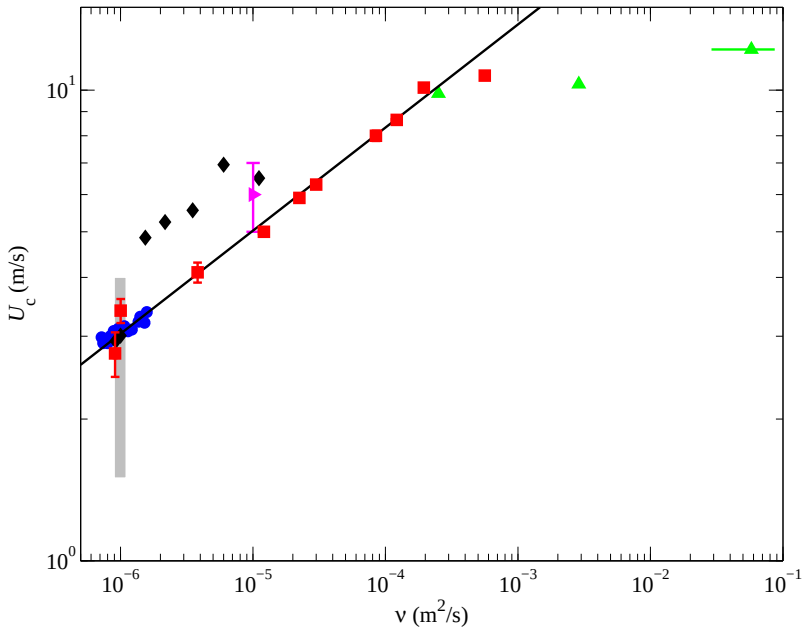

Figure 5.10: Threshold velocity plotted as function of the kinematic viscosity. The red squares (■) correspond to our data, the black diamonds (⧫) to data from [Keulegan, 1951], the green triangles (▲) to data from [Francis, 1956], the blue dots (●) to data from [Kahma and Donelan, 1988] and the magenta triangle (▶) to data from [Gottifredi and Jameson, 1970]. The grey rectangle represents the range of thresholds from the literature obtained experimentally over water. The continuous line is a power fit $U_c = a\nu^n$, with $n = 0.22$ and $a = 62.6$ SI. Note that error bars are often smaller than the markers.

experimental works about wind waves in the literature are performed over water. When the viscosity of the water is available, the value is given as is in the table. If only the water temperature is mentioned, its viscosity is taken as the tabulated value of pure water at this temperature. Otherwise, when neither the viscosity nor the temperature of the water during their wind waves experiments is indicated by the authors, the kinematic viscosity of the water is taken to be about 1.0×10^{-6} m^2.s^{-1} (the tabulated value at 20°C). Our results are in accordance with the thresholds in water in the literature, despite the variations between the results of the different authors. Note that the fact that the power law extends to such a low viscosity as the one of water was not expected by us. Indeed, our set-up was designed with the use of more viscous liquids in mind. In the case of water, the surface drift is greater, the flow in the liquid can be turbulent, and waves are damped over a longer distance, allowing for reflections at the end of the tank to be visible. Despite these changes at low viscosity, it seems that there is a continuum of the behavior of the threshold velocity with respect to viscosity, at least down to the viscosity of water.

It also comes out from the comparison in figure 5.10 that our results are in a fairly good agreement with [Kahma and Donelan, 1988] at low viscosity and [Francis, 1956] at high viscosity. Aiming for the exploration of the effect of viscosity on the minimum wind speed creating waves, Kahma and Donelan carried out laboratory experiments for water at different temperature, ranging from 4 to 35°C [Kahma and Donelan, 1988]. Their results are represented by blue dots in figure 5.10 and are in excellent agreement with

our data over the corresponding range of viscosity [2]. [Francis, 1956] is one of the few sources of data from the literature concerning the wave threshold over a liquid that is not water. His results over two viscous oils and a syrup are displayed in green triangles in figure 5.10 [3]. [Keulegan, 1951] also offers some results over liquids more viscous than water. He observes that the critical velocity decreases with fetch: thresholds measured at the end of his 20 m long wind tunnel are almost 5 times smaller than those taken at the entrance of the tank. Thus, he takes the critical velocity to be the average of the values at fetches $x = 6$, 8 and 10 m, which may explain the difference between his results and ours. His values are plotted with black diamonds and are about 40% above ours. Indeed, contrary to Keulegan who observes that at a given wind velocity, a minimal fetch is necessary before waves are generated, in our set-up, we have not observed any situation in which waves appears at high fetch and not at smaller fetch.

The study of [Gottifredi and Jameson, 1970] is focused on the growth of mechanically-generated waves amplified by wind over water or aqueous glycerol solutions but it also mentions the critical wind velocity in the absence of artificial waves. However, this wind velocity is based on the observation of the wave growth, which may explain a result slightly above ours, as weak wave growths may not have been visible.

Natural wind waves (waves generated by wind in outdoors conditions, for example on a lake or at sea) present a critical velocity that is usually lower than wind waves in laboratory. This may be explained by the fundamental differences between the two systems considered (see section 2.3 on page 55). Indeed, the conditions in which natural wind waves occur are quite different from the ones in which our experiments are performed: unbounded non stationary airflow, turbulent flow in the liquid, presence of unsteady currents under the surface, etc. Thresholds in outdoors conditions are given for information purposes in table 5.3 but they are not represented in figure 5.10.

2. When they performed more than one measurement at a given temperature, the average wind velocity is represented.

3. The threshold associated to the most viscous liquid he used (Lyle's golden syrup, a molasses syrup) is to be interpreted with caution. Indeed, Francis points out that the uncertainty on the viscosity of this liquid is important due the hygroscopic nature of this liquid. As a consequence, an arbitrary error bar of $\pm 50\%$ of the viscosity is added in figure 5.10.

	Reference	Liquid	Kinematic viscosity ($\times 10^{-6}$ m^2/s)	Threshold velocity (m/s)	Notes
1	Roll, 1951	water (outdoors)	~ 1	0.4	cited by [Kahma and Donelan, 1988]
2	[Russell, 1844]			0.85	cited by [Kahma and Donelan, 1988]
3	[Jeffreys, 1925]			1.0-1.2	
4	Van Dorn, 1953			2	cited by [Kahma and Donelan, 1988]
5	[Kahma and Donelan, 1988]	water (laboratory)	0.72-1.58	2.9-3.4	
6	[Donelan and Plant, 2009]		0.81	~ 1.5	
7	[Keulegan, 1951]		0.92	2.9	
8	[Donelan and Plant, 2009]		1.00	~ 1.7	
9	[Wu, 1978]	water (laboratory)	~ 1	1.6	
10	[Hidy and Plate, 1966]			3	
11	[Francis, 1951]			3.1-3.2	
12	[Gottifredi and Jameson, 1970]			3.5	threshold based on visual wave growth
13	[Lorenz et al., 2005]			4-6	
14	[Keulegan, 1951]	sugar solutions of different concentrations	1.54	4.9	
15			2.17	5.2	The critical velocity is the average
16			3.51	5.6	of values taken at different fetches
17			6.00	6.9	($x = 6$, 8 and 10 m)
18			11.1	6.50	
19	[Gottifredi and Jameson, 1970]	glycerol-water solution	10.0	~ 6	threshold based on visual wave growth
20	[Francis, 1956]	oil	250	9.84	
21		oil	290	10.30	
22		syrup	5800	12.20	large uncertainty on the viscosity

Table 5.3: Threshold velocities in the literature.

5.3 Analyses and interpretations

5.3.1 Friction velocity vs wind velocity

It has been argued by some authors that the friction velocity u^* is a more relevant parameter than the mean wind velocity U_a for a fine analysis of wind waves [Phillips, 1957]. Indeed, while U_a is a relevant parameter far from the interface, u^* is the characteristic velocity scale close to the interface, in the viscous sublayer. Moreover, U_a depends on the geometry of the wind channel while u^* is only related to the state of the surface. It is therefore of interest to express the experimental results presented in the previous section with respect to the friction velocity instead of relatively to the wind velocity.

First, let us revisit the definition of u^* relatively to U_a. As we have seen in section 2.2.3 in chapter 2 from our measurements, we can approximate u^* by the linear relation $u^* \simeq 0.05U_a$, that is to say:

$$U_a \simeq 20u^*. \tag{5.3.1}$$

However, following equation (2.2.5) of chapter 2, a more complete theoretical form would be:

$$U_a = \left[\frac{1}{\kappa}\log Re_\tau + C^+\right] u^*, \tag{5.3.2}$$

with $Re_\tau = Hu^*/2\nu_a$ and $C^+ = 5$. Henceforth, u^* refers to the friction velocity derived from equation (5.3.2).

Figure 5.11 shows the friction velocity u^* as a function of the wind velocity U_a compared to its linear approximation (Eq. (5.3.1)). As shown in section 2.2.3, equation (5.3.1) is an acceptable approximation over the range of velocity corresponding to the wrinkles regime for viscosity $\nu = 30 \times 10^{-6}$ m^2/s (i.e. over 1 to 6.3 m.s^{-1}). Indeed, the logarithmic evolution over this range is small enough to be neglected in favor of the linear evolution. However, as we increase the viscosity of the liquid, the waves start to appear at higher wind velocities, and the linear approximation of equation (5.3.1) becomes less reliable over the range of higher velocities corresponding to the wrinkles' regime at these viscosities. Therefore, the experimental results previously presented using U_a will now be analyzed relatively to the friction velocity u^* as defined in equation (5.3.2).

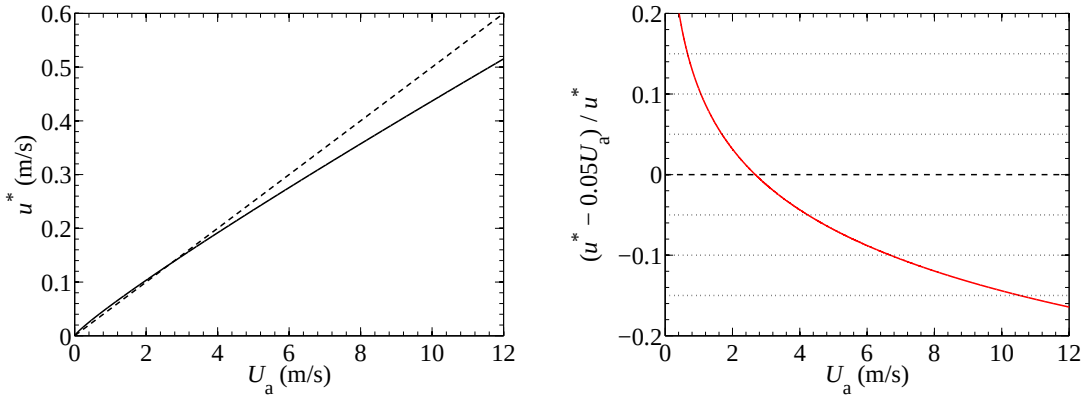

Figure 5.11: (Left) Friction velocity as a function of the wind velocity U_a from equations (5.3.1) (dashed line) and (5.3.2) (continuous line). (Right) Relative difference between the friction velocities derived from equations (5.3.1) and (5.3.2).

5.3.2 Experimental results relatively to the friction velocity

Since u^* may be a more relevant parameter than U_a, let us plot the same data as previously presented relatively to the friction velocity. Figure 5.12 presents the amplitude of the surface deformation as defined in the previous section (see Fig. 5.6), but as a function of the friction velocity. It is found that the amplitude of the surface deformation now increases approximately as $u^{*m'}$ with $m' \in [1.35, 1.65]$, whereas we had previously an evolution of ζ_{rms} as U_a^m with $m \in [0.95, 1.20]$. Note that although equation (5.3.1) would predict $m \simeq m' \simeq 1$, we find that using equation (5.3.2) leads to an approximate power law with a larger exponent $m' \simeq 1.5$. The coefficient $a = \zeta_{rms}/u^{*1.5}$ is plotted as a function of the viscosity ν in figure 5.13. We find that the coefficient a is such that $a = \zeta_{rms}/u^{*1.5} = K\nu^n$ with $n = -0.46 \pm 0.05$ and K $= 3.0 \times 10^{-7}$ SI. Note that the exponent n is compatible with the value of $1/2$.

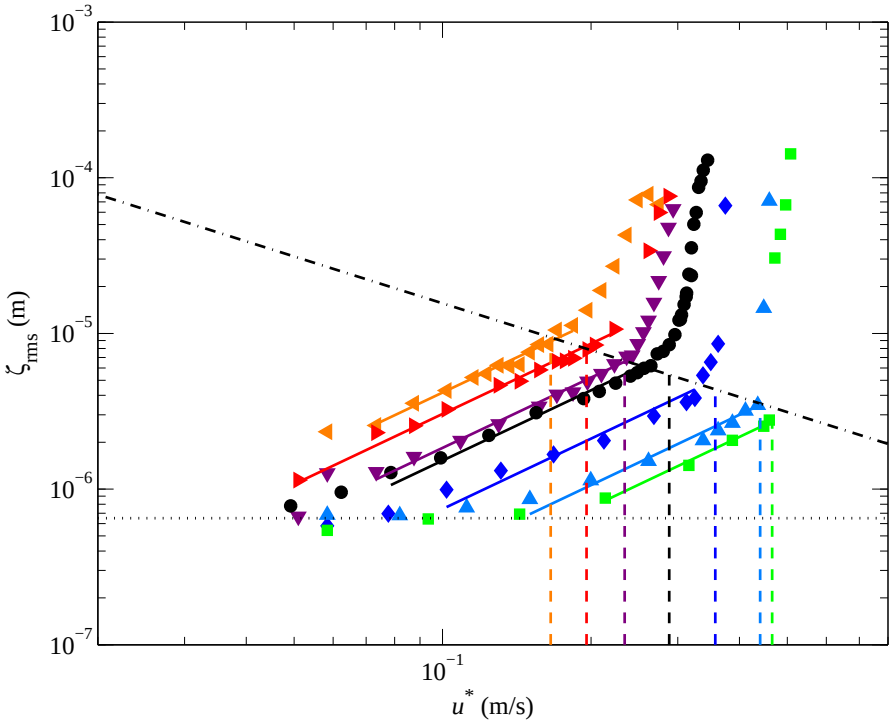

Figure 5.12: R.m.s. of the surface height ζ_{rms} (averaged in time and space over $x = 150 - 300$ mm) as a function the friction velocity u^*. From top to bottom, these results correspond to the viscosities $\nu = 1.0$, 3.9, 12, 30, 85, 195 and 562 $\times 10^{-6}$ m^2.s^{-1}. The continuous lines correspond to fits of power 1.5. The horizontal dotted line gives the lower limit $\zeta_{rms} = 0.65$ μm. The dash-dot line corresponds to $\zeta = c/u^*$ with $c = 1.5 \times 10^{-6}$ m^2.s^{-1}. The vertical lines represent the critical friction velocities u_c^* for each ν.

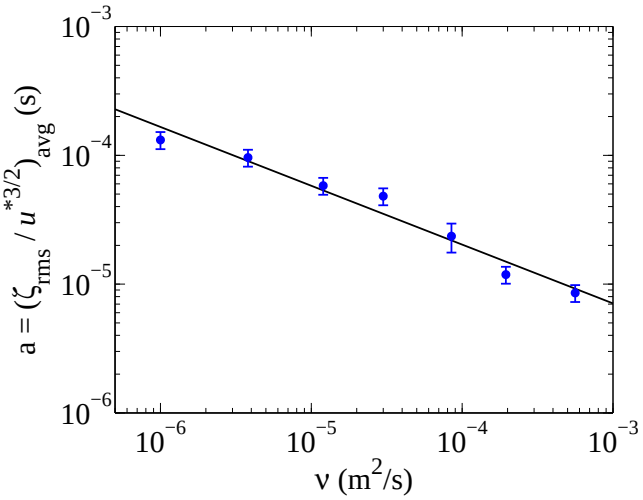

Figure 5.13: Coefficient of the fits in $u^{*1.5}$ in the wrinkles regime in figure 5.12 as a function of the kinematic viscosity. The line shows the fit $(\zeta_{rms}/u^{*1.5})_{avg} = K\nu^{-0.46}$ with $K = 3.0 \times 10^{-7}$ SI.

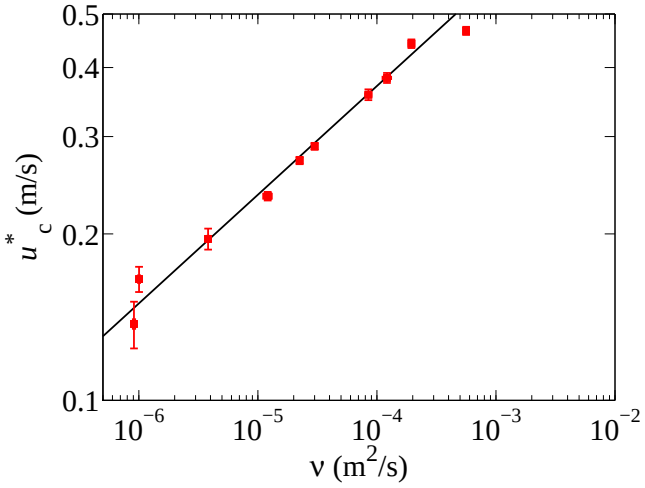

Figure 5.14: Critical friction velocity u_c^* as a function of the kinematic viscosity of the liquid. The continuous line shows the fit $u_c^* = a\nu^{0.20}$ with $a = 2.3$ SI.

5.3.3 Model for the wrinkles

In this section, we propose a model to relate ζ to u^* and ν based on the influence of the pressure fluctuations over a viscous liquid. This model is based on Phillips model, modified to account for the influence of viscosity. In Phillips model, the square of the amplitude of the surface deformation grows linearly in time until the slope of the waves exceeds a certain limit; in our model, we postulate that a viscous saturation arises beforehand.

a) Influence of pressure fluctuations over an interface: viscous saturation of Phillips' model

In order to model the interaction between the turbulent airflow and the interface and evaluate the amplitude of the surface deformation of the wrinkles, the surface deformation is supposed to be the result of the effects of the pressure fluctuations on the interface. From the analysis of [Phillips, 1957] (see section 1.2.1 for more details), in the principal stage of development of wind waves, the amplitude of waves generated by a turbulent airflow that is statistically stationary, uniform in the x direction and applied over the interface during a time t is given by (equation (4.13) in [Phillips, 1957]):

$$\overline{\zeta^2} \simeq \frac{\overline{p^2}t}{2\sqrt{2}\rho^2 V_c g} \tag{1.2.1}$$

where $\overline{p^2}$ is the mean square turbulent pressure on the interface [4] , t the elapsed time and V_c the convection velocity of the pressure fluctuations. V_c as defined by Phillips is the velocity of the frame of reference in which the time scale of the normal stresses fluctuations (i.e. the pressure fluctuations) is the greatest. According to Phillips, the convection velocity of pressure fluctuations of length scale ℓ is approximately the mean wind speed at a height ℓ above the surface. In his model, the pressure fluctuations can trigger a resonance with the interface deformation mode of the corresponding wavelength and the growth of the waves continues until the slope of the waves becomes high enough that nonlinear effects are not negligible anymore. In this approach, the viscosity is not taken into account.

In the case of a viscous liquid, the wave growth may saturate before the nonlinearities become important, in a time scale t given by the dissipation time τ in the liquid. Let Λ be the main wavelength excited at the interface. The dissipation time at this scale for a laminar flow is $\tau = (2\nu(2\pi/\Lambda)^2)^{-1} = \Lambda^2/8\pi^2\nu$ [Lamb, 1995]. The root mean square of the pressure fluctuations $p_{rms} = \overline{p^2}^{1/2}$ at the wall in a fully developed turbulent channel, unavailable at the time of [Phillips, 1957], is nowadays accessible by numerical simulation. It is well described by the empirical law $p_{rms} = f(Re_\tau)\rho_a u^{*2}$ with $f(Re_\tau) = (2.60\ln(Re_\tau) - 11.25)^{1/2}$ (equations (3.2.3) and (3.2.4)). We can interpret the convection velocity V_c as the mean velocity at the altitude above the interface where the pressure fluctuations are maximal. In a turbulent boundary layer, such altitude corresponds to $z^+_{\max} = z_{\max}/\delta_\nu \simeq 20 - 50$ [Jimenez and Hoyas, 2008]. According to the logarithmic law (Eq. (2.2.5)), the mean velocity at this altitude, i.e. the convection velocity, is $u(z_{\max}) = V_c \simeq (13 \pm 1)u^*$. Note that if we use the approximation $u^* \simeq 0.05U_a$, this yields $V_c \simeq (0.65 \pm 0.05)U_a$, which is consistent with this evaluation of the convection velocity $V_c \simeq 0.6U_a$ given by [Choi and Moin, 1990].

Incorporating these expressions of p_{rms}, τ and V_c into equation (1.2.1), we obtain:

$$\overline{\zeta^2} \simeq \frac{f(Re_\tau)^2\rho_a^2 u^{*4}(\Lambda^2/8\pi^2\nu)}{2\sqrt{2}\rho^2((13 \pm 1)u^*)g} \tag{5.3.3}$$

4. The mean pressure is set to zero.

which leads to:

$$\zeta_{rms} \simeq K^* \nu^{-1/2} u^{*3/2} \tag{5.3.4}$$

$$\text{with } K^* = \alpha \phi f(Re_\tau) \tag{5.3.5}$$

with $\alpha = 1/4\pi(\sqrt{2}(13 \pm 1))^{1/2} \simeq (18.6 \pm 0.7) \times 10^{-3}$ and $\phi = \rho_a \Lambda / \rho g^{1/2}$.

Note that K^* still depends on u^* through the factor $f(Re_\tau)$. This dependence is weak: over the entire range of friction velocity over which all wrinkles regimes span, $u^* \in [0.05, 0.5]$ m.s^{-1}, $f(Re_\tau)$ increases by 20%, from 3.7 to 4.4. Moreover, for each liquid of different viscosity, the range of friction velocity corresponding to the wrinkles regime is more restricted. Over each of these ranges, $f(Re_\tau)$ departs from its average value $\overline{f(Re_\tau)}$ over the wrinkles regime by only 5 to 10%. Thus, while this is not expected to hold for wide ranges of u^*, an average value of K^* to describe the evolution of ζ_{rms} may be used as an approximation over the small range of friction velocity of each wrinkles regime. This is confirmed by the fact that fitting the experimental data with $f(Re_\tau)u^{*3/2}$ instead of $u^{*3/2}$ in figure 5.12 leads to a difference that is smaller than the line thickness. As a result, equation (5.3.5) can be simplified using the average value $\overline{K^*}$ and we can write:

$$\zeta_{rms} \simeq \overline{K^*} \nu^{-1/2} u^{*3/2} \tag{5.3.6}$$

$$\text{with } \overline{K^*} = \overline{\alpha} \phi \overline{f(Re_\tau)} \tag{5.3.7}$$

with $\overline{\alpha} = 18.6 \times 10^{-3}$ the average of α, and $\overline{f(Re_\tau)}$ the average value of $f(Re_\tau)$ over the range of friction velocity of the wrinkles regime for the considered liquid. Equation (5.3.6) is in agreement with the experimental results. Indeed, figures 5.12 and 5.13 show that in the wrinkles regime we can fit $\zeta_{rms} \propto u^{*3/2}$ and $\zeta_{rms} \propto \nu^{-1/2}$. Therefore, this model allows us to account for the evolution of the amplitude of the surface deformation both with respect to the kinematic viscosity and with respect to the friction velocity.

b) Validity of the model: complete comparison with data

As mentioned above, the model presented in the previous section leads to an evolution of the amplitude of the surface deformation ζ_{rms} that is in accordance with the experimental results. In order to further test the validity of this model, the applicability of the theoretical coefficient K^* of equation (5.3.4) is explored.

To do so, the experimental results of ζ_{rms} are divided by $\overline{\alpha}\phi\nu^{-1/2}u^{*3/2}$ and plotted as a function of the friction velocity u^*. According to the model, $\zeta_{rms}/\overline{\alpha}\phi\nu^{-1/2}u^{*3/2}$ should evolve as $f(Re_\tau)$. The values in table 5.1 are used for the computation of $\phi = \rho_a\Lambda/\rho g^{1/2}$ for each mixture. However, there is one parameter not in this table the evaluation of which remains: Λ, the wavelength used in the estimation of the dissipation time. Figure 5.15 presents the characteristic lengths Λ_x and Λ_y (the correlation lengths in the x and y directions as defined in chapter 3, section 3.2.3), as a function of the viscosity for a wind velocity chosen in the wrinkles regime. For all but the highest viscosity, the correlation lengths are taken at a wind velocity $U_a = 3.2 \pm 0.2$ m.s^{-1}. However, for the highest viscosity, the FS-SS measurements are still in the lower limit $\zeta_{rms} = 0.65\mu$m at $U_a = 3.2$ m.s^{-1}. The data at the smallest available velocity in the wrinkles regime ($U_a = 4.5$ m.s^{-1}) is used instead. Figure 5.15 shows that the viscosity seems not to have a major influence on the correlation lengths Λ_x and Λ_y. As Λ_x and Λ_y can be interpreted as the characteristic lengths of the response of the pressure fluctuations on the viscous interface, this suggests that the length scale Λ does not depend on viscosity. As a consequence, for

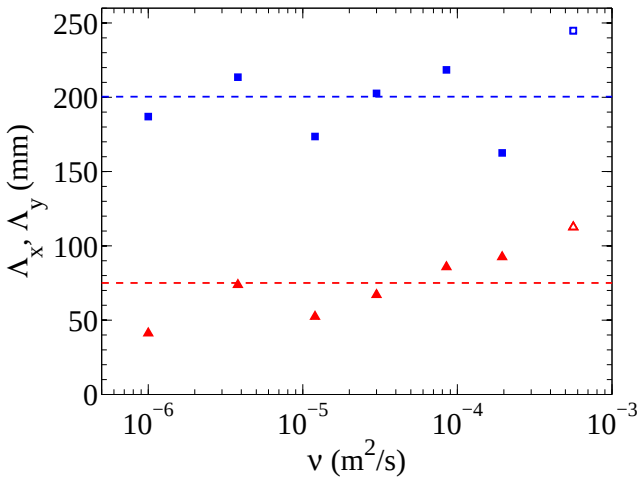

Figure 5.15: Correlation lengths Λ_x in the x direction (■) and Λ_y in the y direction (▲) as a function of the viscosity, in the wrinkles regime. For all but the highest viscosity, the correlation lengths are taken at a wind velocity $U_a = 3.2 \pm 0.2$ m.s^{-1}. Because of the lower limit $\zeta_{rms} = 0.65\mu$m, the data at the smallest available velocity in the wrinkles regime ($U_a = 4.5$ m.s^{-1}) is used instead (open symbols). The two dotted line correspond to the average values $\overline{\Lambda_x} \simeq 200$ mm and $\overline{\Lambda_y} \simeq 75$ mm.

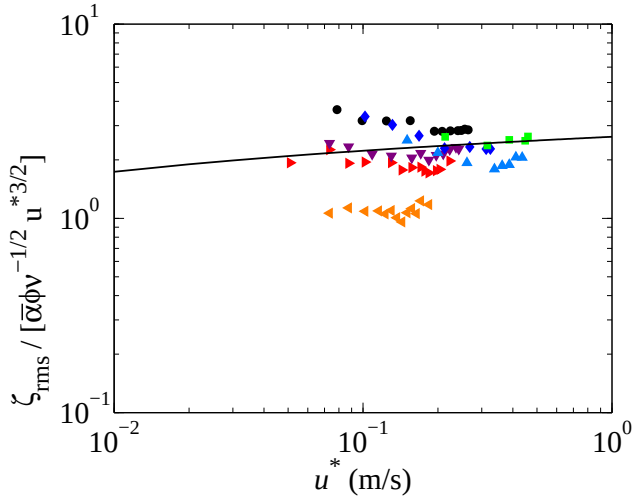

Figure 5.16: Evolution of $\zeta_{rms}/\overline{\alpha}\phi\nu^{-1/2}u^{*3/2}$ relative to the friction velocity. The continuous line corresponds to $0.57f(Re_\tau)$. ϕ is computed using the values in table 5.1 with $\Lambda = \lambda_c$. For the symbols, refer to figure 5.12.

the calculation of ϕ, we take Λ to be here equal to $\lambda_c = 2\pi\sqrt{\gamma/\rho g}$, the capillary wavelength, which is independent of viscosity. The evolution of $\zeta_{rms}/\overline{\alpha}\phi\nu^{-1/2}u^{*3/2}$ as a function of the friction velocity u^* is displayed in figure 5.16. This test is performed only in the range of velocities for which it was previously shown that the power fit $u^{*3/2}$ is applicable (that is to say that the data points at 0.65 μm and those above the wrinkles regime are excluded).

Despite the scatter, the data collapses fairly well: $\zeta_{rms}/\overline{\alpha}\phi\nu^{-1/2}u^{*3/2}$ can be described by $0.57f(Re_\tau)$. The main discrepancy corresponds to the experiments performed with water. It is likely that the low viscosity of water leads to a slightly different behavior of the system, particularly regarding the expression of the viscous dissipation scale. This collapse further confirms the validity of our model. However, the prefactor 0.57 shows that the model may not encompass all of the complexity of the system or that one parameter may not be estimated accurately enough. In particular, the expression of Λ as $2\pi\sqrt{\gamma/\rho g}$ can be subject to criticism. As the lifetime of the pressure fluctuation is of the same order than its time of propagation over its characteristic streamwise length, it may be more accurate to express Λ as depending on the size of the pressure fluctuations rather than on the wavelength associated to free capillary waves.

5.3.4 Critical friction velocity and amplitude of the surface deformation

Let us return to figure 5.12 to look more closely at the amplitude of surface deformation when the threshold is reached. Figure 5.12 shows that this amplitude at the threshold of wave generation seems to decrease as $1/u^*$. Indeed, the transitions to a quicker increase of amplitude appear to roughly correspond to the velocities at which the root mean square of the deformation amplitude reaches c/u^* with $c = 1.5 \times 10^{-6}$ m^2.s^{-1} (dash-dot line). This could suggest that the threshold velocity is related to the thickness of the viscous sublayer $\delta_\nu = \nu_a/u^*$. Attempts in the literature to evaluate the threshold velocity are mostly on stability or dimensional analysis [Keulegan, 1951] [Miles, 1957]. However, based on our results, it looks like trying to relate the critical friction velocity for wave generation u_c^* and the amplitude of the surface deformation could be a fruitful approach. The experimental law of evolution of this deformation amplitude with the friction velocity can be written as:

$$\zeta_{rms} \simeq \overline{K^*}\nu^{-1/2}u^{*3/2}. \tag{5.3.6}$$

Let us consider that the wave threshold is reached when the amplitude of the surface deformation becomes greater than a fraction A of the thickness of the viscous sublayer δ_ν. Thus, we have:

$$\zeta_{rms,c} = K\nu^{-1/2}u^{*3/2} = A\frac{\nu_a}{u_c^*}$$

This leads to:

$$u_c^* \propto \nu^{1/5}. \tag{5.3.8}$$

This exponent 1/5 turns out to be in very good agreement with the experimental results. Figure 5.14 presents the evolution of the critical friction velocity u_c^* for wave formation as a function of the kinematic viscosity of the liquid. The line on figure 5.14 shows the fit $u_c^* = a\nu^n$. The exponent of this power law fit is $n = 0.20 \pm 0.01$ and $a = 2.3$ SI, in accordance with equation (5.3.8) for $A = 0.1$.

It should be noted that these results have to be considered with caution. Indeed, while the transitions from wrinkles to waves are sharp at high viscosity, they are smooth and continuous at lower viscosity, which allows for some flexibility in the plot that can fit the location of the transitions from one regime to the other. Relating the threshold velocity

to the thickness of the viscous sublayer is based on the idea that waves could start to grow when the surface deformation reaches an amplitude comparable to the viscous sublayer thickness. However, the agreement between equation (5.3.8) and experimental results is to be tempered by the fact that this leads to a criterion for wave generation based on the surface deformation reaching only a *tenth* of the viscous sublayer thickness ($A = 0.1$), for which it is difficult to provide a physical interpretation.

5.4 Solitary waves over a highly viscous liquid

For viscosities above about 120×10^{-6} m^2.s^{-1}, a peculiar phenomenon appears at high wind velocities that was not at all present at lower viscosities. This phenomenon specific to high viscosity and high wind velocity arise under the form of solitary waves (SW) of large amplitude. This last section is dedicated to the description of these waves.

5.4.1 Direct observations

When the wind velocity reaches a value U_{sw} over a highly viscous liquid, transverse deformations of great amplitude suddenly appear, starting from $x = 0$ and propagating downstream rather slowly, like small liquid dunes pushed by wind. A picture of such solitary wave is presented in figure 5.17. These large deformations appear close to the wall on one side or the other or on both. They are of length of about 10 cm transversely but are only about 2-3 cm wide. They are curved in a crescent shape and the front and back of the wave are not symmetrical. They propagate downstream at a velocity V_{sw} of order a 0.1 m.s^{-1}, that is to say about 100 times smaller that the wind velocity (or of the order of the surface velocity, since it is a few percent of the wind velocity, see section 2.2.d on page 47). These waves are at least half a centimeter high, which is already three times larger than the highest amplitude of the waves discussed in chapters 3 and 4, and in this chapter until this point. The associated slopes are far above the limit for FS-SS surface reconstruction and the FS-SS technique is no longer applicable.

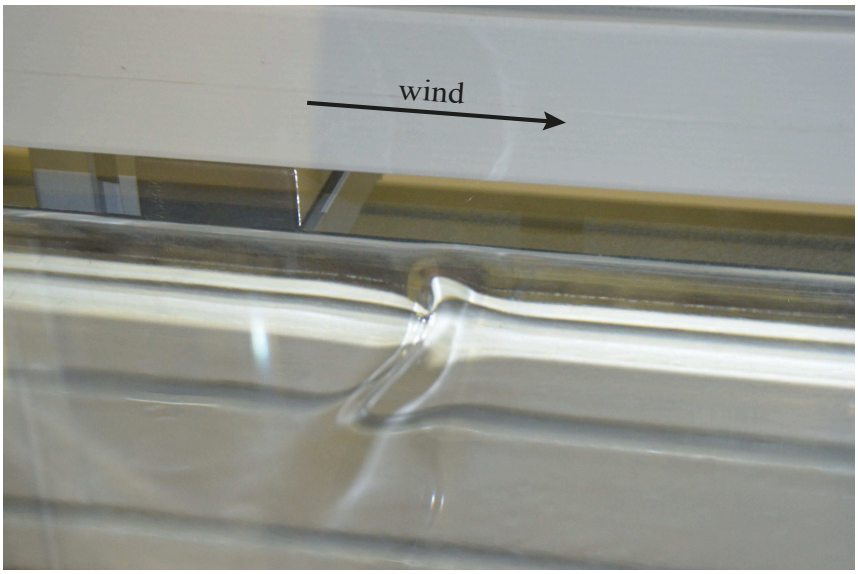

Figure 5.17: Picture of a solitary wave.

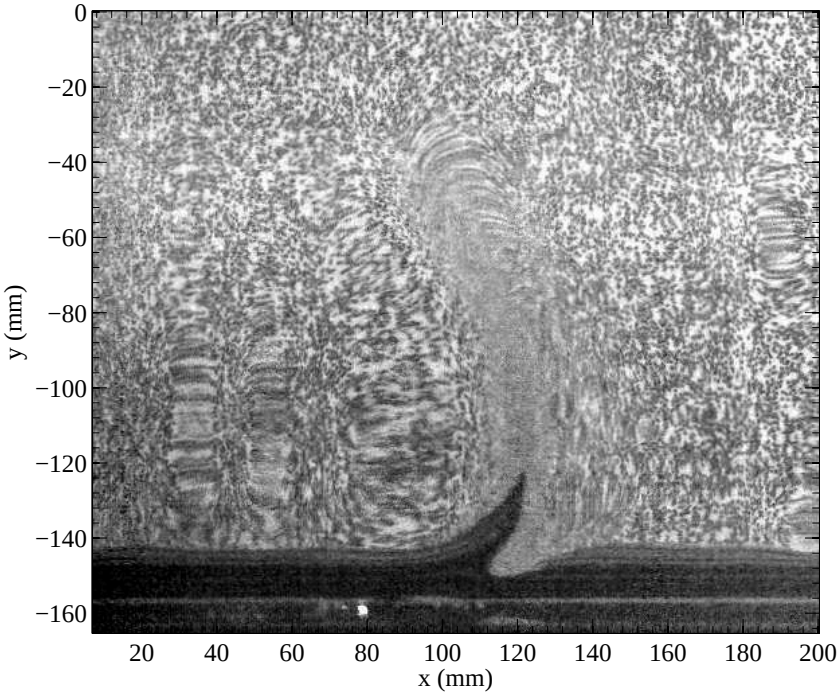

Figure 5.18: Deformation of the dot pattern by a solitary wave. The black spike near the wall corresponds to the deformation of the border of the light sheet seen through the interface.

Nevertheless, the raw recorded images of the dot patterns can be used to observe these solitary waves. Indeed, while differences from the reference frame are hardly visible to the naked eye during typical FS-SS acquisitions, solitary waves correspond to such great surface deformations that they are easily observable on the unprocessed images acquired by the camera (see Fig. 5.18). Figure 5.19 shows some snapshots taken from the recordings at different wind velocities for mixture 10 ($\nu = 562 \times 10^{-6}$ m^2.s^{-1}). The evolution with respect to the wind velocity is fairly similar independently of the mixture's viscosity. For wind velocity slightly above U_{sw}, only one of these deformations at a time can be observed (Fig. 5.19 (a)). After the solitary wave propagates downstream over 30 to 40 cm, its amplitude decreases abruptly and the solitary wave disappears. A few moments later, another solitary wave appears, propagates and disappears in the same way as the previous one, and this phenomenon repeats itself quite regularly. As U_a is increased, the characteristic time between two solitary waves decreases and more than a single solitary wave can be present at the same time (Fig. 5.19 (b)), but not necessarily on the same side on the tank (Fig. 5.19 (c)). The solitary waves also slightly widen from about one third to one half of the total width of the tank when U_a increases. Thus, the greater the wind velocity, the more numerous the solitary waves and the wider they are. Finally, the solitary waves become wide enough to connect to solitary waves on the opposite side through the entire width of the tank (Fig. 5.19 (d)). Once this has occurred, such a fully transverse solitary wave straightens and propagates rapidly to the end of the tank, going above the small dam, making the tank overflow in the process.

While solitary waves arise on one side of the tank before populating the other then the entire width, the preference of the side at which they appear first can change with the mixture or if the experiment is repeated. Nonetheless, solitary waves seem to emerge on the side $y < 0$ somewhat more often than on the opposite side $y > 0$. This probably does

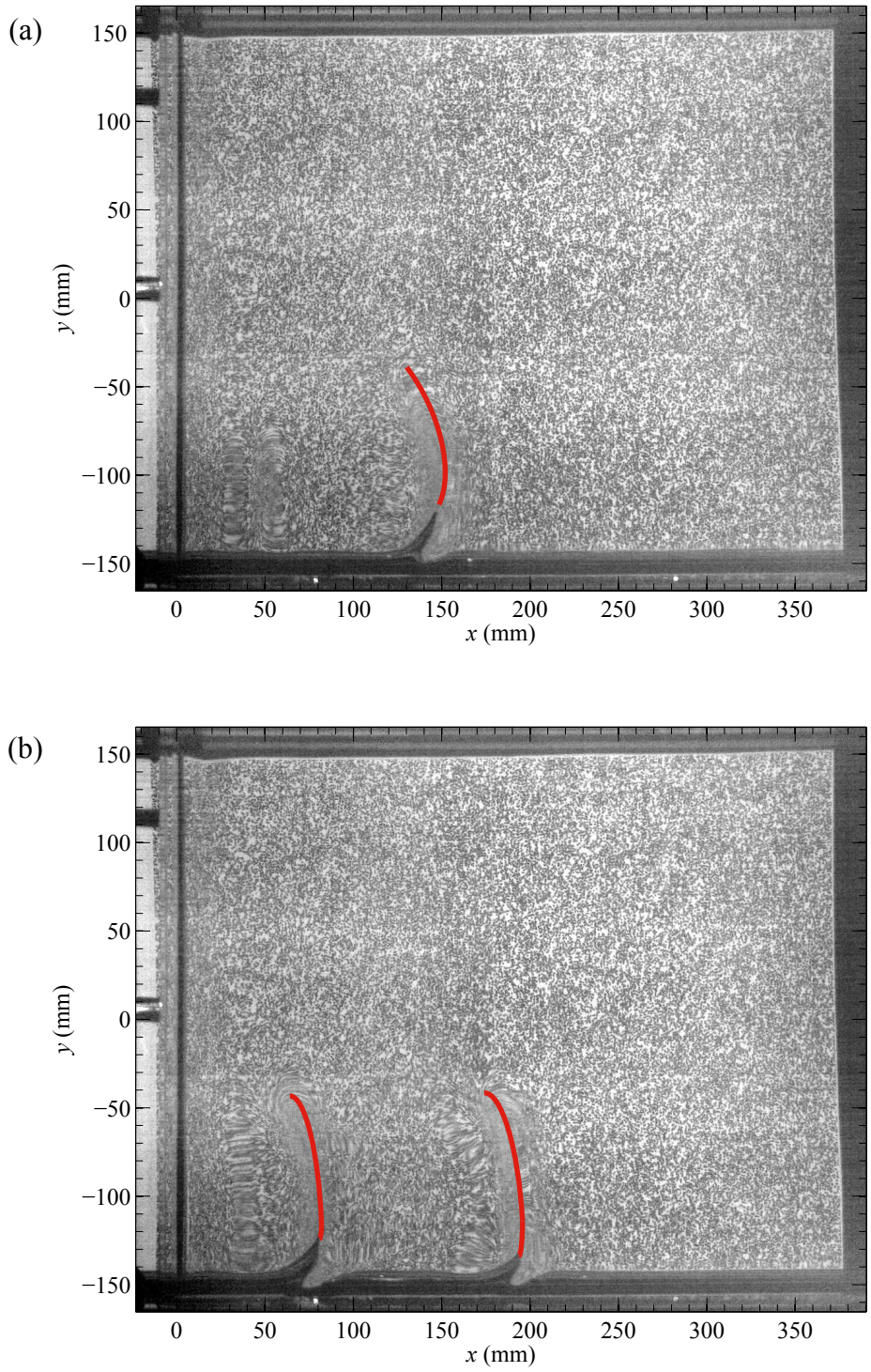

Figure 5.19: Dot patterns in presence of solitary waves for $\nu = 562 \times 10^{-6}$ m^2.s^{-1}, (a) at $U_a = 10.9$ m.s^{-1}, (b) at $U_a = 11.2$ m.s^{-1}. Red lines are added to ease the visualization of the solitary waves.

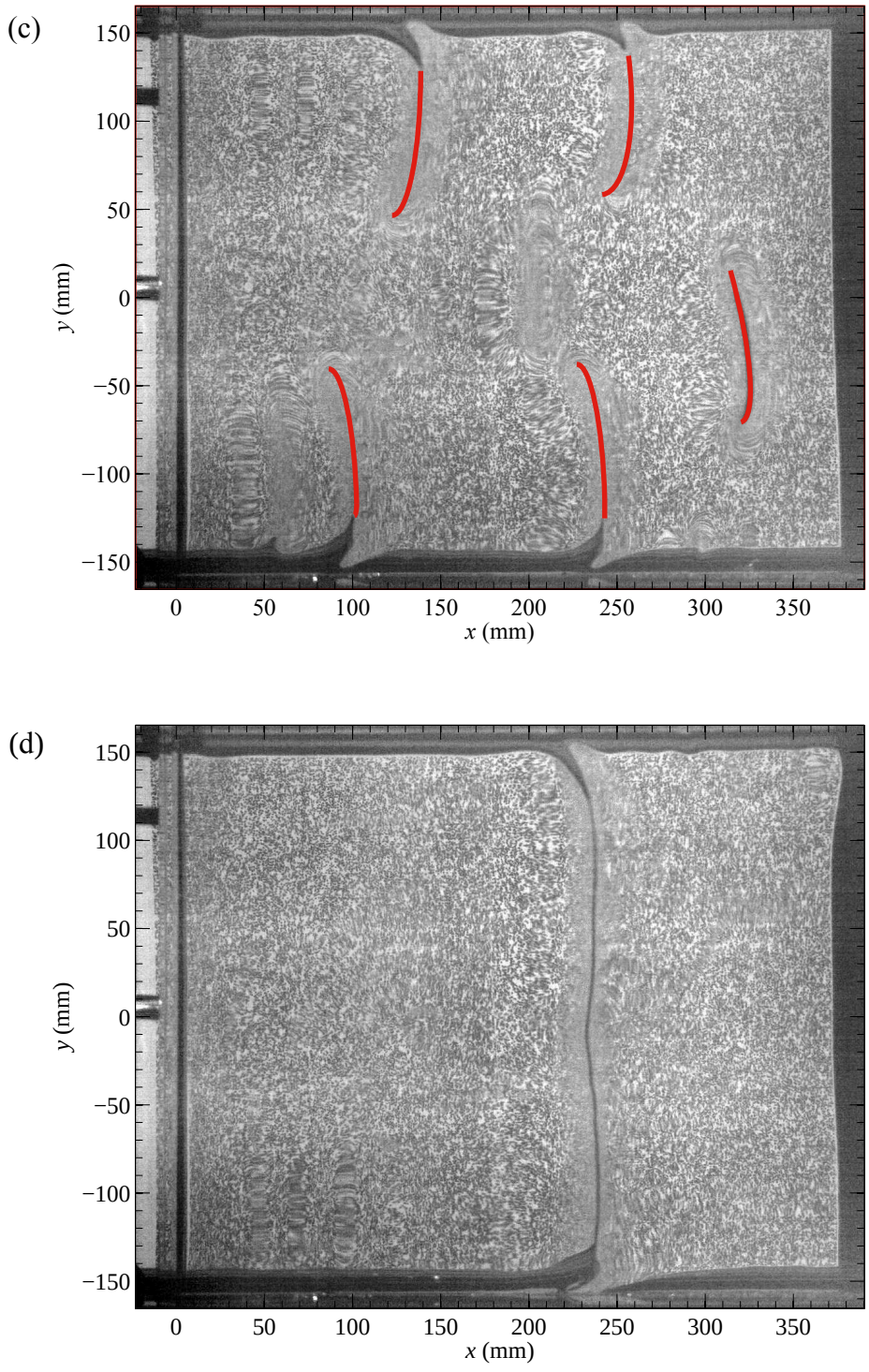

Figure 5.19 (continued). At $U_a = 11.8$ m.s^{-1}, (c) with multiple solitary waves, (d) with a fully transverse solitary wave.

not come from inhomogeneities in the base flow of the wind channel as the uniformity of the transverse mean velocity profile was previously verified (see figure 2.13 on page 44). This is neither from a transverse change of the boundary conditions at $x = 0$. Indeed, to test this hypothesis, the set-up was carefully transversally inclined by an angle $i = 0.1°$, creating at $x = 0$ a rising meniscus on one side of the center line $y = 0$ and a descending meniscus on the other. Relatively to the Plexiglas floor, the liquid is above it by $W/2 \tan(i) \simeq 260$ μm at one side wall and below it by the same amount at the other wall. This inclination (in either direction) did not changed the arrival or behavior of the solitary waves in any visible way, disproving the hypothesis that the leveling of the liquid was an issue.

5.4.2 A few qualitative results

Despite the lack of in-depth experimentation and analysis concerning solitary waves, a few qualitative results can be derived from the direct observations and the analysis of the FS-SS raw recorded images. These results are presented in the following paragraphs, as well as their limitations.

Minimal wind velocity

The minimal wind velocity U_{sw} at which the solitary waves are observed is recorded for viscosities between 122 and 562 $\times 10^{-6}$ m^2.s^{-1} (see table 5.4 and figure 5.20). For the aqueous glycerol mixtures of concentration 88% and above, the observations were done during the initial attempts for FS-SS acquisitions with a highly concentrated glycerol-water solution. Starting from almost pure glycerol, the mixture naturally absorbed water over the course of a few days and solitary waves were observed over the range of corresponding viscosity. Blowing a strong wind over the liquid for an hour ensured that the liquid was properly mixed, and observations were made over a small time scale, over which the liquid's parameters could be considered as constant. The accuracy of determination of U_{sw} depends on the steps of gradual change of the wind blower variator frequency as the wind velocity is increased. As one could have expected, it is found that the minimum velocity U_{sw} slowly increases with viscosity. A power law $U_{\text{sw}} = K\nu^{0.11}$ with $K = 25.2$ SI can be fitted from the data. The evolution of U_{sw} with viscosity is slower than for the one of the threshold velocity ($U_c = a\nu^{0.22}$ with $a = 62.6$ SI). These two power laws intercept for a cut-off viscosity $\nu_c \simeq 210 \times 10^{-6}$ m^2.s^{-1}.

Mixture	T (°C)	ρ ($\times 10^3$ kg/m^3)	ν ($\times 10^{-6}$ m^2/s)	U_{sw} (m/s)
glycerol 88%, water 12% (8)	21	1.230	122 ±10	9.14 ±0.05
glycerol 89%, water 11%	21	1.233	143 ±20	9.26 ±0.05
glucor 80%, water 20% (9)	25	1.34	195 ±10	10.3 ±0.3
glycerol 92%, water 8%	23	1.242	219 ±20	9.54 ±0.05
glycerol 94%, water 6%	27	1.247	229 ±30	9.85 ±0.05
glucor 85%, water 15% (10)	25	1.36	562 ±15	10.9 ±0.3

Table 5.4: Mixtures' parameters for highly viscous liquids.

Note that these results imply that a few points on figure 5.6 on page 98 and figure 5.12 on page 106 correspond to data taken in the presence of solitary waves. Indeed, in these

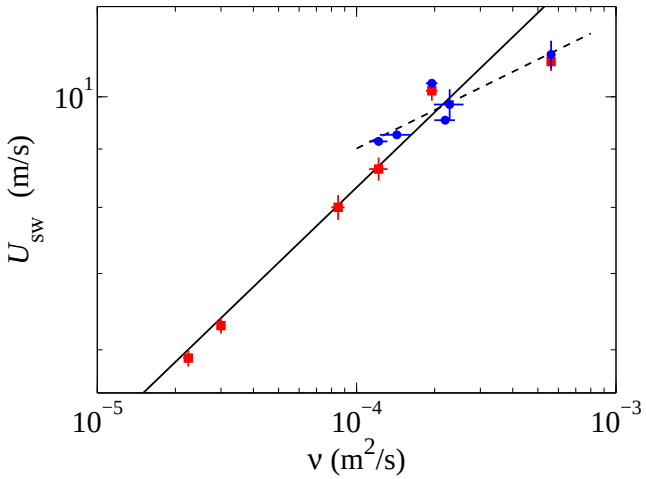

Figure 5.20: Evolution of the minimal wind velocity at which solitary waves are observed as a function of the kinematic viscosity of the liquid. This minimal velocity U_{sw} (●) is compared to the threshold velocity U_c (■) found previously. The dashed line corresponds to the power fit $U_{\text{sw}} = K\nu^{0.11}$ with $K = 25.2$ SI, while the continuous line is the power fit associated to the threshold velocities $U_c = a\nu^{0.22}$, with $a = 62.6$ SI (see figure 5.10 on page 102).

figures, solitary waves are present at the highest velocity for $\nu = 195\times10^{-6}$ m^2.s^{-1} and the four highest velocities for $\nu = 562 \times 10^{-6}$ m^2.s^{-1}. This means that for this later viscosity $\nu = 562 \times 10^{-6}$ m^2.s^{-1}, the threshold U_c actually corresponds the emergence of solitary waves, and not to the transition to the waves' regime as defined in chapter 3.

The precise origin of the solitary waves is unknown at the present time. However, we can postulate that the onset of solitary waves is due to an instability that is set off at high viscosity in our set-up. The general behavior of the solitary waves points toward a subcritical instability. Moreover, as the onset appears to occur independently of the wrinkles or waves (since solitary waves can arise in both regimes), this new instability seems to be decoupled from the one we studied in the rest of this manuscript. The departure from the power law $u_c^* \propto \nu^{1/5}$ at high viscosity would thus be due to the emergence of this second instability, when U_c becomes greater than U_{sw}. Based on the computation of the limit wavelength under which waves cannot propagate (see § 5.1.1 on page 93), it seems likely that the influence of the liquid viscosity on the wave propagation through the over-damping of short wavelength is of particular importance in the generation of the solitary waves.

The appearance and behaviour of these solitary waves are not without reminding of other nonsymmetrical waves in rather different systems, for example, liquid films over inclined planes [Ruyer-Quil et al., 2014] or nonlinear solitons over oil in a confined geometry [Gondret and Rabaud, 1997]; or even waves over non-liquid media: the flutterings of a flag or plastic foil [Connell and Yue, 2007], waves over a viscoelastic gel [Gad-El-Hak et al., 1984], parabolic-type sand dunes [Tsoar and Blumberg, 2002] [Durán et al., 2008], etc. It would be interesting to analyze in the future the possible similarities between those problems.

Propagation velocity and separation length

The propagation velocity of the solitary waves V_{sw} is estimated from visually tracking waves on the raw images. Similarly, the separation length between two waves λ_{sw} is estimated from pairs of waves on the recorded frames. As solitary waves appear to accelerate when they emerge and decelerate when they die out [5], these measurements are performed in between, far enough from the generation and vanishing stages of the solitary waves. This can be achieved by observing the deformation of the border of the light sheet seen through the interface, which materializes by a black spike near the walls (see figures 5.18 and 5.19). V_{sw} and λ_{sw} are recorded at each wind velocity for at least 5 separate solitary waves and at least 5 separate pairs of solitary waves, respectively. The average values of V_{sw} and λ_{sw} are presented in table 5.5, while all the measured values are plotted in figure 5.21. Since FS-SS recordings were performed only for two of the six mixtures for which solitary waves were observed and for only a small range of wind velocities, these experimental results should be interpreted with caution. Nevertheless, a few trends can be deduced from the measurements of V_{sw} and λ_{sw}.

ν ($\times 10^{-6}$ m^2/s)	U_{sw} (m/s)	U_a (m/s)	$(U_a - U_{sw})/U_{sw}$	$\overline{V_{sw}}$ (m/s)	$\overline{\lambda_{sw}}$ (m)
195 $\pm$10	10.3	10.6	0.03	0.169	0.139
562 $\pm$15	10.9	10.6	0	0.066	0.157
562 $\pm$15	10.9	11.2	0.03	0.086	0.116
562 $\pm$15	10.9	11.5	0.06	0.111	0.107
562 $\pm$15	10.9	11.8	0.08	0.141	0.138

Table 5.5: Average propagation velocities and separation lengths of the solitary waves.

The propagation velocity of solitary waves increases over the small range of wind velocity U_a where observations were carried out, consistently with the intuition that a stronger wind will push the wave harder and make it propagate more quickly. Similarly, as one would have expected, a smaller viscosity leads to a higher propagation velocity. Indeed, comparing the results for $\nu = 195 \times 10^{-6}$ m^2.s^{-1} and $\nu = 562 \times 10^{-6}$ m^2.s^{-1} at the same ratio $(U_a - U_{sw})/U_{sw}$ of 3% leads to a propagation velocity about twice greater for the smallest of the two viscosities.

Let us now focus on the propagation velocity of fully transverse solitary waves at the highest wind velocity and viscosity (open symbols in figure 5.21 (left)). While the average velocity of fully transverse waves (0.15 m.s^{-1}) is a little above the average velocity of unconnected solitary waves (0.14 m.s^{-1}), the scatter of the velocity corresponding to fully transverse waves is much greater. Most of the fully transverse waves are of velocity greater or comparable than the one of unconnected waves at the same wind velocity, but some are slower. This may be explained by the fact that the results presented in figure 5.21 concern measurements taken over the first 40 cm of the tank, where fully transverse solitary waves are not necessarily propagating at a constant speed. Indeed, two solitary waves that are connecting are generally misaligned and it seems that a transverse solitary wave starts to accelerate only once straightened, which it does as it propagates. Direct observations show that a fully transverse wave quickly propagates to the end of the tank in less than

5. This suggests that the velocity of the solitary waves may be a function of their amplitude. Indeed, one may expect intuitively that the greater the amplitude of the deformation, the easier it is for the wind to "push" it.

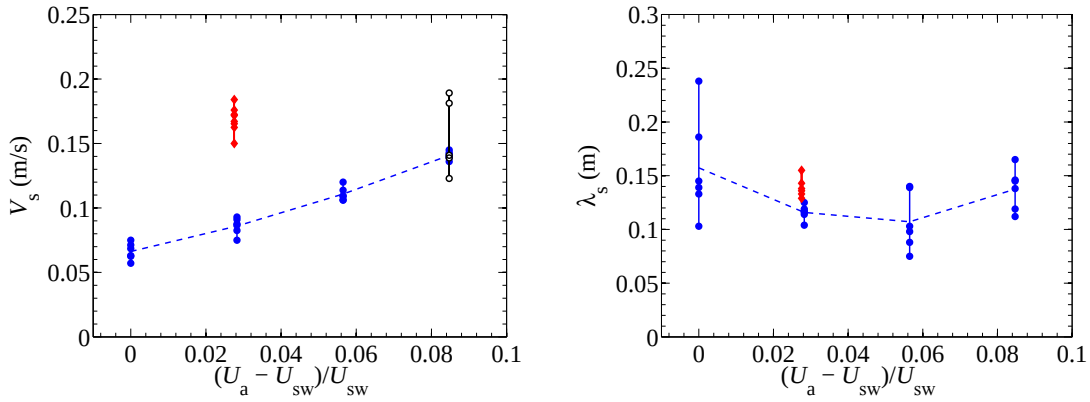

Figure 5.21: Evolution with wind velocity of the propagation velocity V_{sw} of the solitary waves (left) and of separation length λ_{sw} between solitary waves (right), for $\nu = 562 \times 10^{-6}$ m^2.s^{-1} (●) and $\nu = 195 \times 10^{-6}$ m^2.s^{-1} (♦). The dashed line connects the average values given in table 5.5. The open symbols (○) corresponds the propagation velocity of fully transverse solitary waves observed for $\nu = 562 \times 10^{-6}$ m^2.s^{-1}.

3 seconds. Thus, its mean propagation velocity over the entire tank is be of the order of 0.5 m.s^{-1}. However, the maximum velocity measured over the first 40 cm of fetch is below 0.2 m.s^{-1}, which confirms the acceleration of the wave. Note that the non constant velocity of the fully transverse waves may not be the only explanation for the scatter. For example, differences in amplitude may also strongly influence the propagation velocity of the solitary waves.

Contrary to the propagation velocity, the average distance $\overline{\lambda_{sw}}$ separating two waves seems to slightly decrease with wind velocity, at least up to $(U_a - U_{sw})/U_{sw} \simeq 0.06$. However, the scatter is quite large and this result may be questionable. The scatter may be due to the fact that, despite being similar, the propagation velocities of two consecutive waves are not exactly the same, and a solitary wave may catch up or fall behind a little relatively to the preceding or following wave. At $(U_a - U_{sw})/U_{sw} \simeq 0.08$, the decreasing tendency inverts and the average separation length $\overline{\lambda_{sw}}$ slightly increases compared to the preceding value. The scatter of the data, the coexistence of solitary waves on both sides and the occasional emergence of fully transverse waves make it harder to interpret this result and give a definitive conclusion on the apparent increase of $\overline{\lambda_{sw}}$ at high wind velocity.

To conclude, the observation of the solitary waves yield new and interesting results, though still mainly qualitative. A more thorough and complete analysis would be valuable to bring forth more information on this phenomenon.

5.5 Conclusion

In this chapter, wind waves experiments with liquids of different viscosities have been presented to extend the results from chapter 3.

The influence of the viscosity on the evolution of the surface deformation with wind velocity and on the threshold velocity were discussed. In particular, the wrinkles and wave regimes can be identified for all viscosities and results presented in chapter 3 can be found in similar forms over a wide range of viscosity. The transition between the

two regimes becomes more and more abrupt for an increasing viscosity. As the friction velocity seems to be a more relevant parameter than the wind velocity, these results were also presented relatively to the friction velocity. It was found that the amplitude of the surface deformation evolves as $\nu^{-1/2}u^{*3/2}$ in the wrinkles regime. A criterion for wave amplification was introduced on this basis, leading to an evolution of the critical friction velocity as $\nu^{1/5}$, in accordance with the experimental results.

A model was developed to account for this evolution. Starting from the Phillips' model, instead of a slope-based saturation of the effect of the pressure fluctuations on the interface, a viscous cut-off is applied. This model leads to the same evolution of the amplitude of the surface deformation as the experimental data: $\zeta_{rms} \simeq \overline{K^*}\nu^{-1/2}u^{*3/2}$. While this model allows for the collapse of the data in the wrinkles regime to a fairly good extent, experimental results shows that the prefactor $\overline{K^*}$ could be further refined.

In addition to that, a phenomenon specific to high viscosity and high wind velocity was described in the last section of this chapter. Indeed, for a liquid viscous enough and a wind strong enough, peculiar solitary waves appear at the beginning of the tank propagating downstream. A few quantities were measured and rough conclusions were drawn from them. These solitary waves seem to be associated to a distinct instability.

Summary:

- The system behavior is fairly similar over a wide range of viscosity. In particular, the distinction between wrinkles and wave regime can be assessed for all viscosity. The transition between the two regimes becomes more and more abrupt as the viscosity increases.
- The amplitude of the surface deformation evolves as $\nu^{-1/2}u^{*3/2}$ in the wrinkles regime. The critical velocity increases with viscosity as $\nu^{1/5}$.
- A model based on a viscous saturation of Phillips model was developed. It accounts for the evolution of the amplitude of surface deformation with friction velocity and viscosity observed experimentally.
- Solitary waves, possibly associated to a distinct subcritical instability, appear at high viscosity and velocity.

Chapter 6

General conclusion and outlook

Conclusion

Despite the considerable amount of research on the subject and the recent advances in numerical simulations and visualization instrumentation, wind waves still foster a number of open questions. The main part of the literature focuses on wind waves over water and on the wave behavior past the wave generation threshold. In this context, my PhD aimed for a better understanding of the deformation by wind of a viscous interface, but also for an improved comprehension of the influence in this matter of the viscosity of the liquid.

To do so, a new experimental set-up was designed and built. The FS-SS method of visualization was adapted onto it in order to take advantage of its great vertical resolution to explore the first surface deformations. To simplify the problem, the idea was to depart from the literature and carry out the experiments with a liquid much more viscous than water. Indeed, because of this large viscosity, the surface deformations that are not amplified can only propagate over a limited distance and the flow in the tank stays laminar. This last point was verified during the characterization of the flow in the tank and wind tunnel. Performing PIV measurements, the flow in the liquid was indeed observed under the threshold velocity to be laminar, quasi uniform and bidimensional with its mean velocity following the parabolic law solution of the problem for a stationary Stokes flow. Carrying out hot-wire measurements, the airflow characteristics were also assessed and it was found that below the wave generation threshold, the airflow is the same as turbulent flow over a flat fixed wall. This outcome allowed us to later use results from direct numerical simulation databases to get around the experimental difficulties of accessing the pressure field in the airflow close to the interface. The friction velocities deduced from the profiles in the air and in the liquid were shown to be similar, which leads to a single linear empirical law relating the wind velocity and the friction velocity.

Using a liquid thirty times more viscous than water, the surface deformation by the action of wind was explored in details with the FS-SS method of visualization. The experimental results clearly show that there are two regimes of surface deformation.

First, at low wind velocity, the surface of the liquid is populated with small-amplitude disordered surface deformations that we called “wrinkles”. These wrinkles are elongated in the streamwise direction, propagate rapidly downstream, and their amplitude grows linearly with the wind velocity, in an approximately linear manner. However, the wrinkles bear no significant evolution with fetch (the distance of liquid over which the wind blows). These wrinkles can be interpreted as the traces on the interface of the pressure fluctuations

in the turbulent boundary layer above the surface. This is suggested in particular by the comparison of the spatial structures and spatio-temporal dynamics of the surface deformation and those of these turbulent fluctuations.

Secondly, past a certain threshold, at higher wind velocity, well-defined transverse waves of much larger amplitude propagate downstream with their crests quasi normal to the wind direction, yet with dislocations close to the center line. The wave amplitude increases much more quickly with the wind velocity than the wrinkles', and contrary to the wrinkles, the waves' amplitude grows with fetch. Indeed the amplitude of the waves can be fitted exponentially at short fetch. At larger fetch however, nonlinearities play a significant role and the spatial growth of the wave is slower and slower in the downstream direction. Nevertheless, the exponential growth rate measured at small fetch allows to accurately define a critical wind velocity, when the spatial growth rate becomes positive.

Still, the transition from wrinkles to waves is not as abrupt as the precision on the velocity threshold makes it look like. Indeed, in a significant range of velocity around the threshold, both wrinkles and waves are present on the interface. The experimental results suggest that below the critical velocity, waves are locally excited by the wrinkles but are spatially damped, which leads to an apparent zero growth rate and the interface gradually shifts from being dominated by wrinkles to being dominated by transverse waves as the wind speed increases.

The spatial evolution of the wave characteristics in the waves regime was studied subsequently. The effects of nonlinearities lead to an increase of the local wavelength and a decrease of the dominant frequency with fetch. The typical wave steepness also increases with fetch, and may eventually saturate. The evolution of the local phase velocity, defined as the product of the locally predominant wavelength and frequency, is less straightforward. This may be due to the fact that the range of excited modes is quite large and that observed waves are therefore not strictly monochromatic.

The frequency and wavenumber downshift observed in our experiments for waves of small amplitude propagating over short fetch are similar to those reported over water in experiments in longer tanks or at sea. However, the origin of this downshift bears no consensus.

Corrections to the free linear waves inviscid dispersion relation can be made. In our case, all corrections but one, the one due to the current in the tank, may be neglected. Indeed, it was found that the locally dominant wavelength and frequency qualitatively verify the corrected dispersion relation once the drift current is taken into account.

Finally, wind waves experiments with liquids of different viscosities were performed. It was found that many of the results reported during the experiments with the liquid thirty times more viscous than water can be extended over more than two decades of viscosity. In particular, the two regimes of surface deformation were observed at all the viscosities. However, the transition from wrinkles to waves is more and more abrupt as the viscosity increases, meaning that the range of wind velocity around the threshold where both wrinkles and waves cohabit shrinks for more viscous liquids. The critical velocity itself increases with the viscosity to the power 1/5, up to very high viscosities where solitary waves, possibly associated to a distinct instability, were observed.

The evolution of the wrinkles' amplitude with the wind strength is similar for all viscosities. Switching from the wind velocity U_a to the friction velocity u^* for a more refined analysis, it turned out that the linear approximation of the relationship between the two is not accurate enough for such an analysis. Using the complete form of the

friction velocity, the amplitude of the surface deformation in the wrinkles regime evolves as $\nu^{-1/2}u^{*3/2}$. To account for this evolution, a model was developed based on viscous saturation applied to Phillips' model. This new model is able to capture the evolution of the surface deformation both with respect to the viscosity and to the friction velocity.

Outlook

Evolution of a moving local deformation imposed over a viscous liquid

The agreement between our model and experimental data at different viscosity shows the clear correlation between wrinkles and pressure fluctuations. One may note however that, while the analysis of the spatial structures and spatio-temporal dynamics of the surface deformations below the threshold in chapter 3 shows a quantitative agreement with the corresponding characteristics of the pressure fluctuations, this agreement only occurs over a restricted range of low velocities. At higher velocity, viscosity and capillarity have a strong effect on the response of the interface to the pressure fluctuations: the characteristics lengths and velocity of the surface deformations depart from the expected values they would have if the pressure fluctuations had an instantaneous effect on the interface. The actual response is much harder to theorize.

An interesting approach would be to reproduce in a controlled fashion the effect of the pressure fluctuations action on the interface. This can be done experimentally with the FS-SS method by studying the evolution of a perturbation over a liquid surface, for example by locally blowing air over a viscous interface. The inherent difficulty with this problem is the duality of the important time scales: the characteristic time needed for the surface to be fully deformed while the pressure is applied and the characteristic time over which the pressure is actually applied. In the wind waves problem, the latter can be smaller than the former since the pressure fluctuations are intermittent and advected downstream by the airflow. Experiments can help decouple these time scales by either focusing on the interface response to a fixed but time-dependent pressure or to a constant moving pressure.

Note that this approach may be restricted due to the lower limit of the FS-SS method because of the residual vibrations. Recently, the camera has been mounted on a sturdier support and a switch was installed on the camera to temporally stop its fan during acquisitions. In these conditions, the residual vibrations should be reduced sufficiently that the FS-SS lower limit is not of concern anymore (provided that the experiments keep on being carried out during evening or night to avoid outside sources of vibrations). In addition, since the accuracy of the FS-SS technique is directly related to the distance between the interface and the dot pattern, moving this pattern further away should allow to improve the already excellent vertical resolution of the method and to explore even smaller surface deformations.

Theoretical stability analysis

As mentioned in chapter 1, a large number of papers deal with wave generation through the stability analysis of the mean velocity profiles of the air and liquid flows, and the results depend greatly on the shape of those profiles. While stability analysis for a system with a classical turbulent air profile is quite common, the parabolic laminar flow in the liquid is unfortunately less typical. To my knowledge, there is no publication that fully handles the theoretical stability of such a system.

The comparison of our experimental study of wind waves with a stability analysis being of particular interest, this approach has been tested in collaboration with P. D. M. Spelt and L. Ó Náraigh. Using a slightly modified version of their method in [Ó Náraigh et al., 2011] applied to the mean velocity profiles we obtained by hot-wire or PIV measurement, Spelt and Ó Náraigh conducted a linear stability analysis of our system in the case of the 80% glycerol-20% water mixture ($\nu = 30 \times 10^{-6}$ m^2.s^{-1}). Their analysis resulted in the flow being unstable for all velocities studied ($U_a = 5$, 6 and 7 m.s^{-1}). An energy budget analysis places the most unstable mode in the category of an instability induced by tangential disturbances (using the instability classes from [Boomkamp and Miesen, 1996], see section 1.3.2 on page 18). Their theoretical spatial growth rates fairly agree with our experimental measurement, but the associated wavelengths and phase velocities are quite different.

Confirming these results would require to run a linear direct numerical simulation as in [Ó Náraigh et al., 2013]. It would be also interesting to investigate the stability in the case of the other liquids of different viscosity. In any case, these first results are promising and incite further investigation.

Mechanically-forced wind waves

Since the range of unstable modes excited by wind is fairly large and each mode seems to grow at a different rate, it would be interesting to compare purely wind-induced waves to waves of a single frequency affected by wind. To do so, waves can be mechanically generated at a particular frequency in the tank, for example by the oscillation of a rod at a close distance below the interface.

Knowing that even slight perturbations of the interface are picked up by the FS-SS visualization, the set-up used for the forcing must meet a certain number of requirements. First, the forcing rod should be entirely under the surface in order to minimize the interactions with the airflow and avoid the parasitic waves that would be created for example if the support of the rod were going through the interface. Second, the forcing must generate as little vibrations as possible, as preliminary tests on the wind waves set-up proved that slight vibrations are enough to generate longitudinal waves propagating from the sides of the tank to its center that are very visible in the FS-SS reconstruction. These requirements lead to the following design (see Fig. 6.1). The rod is supported by two metal bars and a metal wire connects the rod to a shaker located downwind outside the set-up. This wire is thus the only part of the forcing system that goes through the interface and it does so at a safe distance from the oscillating rod. A generator feeds the shaker with a periodic generation function: the shaker periodically pulls on the wire, causing the rod to oscillate in translation under the interface. Note that if the forcing is not realized close to fetch $x = 0$, part of the generated waves propagate in the upstream direction, allowing to also explore the wave attenuation due to opposing wind.

I designed and tested this forcing concept, while Antoine Hector recently installed the forcing system into the tank and is now carrying out preliminary tests in presence of wind during his internship at the laboratory FAST in April 2016. One goal is to study the amplification or decay of modes based on the wind velocity, in order to better characterize the instability. The preliminary results in this matter are encouraging and more experiments are planned.

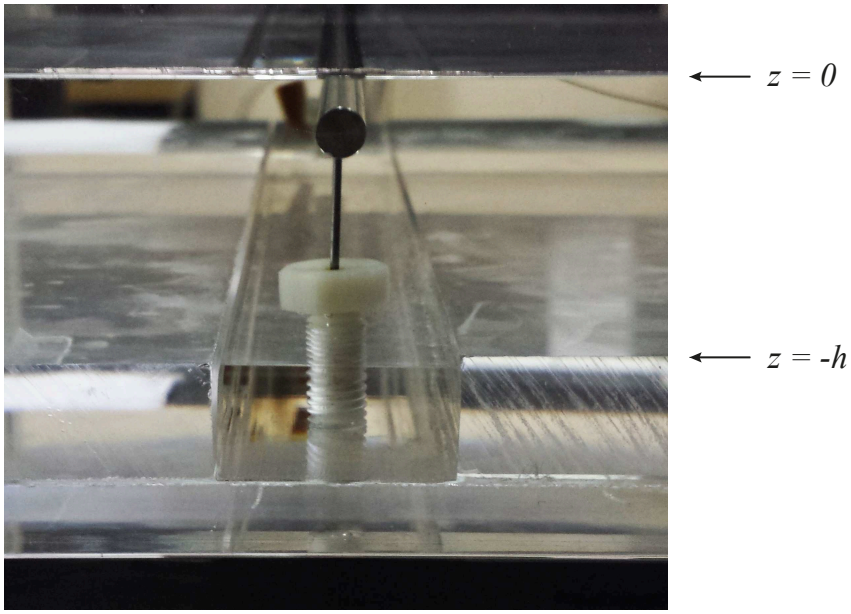

Figure 6.1: Close-up picture of the oscillating rod of the forcing system. The distance between the rod and the surface can be adjusted thanks to the plastic screws in which the bars supporting the rod are inserted.

Nonlinear evolution of wind waves

In order to account for the spatial evolution of the waves' characteristics in the wave regime, we attempted to develop a model based on the assumption that each unstable mode grows independently downstream and saturates when reaching a certain slope. The nonlinearities would then arise from the sequential saturation of these non interacting unstable modes as they reach the limiting slope one after the other when traveling downstream. While a discrete description leads to encouraging results, a mathematically rigorous continuous description proved to be a (still standing) challenge. Indeed, in the spectral description, the criterion for the saturation of one mode can not be defined based on a limiting steepness and another more adequate criterion remains to be found.

There may be two other more fundamental reasons that cause our difficulties. First, as discussed in [Annenkov and Shrira, 2013], the inherent broadness of the range of excited modes makes it difficult to precisely define the waves' characteristics. Indeed, characterizing without ambiguity a given wave field by a single frequency or wavelength, even just locally, requires a narrow band so that the most energetic mode alone can depict the whole wave field. As a consequence, the definition of the local wavelength or frequency may not be as simple as it seems and the characteristics of broadband wind waves may be accurately described only by a spectral approach.

This leads to the second problem: the spectral description itself. Indeed, Huang et al. argue that the Fourier spectrum, very commonly used in the analysis of the frequency downshift of wind waves, is "a very poor way" to analyze or quantify the downshift phenomenon [Huang et al., 1999] [1]. Arguing that the perturbation approach used in Fourier view is limited to only small linearities and that the solution to a collection of linear

1. To quote them: "Is the peak frequency change a good measure of downshift? Or is Fourier spectral analysis a good tool for studying downshift? The answer to both these questions is no."

equations may have different physical and mathematical properties than the solution to a nonlinear equation, they propose a Hilbert spectrum analysis method as an alternative. To my knowledge, their suggestion has not been successfully followed and a full explanation of the frequency downshift using Hilbert spectrum analysis remains to be developed. It thus would be interesting to attempt a Hilbert spectrum analysis of our experimental data.

Solitary waves

A last topic that could be explored in the future is the phenomenon of solitary waves reported for strong winds over very viscous liquids (see section 5.4 on page 112). More information is obviously required to better characterize these solitary waves. In particular, knowing how the amplitude of a solitary wave evolves during its propagation and how this amplitude relates to its propagation velocity is of particular importance. Unfortunately, the FS-SS method is of little help in this matter, as such high amplitudes are out of its range. Another technique with the appropriate measurement range would have to be implemented on the set-up. For example, fringe profilometry with its micrometric range may be used [Cobelli et al., 2009]. Due to the relatively high amplitude and spatial extension of the solitary waves, the influence of the depth of the tank is an open problem as well. The question of this influence of the liquid depth could be addressed by removing the 15-mm thick Plexiglas plate originally put at the bottom of the tank to reduce the liquid height to $h = 35$ mm. Using plates of a different thickness (or no plate at all) would allow to vary the liquid depth at will up to 50 mm.

From a more theoretical point of view, one could also examine whether this name of "solitary waves" is really suited in the physical sense for these large-amplitude slowly propagating deformations, i.e. whether these so-called solitary waves we observe actually are solitary waves. While there is no consensus of the exact definition of a soliton, three properties are generally ascribed to solitons: localness (the wave is localized within a region), shape permanence (the wave retains the same form as it propagates) and reversible interactions with other solitons (after a collision, two waves emerge unchanged) [Helal, 2009]. Determining if the solitary waves we observe in our system at high viscosity and high wind velocity do verify these properties would help defining the equations related to this phenomenon. The Korteweg-de Vries equation is often used to describe solitons in water [Michallet and Barthelemy, 1998] [Charru, 2011], but it should be noted that other possibly applicable equations, like the nonlinear Schrödinger equation, used to described the nonlinear evolution of a wave packet, have soliton solutions [Peregrine, 1983]. As pointed out in chapter 5, the solitary waves we observe could derive from the short wavelength cut-off due to viscosity or may be compared to nonsymetrical waves (that are not necessary solitary) in quite different systems, possibly leading to very different equations.

Appendix A

FS-SS: Experiments and computations

General view

Graphic A.1 details the different steps during an experiment.

A few precautions are to be taken before any acquisition. The tilts of the camera, tank and mirror are checked. The density and temperature of the liquid are measured at the beginning and end of the experiment. The liquid is thoroughly mixed and a maximum of the surface pollutants is eliminated after having gathered them at the end of the tank by blowing a strong wind. After that, the level of liquid is adjusted in absence of wind to be precisely at $x = 0$ by using the tangential reflection of a laser sheet intersecting the upstream plate and the liquid surface. No liquid is to be added or subtracted after this operation. Indeed, the reference image used for the FS-SS computation is acquired when the liquid is at rest at $x = 0$ with the wind blower off. If liquid overflows from the tank because of waves of great amplitude, the liquid is leveled again and a new reference image is taken. The temperature is checked frequently during the experiment. If the variation to the mean temperature is of more that 0.5°C, acquisitions have to be discarded because of the resulting variation of the viscosity of the liquid.

Once the reference image have been acquired, the wind blower is turned on to the adequate wind velocity. After waiting a few minutes for the system to reach its stationary state, an acquisition can be started. Then, the recorded images are transferred from the camera to the computer before the next acquisition.

A laser was installed to evaluate the presence of vibrations likely to disturb the experiments. The laser dot is reflected on the surface of the liquid in the tank to a sheet of graph paper taped on the opposing wall of the room. When the dot is moving while the liquid is supposed totally at rest, it means that small vibrations are transmitted to the set-up from the ground and that FS-SS acquisitions should not be performed for wind velocities below the waves threshold. If they are, the surface fields present long transverse waves propagating from the walls to the center of the tank (see Fig. A.2).

Computations

Displacement field

The images are imported into Davis 8.1 from the format *.tiff* and converted into the format *.IM7*. Once the calibration of the images is done, the displacement fields are

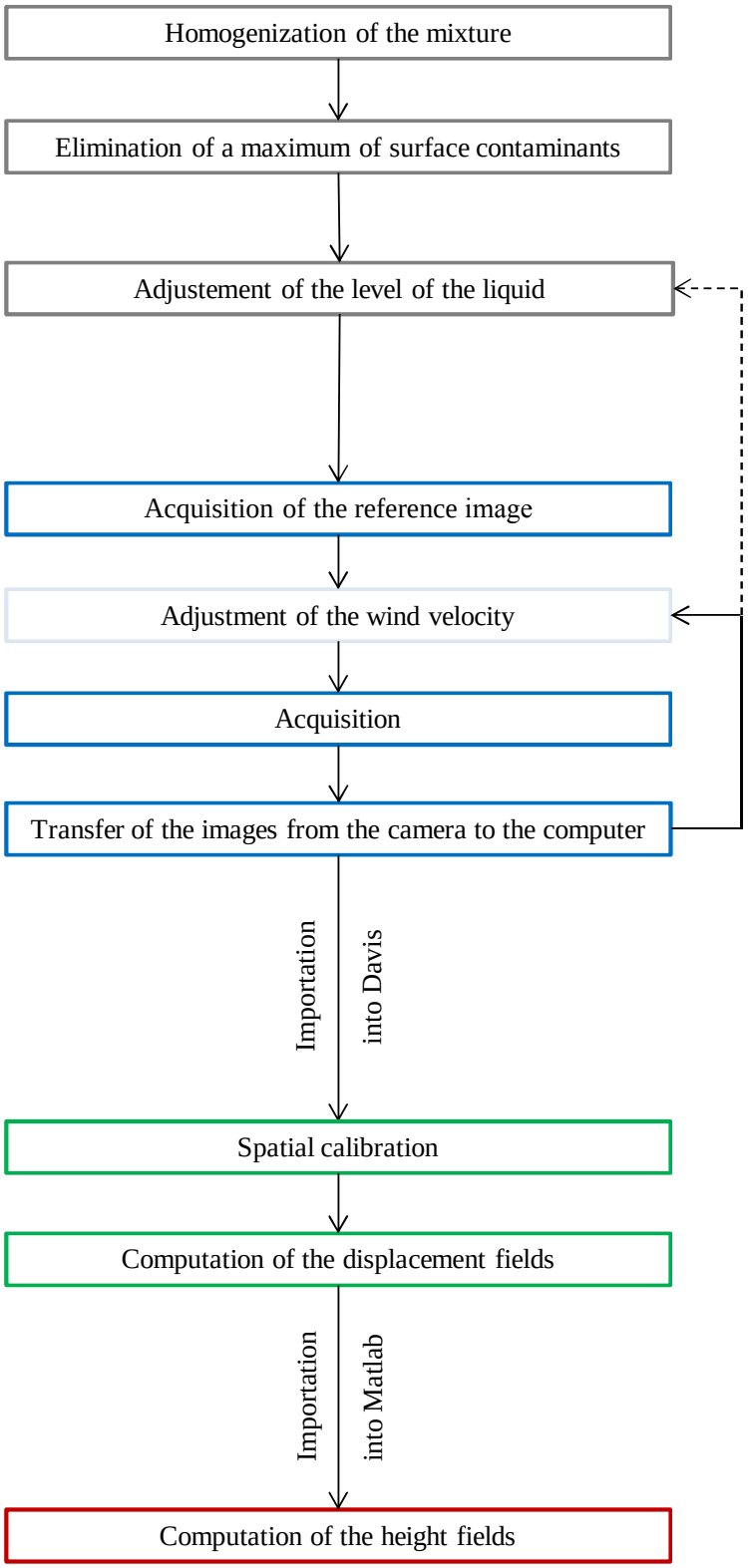

Figure A.1: Graphic of the different steps during an experiment and the subsequent FS-SS computations.

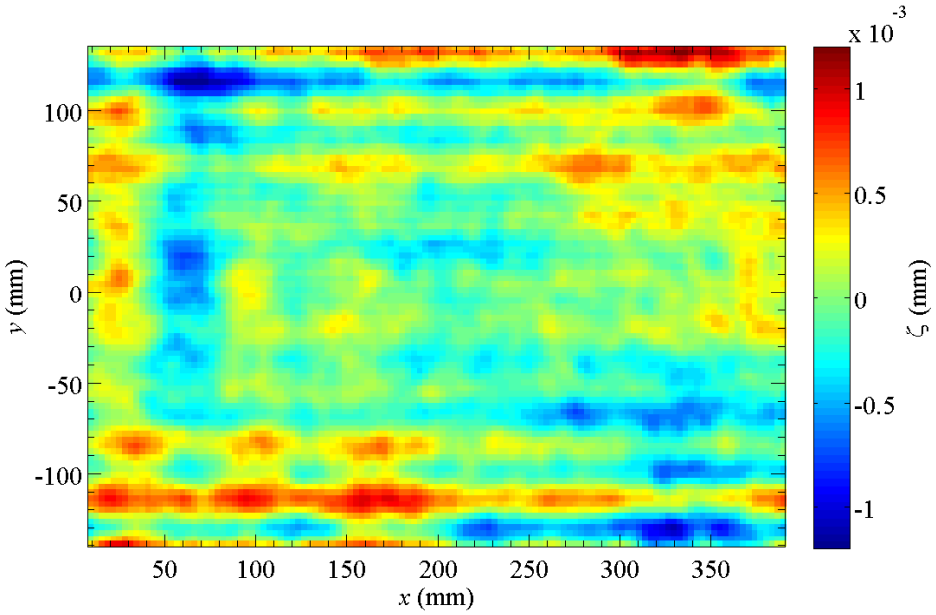

Figure A.2: Parasitic waves originating from vibrations of the lateral walls ($y = \pm 150$ mm).

computed and returned in *.VC7* format. To quicken the computations, a 'mask' is created to discard the regions of the field of view outside the dot pattern.

The displacement fields are computed by cross-correlation similarly to the classical PIV method. Each frame is separated in interrogation windows. For each interrogation windows, the Davis software searches where the content of that window has moved from its initial position in the reference image. To do so, cross-correlation is computed in the vicinity around the window that is being considered. The displacement is defined by the location of the highest correlation peak. The best results are obtained with three passes: the first one with interrogation windows of size of 32×32 pixels, then two passes with windows of size 16×16 pixels (decreasing the window size allows to refine the computation). The first two passes use the standard cross-correlation function, the last one uses a normalized version of it.

Surface height field

The *.VC7* files are imported into Matlab and the computation of the height fields is realized using the function *surfheight* of the Matlab toolbox PIVMat developed by Moisy [1]. This function takes in input the displacement field, the equivalent mean height of liquid, the refractive index, the distance from the camera to the pattern and the position of the center of the camera [2] and gives in return the height field $\zeta(x, y, t)$. Some options can be chosen in order to take into account the parallax (option 'remap') or to subtract the average displacement (option 'submean'). Both these options are used in the computations.

1. More information on this toolbox and the implementation of the FS-SS method can be found on the FAST website, see `http://www.fast.u-psud.fr/pivmat/` and `http://www.fast.u-psud.fr/~moisy/sgbos/tutorial.php`.

2. Adding the distance from the camera to the pattern and the position of the center of the camera to the input variables is not absolutely necessary for the computation of the surface height but leads to more accurate results. In their absence, the camera is supposed to be infinitely far away from the pattern and perfectly centered.

In particular, the option 'submean' allows to remove the uniform displacement added by the slight vibration of the camera due to its cooling fan. However, it induces an artificial change in the mean displacement field when a wave enters or leaves the field of visualization that translate into oscillation of the surface field around the center of the field in the x direction. This oscillation does not change the global root mean square of the amplitude of the surface deformation (over the entire field of view). However, it has a strong influence of the local root mean square of the deformation amplitude: it leads to the overestimation of this root mean square in the outermost regions of the field. This effect is counteracted by the use of a highpass filter. Since the highest wavelength of the wind waves is a factor of 4 smaller than the dimension in the x direction of the field of view, the global oscillation of the field can be efficiently filtered out. This issue has been recently resolved by the addition of a switch on the camera in order to be able to temporally stop its fan during acquisitions.

Appendix B

Thesis abstract in French

Malgré les nombreux travaux théoriques, expérimentaux et numériques sur le sujet, un certain nombre de questions demeure sans réponse précise à propos de la formation des vagues sous l'effet du vent. Les mécanismes de génération et de croissance des vagues induites par un écoulement d'air restent encore mal compris et les prédictions fournies par les modèles existants (les plus classiques étant ceux de Kelvin-Helmholtz [von Helmholtz, 1868] [Thomson, 1871], de Phillips [Phillips, 1957] et de Miles [Miles, 1957]) sont souvent contradictoires et assez éloignées de la réalité. Afin d'étudier l'origine de la formation des premières vagues par le vent, j'aborde ce problème dans ma thèse selon une approche peu explorée : l'étude expérimentale de la déformation sous l'effet du vent de la surface d'un liquide fortement visqueux.

Montage expérimental

Le montage expérimental est constitué d'une cuve en Plexiglas mesurant 1.5 m de long sur 296 mm de large et de profondeur 35 mm (cette profondeur est suffisante pour être dans l'approximation des grandes profondeurs pour les ondes observées). Cette cuve est surmontée par un canal de même largeur et de hauteur 105 mm, complété en amont et aval de la cuve par deux zones planes de 26 cm (voir Fig. B.1). La cuve est remplie de liquide de telle façon à ce que le niveau du liquide coïncide exactement avec la surface inférieure du canal. Une soufflerie injecte de l'air dans le canal à une vitesse moyenne ajustable entre 1 et 10 m/s. Contrairement à la majeure partie de la littérature sur le sujet, le liquide utilisé n'est pas de l'eau mais un liquide sensiblement plus visqueux (1 à 600 fois la viscosité de l'eau, suivant les expériences). Cela a en pratique l'avantage de simplifier le problème : l'écoulement dans le liquide reste laminaire et les perturbations de l'interface qui ne sont pas amplifiées ne peuvent se propager que sur une distance limitée.

La mesure de la hauteur du liquide est réalisée par la méthode optique Free Surface-Synthetic Schlieren (FS-SS) [Moisy et al., 2009]. Pour cela, un motif aléatoire de points disposé sous la cuve est filmé par une caméra rapide à travers l'interface sur un large champ de visualisation. Un calcul par corrélation d'image permet d'en déduire le déplacement apparent des points entre l'image de référence (quand le liquide est au repos) et l'image déformée (quand l'interface est perturbée) à partir duquel la topographie de l'interface peut être entièrement reconstruite avec une résolution verticale micrométrique.

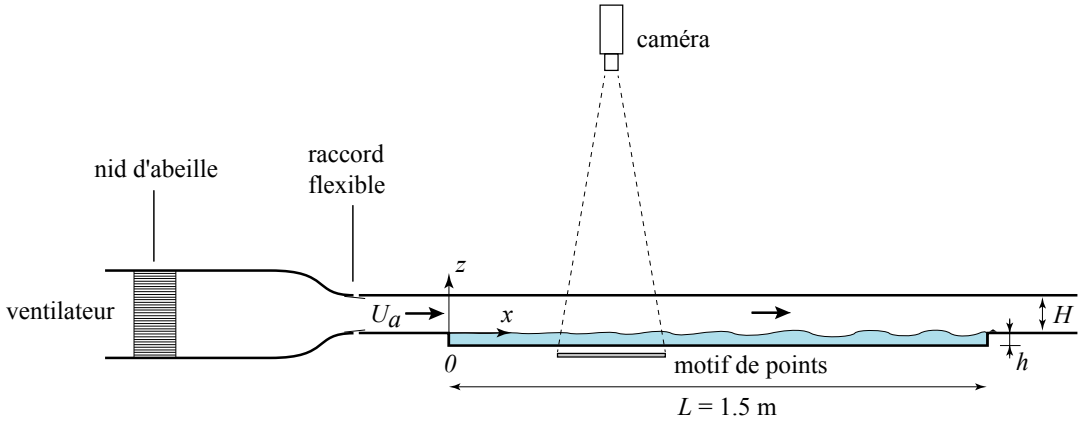

Figure B.1: Schéma du montage expérimental.

Résultats principaux

• Deux régimes de déformation de l'interface

Dans un premier temps, les expériences ont été conduites sur un liquide trente fois plus visqueux que l'eau. Grâce aux données expérimentales obtenues par FS-SS (voir Fig. B.2), deux régimes de déformation de l'interface liquide-air ont été mis en évidence. À vitesse de vent faible, l'interface est recouverte de "wrinkles", des perturbations de faible amplitude à peine visibles à l'œil nu, désorganisées spatialement et globalement alignées dans le sens de l'écoulement. À plus forte vitesse, au-dessus d'une vitesse critique de vent, apparaissent des vagues transverses perpendiculaires à la direction du vent et quasi-parallèles entre elles.

Les distinctions entre les deux régimes sont détaillées dans ces travaux de thèse. En particulier, à faible vitesse de vent, l'amplitude des vagues augmente lentement avec la vitesse du vent en suivant une loi de puissance avec un exposant proche de l'unité. Au dessus d'un certain seuil, l'amplitude continue de croître avec la vitesse du vent mais beaucoup plus rapidement que dans le premier régime, d'où la rupture de pente nette au passage entre les deux régimes (voir Fig. B.3). De plus, les wrinkles ne croissent pas avec la distance depuis le début de la cuve (fetch) alors que l'amplitude des vagues transverses augmentent avec cette distance (d'abord exponentiellement, puis plus lentement en aval quand les effets non-linéaires ne sont plus négligeables). Par ailleurs, la comparaison des structures spatiale et spatio-temporelle des wrinkles avec des résultats de simulations numériques de l'écoulement d'air au-dessus d'une paroi [Jimenez and Hoyas, 2008] montrent que l'on peut interpréter les wrinkles comme la réponse de l'interface visqueuse aux fluctuations de pression dans la couche limite turbulente.

• Non-linéarités des vagues de vent

Les non-linéarités émergeant au-dessus du seuil ont aussi été étudiées. Il apparaît que ces non-linéarités affectent significativement les vagues de vent observées, de faibles amplitudes se propageant sur de faibles distances (voir Fig. B.4), et ce de façon similaire à ce qui peut être constaté par exemple en mer pour des vagues de plus grandes amplitude se propageant sur de plus grandes distances. En particulier, on retrouve deux phénomènes souvent mentionnés dans la littérature : l'augmentation de la longueur d'onde avec le fetch et la diminution de la fréquence avec le fetch (voir Fig. B.5). Si des pistes existent pour expliquer ces effets non-linéaires, la question de leur origine reste cependant ouverte.

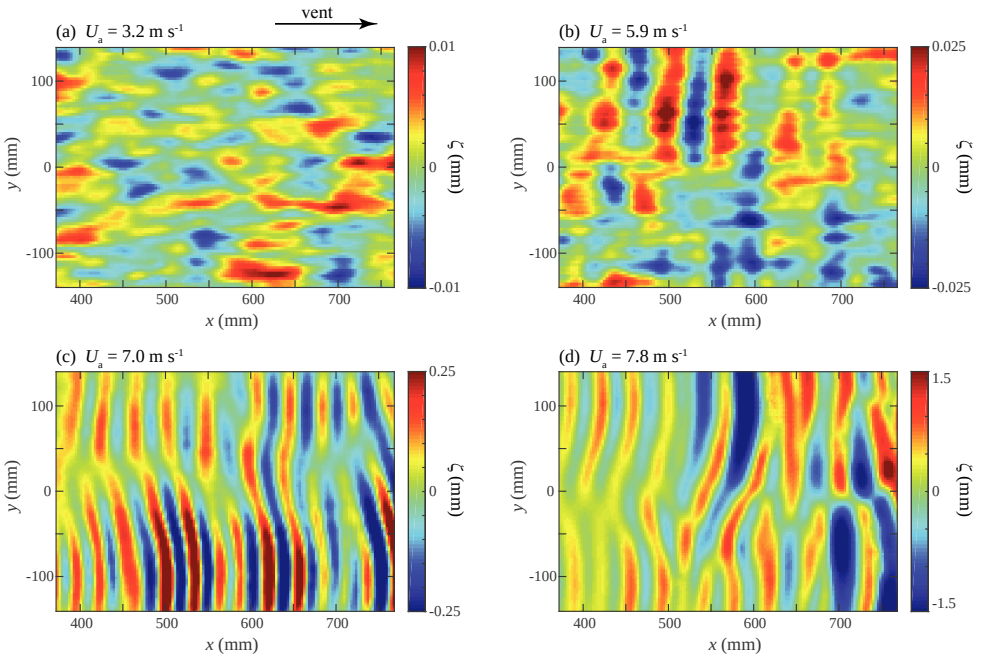

Figure B.2: Champ de hauteur instantanés mesurés par FS-SS pour des vitesses de vent croissantes. (a) $U_a = 3.2$ m.s^{-1}, montrant des wrinkles désorganisés de faible amplitude dans la direction du vent. (b) $U_a = 5.9$ m.s^{-1}, montrant une combinaison de wrinkles et d'ondes transversales. (c) $U_a = 7.0$ m.s^{-1}, montrant des vagues transversales bien définies de longueur d'onde moyenne $\lambda = 35$ mm. (d) $U_a = 7.8$ m.s^{-1}, montrant des vagues de grande amplitude de longueur d'onde moyenne $\lambda = 44$ mm avec un désordre croissant. Le vent souffle de la gauche vers la droite. Remarque : l'échelle de couleurs n'est pas la même pour les quatre champs de hauteur.

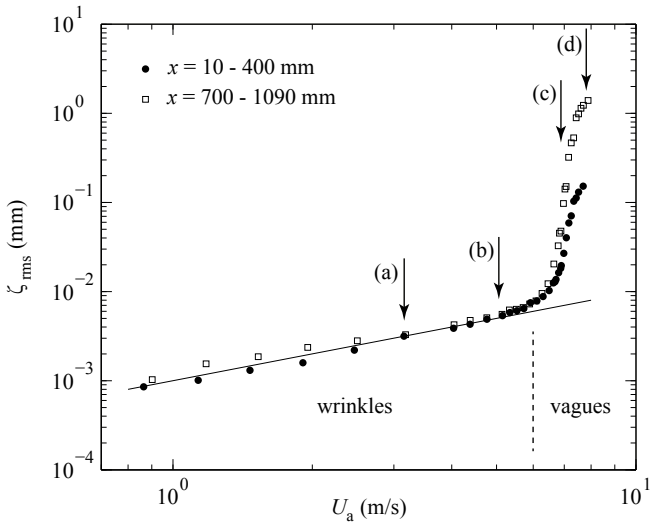

Figure B.3: Amplitude moyenne des déformations ζ_{rms} en fonction de la vitesse du vent U_a. Les données sont moyennées sur la fenêtre de visualisation 390 × 280 mm centré à deux valeurs de fetch $x = 205$ mm (•) et $x = 895$ mm (□). Les lettres et les flêches verticales correspondent aux quatre champs de hauteur instantanés de la figure B.2. La ligne continue correspond à l'approximation linéaire $\zeta_{\text{rms}} = \alpha U_a$, avec $\alpha = 10^{-6}$ s.

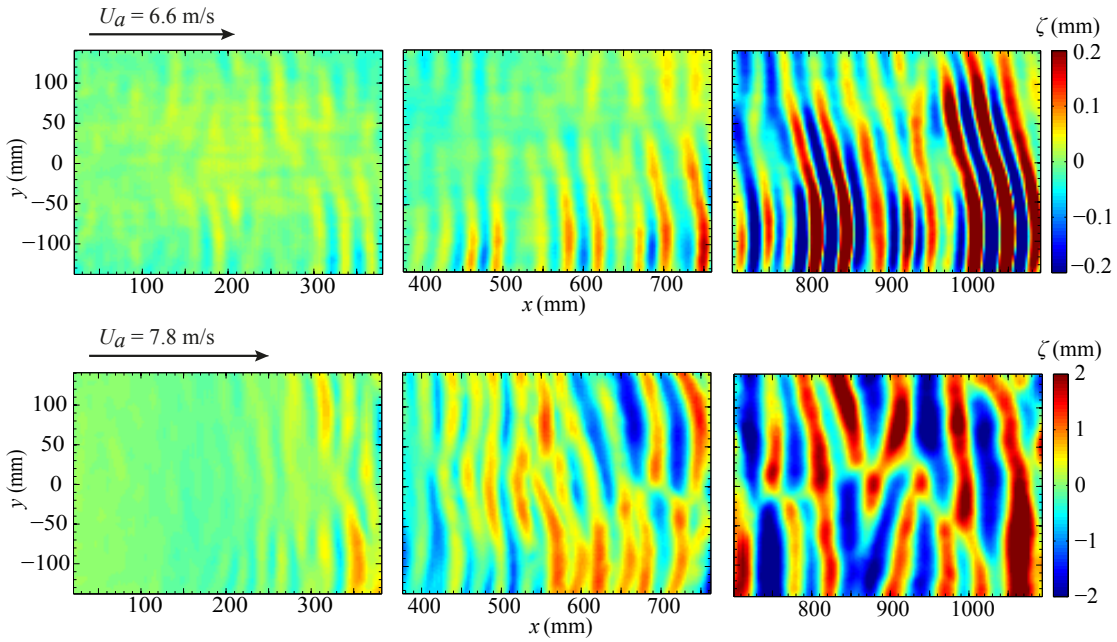

Figure B.4: Champ de hauteur $\zeta(x, y, t)$ pour deux vitesses de vent $U_a = 6.6$ m.s^{-1} (haut) et $U_a = 7.8$ m.s^{-1} (bas). Le vent souffle de la gauche vers la droite. L'enregistrement sur chaque portion de fetch est réalisée durant une acquisistion différente. Remarque : l'échelle des couleurs n'est pas la même sur les deux lignes (la même couleur représente une déformation dix fois plus grande sur la deuxième ligne que sur la première).

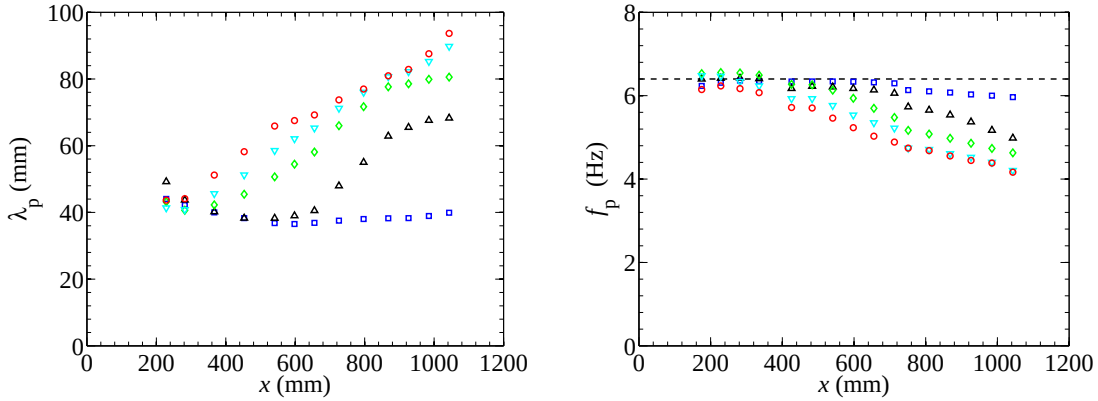

Figure B.5: Longueur d'onde dominante $\lambda_p(x)$ (gauche) et fréquence dominante $f_p(x)$ (droite) en fonction du fetch x, pour les vitesses de vent $U_a = 6.6$ (□), 6.9 (△), 7.2 (◇), 7.5(▽) et 7.8 m.s^{-1}(○).

• Influence de la viscosité du liquide sur la formation des vagues de vent

La viscosité du liquide a par la suite été changée sur une large gamme (1 à 600 fois la viscosité de l'eau). Les expériences montrent que les deux régimes de déformation de l'interface sous l'effet du vent précédemment identifiés pour un liquide trente fois plus visqueux que l'eau se retrouvent sur l'ensemble des viscosités parcourues (voir Fig. B.6). Le seuil de génération des vagues augmente avec la viscosité du liquide. Plus précisément, la vitesse de friction critique évolue selon une loi de puissance d'ordre 0.20 (voir Fig. B.7) :

$$u_c^* \propto \nu^{0.20} \tag{B.0.1}$$

Il découle également des données expérimentales que dans le régime des wrinkles, l'amplitude des wrinkles évolue comme la vitesse de friction à la puissance 3/2 et comme la viscosité cinématique à la puissance -1/2 (voir Fig. B.6) :

$$\zeta_{rms} \propto u^{*3/2} \nu^{-1/2} \tag{B.0.2}$$

Suite à ces résultats, un modèle décrivant l'évolution de l'amplitude des wrinkles en fonction du vent et de la viscosité du liquide a été développé à partir d'une saturation visqueuse du modèle de Phillips. Ce modèle permet de renormaliser les résultats sur une courbe maîtresse, à l'exception des données obtenues dans l'eau (voir Fig. B.8), confirmant la validité du modèle.

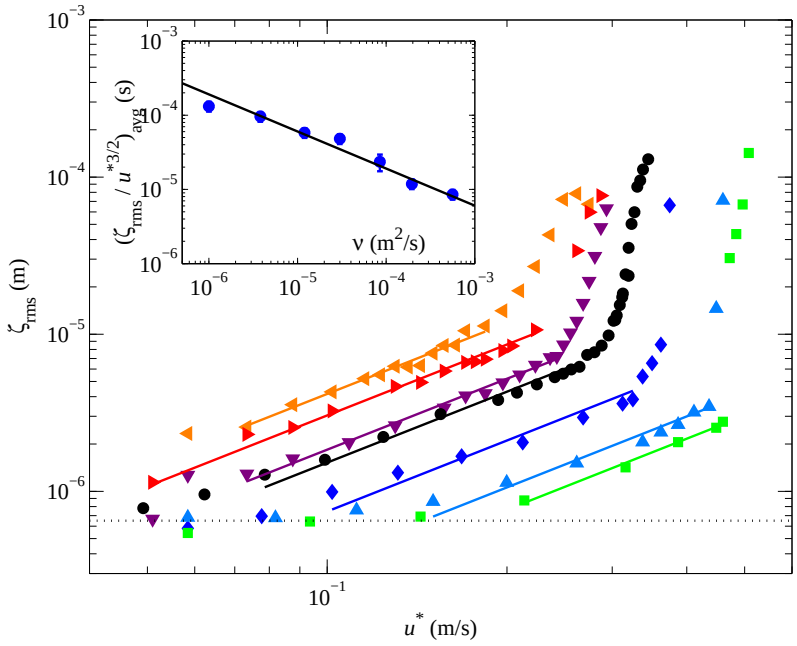

Figure B.6: Moyenne quadratique de la hauteur de l'interface (moyennée en temps et en espace sur x = 150-300 mm) en fonction de la vitesse de friction. De haut en bas, ces résultats correpondent à une viscosité ν = 1.0, 3.9, 12, 30, 85, 195 and 562 $\times 10^{-6}$ m^2.s^{-1}. Les lignes continues correspondent à une évolution en puissance 3/2. La ligne horizontale pointillée est une limite basse ζ_{rms} = 0.65 μm liée aux vibrations résiduelles. Encart : Coefficient $\zeta_{rms}/u^{*3/2}$ dans le régime des wrinkles en fonction de la viscosité cinématique ν. La ligne montre le fit $\alpha\nu^{-1/2}$ avec $\alpha = 1.9 \times 10^{-7}$ m$^{1/2}$.s.

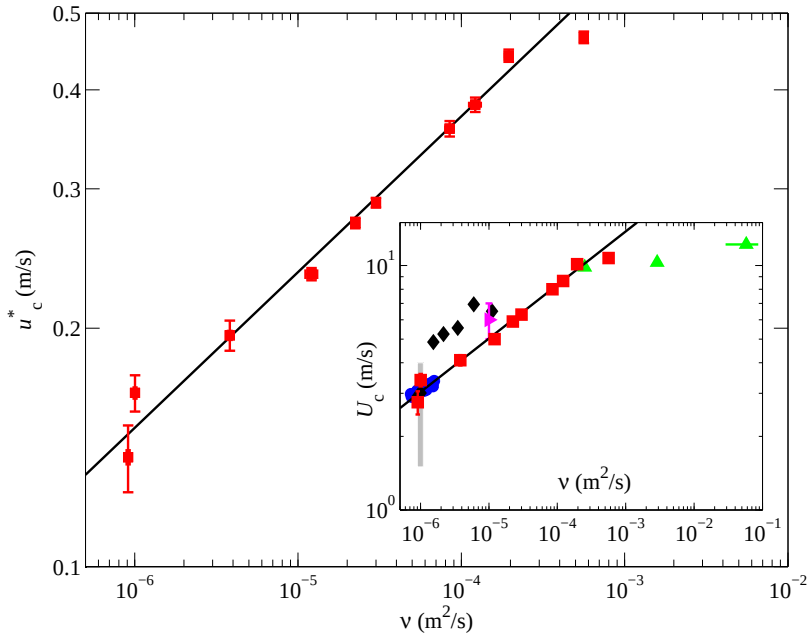

Figure B.7: Vitesse de friction critique u_c^* en fonction de la viscosité cinématique du liquide. La ligne continue montre le fit $u_c^* = a\nu^{0.20}$ avec $a = 2.3$ SI. Encart : Vitesse seuil de génération des vagues en fonction de la viscosité cinématique. Les carrés rouges (■) correspondent à nos données expérimentales ; les losanges noires (⧫), les triangles verts (▲), les points bleus (●) et le triangle magenta (►) correspondent respectivement aux données de [Keulegan, 1951], [Francis, 1956], [Kahma and Donelan, 1988] et [Gottifredi and Jameson, 1970]. Le rectangle gris représente l'intervalle des vitesses seuil de la littérature obtenues avec de l'eau. La ligne continue est une loi de puissance $U_c = a\nu^n$, avec $n = 0.22$ et $a = 62.6$ SI.

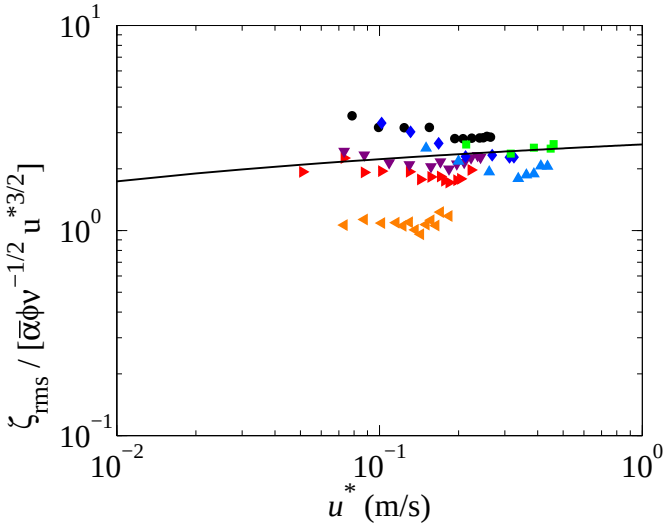

Figure B.8: Évolution de $\zeta_{rms}/\overline{\alpha}\phi\nu^{-1/2}u^{*3/2}$ en fonction de la vitesse de friction. La ligne continue correspond à $0.57f(Re_\tau)$. Pour les symboles, se référer à la figure B.6.

Bibliography

[André and Bardet, 2014] André, M. A. and Bardet, P. M. (2014). Velocity field, surface profile and curvature resolution of steep and short free-surface waves. *Exp. Fluids*, 55(4):1–19.

[Annenkov and Shrira, 2013] Annenkov, S. Y. and Shrira, V. I. (2013). Large-time evolution of statistical moments of wind–wave fields. *J. Fluid Mech.*, 726:517–546.

[Babanin, 2011] Babanin, A. (2011). *Breaking and dissipation of ocean surface waves*. Cambridge University Press.

[Babanin et al., 2012] Babanin, A. V., Onorato, M., and Qiao, F. (2012). Surface waves and wave-coupled effects in lower atmosphere and upper ocean. *Journal of Geophysical Research: Oceans*, 117(C11).

[Barthelet et al., 1995] Barthelet, P., Charru, F., and Fabre, J. (1995). Experimental study of interfacial long waves in a two-layer shear flow. *J. Fluid Mech.*, 303:23–53.

[Belcher and Hunt, 1993] Belcher, S. E. and Hunt, J. C. R. (1993). Turbulent shear flow over slowly moving waves. *J. Fluid Mech.*, 251:109–148.

[Benjamin, 1959] Benjamin, T. B. (1959). Shearing flow over a wavy boundary. *J. Fluid Mech.*, 6(02):161–205.

[Benjamin and Feir, 1967] Benjamin, T. B. and Feir, J. E. (1967). The disintegration of wave train on deep water, i: Theory. *J. Fluid Mech.*, 27:417–430.

[Blennerhassett, 1980] Blennerhassett, P. J. (1980). On the generation of waves by wind. *Philosophical Transactions of the Royal Society of London. Series A, Mathematical and Physical Sciences*, pages 451–494.

[Bliven et al., 1986] Bliven, L. F., Huang, N. E., and Long, S. R. (1986). Experimental study of the influence of wind on Benjamin–Feir sideband instability. *J. Fluid Mech.*, 162:237–260.

[Bole and Hsu, 1969] Bole, J. B. and Hsu, E. Y. (1969). Response of gravity water waves to wind excitation. *J. Fluid Mech.*, 35(04):657–675.

[Boomkamp and Miesen, 1996] Boomkamp, P. and Miesen, R. (1996). Classification of instabilities in parallel two-phase flow. *International Journal of Multiphase Flow*, 22:67–88.

[Bretschneider, 1951] Bretschneider, C. L. (1951). Revised wave forecasting relationships. *Coastal Engineering Proceedings*, 1(2):1.

[Buckley and Veron, 2016] Buckley, M. P. and Veron, F. (2016). Structure of the airflow above surface waves. *Journal of Physical Oceanography*, 46(5):1377–1397.

[Carter and Govan, 2016] Carter, J. D. and Govan, A. (2016). Frequency downshift in a viscous fluid. ArXiv:1601.03932.

[Caulliez, 1987] Caulliez, G. (1987). Measuring the wind-induced water surface flow by laser doppler velocimetry. *Exp. Fluids*, 5(3):145–153.

[Caulliez, 2013] Caulliez, G. (2013). Dissipation regimes for short wind waves. *Journal of Geophysical Research: Oceans*, 118(2):672–684.

[Caulliez and Collard, 1999] Caulliez, G. and Collard, F. (1999). Three-dimensional evolution of wind waves from gravity-capillary to short gravity range. *European Journal of Mechanics-B/Fluids*, 18(3):389–402.

[Caulliez et al., 2007] Caulliez, G., Dupont, R., and Shrira, V. (2007). Turbulence generation in the wind-driven subsurface water flow. In *Transport at the Air-Sea Interface*, pages 103–117. Springer.

[Caulliez et al., 2008] Caulliez, G., Makin, V., and Kudryavtsev, V. (2008). Drag of the water surface at very short fetches: Observations and modeling. *Journal of Physical Oceanography*, 38(9):2038–2055.

[Caulliez et al., 1998] Caulliez, G., Ricci, N., and Dupont, R. (1998). The generation of the first visible wind waves. *Phys. Fluids*, 10(4):757–759.

[Charru, 2011] Charru, F. (2011). *Hydrodynamic Instabilities*, volume 37. Cambridge University Press.

[Charru and Hinch, 2000] Charru, F. and Hinch, E. J. (2000). 'phase diagram' of interfacial instabilities in a two-layer Couette flow and mechanism of the long-wave instability. *J. Fluid Mech.*, 414:195–223.

[Cherukat et al., 1998] Cherukat, P., Na, Y., Hanratty, T. J., and McLaughlin, J. B. (1998). Direct numerical simulation of a fully developed turbulent flow over a wavy wall. *Theoretical and computational fluid dynamics*, 11(2):109–134.

[Choi and Moin, 1990] Choi, H. and Moin, P. (1990). On the space-time characteristics of wall-pressure fluctuations. *Physics of Fluids A: Fluid Dynamics (1989-1993)*, 2(8):1450–1460.

[Cobelli et al., 2009] Cobelli, P. J., Maurel, A., Pagneux, V., and Petitjeans, P. (2009). Global measurement of water waves by Fourier transform profilometry. *Exp. Fluids*, 46(6):1037–1047.

[Cochard and Ancey, 2008] Cochard, S. and Ancey, C. (2008). Tracking the free surface of time-dependent flows: image processing for the dam-break problem. *Exp. Fluids*, 44(1):59–71.

[Connell and Yue, 2007] Connell, B. S. H. and Yue, D. K. P. (2007). Flapping dynamics of a flag in a uniform stream. *J. Fluid Mech.*, 581:33–67.

[Conte and Miles, 1959] Conte, S. D. and Miles, J. W. (1959). On the numerical integration of the orr-sommerfeld equation. *Journal of the Society for Industrial and Applied Mathematics*, 7(4):361–366.

[Dalziel et al., 2000] Dalziel, S. B., Hughes, G. O., and Sutherland, B. R. (2000). Whole-field density measurements by 'synthetic schlieren'. *Exp. Fluids*, 28(4):322–335.

[De Angelis et al., 1997] De Angelis, V., Lombardi, P., and Banerjee, S. (1997). Direct numerical simulation of turbulent flow over a wavy wall. *Phys. Fluids (1994-present)*, 9(8):2429–2442.

[Deardorff, 1967] Deardorff, J. W. (1967). Aerodynamic theory of wave growth with constant wave steepness. *J. Oceanographical Soc. Japan*, 23(6):278–297.

[Deck et al., 2014] Deck, S., Renard, N., Laraufie, R., and Weiss, P.-É. (2014). Large-scale contribution to mean wall shear stress in high-Reynolds-number flat-plate boundary layers up to 13650. *J. Fluid Mech.*, 743:202–248.

[Dias and Kharif, 1999] Dias, F. and Kharif, C. (1999). Nonlinear gravity and capillary-gravity waves. *Annual Review of Fluid Mechanics*, 31(1):301–346.

[Donelan et al., 2006] Donelan, M. A., Babanin, A. V., Young, I. R., and Banner, M. L. (2006). Wave-follower field measurements of the wind-input spectral function. Part II: Parameterization of the wind input. *Journal of Physical Oceanography*, 36(8):1672–1689.

[Donelan and Plant, 2009] Donelan, M. A. and Plant, W. J. (2009). A threshold for wind-wave growth. *Journal of Geophysical Research*, 114(C7):C07012.

[Durán et al., 2008] Durán, O., Silva, M., Bezerra, L., Herrmann, H., and Maia, L. (2008). Measurements and numerical simulations of the degree of activity and vegetation cover on parabolic dunes in north-eastern Brazil. *Geomorphology*, 102(3):460–471.

[Dysthe, 1979] Dysthe, K. B. (1979). Note on a modification to the nonlinear Schrödinger equation for application to deep water waves. In *Proceedings of the Royal Society of London A: Mathematical, Physical and Engineering Sciences*, volume 369, pages 105–114. The Royal Society.

[Ebuchi et al., 1987] Ebuchi, N., Kawamura, H., and Toba, Y. (1987). Fine structure of laboratory wind-wave surfaces studied using an optical method. *Boundary-Layer Meteorology*, 39(1-2):133–151.

[Eckart, 1953] Eckart, C. (1953). The generation of wind waves on a water surface. *Journal of Applied Physics*, 24(12):1485–1494.

[Ellingsen and Brevik, 2014] Ellingsen, S. A. and Brevik, I. (2014). How linear surface waves are affected by a current with constant vorticity. *Eur. J. Phys.*, 35:025005.

[Falcão, 2010] Falcão, A. F. O. (2010). Wave energy utilization: A review of the technologies. *Renewable and sustainable energy reviews*, 14(3):899–918.

[Francis, 1951] Francis, J. R. D. (1951). The aerodynamic drag of a free water surface. *Proceedings of the Royal Society of London. Series A. Mathematical and Physical Sciences*, 206(1086):387–406.

[Francis, 1954] Francis, J. R. D. (1954). Wave motions and the aerodynamic drag on a free oil surface. *Phil. Mag.*, 45:695–702.

[Francis, 1956] Francis, J. R. D. (1956). LXIX. Correspondence. Wave motions on a free oil surface. *Philosophical Magazine*, 1(7):685–688.

[Fulgosi et al., 2003] Fulgosi, M., Lakehal, D., Banerjee, S., and De Angelis, V. (2003). Direct numerical simulation of turbulence in a sheared air–water flow with a deformable interface. *Journal of fluid mechanics*, 482:319–345.

[Funada and Joseph, 2001] Funada, T. and Joseph, D. (2001). Viscous potential flow analysis of Kelvin–Helmholtz instability in a channel. *J. Fluid Mech.*, 445:263–283.

[Gad-El-Hak et al., 1984] Gad-El-Hak, M., Blackwelder, R. F., and Riley, J. J. (1984). On the interaction of compliant coatings with boundary-layer flows. *J. Fluid Mech.*, 140:257–280.

[Gaster, 1962] Gaster, M. (1962). A note on the relation between temporally-increasing and spatially-increasing disturbances in hydrodynamic stability. *J. Fluid Mech.*, 14(02):222–224.

[Ghafoor et al., 2000] Ghafoor, N. A.-L., Zarnecki, J. C., Challenor, P., and Srokosz, M. A. (2000). Wind-driven surface waves on Titan. *Journal of Geophysical Research: Planets*, 105(E5):12077–12091.

[Gomit, 2013] Gomit, G. (2013). *Développement de techniques de mesure de surfaces libres par moyens optiques: Application à l'analyse de l'écoulement généré par un modèle de bateau en bassin des carènes*. PhD thesis, Université de Poitiers.

[Gondret et al., 1999] Gondret, P., Ern, P., Meignin, L., and Rabaud, M. (1999). Experimental evidence of a nonlinear transition from convective to absolute instability. *Phys. Rev. Lett.*, 82:1442–1445.

[Gondret and Rabaud, 1997] Gondret, P. and Rabaud, M. (1997). Shear instability of two-fluid parallel flow in a Hele-Shaw cell. *Phys. Fluids*, 9:3267–3274.

[Gottifredi and Jameson, 1970] Gottifredi, J. and Jameson, G. (1970). The growth of short waves on liquid surfaces under the action of a wind. *Proceedings of the Royal Society of London. A. Mathematical and Physical Sciences*, 319(1538):373–397.

[Graham et al., 2013] Graham, J., Lee, M., Malaya, N., Moser, R., Eyink, G., Meneveau, C., Kanov, K., Burns, R., and Szalay, A. (2013). Turbulent channel flow data set. Technical report, John Hopkins University.

[Grare et al., 2013] Grare, L., Peirson, W., Branger, H., Walker, J., Giovanangeli, J.-P., and Makin, V. (2013). Growth and dissipation of wind-forced, deep-water waves. *J. Fluid Mech.*, 722:5–50.

[Guyon et al., 2012] Guyon, E., Hulin, J.-P., and Petit, L. (2012). *Hydrodynamique Physique*. Editions CNRS, 3rd edition.

[Hara and Mei, 1991] Hara, T. and Mei, C. C. (1991). Frequency downshift in narrow-banded surface waves under the influence of wind. *J. Fluid Mech.*, 230:429–477.

[Hara and Mei, 1994] Hara, T. and Mei, C. C. (1994). Wind effects on the nonlinear evolution of slowly varying gravity—capillary waves. *J. Fluid Mech.*, 267:221–250.

[Hasselmann and Bösenberg, 1991] Hasselmann, D. and Bösenberg, J. (1991). Field measurements of wave-induced pressure over wind-sea and swell. *J. Fluid Mech.*, 230:391–428.

[Hayes et al., 2013] Hayes, A. G., Lorenz, R. D., Donelan, M. A., Manga, M., Lunine, J. I., Schneider, T., Lamb, M. P., Mitchell, J. M., Fischer, W. W., Graves, S. D., et al. (2013). Wind driven capillary-gravity waves on Titan's lakes: Hard to detect or non-existent? *Icarus*, 225:403–412.

[Helal, 2009] Helal, M. A. (2009). Introduction to solitons. In *Encyclopedia of Complexity and Systems Science*, pages 8504–8506. Springer.

[Hewitt, 2013] Hewitt, G. (2013). *Annular two-phase flow*. Elsevier.

[Hidy and Plate, 1966] Hidy, G. M. and Plate, E. J. (1966). Wind action on water standing in a laboratory channel. *J. Fluid Mech.*, 26(04):651–687.

[Hooper and Boyd, 1983] Hooper, A. P. and Boyd, W. G. C. (1983). Shear-flow instability at the interface between two viscous fluids. *J. Fluid Mech.*, 128:507–528.

[Hooper and Grimshaw, 1985] Hooper, A. P. and Grimshaw, R. (1985). Nonlinear instability at the interface between two viscous fluids. *Phys. Fluids (1958-1988)*, 28(1):37–45.

[Hsu and Hsu, 1983] Hsu, C.-T. and Hsu, E. Y. (1983). On the structure of turbulent flow over a progressive water wave: Theory and experiment in a transformed wave-following coordinate system. part 2. *Journal of Fluid Mechanics*, 131:123–153.

[Hsu et al., 1981] Hsu, C.-T., Hsu, E. Y., and Street, R. L. (1981). On the structure of turbulent flow over a progressive water wave: theory and experiment in a transformed, wave-following co-ordinate system. *Journal of Fluid Mechanics*, 105:87–117.

[Hu et al., 2006] Hu, Z., Morfey, C. L., and Sandham, N. D. (2006). Wall pressure and shear stress spectra from direct simulations of channel flow. *AIAA journal*, 44(7):1541–1549.

[Huang et al., 1999] Huang, N. E., Shen, Z., and Long, S. R. (1999). A new view of nonlinear water waves: Hilbert spectrum 1. *Annual Review of Fluid Mechanics*, 31(1):417–457.

[Huerre and Rossi, 1998] Huerre, P. and Rossi, M. (1998). Hydrodynamic instabilities in open flows. *Collection Alea Saclay Monographs and Texts in Statistical Physics*, pages 81–294.

[Iwamoto, 2002] Iwamoto, K. (2002). Database of fully developed channel flow. *Dept. of Mech. Eng., The Univ. of Tokyo, THTLAB Internal Report*, (No. ILR-0201).

[Iwamoto et al., 2002] Iwamoto, K., Suzuki, Y., and Kasagi, N. (2002). Reynolds number effect on wall turbulence: Toward effective feedback control. *Int. J. Heat and Fluid Flow*, 23:678–689.

[Janssen, 2004] Janssen, P. (2004). *The interaction of ocean waves and wind*. Cambridge University Press.

[Jeffreys, 1925] Jeffreys, H. (1925). On the formation of water waves by wind. *Proceedings of the Royal Society of London. Series A, Containing Papers of a Mathematical and Physical Character*, 107(742):189–206.

[Jimenez et al., 2004] Jimenez, J., Del Alamo, J. C., and Flores, O. (2004). The large-scale dynamics of near-wall turbulence. *J. Fluid Mech.*, 505:179–199.

[Jimenez and Hoyas, 2008] Jimenez, J. and Hoyas, S. (2008). Turbulent fluctuations above the buffer layer of wall-bounded flows. *J. Fluid Mech.*, 611:215–236.

[Kahma and Donelan, 1988] Kahma, K. and Donelan, M. A. (1988). A laboratory study of the minimum wind speed for wind wave generation. *J. Fluid Mech.*, 192:339–364.

[Karageorgis, 2012] Karageorgis, P. (2012). Dispersion relation for water waves with non-constant vorticity. *European Journal of Mechanics-B/Fluids*, 34:7–12.

[Katsis and Akylas, 1985] Katsis, C. and Akylas, T. R. (1985). Wind-generated surface waves on a viscous fluid. *Journal of Applied Mechanics*, 52(1):208–212.

[Kawai, 1979] Kawai, S. (1979). Generation of initial wavelets by instability of a coupled shear flow and their evolution to wind waves. *J. Fluid Mech.*, 93(4):661–703.

[Keulegan, 1951] Keulegan, G. H. (1951). Wind tides in small closed channels. *Journal of Research of the National Bureau of Standards*, 46:358–381.

[Kiefhaber, 2014] Kiefhaber, D. (2014). *Optical measurement of short wind waves - from the lab to the field*. PhD thesis, University of Heidelberg.

[Kiefhaber et al., 2014] Kiefhaber, D., Reith, S., Rocholz, R., and Jähne, B. (2014). High-speed imaging of short wind waves by shape from refraction. *Journal of the European Optical Society-Rapid publications*, 9:14015.

[Kim et al., 2011] Kim, H., Padrino, J. C., and Joseph, D. D. (2011). Viscous effects on Kelvin–Helmholtz instability in a channel. *J. Fluid Mech.*, 680:398–416.

[Komen et al., 1996] Komen, G. J., Cavaleri, L., Donelan, M., Hasselmann, K., Hasselmann, S., and Janssen, P. (1996). *Dynamics and modelling of ocean waves*. Cambridge university press.

[Kudryavtsev et al., 2014] Kudryavtsev, V., Chapron, B., and Makin, V. (2014). Impact of wind waves on the air-sea fluxes: A coupled model. *Journal of Geophysical Research: Oceans*, 119(2):1217–1236.

[Kunishi, 1963] Kunishi, H. (1963). An experimental study on the generation and growth of wind waves. *Disaster Prevention Research Institute, Kyoto University*, 61:1–41.

[Kurata et al., 1990] Kurata, J., Grattan, K. T. V., Uchiyama, H., and Tanaka, T. (1990). Water surface mesurement in a shallow channel using the transmitted image of a grating. *Rev. Sci. Instrum.*, 61:736.

[Lake and Yuen, 1978] Lake, B. M. and Yuen, H. C. (1978). A new model for nonlinear wind waves. Part 1. Physical model and experimental evidence. *J. Fluid Mech.*, 88(01):33–62.

[Lake et al., 1977] Lake, B. M., Yuen, H. C., Rungaldier, H., and Ferguson, W. E. (1977). Nonlinear deep-water waves: theory and experiment. Part 2. Evolution of a continuous wave train. *J. Fluid Mech.*, 83(01):49–74.

[Lamb, 1995] Lamb, H. (1995). *Hydrodynamics*. Sixth edition, Cambridge University Press.

[Larson and Wright, 1975] Larson, T. R. and Wright, J. W. (1975). Wind-generated gravity-capillary waves: Laboratory measurements of temporal growth rates using microwave backscatter. *J. Fluid Mech.*, 70(03):417–436.

[LeBlond and Mainardi, 1987] LeBlond, P. and Mainardi, F. (1987). The viscous damping of capillary-gravity waves. *Acta Mechanica*, 68:203–222.

[LeBlond and Mysak, 1981] LeBlond, P. H. and Mysak, L. A. (1981). *Waves in the Ocean*. Elsevier.

[Leckler et al., 2015] Leckler, F., Ardhuin, F., Peureux, C., Benetazzo, A., Bergamasco, F., and Dulov, V. (2015). Analysis and interpretation of frequency-wavenumber spectra of young wind waves. *J. Phys. Oceanogr.*, 45:2484–2484.

[Li et al., 2008] Li, Y., Perlman, E., Wan, M., Yang, Y., Burns, R., Meneveau, C., Burns, R., Chen, S., Szalay, A., and Eyink, G. (2008). A public turbulence database cluster and applications to study lagrangian evolution of velocity increments in turbulence. *J. Turbulence*, 9(31).

[Liao and Kaihatu, 2012] Liao, Y.-P. and Kaihatu, J. M. (2012). The numerical investigation of wave generation by low speed winds. *Coastal Engineering Proceedings*, 1(33):57.

[Liberzon, 2010] Liberzon, D. (2010). *Experimental study of the initial stages water waves generation by wind*. PhD thesis, Tel Aviv University.

[Liberzon and Shemer, 2011] Liberzon, D. and Shemer, L. (2011). Experimental study of the initial stages of wind waves' spatial evolution. *J. Fluid Mech.*, 681:462–498.

[Lighthill, 1978] Lighthill, J. (1978). *Waves in fluids*. Cambridge University Press, Cambridge.

[Lighthill, 1962] Lighthill, M. J. (1962). Physical interpretation of the mathematical theory of wave generation by wind. *J. Fluid Mech.*, 14:385–398.

[Lin et al., 2008] Lin, M.-Y., Moeng, C.-H., Tsai, W.-T., Sullivan, P. P., and Belcher, S. E. (2008). Direct numerical simulation of wind-wave generation processes. *J. Fluid Mech.*, 616:1–30.

[Lindsay, 1984] Lindsay, K. A. (1984). The Kelvin-Helmholtz instability for a viscous interface. *Acta mechanica*, 52(1):51–61.

[Lombardi et al., 1996] Lombardi, P., De Angelis, V., and Banerjee, S. (1996). Direct numerical simulation of near-interface turbulence in coupled gas-liquid flow. *Physics of Fluids (1994-present)*, 8(6):1643–1665.

[Longo, 2012] Longo, S. (2012). Wind-generated water waves in a wind tunnel: Free surface statistics, wind friction and mean air flow properties. *Coastal Engineering*, 61:27–41.

[Longo et al., 2012] Longo, S., Chiapponi, L., Clavero, M., Mäkelä, T., and Liang, D. (2012). Study of the turbulence in the air-side and water-side boundary layers in experimental laboratory wind induced surface waves. *Coastal Engineering*, 69:67–81.

[Longuet-Higgins, 1953] Longuet-Higgins, M. S. (1953). Mass transport in water waves. *Philosophical Transactions of the Royal Society of London. Series A, Mathematical and Physical Sciences*, 245(903):535–581.

[Longuet-Higgins and Stewart, 1961] Longuet-Higgins, M. S. and Stewart, R. W. (1961). The changes in amplitude of short gravity waves on steady non-uniform currents. *J. Fluid Mech.*, 10(04):529–549.

[Lorenz et al., 2005] Lorenz, R. D., Kraal, E. R., Eddlemon, E. E., Cheney, J., and Greeley, R. (2005). Sea-surface wave growth under extraterrestrial atmospheres: Preliminary wind tunnel experiments with application to Mars and Titan. *Icarus*, 175(2):556–560.

[Lorenz et al., 2010] Lorenz, R. D., Newman, C., and Lunine, J. I. (2010). Threshold of wave generation on Titan's lakes and seas: Effect of viscosity and implications for Cassini observations. *Icarus*, 207(2):932–937.

[Massel, 1996] Massel, S. R. (1996). *Ocean surface waves: their physics and prediction*, volume 11. World scientific.

[Matas, 2015] Matas, J.-P. (2015). Inviscid versus viscous instability mechanism of an air–water mixing layer. *Journal of Fluid Mechanics*, 768:375–387.

[Meier, 2002] Meier, G. (2002). Computerized background-oriented schlieren. *Exp. Fluids*, 33(1):181–187.

[Melville, 1982] Melville, W. K. (1982). The instability and breaking of deep-water waves. *J. Fluid Mech.*, 115:165–185.

[Michallet and Barthelemy, 1998] Michallet, H. and Barthelemy, E. (1998). Experimental study of interfacial solitary waves. *J. Fluid Mech.*, 366:159–177.

[Miles, 1957] Miles, J. W. (1957). On the generation of surface waves by shear flows. *J. Fluid Mech.*, 3:185–204.

[Miles, 1959a] Miles, J. W. (1959a). On the generation of surface waves by shear flows. Part 2. *J. Fluid Mech.*, 6:568–582.

[Miles, 1959b] Miles, J. W. (1959b). On the generation of surface waves by shear flows. Part 3. Kelvin-Helmholtz instability. *J. Fluid Mech.*, 6(04):583–598.

[Miles, 1962] Miles, J. W. (1962). On the generation of surface waves by shear flows. Part 4. *J. Fluid Mech.*, 13(03):433–448.

[Miles, 1967] Miles, J. W. (1967). On the generation of surface waves by shear flows. Part 5. *J. Fluid Mech.*, 30(01):163–175.

[Miles, 1993] Miles, J. W. (1993). Surface-wave generation revisited. *J. Fluid Mech.*, 256:427–441.

[Mitsuyasu and Honda, 1982] Mitsuyasu, H. and Honda, T. (1982). Wind-induced growth of water waves. *J. Fluid Mech.*, 123:425–442.

[Mitsuyasu and Rikiishi, 1978] Mitsuyasu, H. and Rikiishi, K. (1978). The growth of duration-limited wind waves. *J. Fluid Mech.*, 85(04):705–730.

[Moisy et al., 2012] Moisy, F., Michon, G.-J., Rabaud, M., and Sultan, E. (2012). Cross-waves induced by the vertical oscillation of a fully immersed vertical plate. *Phys. Fluids (1994-present)*, 24(2):022110.

[Moisy et al., 2009] Moisy, F., Rabaud, M., and Salsac, K. (2009). A synthetic schlieren method for the measurement of the topography of a liquid interface. *Exp. Fluids*, 46:1021–1036.

[Montalvo et al., 2013] Montalvo, P., Dorignac, J., Manna, M. A., Kharif, C., and Branger, H. (2013). Growth of surface wind-waves in water of finite depth. A theoretical approach. *Coastal Engineering*, 77:49–56.

[Morland and Saffman, 1993] Morland, L. C. and Saffman, P. G. (1993). Effect of wind profile on the instability of wind blowing over water. *J. Fluid Mech.*, 252:383–383.

[Newman, 1977] Newman, J. N. (1977). *Marine hydrodynamics*. MIT press.

[Ó Náraigh et al., 2011] Ó Náraigh, L., Spelt, P., Matar, O. K., and Zaki, T. A. (2011). Interfacial instability in turbulent flow over a liquid film in a channel. *International Journal of Multiphase Flow*, 37(7):812–830.

[Ó Náraigh et al., 2013] Ó Náraigh, L., Spelt, P. D., and Shaw, S. J. (2013). Absolute linear instability in laminar and turbulent gas–liquid two-layer channel flow. *J. Fluid Mech.*, 714:58–94.

[Ó Náraigh et al., 2014] Ó Náraigh, L., Valluri, P., Scott, D. M., Bethune, I., and Spelt, P. D. M. (2014). Linear instability, nonlinear instability and ligament dynamics in three-dimensional laminar two-layer liquid–liquid flows. *J. Fluid Mech.*, 750:464–506.

[Otto et al., 2013] Otto, T., Rossi, M., and Boeck, T. (2013). Viscous instability of a sheared liquid-gas interface: Dependence on fluid properties and basic velocity profile. *Phys. Fluids (1994-present)*, 25(3):032103.

[Padrino and Joseph, 2007] Padrino, J. C. and Joseph, D. D. (2007). Correction of Lamb's dissipation calculation for the effects of viscosity on capillary-gravity waves. *Phys. Fluids (1994-present)*, 19(8):082105.

[Paquier et al., 2015] Paquier, A., Moisy, F., and Rabaud, M. (2015). Surface deformations and wave generation by wind blowing over a viscous liquid. *Phys. Fluids*, 27:122103.

[Pedlosky, 2003] Pedlosky, J. (2003). *Waves in the ocean and atmosphere: introduction to wave dynamics*. Springer Science & Business Media.

[Peirson and Garcia, 2008] Peirson, W. L. and Garcia, A. W. (2008). On the wind-induced growth of slow water waves of finite steepness. *J. Fluid Mech.*, 608:243–274.

[Peregrine, 1983] Peregrine, D. H. (1983). Water waves, nonlinear Schrödinger equations and their solutions. *The Journal of the Australian Mathematical Society. Series B. Applied Mathematics*, 25(01):16–43.

[Perlman et al., 2007] Perlman, E., Burns, R., Li, Y., and Meneveau, C. (2007). Data exploration of turbulence simulations using a database cluster. In *Supercomputing SC07, ACM, IEEE*.

[Phillips, 1957] Phillips, O. M. (1957). On the generation of waves by turbulent wind. *J. Fluid Mech.*, 2(05):417–445.

[Plant, 1982] Plant, W. J. (1982). A relationship between wind stress and wave slope. *Journal of Geophysical Research: Oceans (1978–2012)*, 87(C3):1961–1967.

[Plant and Wright, 1977] Plant, W. J. and Wright, J. W. (1977). Growth and equilibrium of short gravity waves in a wind-wave tank. *J. Fluid Mech.*, 82(04):767–793.

[Plate et al., 1969] Plate, E. J., Chang, P. C., and Hidy, G. M. (1969). Experiments on the generation of small water waves by wind. *J. Fluid Mech.*, 35(4):625–656.

[Plate and Hidy, 1967] Plate, E. J. and Hidy, G. M. (1967). Laboratory study of air flowing over a smooth surface onto small water waves. *Journal of Geophysical Research*, 72(18):4627–4641.

[Pomeau and Le Berre, 2011] Pomeau, Y. and Le Berre, M. (2011). Nonlinearity and nonequilibrium together in Nature: wind waves in the open ocean. *The European Physical Journal D*, 62(1):73–80.

[Przadka et al., 2012] Przadka, A., Cabane, B., Pagneux, V., Maurel, A., and Petitjeans, P. (2012). Fourier transform profilometry for water waves: how to achieve clean water attenuation with diffusive reflection at the water surface? *Exp. Fluids*, 52(2):519–527.

[Raupach et al., 1991] Raupach, M. R., Antonia, R. A., and Rajagopalan, S. (1991). Rough-wall turbulent boundary layers. *Applied Mechanics Reviews*, 44(1):1–25.

[Ricci, 1992] Ricci, N. (1992). *Etude expérimentale des processus physiques responsables de la génération des premières vagues de vent.* PhD thesis, Université Aix-Marseille II.

[Russell, 1844] Russell, J. S. (1844). On waves. In *Report of fourteenth meeting of the British Association for the Advancement of Science, York*, pages 311–390.

[Ruyer-Quil et al., 2014] Ruyer-Quil, C., Kofman, N., Chasseur, D., and Mergui, S. (2014). Dynamics of falling liquid films. *The European Physical Journal E*, 37(4):1–17.

[Savtchenko et al., 1997] Savtchenko, A., Tang, S., and Wu, J. (1997). Effects of surfactant on the growth of wind waves - Simultaneous observations with optical and microwave sensors. *Journal of Marine Systems*, 13(1):273–282.

[Schlichting, 2000] Schlichting, H. (2000). *Boundary Layer Theory.* Springer, 8th edition.

[Schnieders, 2015] Schnieders, J. (2015). *Analyzing the footprints of turbulence producing mechanisms at the free water surface.* PhD thesis, University of Heidelberg.

[Segur and Oberstar, 1951] Segur, J. B. and Oberstar, H. E. (1951). Viscosity of glycerol and its aqueous solutions. *Industrial & Engineering Chemistry*, 43(9):2117–2120.

[Siddiqui and Loewen, 2007] Siddiqui, M. K. and Loewen, M. R. (2007). Characteristics of the wind drift layer and microscale breaking waves. *J. Fluid Mech.*, 573:417–456.

[Soap and Detergent Association, 1990] Soap and Detergent Association (1990). Glycerine: an overview. *Glycerine & Oleochemical Division, New York, NY.*

[Stewart, 1967] Stewart, R. W. (1967). Mechanics of the air–sea interface. *Phys. Fluids (1958-1988)*, 10(9):S47–S55.

[Sullivan et al., 2000] Sullivan, P. P., McWilliams, J. C., and Moeng, C.-H. (2000). Simulation of turbulent flow over idealized water waves. *J. Fluid Mech.*, 404:47–85.

[Sutherland, 1968] Sutherland, A. J. (1968). Growth of spectral components in a wind-generated wave train. *J. Fluid Mech.*, 33(03):545–560.

[Tang and Wu, 1992] Tang, S. and Wu, J. (1992). Suppression of wind-generated ripples by natural films: A laboratory study. *Journal of Geophysical Research: Oceans*, 97(C4):5301–5306.

[Taylor, 1940] Taylor, G. I. (1940). Generation of ripples by wind blowing over a viscous fluid. *The Scientific Papers of G. I. Taylor*, 3:244–254.

[Teixeira and Belcher, 2006] Teixeira, M. and Belcher, S. E. (2006). On the initiation of surface waves by turbulent shear flow. *Dynamics of atmospheres and oceans*, 41(1):1–27.

[Thomson, 1871] Thomson, W. (1871). XLVI. Hydrokinetic solutions and observations. *The London, Edinburgh, and Dublin Philosophical Magazine and Journal of Science*, 42(281):362–377.

[Tokinaga and Xie, 2011] Tokinaga, H. and Xie, S.-P. (2011). Wave- and Anemometer-Based Sea Surface Wind (WASWind) for Climate Change Analysis. *Journal of Climate*, 24(1):267–285.

[Tsai et al., 2005a] Tsai, W.-T., Chen, S.-M., and Moeng, C.-H. (2005a). A numerical study on the evolution and structure of a stress-driven free-surface turbulent shear flow. *J. Fluid Mech.*, 545:163–192.

[Tsai, 2002] Tsai, Y.-S. (2002). *The interaction of gravity-capillary water waves with a laminar air flow.* PhD thesis, University College London (University of London).

[Tsai et al., 2005b] Tsai, Y. S., Grass, A. J., and Simons, R. R. (2005b). On the spatial linear growth of gravity-capillary water waves sheared by a laminar air flow. *Phys. Fluids*, 17:095101.

[Tsoar and Blumberg, 2002] Tsoar, H. and Blumberg, D. (2002). Formation of parabolic dunes from barchan and transverse dunes along Israel's mediterranean coast. *Earth Surface Processes and Landforms*, 27(11):1147–1161.

[Tsubaki and Fujita, 2005] Tsubaki, R. and Fujita, I. (2005). Stereoscopic measurement of a fluctuating free surface with discontinuities. *Measurement Science and Technology*, 16(10):1894.

[Tulin, 1996] Tulin, M. P. (1996). Breaking of ocean waves and downshifting. In *Waves and Nonlinear Processes in Hydrodynamics*, pages 177–190. Springer.

[Valenzuela, 1976] Valenzuela, G. R. (1976). The growth of gravity-capillary waves in a coupled shear flow. *J. Fluid Mech.*, 76(02):229–250.

[Van Driest, 1956] Van Driest, E. R. (1956). On turbulent flow near a wall. *J. of Aero. Sc. (Institute of the Aeronautical Sciences)*, 23(11):1007–1011.

[van Gastel et al., 1985] van Gastel, K., Janssen, P., and Komen, G. J. (1985). On phase velocity and growth rate of wind-induced gravity-capillary waves. *J. Fluid Mech.*, 161:199–216.

[Veron and Melville, 2001] Veron, F. and Melville, W. K. (2001). Experiments on the stability and transition of wind-driven water surfaces. *J. Fluid Mech.*, 446(10):25–65.

[von Helmholtz, 1868] von Helmholtz, H. L. (1868). On discontinuous movements of fluids. *Philos. Mag.*, 36:337–346.

[Waseda et al., 2001] Waseda, T., Toba, Y., and Tulin, M. P. (2001). Adjustment of wind waves to sudden changes of wind speed. *Journal of oceanography*, 57(5):519–533.

[Wilson et al., 1973] Wilson, W. S., Banner, M. L., Flower, R. J., Michael, J. A., and Wilson, D. G. (1973). Wind-induced growth of mechanically generated water waves. *J. Fluid Mech.*, 58(3):435–460.

[Wu, 1975] Wu, J. (1975). Wind-induced drift currents. *J. Fluid Mech.*, 68(01):49–70.

[Wu, 1978] Wu, J. (1978). A note on minimum wind stress for wave inception. *Tellus*, 30(1):93–96.

[Yang and Shen, 2011] Yang, D. and Shen, L. (2011). Simulation of viscous flows with undulatory boundaries: Part II. Coupling with other solvers for two-fluid computations. *Journal of Computational Physics*, 230(14):5510–5531.

[Yih, 1967] Yih, C.-S. (1967). Instability due to viscosity stratification. *J. Fluid Mech.*, 27(02):337–352.

[Young and Wolfe, 2014] Young, W. R. and Wolfe, C. L. (2014). Generation of surface waves by shear-flow instability. *J. Fluid Mech.*, 739:276–307.

[Zavadsky et al., 2013] Zavadsky, A., Liberzon, D., and Shemer, L. (2013). Statistical analysis of the spatial evolution of the stationary wind wave field. *Journal of Physical Oceanography*, 43(1):65–79.

[Zavadsky and Shemer, 2012] Zavadsky, A. and Shemer, L. (2012). Characterization of turbulent airflow over evolving water-waves in a wind-wave tank. *Journal of Geophysical Research: Oceans (1978–2012)*, 117(C11):1–21.

[Zhang and Cox, 1994] Zhang, X. and Cox, C. S. (1994). Measuring the two-dimensional structure of a wavy water surface optically: A surface gradient detector. *Exp. Fluids*, 17(4):225–237.

ÉCOLE DOCTORALE
Sciences mécaniques et énergétiques, matériaux et géosciences (SMEMAG)

Titre : Génération et croissance des vagues à la surface d'un liquide visqueux sous l'effet du vent)
Mots clés : Ondes de surface, instabilités hydrodynamiques, génération d'ondes par le vent.

Résumé : Bien qu'ayant suscité de nombreuses études sur le sujet, un certain nombre de questions à propos de la formation des vagues sous l'effet du vent restent sans réponse précise. Dans ma thèse, j'aborde ce problème selon une approche peu explorée : l'étude expérimentale de la déformation sous l'effet du vent de la surface d'un liquide fortement visqueux. En effet, contrairement à la majeure partie de la littérature sur le sujet, le liquide que j'utilise n'est pas de l'eau mais un liquide sensiblement plus visqueux. Indépendamment des questions fondamentales sous-jacentes, cela a en pratique l'avantage de simplifier le problème. En effet, du fait de la forte viscosité du liquide, l'écoulement dans le liquide reste laminaire et les perturbations de l'interface qui ne sont pas amplifiées ne peuvent se propager que sur une distance limitée. Pour observer ces déformations de l'interface liquide-air, j'ai développé un nouveau montage expérimental sur lequel a été mise en œuvre la méthode de visualisation Free Surface Synthetic Schlieren (FS-SS). Cette technique non intrusive a permis de mesurer avec une résolution micrométrique les amplitudes de déformations de la surface et d'accéder aux premières déformations à faible vitesse de vent.

Dans un premier temps, les expériences ont été conduites sur un liquide trente fois plus visqueux que l'eau. Grâce aux données expérimentales obtenues par FS-SS, deux régimes de déformation de l'interface liquide-air ont été mis en évidence. À vitesse de vent faible, l'interface est recouverte de "wrinkles", des perturbations de faible amplitude désorganisées spatialement et globalement alignées dans le sens de l'écoulement. Ces wrinkles peuvent être interprétés comme l'effet sur l'interface des fluctuations de pression de l'écoulement turbulent d'air. à plus forte vitesse, au-dessus d'une vitesse critique, apparaissent des vagues transverses quasi-parallèles entre elles et perpendiculaires à la direction du vent. Les distinctions entre les deux régimes ont été détaillées et les non-linéarités émergeant au-dessus du seuil ont aussi été étudiées. Par la suite, la viscosité du liquide a été changée sur une large gamme. Il ressort des expériences que les deux régimes de déformation de l'interface sous l'effet du vent peuvent être identifiés pour l'ensemble des viscosités parcourues. Suite à ces résultats, un modèle décrivant l'évolution de l'amplitude des wrinkles en fonction du vent et de la viscosité du liquide a été développé.

Title : Generation and growth of wind waves over a viscous liquid
Keywords : Surface waves, hydrodynamic instabilities, wave generation by wind, wind waves.

Abstract: Despite numerous studies on the subject, the development of waves under the action of wind still retains a certain number of open questions. In my PhD, I approach this problem through a fairly uncommon angle: the experimental study of the deformation by wind of the surface of a highly viscous liquid. Indeed, contrary to the major part of the literature on the matter, the liquid I used is not water but a significantly more viscous liquid. Regardless of the fundamental underlying questions, this has the practical advantage of simplifying the problem. Indeed, due to the high viscosity of the liquid, the flow in the liquid stays laminar and the unamplified perturbations of the interface can only propagate over a limited distance.
To observe these deformations at the liquid-air interface, I have developed a new experimental set-up upon which the Free Surface Synthetic Schlieren (FS-SS) method of visualization was implemented. This non-intrusive technique allowed to measure with a micrometric accuracy the amplitude of the surface deformation and to access the first deformations at low wind velocity.

First, experiments were conducted over a liquid thirty times more viscous than water. The experimental data obtained by FS-SS show two regimes of deformation of the liquid-air interface. At low wind velocity, the interface is populated with "wrinkles", small-amplitude streamwise spatially disorganized perturbations. These wrinkles can be interpreted as the effect on the interface of the pressure fluctuations in the turbulent wind. At higher windspeed, above a critical velocity, transverse waves appear with quasi-parallel crests perpendicular to the wind direction. The distinctions between the two regimes have been detailed and the nonlinearities emerging above the threshold have also been studied.
Then, the viscosity of the liquid has been changed over a large range. It results from the experiments that the two regimes of surface deformation by wind can be identified for all the viscosities explored. Following these results, a model was developed to account for the evolution of the wrinkles' amplitude both with wind velocity and with viscosity.

Université Paris-Saclay
Espace Technologique / Immeuble Discovery
Route de l'Orme aux Merisiers RD 128 / 91190 Saint-Aubin, France